The University of Nottingham

UNITED KINGDOM · CHINA · MALAYSIA

Microstructure, mechanical properties and sliding wear behaviour of thermally sprayed cermet coatings.

Alhammali A. A. Younis

Thesis submitted to the University of Nottingham for the degree of Doctor of Philosophy

May 2016

Abstract

Thermally sprayed tungsten carbide cermet coatings are extensively used in engineering applications, such as cutting tools, rock and earth drilling tools. When coatings are compared, they often differ in a number of ways, such as being deposited from powder feedstock with different characteristics (e.g. particle size, powder porosity, method of manufacture, different carbide grain sizes, different volume fractions of binder, different binder types) and with different thermal spray systems. When a number of factors are varied at once, then it is very difficult to identify the causes of any differences observed in coating microstructure and performance.

In the current study, an attempt was made to vary just one variable at a time whilst keeping (as far as possible) the other variables constant. Experiments evaluated the independent effect of three parameters on the microstructure and performance of tungsten-carbide based coatings as follows: (a) metal binder type (comparing WC-12wt%Co and WC-12wt%Ni); (b) WC grain size (coarse and fine carbide size in WC-17wt%Co); and (c) metal binder content (WC-12wt%Co and WC-17wt%Co with similar carbide grain size). All feedstock powders used were agglomerated and sintered with similar particle size (-45+15 μm), deposited on mild steel substrates using a Metallisation MET-JET 4L kerosene-fuelled HVOF system. Coatings were characterized in terms of their microstructure, mechanical properties, and dry sliding wear behaviour. The research also addressed the possibility of using scratch testing as a method for evaluating the fracture mechanism of thick coatings and as a tool for predicting their wear behaviour.

The experimental results show more decomposition of WC (into W_2C and W) in the WC-12Co coating compared with the WC-12Ni coating. This could be due to melting occurring at lower temperature in the W-Co-C system than in the W-Ni-C system during particle heating in the spray gun. There also appeared to be more amorphous phase formation in the WC-12Co coating. Hardness and fracture toughness are both higher in the WC-12Co coating than in the WC-12Ni coating. Additionally, the WC-12Co coating required higher loads to induce fracture in the scratch test. In sliding

wear, both the WC-12Co and WC-12Ni exhibited a similar wear mechanism in mild wear but the WC-12Co coating withstood a higher applied load before the transition to severe wear.

The effect of the WC grain size on the WC-17Co coating was evaluated. The results show that fine and coarse carbide coatings have similar microstructural features. However, the fine carbide WC-17Co coating exhibited a higher hardness and lower fracture toughness. Furthermore, the fine carbide WC-17Co coating required higher loads to induce fracture in the scratch test compared to the coarse carbide WC-17Co coating. In sliding wear, both coatings exhibited a similar wear mechanism and rate in mild wear. However, the WC-17Co coating with fine WC grain size withstood higher loads before the transition from mild to severe wear.

The coating with lower metal binder content (WC-12Co) exhibited higher levels of decomposition compared with the coating with higher metal binder content (WC-17Co). Increasing the binder content resulted in reduction in the microhardness, increased the fracture toughness and reduced critical loads through all scratch test sections. In sliding wear, the coating with the higher binder content exhibited a wear rate up to four times higher than that of the coating with the lower binder content.

Overall, coatings with higher critical load during scratch testing also exhibited higher wear resistance. A linear relationship between the scratch critical load for development of semi-circular cracks and the mild – severe wear transition load is demonstrated. Consequently, it is proposed that scratch testing may be used to predict load bearing capacity in sliding wear.

Acknowledgements

I would like to thank my supervisors, Professor Graham McCartney and Professor Philip Shipway, for their patient guidance, encouragement and advice that they have readily provided throughout my time as their student. My appreciation is beyond expression to Dr. Katy Voisey for her support.

I would also like to thank all staff members within the Materials Engineering Department of the University of Nottingham for their help with the laboratory experimental work.

I would like to express my deepest gratitude to all my friends, and single out Dr. Mustafa Amami and Dr. Hocine Dridi, for their encouragement and for making my life in England most enjoyable and memorable.

Much love and thanks to my parents, wife, children, and siblings who are the source of my happiness: it is the unfailing support of my family that has enabled me to complete this Ph.D. project.

Thank you all.

Table of Contents

Tables List

Figures List

CHAPTER 1 Introduction

1.1 Introduction

Surface engineering includes the application of traditional and innovative surface technologies to improve the properties of bulk materials. Surface engineering has an important technological, economic and environmental impact on modern science through the cost reduction, increased productivity, design changes and technical innovation. (Bell 1992; Bell et al. 1998; and ASM Handbook Vol. 5 Surface Engineering 1994). Coating technology is one of the most common methods to protect the surfaces of engineering components from wear and corrosion. Coatings are mainly desirable and occasionally important for many reasons including unique properties, economics, materials protection, or design flexibility. This near-surface area is created by depositing a coating onto bulk material surface by processes such as physical or chemical vapour deposition, electro deposition, and thermal spraying (Bunshah 2001; Davis 2004).

Thermal spray coating processes (TS) are a set of coating processes that use thermal energy produced by combustion or electrical methods. TS tends to be gathered into three groups: combustion flame, electric arc, and plasma arc spray. A broad range of materials can be used as TS coating materials. TS applies coatings to substrates without significant heat input. TS is also able to strip off and recoat worn or damaged coatings without changing part properties or dimensions. TS can be distinguished according to the particle velocity and temperature. (Pawlowski 2008)

High velocity oxy-fuel (HVOF) is one of the combustion-based methods. The combination of reasonable particle temperatures with high particle velocities in HVOF processes give dense, high adhesion, and low oxidation coatings. The field of hard metals and cermet coatings, such as WC-Co, WC-Ni and Cr_3C_2-NiCr is the main application of HVOF due to the extremely high wear resistance and density (Hashmi 2014). Currently, liquid-fuelled systems have started to be used with HVOF instead of gas-fuelled systems due to the low-cost of kerosene fuels and the superior acceleration of liquid-fuelled guns. Also, liquid-fuelled HVOF systems provide dense coatings, with

good bonding, higher particle velocities, lower temperatures, and higher wear resistance than air plasma sprayed (APS) coatings (Sudaprasert et al. 2003; Zhang et al. 2003)

Due to their excellent combination of hardness, fracture toughness and wear resistance, ceramic–metal (cermet) composites are extensively used to give wear resistance to parts such as cutting, and drilling (Çelik 2013; Shao et al. 2003). WC-based cermets, such as WC-Co have been chosen to be commonly used in industrial sectors to increase the wear resistance of machine parts (Çelik 2013; Dvornik and Zaytsev 2013; Gu et al. 2012; Żórawski 2013). The WC-based cermets, mix the hard WC phase and a ductile metallic binder phase with different proportions to provide materials with a wide range of properties (Nahvi and Jafari 2016).

The properties and performance of WC cermet coatings depend on the size, shape and distribution of WC carbides, and the composition and content of the metallic matrix as well, which together form the coating microstructure. For optimal performance, the coating ought to have large extent of retained WC particles finely dispersed within the metallic matrix which reflects the relation between deposition parameters, coating microstructure and wear resistance (Aristizabal et al. 2010; Mateen et al. 2011; Nerz et al. 1992; Saha and Khan 2010). This depends fundamentally on the WC decomposition level during HVOF coating, leading to the formation of non-WC phases and complex carbides in the coating microstructure (Babu et al. 2008; Li et al. 1996; Yang et al. 2003b). Due to their high brittleness, these non-WC phases degrade the wear performance of the cermet coatings by decreasing the fracture toughness. WC decomposition is a function of powder characteristics, flame temperature and particles velocity (Guilemany et al. 2005; Ishikawa et al. 2005; Stewart et al. 1999; Yang et al. 2006).

Scratch test is one of significantly used, quick, and effective techniques to get the critical loads coupled with adhesion properties of coating. Scratch test is typically used to measure adhesion of thin coatings. However, Ghabchi et al. (2014) used scratch tests to develop a damage mechanism map for thermal sprayed WC–CoCr coatings. The results pointed to a significant role of stresses and modulus on resistance to scratch. Coatings with higher developing stress and modulus resulting from improved melting

show higher critical load for delaminating. The methodology gives a strategy for using the in situ process monitoring as a tool for describing coating behaviour under contact load situations.

Due to their good corrosion and wear resistance, excellent wetting, adhesion, and adequate mechanical properties such as toughness, stiffness and thermal conductivity, tungsten carbide-based cermet has become extensively used in a great number of applications, such as cutting tools, rock and earth drilling tools, drawing and sheet metal forming tools and dies, wear components such as nozzles, plunges, cutters of paper and other engineering applications (Kübarsepp et al. 2001b). However for the developments in the area of hardmetal, finding alternative materials for replacing Co as the binder phase is essential where the shortage of Co makes it a high-priced product and the main ore areas are less reachable to the industrial sectors. Also, the low corrosion of WC-Co cannot meet the increasing requirements under different working conditions. Moreover, Co is classified as toxic and carcinogenic and the Co dust is principally responsible for work-related diseases of plant maintenance workers.

Based on these reasons, there has been a significant effort to replace cobalt with other metals. The most likely alternative binders are the transition metals iron and nickel associated with cobalt. Nickel has received the most attention as an alternative as its structure and physical properties are similar to cobalt. However, cobalt is metastable and can transform to hcp structure and it is much more strongly magnetic (Tekmen et al. 2004; Voitovich et al. 1996). One of the core researches in this area is that carried out by Berger (2008) where he compared WC-Co with WC-Ni cermet coatings to investigate the impact of the metal binder type. The research studied the erosion and oscillating sliding wear resistance of HVOF-sprayed WC–Co and WC–Ni based coatings alloyed with different amounts of chromium. WC–Co and WC–Ni with five chromium alloyed feedstock agglomerated and sintered powders were sprayed with a liquid fuelled HVOF-spray process. Starting feedstock powders of both WC-Co and WC-Ni consisted of WC and metallic (Co/Ni) phases, while the coatings contain W_2C and metallic tungsten in addition to retained powder phases. The results illustrated that WC-Co coating has higher hardness than the WC-Ni coating. Also, using cobalt as a metal binder enhanced the erosive wear resistance. A dependence on the chromium

content was not detected. Metal binder type and chromium content do not give sizeable impact on the sliding wear alongside a hard metal counter body.

Celik et al (2006) assess the microstructural and mechanical properties of WC-13wt%Co and WC-12wt%Ni cermet coatings for a roller cylinder. The results showed that all coatings have highly dense structure as well as similar microstructure. This is in addition to their low oxide and porosity contents and the good contact to the substrate. The results show also that the microhardness of WC–Ni is higher than WC–Co which can be attributed to the higher thickness of WC-Ni. Moreover, the total wear loss of WC–Co is more than WC–Ni. However, the WC-based cermet powders were not completely identical, since the metal binder content is different (13wt% Co and 12wt% Ni). Also, there is NiAl bond coat between the WC-based cermet coatings and the stainless steel substrate. Furthermore, the coating thickness of WC-Co was 250 µm and 315 µm for WC-Ni coating. All these factors make it hard to compare the mechanical properties and the wear behaviour of WC-Co and WC-Ni coatings in the right way.

In general, compared with WC–Co system, which has been widely investigated due to its commercial importance, there is still limited information and a lack of knowledge on alternative binders such as those based on Nickel. Furthermore, to date, there is no systematic study that has been performed to clearly investigate the effect of metal binder type, WC grain size, and metal binder content on the coatings microstructure, mechanical properties, and sliding wear behaviour. Furthermore, more investigations on utilising scratch test with thick coatings are needed. Thus it appears to be worthwhile to carry out investigations to cover these points which will be the focus of this research.

1.2 Aims and Objectives

The aim behind this project is to provide more investigations on microstructure, mechanical properties and sliding wear behaviour of thermally sprayed cermet coatings. This will be carried out throughout the following objectives:

1- Investigating the effect of metal binder type on the coatings microstructure, mechanical properties, and dry sliding wear behaviour using WC-12wt%Co and WC-12wt%Ni feedstock powders. Both powders are agglomerated and sintered with similar particle size (-45+15 µm).
2- Investigating the effect of WC grain size (cores and fine) on the coatings microstructure, mechanical properties, and dry sliding wear behaviour using WC-17wt%Co feedstock powder. Both cores and fine powders are agglomeration and sintering with similar particle size (-45+15 µm).
3- Investigating the effect of metal binder content on the coatings microstructure, mechanical properties, and dry sliding wear behaviour using WC-12wt%Co and WC-17wt%Co feedstock powders. Both powders are agglomeration and sintering with similar particle size (-45+15 µm).
4- Investigating the possibility of using scratch test as a new method for evaluating thick coatings fracture mechanism and predicting their wear behaviour.

1.3 Thesis Structure

The first chapter of this thesis includes general introduction and the aim and objectives of the project. This is followed by Literature Review which includes the main researches carried out in the area of thermal spray WC-M cermet coating and the most significant progress in this subject. Chapter three illustrates the experimental procedures where the specific materials and techniques used to produce the coatings are explained in details. The tests used to characterise the coatings will be also described. Chapter four investigates the effect of metal binder type on microstructure, mechanical properties and dry sliding wear behaviour of thermally sprayed WC-M cermet coatings, including the results and discussion. Chapter five investigates the effect of the WC grain size on microstructure, mechanical properties and dry sliding wear behaviour of thermally sprayed WC-17Co coatings, including the results and discussion. Chapter six includes extracting the effect of metal binder content on the coatings microstructure, mechanical properties, and dry sliding wear behaviour based on the results of chapters four and five. The last chapter gives general conclusions about the objectives investigated throughout this project and illustrates a number of recommendations and future works related to this research.

CHAPTER 2 Literature Review

This chapter will be split into two sections. In first section brief fundamentals knowledge related to the subject will be given. In the second section, the previous studies related to the objectives covered in this study will be illustrated.

2.1 Fundamental knowledge

In this section brief basic knowledge related to the study topic will be covered. This will include surface engineering and thermal spray coatings, hardmetals and cermet coatings, wear types and theory and finally basic fundamentals of scratch test.

2.1.1 Surface engineering

Extending the life of engineering components, improving their performance, and enhancing their appearance are very essential. As the performance demands have increased the significance of surface engineering (cleaning, finishing, and coating) have increased as well. The term surface engineering was defined in the ASM Handbook Volume 5 as follows: "treatment of the surface and near-surface regions of a material to allow the surface to perform functions that are distinct from those functions demanded from the bulk of the material" (ASM Handbook, Volume 5, Surface Engineering, 1994). Surface engineering includes the application of traditional and innovative surface technologies to create a composite material with properties unattainable in either the bulk or surface material. Normally, surface technologies are applied to existing designs of engineering components. However, ideally, surface engineering involves the design of the component with knowledge of the surface treatment to be employed (Bell 1992). Surface engineering has become a well-known technology and has had an important technological, economic and environmental impact on modern science and technology through the cost reduction, increased profitability, design changes and technical innovation. Certainly, it is now broadly documented that surface engineering is a vital technology that will support almost all industrial sectors (Bell et al. 1998).

A surface is defined as “an interface between a solid object and its surroundings”. The object is restricted to a solid, since coatings are applied to surfaces to protect them when they interface with other solids, liquids, or gases, or to improve the surface for aesthetic goals. In the performance of the component, these interfaces include physical, chemical, electrical, and other forces. These forces can lower the performance of these components or even cause them to fail. The effects of these forces could be mitigated by applying the right coating on the component surface. Composites are the most materials commonly used in high technology applications. Their near-surface region properties are differing from those of the bulk materials. This is caused by the requirement that the material exhibit a combination of different, and sometimes conflicting, properties. For instance, a specific engineering component could be obligatory to have high hardness and toughness to resist brittle crack propagation. This combination of properties could be achieved by applying a composite material with high surface hardness and a tough core. Overall, coatings are mostly desirable, or sometimes crucial, for many reasons including unique properties, economics, materials conservation, or design flexibility which can be achieved by separating the surface properties from the bulk properties. This near-surface region is created by depositing a coating onto bulk material surface by processes such as physical or chemical vapour deposition, electrodeposition, and thermal spraying (Bunshah 2001; Davis 2004).

2.1.1.1 Thermal spray coatings

Thermal spray is a general term used to characterise a set of coating processes which use the thermal energy produced by combustion or electrical methods. The thermal spray processes are usually gathered into three major groups: flame spray, electric arc spray, and plasma arc spray, with a number of subsets falling under each group as illustrated in Figure 2-1. The coating material (in powder, wire, or rod form) is heated to a molten or semi-molten state (Pawlowski 2008).

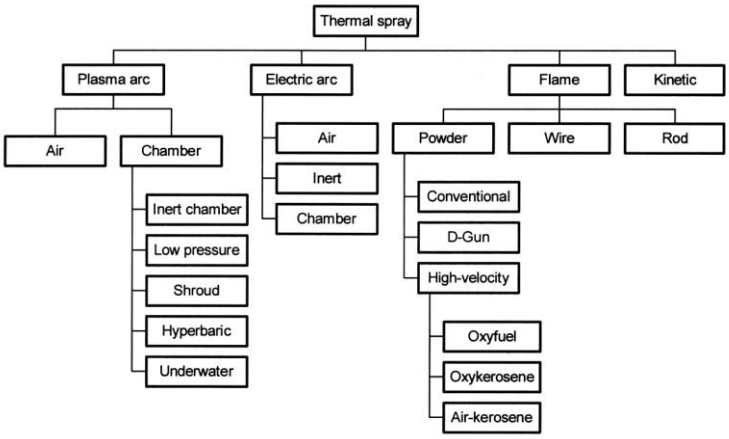

Figure 2-1: Thermal spray processes and subsets, adapted from (Davis 2004).

Simultaneously, heated particles are accelerated and pushed to a prepared substrate by either process gases or atomisation jets. The high temperatures and speeds that particles achieved during the coating process are resulting in important droplet deformation on impact at a substrate surface, creating lamellar thin layer, frequently termed "splats". Splat is the single impacted droplet/particle, as illustrated in Figure 2-2. Overlapped splats are solidified and adhered together to form the coating layers. So, the splat is the basic structural building block in thermal spray coatings. Splats are produced when the accelerated, particles impact the substrate surface. Individual splats are normally thin (~1 to 20 μm), and each droplet cools at very high rates (>10^6 K/s for metals) to form the coating.

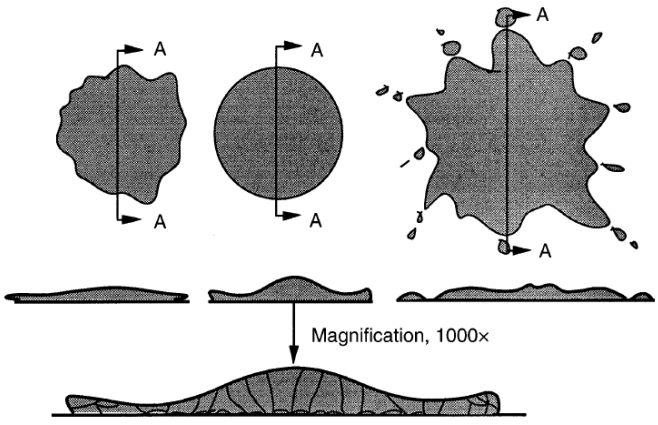

Figure 2-2: Schematic thermal spray splat structures, adapted from (Davis 2004).

The coating properties are determined from the different features such as the lamellar coating structure, unmelted particles, coating porosity, oxide inclusions, grains size, coating phases, cracks, and bond interfaces. Figure 2-3 shows the schematic of thermally sprayed coating microstructure illustrating most of these features. These coating defects differ according to the spray process, selected coating parameters, and the sprayed material.

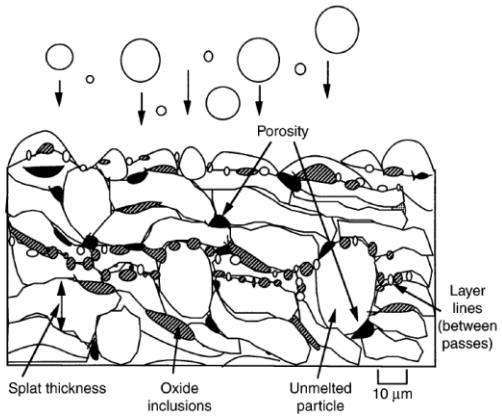

Figure 2-3: Schematic illustration of thermal spray coating microstructure viewing the common features, adapted from (Davis 2004).

The schematic representation of a powder spray process in Figure 2-4 is showing the major process characteristics affecting coating quality.

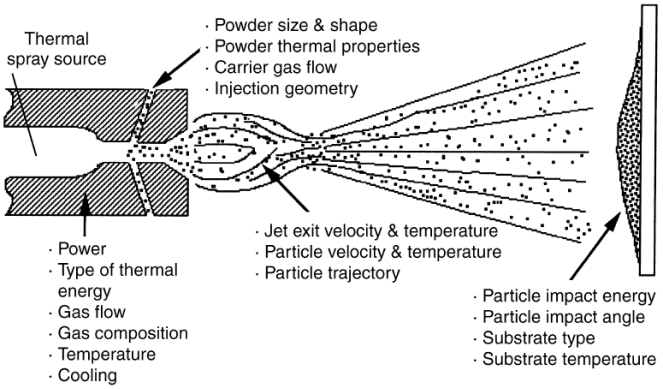

Figure 2-4: Typical thermal spray process parameters and variables, adapted from (Davis 2004).

The main advantages of thermal spray coating processes could be summarised in three points. First, a broad range of materials that can be produce coatings. Almost any material that melts without decomposing can be used. Second, most thermal spray processes can apply coatings to substrates without significant heat input. The third advantage is the ability to strip off and recoat worn or damaged coatings without changing part properties or dimensions. However, the major disadvantage of thermal spray coating processes is the line-of-sight nature of these deposition processes. They can only coat what the torch can "see". Also, there are size restrictions, small, deep cavities into which a torch will not fit are impossible to coat (Davis 2004).

Thermal spray processes can be distinguished according to the particle velocity and process temperature, as exhibited in Figure 2-5. Financial factors such as deposition efficiency and powder feed rates are further reasons for the realisation of efficient coating solutions. Regarding hardmetal coatings, coating development is currently motivated by the search for the optimum combination of particle velocity and process temperature to create dense coatings at high deposition efficiency and high powder feed rates (Berger 2015).

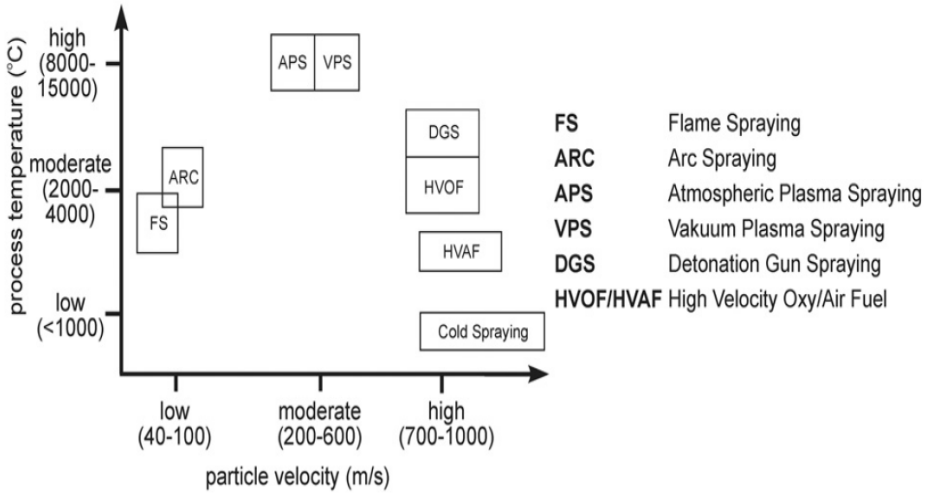

Figure 2-5: Schematic illustration of grouping of process temperature and velocity for the different thermal spray processes (Berger 2015).

2.1.1.2 High velocity oxy-fuel spraying

High-velocity flame spraying (HVFS), commonly called HVOF was developed at the beginning of the 1980s, and used industrially just during last few decades. The first module of this system was the JetKote process, which established by Browning Engineering. Unlike detonation spray, HVOF operates on a continuous steady-state basis (Bunshah 2001).

High-velocity flame spraying (HVFS) includes a number of different combustion flame coating processes such as high-velocity oxygen-fuel (HVOF), high-pressure high-velocity oxygen-fuel (HP-HVOF), high-velocity air-fuel (HVAF), high-velocity impact-fusion spraying, and other novel techniques, for instance, the warm spraying process. In all processes the fuel, (gaseous or liquid), is combusted in a combustion chamber of the gun with oxidizer (oxygen or air). Mainly all processes are similar, however they are different from each other in terms of gun design, fuel type, oxidizer type and particle temperature and velocity. The thermal energy of HVOF process is partially replaced with the high kinetic energy, this increases the particle velocity. The particle temperature in this coating process is not extremely high as in many other spray processes, such as plasma spraying. Particle temperature is kept as low as possible at a level where the deposition process has adequate deposition efficiency.

Figure 2-6 compares HVOF processes in terms of particle temperature versus particle velocity. The arrow shows development movement in which process temperature is decrease at the same time as particle velocity increase (Hashmi 2014).

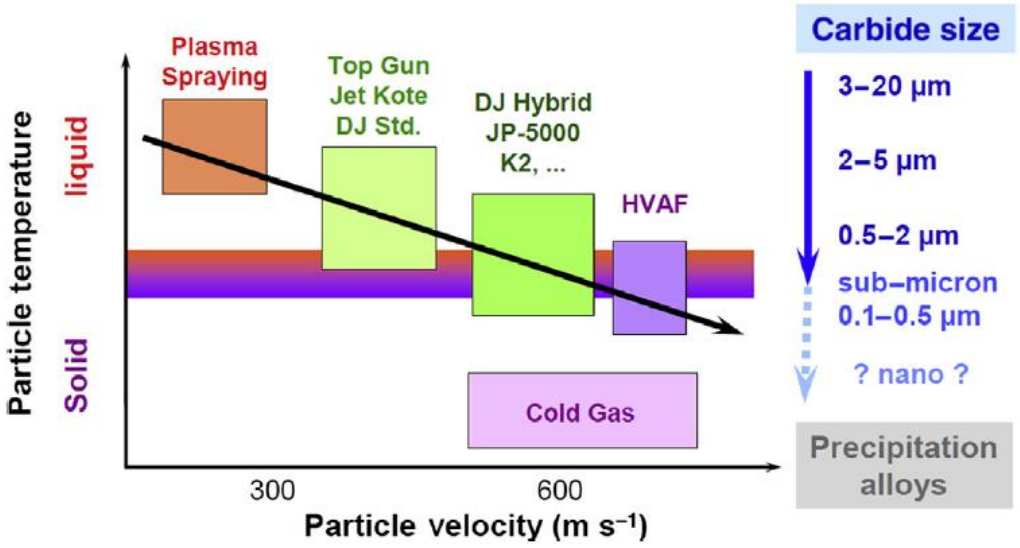

Figure 2-6: Overview of particle temperatures and velocities for plasma spraying and various HVOF spraying systems (Hashmi 2014).

The combination of moderate particle temperatures with high particle velocities in HVOF processes produce dense, high adhesion, and low oxidation coatings. As HVOF processes were principally developed for tungsten carbide based cermet (WC-Co) coatings, the high retained carbides (WC) in the coating microstructure are a further clear advantage of this process. This consequently leads to the significant improvement in mechanical and wear properties compared to other thermal spray processes, such as, plasma sprayed coatings (Hashmi 2014).

The quality of HVOF coatings mainly depends on the particle temperature and velocity. The HVOF gun can produce a supersonic flame with a maximum velocity of 2530 ms^{-1} and a maximum temperature of 3200 K (Cheng et al. 2001).

The high-velocity oxy-fuel guns can be divided into four major designs:

First design is axially aligned combustion chambers and nozzles. The fuel gases are provided into the combustion chamber through a mixer. Powder particles and carrier gas are injected into the combustion chamber through a powder port in the centre of the mixer face, Figure 2-7a.

Second, the combustion chamber feed hot fuel gases through a right angle connector into the nozzle. Coating powder is injected in the rear face of the connector through a port; this centres the powder stream within the nozzle, Figure 2-7b.

Third HVOF gun design is a modification of conventional flame gun. The combustion chamber may or may not be restricted by a water cooling nozzle where the powder stream and carrier gas is injected, Figure 2-7c.

The fourth HVOF gun design is high-pressure, kerosene-fuelled spray systems. The coating powder is radially injected downstream of the combustor exit, Figure 2-7d (Davis 2004).

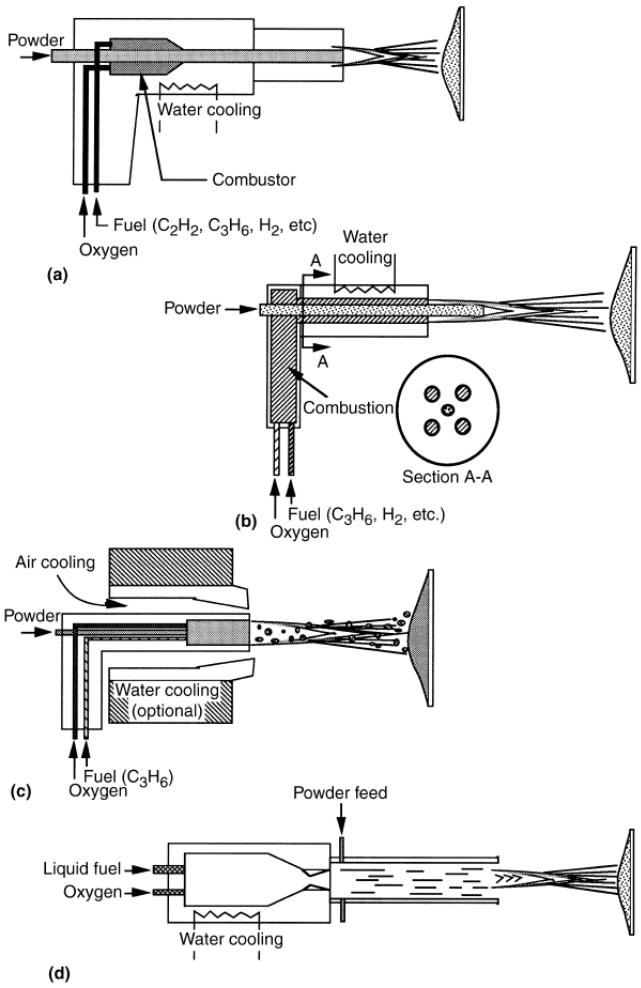

Figure 2-7: Commercially available high-velocity oxy-fuel thermal spray guns. (a) HV-2000. (b) JetKote. (c) Diamond Jet (D-J). (d) JP-5000 (Davis 2004)

2.1.1.3 Liquid fuel HVOF

Recently, the high-velocity oxygen fuel (HVOF) thermal spraying moved from gas-fuelled to liquid-fuelled systems. The use of low-cost fuels such as kerosene is the major advantage from this development. Furthermore, liquid-fuelled HVOF guns give superior acceleration to the gas flow and high momentum output to powder particles due to the convergent–divergent nozzle design. Researchers report that liquid-fuelled HVOF systems produce dense highly bonded coatings without over-melting the powder particles compared to gas-fuelled systems (Zhang et al. 2003).

Sudaprasert et al. (2003) studied the sliding wear behaviour of WC–Co coatings HVOF sprayed with both liquid-fuelled (HVOLF) and gas-fuelled (HVOGF) systems. They reported that during the gas fuelled spraying of coatings (HVOGF) the metal binder (cobalt) is fully melted, this leads to higher decomposition of the WC particles and forms a highly alloyed matrix. Even though the matrix phase is slightly brittle due to its amorphous structure the cohesion of this coating is high, with well bonded carbides to the matrix. In contrast, through the liquid fuelled sprayed coatings (HVOLF) the metal binder is partially melted as a shell around the powder particle where the core remains solid. On impact with the substrate to form the coating, the solid core experiences major mechanical damage causing fracture of the WC particles and decreasing the cohesion of the carbide–matrix. Even though the decomposition of cermet powders in thermally sprayed coatings has been known to reduce the wear resistance, coatings produced with low decomposition degree also leads to mechanical damage of the particles on impact and consequently the wear resistance can be affected by another mechanism, specifically the easy removal of damaged material during wear process.

Schwetzke and Kreye (1999) studied the cermet coating with different high-velocity oxygen fuel spray systems (JetKote, Top Gun, Diamond Jet (DJ) Standard, DJ 2600, DJ 2700, JP-5000, and Top Gun-K) using agglomerated and sintered WC-17Co powder with particle size of –45 + 10 μm. They investigate the decomposition and oxidation of the coating material through different spray processes. Coatings hardness, bond strength, abrasive wear, and corrosion resistance were characterised according to

coating process. Table 2-1 shows the fuels and the process parameters used, and the results of coating hardness and abrasive wear. The degree of phase transformation of starting powder is depending on the spray system and spray parameters. This study reports that phase transformation has insignificant effect on coating properties. So, when the optimum powder and process parameters are selected, coatings of high hardness and wear resistance can be produced with all HVOF spray systems. Phase transformation is depending on the heat transferred to the powder particles, on the flame temperature, and on the powder type used. In the gas fuelled HVOF systems, such as Top Gun system, the powder is injected directly into the combustion chamber. This consequently increases the degree of phase transformations. In contrast, with liquid fuelled HVOF spray systems, such as JP-5000 and Top Gun-K, when the powder is injected behind the combustion chamber, where the flame temperature is low, low degree of phase transformation occurs. The same results are reported when the flame temperature is reduced by cooling air as in the DJ 2600 and 2700 systems. Hardness and bond strength of the coatings are mostly affected by the particles impact velocity, thus, with liquid fuelled HVOF systems a converging-diverging nozzle is used, which provides superior particle velocities.

Table 2-1: Spray parameters and properties of WC-17Co Coatings sprayed with different HVOF systems and fuels (Schwetzke and Kreye 1999).

High velocity oxygen-fuel system	Fuel	Fuel flow, m^3/h	Oxygen flow, m^3/h	Oxygen/ fuel ratio	Powder feed rate, g/min	Carbon content, wt%	Carbon loss, %	Hardness, 0.3 HV	Abrasive wear, mg/1200 DS
Jet Kote	Hydrogen	25.5	12.8	0.5	30-40	3.8	27	1080	4.0
	Propane	3.0	18.0	6.0	30-40	2.8	46	1200	3.3
	Ethylene	4.8	28.4	5.9	30-40	3.1	40	1240	2.9
Top Gun	Hydrogen	26.0	13.0	0.5	30-40	1.7	67	1080	8.4
	Propane	3.0	15.0	5.0	30-40	2.2	58	1240	3.8
	Ethylene	4.7	14.1	3.0	30-40	2.1	60	1110	5.5
DJ Standard	Propane	4.4	15.8	4.6	40-50	3.4	35	980	4.5
DJ 2600	Hydrogen	38.2	12.8	0.45(a)	60-70	3.2	38	1340	3.0
DJ 2700	Propane	4.1	14.5	4.6(a)	60-70	3.5	33	1390	2.9
	Ethylene	6.8	15.0	2.9(a)	60-70	3.1	40	1400	3.5
JP-5000	Kerosene	20.8 l/h	53.6	4.3(b)	80	3.3	37	1490	3.6
Top Gun-K	Kerosene	18.0 l/h	55.0	5.1(b)	80	3.7	29	1330	3.1

Spray powder: WC-Co 83-17, agglomerated sintered, –45 + 10 µm, carbon content 5.2 wt%. DS, double stroke. (a) Including the oxygen fraction of the compressed air. (b) Standardized mass ratio oxygen/kerosene.

2.1.2 Hardmetals and cermet coatings

Hardmetals and cemented carbides are two terms which describe the same thing; “Hardmetals” is a term used in Europe, where “Cemented carbides” is commonly used in USA but also in European English literature. In industry, the hardmetals that contain WC phase are usually termed “cemented carbides” (Ortner et al. 2014).

Cermet, the original term was created by linking ceramic and metal into a one word to describe a composite. This mixture of phases keeps the required properties of metals and ceramics (Mura et al. 2013). Cermets based on Ti(C, N) and show high wear resistance at high cutting rates when compared to conventional WC–Co hardmetals. Moreover they show long lifetimes and an excellent surface quality of machined materials (Ortner et al. 2014).

Even though both powder metallurgy (PM) and thermal spray (TS) use mainly similar hard phase-binder metal composite materials, the improvement of both areas happened nearly independently from each other. Moreover, the traditional terms for these composites is different in each area and frequently leads to misunderstandings (Berger 2007). Bulk parts produced by PM, are called “hardmetals” or “cemented carbides”, where the term “cemented carbides” is often used for WC-based composites only. Different meanings were given for the term ‘cermet’ (Ortner et al. 2014). Frequently it is connected to TiC-Ni based composites. In thermal spray all hard phase based coatings are generally termed as “carbide coatings”, however, occasionally also as “cermet”. It appears that the term “hardmetal coatings” best describes the state-of-the-art thermal spray coatings of this class of material (Berger 2015).

2.1.2.1 Hardmetals

Hardmetals or cemented carbides (sometimes called sintered carbides) are the composite materials that consist of one or more, hard components and a ductile metal binder which provides a certain degree of toughness. Hardmetals were first commercially available from German company Friedrich Krupp AG 1927, given the name "Widia" from German words "wie Diamant" which means “like diamond”.

Hardmetals are produced by liquid phase sintering of mixed and compressed powder mixture of carbides of the transition metals (such as WC, TiC, TaC) with mainly cobalt as metal binder. Properties of composite material mainly depend on the properties of their individual phases, such as, size and distribution of those phases, state of aggregation of the carbide particles, and the interfacial energies and the state of stress between the individual phases. Hardmetals mainly were used for wire drawing dies and as wear resistant materials. Hardmetals are used for metal cutting applications after the titanium carbide (TiC) was used as a further additive to the basic tungsten carbide-cobalt composition. Nowadays more than 80% of hardmetals is used for metal cutting industry (Ettmayer 1989).

Cemented tungsten carbides (hardmetals) and cermets are mostly used for wear applications. They are used in all types of wear applications including abrasive, sliding, fretting and erosive wear. Applications of tungsten carbide-based hardmetals include cutting, rock and earth drilling tools, drawing and sheet metal forming tools (Kübarsepp et al. 2001a; Verdon et al. 1998).

The exceptional wear resistance of the cemented carbides is attributed to their unique combination of high hardness and fracture toughness. Cermet composition and microstructure extensively effect their mechanical properties and wear resistance. For instance, for WC-Co alloys of the same carbide grain size, the hardness decreases with increasing binder volume fraction and binder mean free path, while the fracture toughness shows an opposite trend. The relationships between wear resistance and the compositional and microstructural parameters are generally more complex. Even given the complex role of the microstructure it is obvious that both hardness and fracture toughness are significant mechanical properties that control the wear resistance of cermet (Shetty et al. 1985).

Hardmetal properties such as the hardness, wear resistance, and strength are affected mainly by the WC grain size and volume fraction. In the sintered hardmetals, the WC grains touch one another and form a continuous "skeleton" of carbide, with the cobalt binder filling the spaces between the carbide grains. This is attributed to the fairly low cobalt contents used (6 wt% to 10 wt%) in most sintered hardmetals (Exner 1979).

It is well known that decreasing the carbide grain size in WC–Co hardmetals increases the hardness and improve the wear resistance (Pugsley and Allen 1999).

Carbide grain size and volume fraction are the main factors impacting WC–Co hardmetals properties. The wear resistance of sintered WC–Co hardmetals is increased as the carbide grain size is decreased (Jia and Fischer 1997; O'quigley et al. 1997). Nanostructured sintered WC–Co hardmetals are reported to improve performance in both sliding and abrasive wear (Jia and Fischer 1996a; Kear and McCandlish 1993). These improvements in nanostructured hardmetals could be attributed to the fact that as the carbide grain size is decreased, for given cobalt content, the matrix mean free path is reduced causing greater constraint, increased hardness and reduced tendency for binder phase extrusion (Shipway et al. 2005).

2.1.2.2 Cermet coatings

Thermal spray coating processes characterise a vital and fast growing group of surface engineering technologies. Hardmetals (cermets) are one of the greatest main groups of materials deposited by thermal spray. Schoop, the Swiss inventor of thermal spray, 1942, reported the first preparation of a cermet coating using an arc spray thermally process. Large parts which for technical and economic reasons cannot be produced by powder metallurgy can be coated by cermets using thermal spray processes (Ortner et al. 2014).

Cermet coatings are mainly applied to protect engineering components from various forms of wear in different industry sectors. Currently HVOF has become the most widely used industrial coating process to deposit thermal cermet coatings. The main commercially available hardmetal feedstock powders are WC–12Co, WC–17Co, WC–10Co–4Cr, WC–20CrC–7Ni and Cr_3C_2–(20–25) NiCr. The main difference between sintered hardmetals and thermally sprayed cermet coatings is that the coating microstructures are not as exactly as for the same composition of a sintered body. However, developments in thermal spray technology and feedstock materials have now narrowed the coating property ranges of individual compositions (Berger 2007; Berger 2015).

2.1.3 Wear

A simple and valuable definition of wear is "damage to a solid surface, generally involving progressive loss of material, due to relative motion between that surface and a contacting substance or substances" This definition, purposely, does not mention the mechanisms by which the wear takes place. This could be purely mechanical involving plastic deformation or brittle fracture, or it may include important chemical aspects, for instance oxidation of a metal or hydration of a ceramic. In many applied cases, both chemical and mechanical processes play a role (Stachowiak 2006).

There are many efforts to predict sliding wear rate. The majority of the related scientific studies states Archard's wear formula as the most recognised in the field of sliding wear:

$$W = \frac{k \,.\, s \,.\, F_n}{H} \tag{1}$$

Where:

W Is the wear volume

k Is the dimensionless wear coefficient

s Is the sliding distance

F_n Is the normal load

H Is the Vickers hardness number of the softer material

Lancaster (1967) proposed the modified empirical wear formula:

$$k = \frac{W}{F_n \,.\, s} \tag{2}$$

This wear coefficient k with units of $mm^3\ N^{-1}\ m^{-1}$ is more useful for the comparison of the wear behaviour of different materials than Archard's equation. Wear coefficient k is the indicator of material wear rate under specific conditions and is different for different materials (Pirso et al. 2006).

Figure 2-8 illustrates the range of values of k seen in different types of wear. Under unlubricated sliding conditions (dry sliding), k will be in the range 10^{-6} to 10^{-2}. Frequently, two dissimilar regimes of wear are distinguished, termed mild and severe. These different regimes are not only due to different wear rates; however, they also represent significantly different mechanisms of material loss. In metals, for instance, during mild wear the debris is finer and formed of oxide particles. Whereas severe sliding wear is linked with large metallic debris particles. However, with ceramics mild wear results from the removal of reacted surface material, while the severe wear is mostly related to brittle fracture, ‘(Stachowiak 2006).

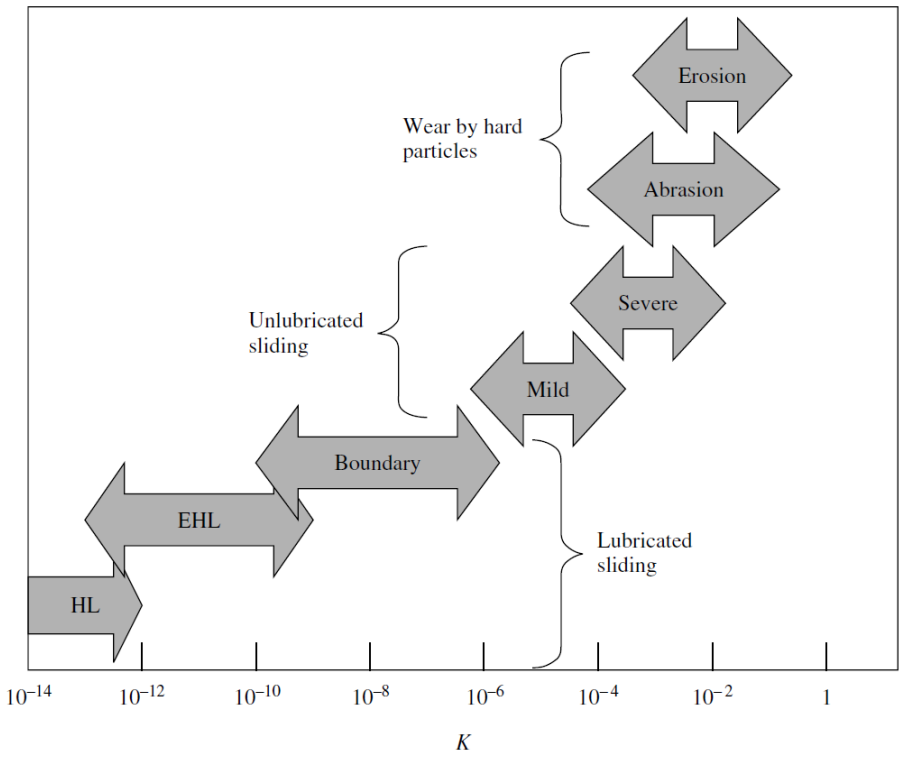

Figure 2-8: Schematic representation of the range of wear coefficient K exhibited under different conditions of wear. HL = hydrodynamic lubrication; EHL = elasto hydrodynamic lubrication (Stachowiak 2006).

2.1.3.1 Wear mechanisms and modes

A wear mechanism is a wear process classification by which material is removed from the contact surface. Common wear mechanisms are adhesive, abrasive, fatigue and

chemical wear. In actual contact it is very common that different wear mechanisms are acting at the same time. This depends on the contact conditions and will result in a specific type of wear. A wear mode is an organisation of contact type, which is characterised by a detailed kind of movement, geometry or environment. Wear modes are including sliding wear, rolling wear, fretting, erosion, impact wear and cavitation. The most common basic wear mechanisms are shown in Figure 2-9.

Adhesive (sliding) wear

Asperity junctions form when asperities of one surface contact with asperities of the counter surface and they might adhere to each other, as illustrated in Figure 2-9a. Bulk of the softer asperities is separated and material is removed due to the relative tangential motion of the surfaces. In adhesive (sliding) wear the surface material properties, protecting surface films and contaminants, play essential roles (Holmberg and Matthews 2009).

Abrasive wear

In abrasive wear the plastic deformation takes place during asperity deformation, as shown in Figure 2-9b. In contacts when one of the surfaces is significantly harder than the other, abrasive wear occurs also when hard particles are introduced between two surfaces. Asperities of harder surface are pressed into the softer surface, this results in plastic flow of the softer material around the hard one. Ploughing and removal of softer material takes place when the harder surface moves tangentially, resulting in grooves or scratches in the surface. Depending on the degree of penetration and the geometry of the harder surface, the removal of material can take different forms, such as ploughing, wedge formation or cutting.

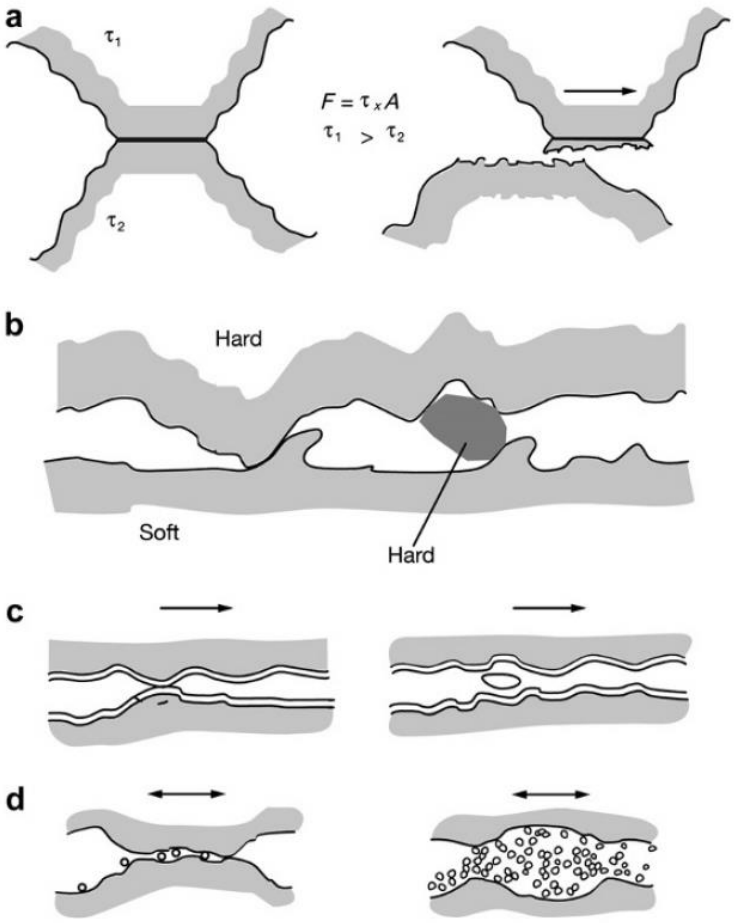

Figure 2-9: The basic mechanisms of wear are (a) adhesive, and (b) abrasive, (c) fatigue and (d) chemical wear, (Holmberg and Matthews 2009).

2.1.3.2 Factors Influencing Sliding Wear

There are several factors which can influence the sliding wear behaviour. As illustrated in Figure 2-10, sliding wear behaviour depends mostly on three main factors, namely, counterface nature, specimen and sliding condition. Material composition and microstructure influence both counterface and specimens properties. Furthermore, surface finish is an essential factor. Wear behaviour mainly depends on contact pressure and test environment, resulting in a wide range of wear rates and mechanisms in all types of materials. Moreover, wear behaviour depends on sliding distance, contact area, test duration and sliding velocity. Furthermore, the mechanical properties of materials are affected by test temperature and can cause thermally activated chemical processes (Sudaprasert 2002).

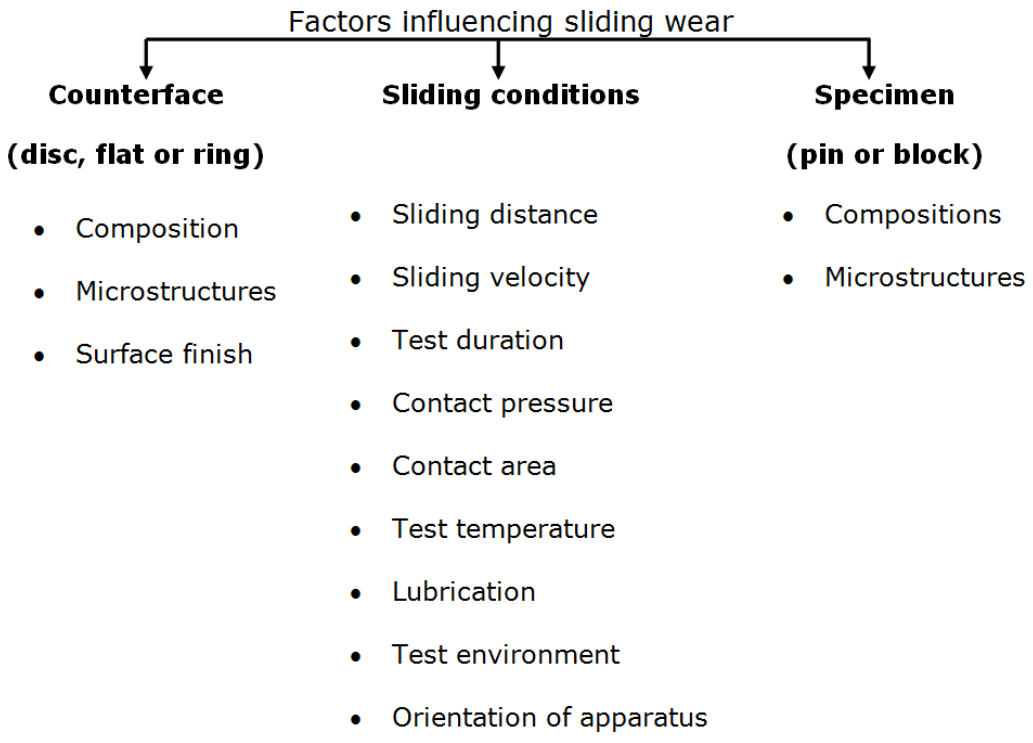

Figure 2-10: Factors influencing sliding wear, (Sudaprasert 2002).

2.1.4 Scratch test

Scratch tests are mainly used to measure thin coatings adhesion. However, recently there has been an attempt to use scratch test with thick thermally sprayed coatings to investigate their fracture mechanism, assess the cohesion between the coating layers and to predict their wear behaviour.

According to Holmberg et al. (2003) the scratch test is a pulling of diamond stylus over sample surface under a normal force. This force is raised either regularly or constantly till observing failure. This last happens when the normal load reaches the critical value. Figure 2-11 illustrates the schematic representation of the scratch test apparatus. Using the scratch test for coatings with thickness of 0.1 to 20 µm is in the main accepted which comprises a considerable number of applications.

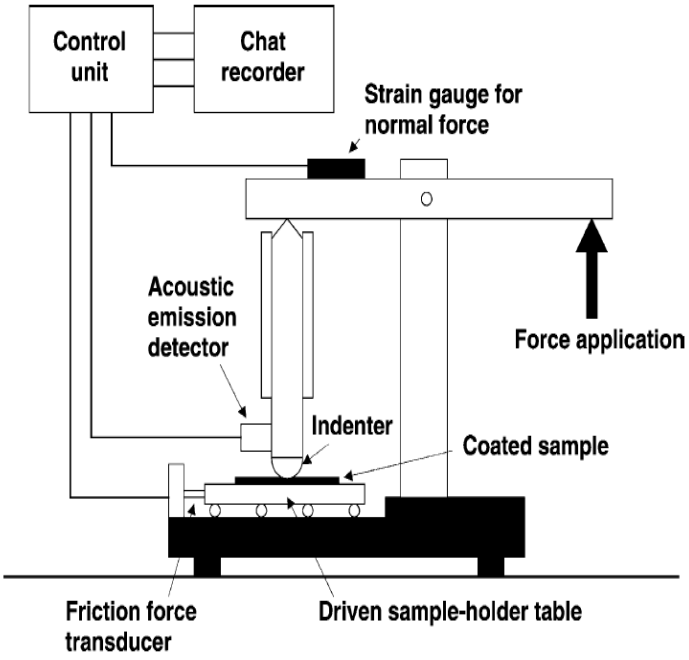

Figure 2-11: Schematic of the scratch test apparatus (Holmberg et al. 2003).

The diamond stylus has a Rock-well C geometry with a 120° cone and a 200 µm radius sphere-shaped tip described in the European Standard EN 10109-2. The suggested loading rates are fluctuated from 10 to 100 N/min with 10 mm/min indenter transverse speed. For more details about the scratch test procedure, the reader is referred to (Holmberg and Mathews 1994; Jacobs et al. 2003).

Figure 2-12 illustrates the scratch stylus sliding along the coated sample. The figure shows also the material loading and response conditions which can be divided, according to (Holmberg et al. 2006) into three independent phases, namely: ploughing, interface sliding and pulling a free-standing coating. This can help to explain the complicated contact and distortion procedures.

The first phase illustrates the ploughing of a stylus in the substrate material. The layer material is distorted by plastic or elastic deformation and a groove is created. In the case of being the stylus frontage surface sliding in contrast to the coating is frictionless; the plastic distortion is the only performed work to be considered. The second phase shows the bending and drawing of an isolated coating corresponding a

sheet between a frictionless roller and a fixed sphere-tipped cone which has an equivalent geometry to the sliding stylus. The higher surface of the coating rubs against the stylus frontage surface. The needed force for pulling the coating is similar to that of the frictional force on the coating. The bending movements produce stresses and stress issue in the coating when represented between the surfaces. In the last phase, the work carried out for overcoming friction is taking into consideration.

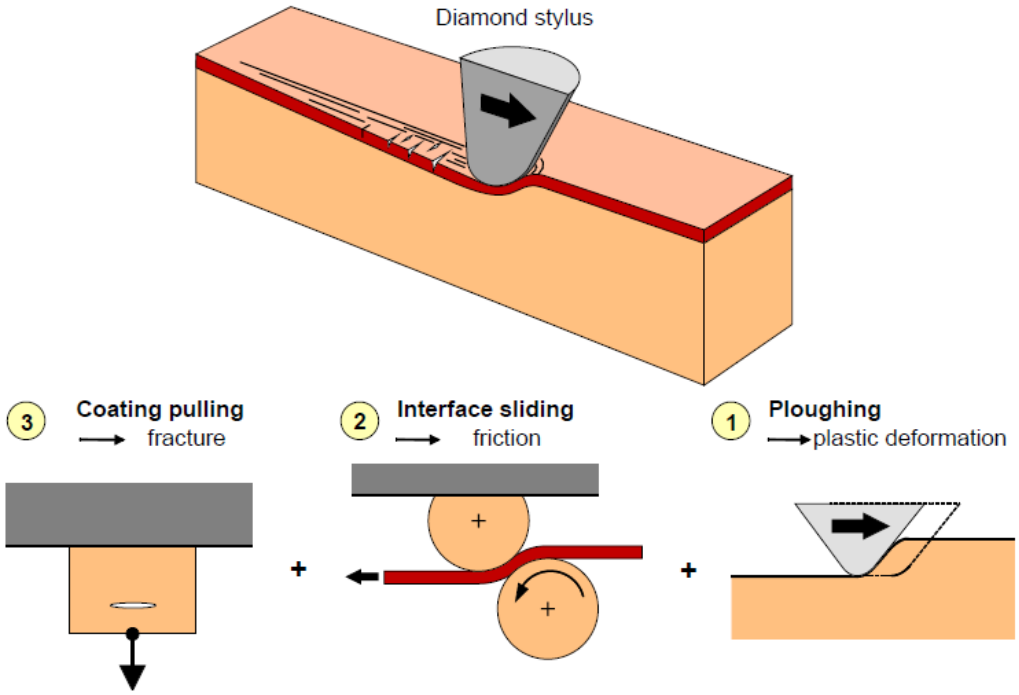

Figure 2-12: A schematic illustration of the stylus sliding on a coated sample. The material loading and response conditions have been divided into three independent phases: ploughing, interface sliding, and pulling the coating (Holmberg et al. 2006).

Scratch test is one of extensively used, quick, and effectual techniques to achieve the critical loads associated with adhesion properties of coating. The test can be divided into two main tests, namely: scratch hardness test and scratch adhesion test. The first is a scratch with constant normal load on the tested sample and on a reference sample using a stylus. The sample scratch hardness is specified based on the scratch width data. The second test is carried out by applying either a regularly increasing or constant load. Number of scratch tests is carried out with constant normal loads on a coating to provide the critical load with which the coating shows failure. Acoustic emission and

electrical surface resistance are observed instantaneously throughout the constant load scratch test to check the failure. From constant load test, higher statistical confidence can be achieved but it involves more processing time (Bull 1991; Bull 1997; Kuiry 2012).

In the progressive load scratch test, a stylus is moved over a sample surface with a linearly rising load till failure happens at critical loads. The failure actions are inspected by an optical microscope. Normal and tangential force are detailed and Acoustic Emission is also observed.

Kuiry (2012) reports that critical load depends on several factors, such as adhesion of coating-substrate, radius of stylus-tip, load up rate, mechanical features of substrate and coating, coating thickness, coating residual stress, flaw size distribution at substrate-coating interface, and friction between stylus-tip and coating. Progressive load test is appropriate for fast evaluation and quality confidence of coating. Consequently, it is more common for research purposes and development work on coating area.

2.2 Previous studies on thermally sprayed WC-M cermet coatings

In this section of chapter 2, the previous published studies related to the objectives of this study will be illustrated. This will include giving critical reviews showing the gaps in these studies which lead to the need for more investigations in this area. This critical review will include the metal binder type, WC grain size and metal binder content and their effects on the microstructure, mechanical properties and wear behaviour of thermally sprayed WC-M cermet coatings.

2.2.1 Effect of metal binder type

The developments in cermet coatings focus to finding alternative materials for replacing cobalt as the metal binder phase is very crucial due to the shortage of Co increases its price also the main ore areas are less reachable to the industrial areas. Furthermore, the low corrosion resistance of WC-Co cannot meet the increasing requirements under different working conditions. Moreover, Co is classified as toxic

and carcinogenic and the Co dust is principally responsible for work-related diseases of plant maintenance personnel. However, the lack of knowledge about WC-Ni cermet coatings compared to WC-Co cermet coatings is very obvious, as can be seen from following literature review.

The developments have been mainly focused to replace the cobalt binder completely or partially. The most expected alternative binders are the transition metals iron and nickel. Most attention was directed to the nickel as an alternative metal binder of cobalt. Its structure and properties are mostly similar, and the lattice parameter of fcc nickel (0.352 nm) is only slightly less than fcc cobalt (0.354 nm). The major differences are, fcc cobalt is metastable and can transform to hcp below 417 °C, also cobalt is much more strongly magnetic. Cobalt melting point is 1493°C however; it forms a ternary eutectic with W-C-Co system at only 1275°C. Even though, nickel melting point is lower than cobalt at 1453°C, the ternary eutectic temperature with W-C-Ni system is 70°C higher at 1342°C. Both cobalt and nickel wet WC and produce full density cermets without anomalous grain growth indicating good wetting. The complete replacement of cobalt by nickel has been reported to cause a fall of coating hardness 100 HV to 200 HV (Tracey 1992).

Guilemany et al. (1995; 1997) have investigated the microstructure of WC-17wt%Ni thermally sprayed HVOF coatings. The powder used in these studies was formed by coating WC particles with nickel. Both studies focus on examining the coating microstructure, which about similar to the WC-Co coatings microstructure. However, researchers do not show how the nickel metal binder can improve the mechanical properties and enhance the wear performance of cermet coatings.

Voyer and Marple (1999) have investigated the sliding wear performance of agglomerated-sintered WC-12Co and fused and crushed WC-10Ni cermet coatings deposited on steel substrates using both of high velocity oxy-fuel HVOF and high power plasma spraying HPPS. The wear of both the coatings was determined by measuring the weight loss following the test. HPPS-deposited coatings, which had a higher level of porosity, exhibited better wear resistance than the HVOF-processed coatings. However, it shows lower hardness. Through their discussion researchers do

not discuss the effect of different metal binder. Furthermore, the study looks to compare high velocity oxy-fuel (HVOF) with high power plasma spraying (HPPS) coating processes rather than studying metal binder effect. Also, it is hard to compare the coatings according the metal binder type, since the metal content is different (12Co and 10Ni). Moreover, they state that the average size of the carbide grains in the WC-10Ni coating appeared to be smaller than that of the WC-12Co coating and this can effect results in a significant way. Finally, they present the microstructure images for each of the coatings at different magnifications, which make it really hard to compare between both coatings.

Celik et al (2006) and Culha et al. (2009) evaluated the microstructural and mechanical properties of WC-13wt%Co and WC-12wt%Ni cermet coatings for a roller cylinder, and the effect of indentation size on mechanical properties of HVOF cermet coatings. Both coatings were fabricated on NiAl deposited on 316 L stainless steel substrates by using HVOF technique. Microhardness, surface roughness and adhesion strength of the coatings were measured. The metallographic observations showed that all coatings had a similar coating microstructure and good contact to the substrate, highly dense structures, and low oxide and porosity contents. In addition to structural and microstructural results, microhardness values of WC–Co, WC–Ni, NiAl coatings and stainless steel were measured to be 1700, 1750, 450 and 220 HV, respectively. It was found that the adhesion force value of WC–Co coating (125.9 MPa) is higher than WC–Ni coating (76.2 MPa). In order to determine wear loss, friction coefficient and wear mechanism, wear tests were performed for the WC–Co and WC–Ni coated NiAl deposited on stainless steel substrates at 50 and 100 N loads under dry sliding conditions through a pin-on-plate arrangement against AISI 303 L steel counter body. The total wear loss of the WC–Co coating is more than the WC–Ni coating on NiAl deposited stainless steel substrates. However, the WC-based cermet powders were not completely identical, since the metal binder content is deferent (13wt% Co and 12wt% Ni). Also, there is NiAl bond coat between the WC-based cermet coatings and the 316 L stainless steel substrate. Furthermore, the coating thickness of WC-Co was 250 µm and 315 µm for WC-Ni coating. All these factors make it hard to compare the mechanical properties and the wear behaviour of WC-Co and WC-Ni coatings in the right way.

Berger (2008) studied the erosion and oscillating sliding wear resistance of HVOF-sprayed WC–12wt%Co and WC–12wt%Ni based coatings alloyed with different amounts of chromium. WC–12wt%Co and WC–12wt%Ni as well as five chromium alloyed feedstock agglomerated and sintered powders were sprayed with a liquid fuelled HVOF-spray process. Starting feedstock powders of both WC-Co and WC-Ni consist of WC and metallic (Co/Ni) phases, while there coatings represent W_2C and metallic tungsten in addition to retained powder phases. The WC–Co coating shows higher hardness than the WC-Ni coating. Using cobalt as metal binder improved the erosive wear resistance. A dependence on the chromium content was not detected. Metal binder type and chromium content do not show significant effect on the sliding wear against a hardmetal counter body. This could be the only study comparing the WC-based cermet coatings due to the metal binder type. However, it does not discuss the reasons why the WC-Co shows better hardness and wear resistance.

The literature survey undertaken reveals that, except for the work done by Berger (2008), even with its limitations, there is no systematic study focusing as main task on the effect of metal binder type in the coating microstructure, mechanical properties and sliding wear behaviour. Therefore, this gap can be fulfilled during this study by evaluating the effect of metal binder type in WC-M cermet thermally sprayed coating in the coating microstructure, mechanical properties such as microhardness, fracture toughness and scratch test, and also its effect on the sliding wear behaviour.

2.2.2 Effect of carbide grain size

Carbide grain size is one of the greatest vital parameters that effects mechanical properties and wear behaviour of carbide based coatings. Abrasive wear performance of cermet coatings shows an improvement by reducing the carbide grain size (Jia and Fischer 1996b). The binder mean free path is decreased as the carbide size becomes smaller, consequential in higher resistance against deformation and material loss. Reducing the WC grain size to the nano scale to investigate the wear resistance of HVOF WC-Co has been pursued by many researchers, (Stewart et al. 1999; Watanabe et al. 2006; Yang et al. 2003a). On the other hand, for thermal spray coatings, different researchers have shown sometimes contradictory wear resistance results for the effect of

reducing carbide size from conventional to nano, (He et al. 2002; Shipway and Hogg 2005). The following are some available studies related to the subject on the literature.

Chivavibul, P. et al. (2007) examine the effects of carbide grain size and cobalt binder content on the microstructure and mechanical properties of HVOF-sprayed WC–Co coatings. Twelve feedstock WC–Co powders with different WC grain sizes (0.2, 2, and 6 μm) and metal binder contents (8, 12, 17 and 25 wt%) were sprayed by High velocity oxy-fuel (HVOF) on carbon steel substrates. They report that the increasing of Co content decreased the hardness of the coating due to the reduction of WC and W_2C phase. This agrees with a general trend observed for HVOF coatings and sintered materials. Hardness of the coating does not increase with carbide grain size reduction in starting powders. Microstructure properties such as porosity and amount of W_2C phase and the peening effect show a great influence on the coating hardness. While the hardness and Young's modulus decreased with increasing cobalt content from 1600 to 1100 Hv and from 400 to 300 GPa respectively, the fracture toughness remained in the range from 4 to 6 MPa $m^{1/2}$.

Watanabe et al. (2006) evaluated the interface fracture toughness of HVOF sprayed coatings of WC–12 wt.%Co powders on carbon steel substrates with different WC grain sizes of 0.2 to 7.0 μm by the pre-notched four-point bending test to study the WC grain sizes effect high adhesion mechanisms of this coating system. The connection between the splat microstructure and the toughness variation was examined by using the focused-ion-beam (FIB) to inspect the cross-section of WC–Co splats around the interface. The interface fracture toughness of WC–12 wt.% Co coating/carbon steel substrate increases from 600 to 1800 J/m^2 as the WC particle size increases. The intrusion of WC particles into the substrate, compaction of the underlying microstructure, and the volume fraction of the metallic binder phase in the coating are main features in achieving the exceptional adhesion of this coating system.

Usmani et al (1997) have investigated the effect of the carbide grain size and cobalt content of thermally sprayed WC-Co on the microstructure and mechanical properties of the coatings. An effort has been made to relate these properties to the wear behaviour. Three experimental WC-17wt%Co powders with fine (1.2 μm), medium (3.8

μm) and coarse (7.9 μm) carbide size distributions were prepared by spray drying an aqueous slurry of WC and Co powders under identical processing conditions. For comparison purposes, a fourth commercial WC-17wt% powder was used, which was produced by a slightly different production process. All the coatings were deposited by using a high velocity oxygen fuel (HVOF) system onto mild steel substrates. The thickness of as sprayed coating was about 450μm, followed by grinding and polishing to 300 – 400 μm for the sliding wear test. The results show that a finer carbide size in starting powder leads to a higher degree of decomposition of the WC to W_2C phase, this consequently leads to higher hardness and lower indentation fracture toughness coatings. The carbide grain size does not have a major effect on the sliding friction performance of the coatings. Due to the low fracture toughness of the coatings with fine carbide size, the coatings fracture during sliding wear occurs by matrix crack propagation with minimum tortuosity. Coating fracture occurs by propagation of cracks at the carbide/matrix interface and into the coarse carbides with coarse carbide grain size distributions.

Q. Yang et al. (1996b) have examined the effect of carbide grain size on sliding wear behaviour of WC-12wt%Co thermally sprayed coatings. Agglomerated spherical WC-12wt%Co powders in three different carbide grain sizes (1.2-1.8 μm fine, 3.0-4.2 μm medium and 7.5-12.0 μm course) were prepared. High velocity oxy-fuel system was used to deposit the powders onto steel substrate, with 70% acetylene and 30% propylene as the fuel gas. The as coated coating thickness was about 400μm, followed by grinding and polishing to about 300-250 μm for sliding wear test. Coating microstructure, hardness and plate-on-plate dry sliding wear behaviour using Al_2O_3 counterpart have been examined. Coating characterization shows that a decrease in carbide grain size in the starting powder led to a slightly higher degree of WC decomposition, an increase of low load hardness, and a decrease of high load hardness and indentation fracture toughness, thus a decrease of splat cohesion. The coating wear rate was very low and increased with increasing carbide grain size. Due to the retention of the soft and ductile cobalt matrix in the coatings, cobalt extrusion followed by carbide removal, or carbide fracture is the main material removal mechanisms of the WC–Co coatings instead of splat delamination and binder/carbide interfacial fracture. The extruded cobalt acts as binder to form a ductile and adherent tribofilm by the

reattached debris on the worn surface to protect the surface from further damage. Therefore, the coatings showed a very low wear rate. Because a pull-out of single carbide particle provides less damage to the finer coating and also because the debris consisting of finer carbides are less effective as the third-body abrasives, the sliding wear rate decreases with decreasing carbide size in the coatings.

Ghabchi et al. (2005) have investigated the possible advantages in mechanical properties and wear behaviour by reducing WC grain size. Two WC-CoCr powders; conventional with 1-3 μm WC grain size and sub-micron with 0.4 μm WC grain size were used. HVOF DJ-Hybrid gun was used to deposit all coatings, using the hydrogen as the fuel gas. Coatings were deposited on stainless steel substrates. Two set of spray parameters were selected, parameter "A" provides higher temperature with lower velocity, while parameter "B" provides lower temperature with higher velocity. Dry and wet abrasion wear behaviour of the coatings was evaluated. As a comparative tool W_2C/WC ratio was measured to examine the dissolution of WC into the matrix. In sub-micron powder WC dissolution is more sensitive to spraying parameters. In contrast, for conventional powder dissolution of WC is not sensitive to the spraying parameters. No correlation between W_2C and wear performance in wet and dry abrasion test was observed. However, the hardness value was higher for higher W_2C content. Furthermore, wear mechanisms under both wet and dry abrasion conditions were investigated. There is no significant change in dry wear behaviour with reducing carbide grain size. In contrast, the wear was reduced by 50% by reducing carbide grain size during wet abrasion test. To achieve the best wear-resistant carbide-based coatings, modifying the carbide size will be more effective if we have sufficient information on abrasive particle characteristics (size, hardness, and shape).

The literature survey undertaken reveals that, except the work done by Chivavibul et al. (2007) there is no systematic study focusing as main task on the effect of carbide grain size in the mechanical properties and sliding wear behaviour. Consequently, this gap can be fulfilled during this research by evaluating the effect of carbide grain size in WC-Co thermally sprayed coating in the mechanical properties such as microhardness, fracture toughness and scratch test, and also its effect on the sliding wear performance.

2.2.3 Effect of metal binder content

It is well known that the hardness of the WC-Co cemented carbides decreases with increasing cobalt content (Milman et al. 1999; Saito et al. 2006).

For thermally sprayed WC-M cermet coatings, even though, most coatings materials are WC-12Co and WC-17Co, there is no systematic study analysing the effect of the metal binder content on the coating microstructure, mechanical properties and wear performance except the full systematic study delivered by Chivavibul et al. (2007). Therefore, this gap can be fulfilled through this study by evaluating the effect of Co content in WC-Co thermally sprayed coating in coating microstructure, mechanical properties and the sliding wear performance.

Chivavibul et al. (2007) evaluated the effect of WC grain size and Co content on HVOF WC-Co coatings. Twelve WC–Co powders with different WC grain sizes and cobalt contents, (Table 2-2), were deposited on carbon steel substrates using HVOF spraying process.

Table 2-2: Powder properties (Chivavibul et al. 2007).

Type	Powder		Composition (wt.%)			Apparent density (g/cm^3)
	Carbide Size (μm)	Co Content (wt.%)	W	Co	C	
F8	0.2	8	86.5	7.7	5.8	5.63
F12	0.2	12	83.5	11.0	5.5	4.97
F17	0.2	17	77.5	17.4	5.1	4.48
F25	0.2	25	70.4	24.9	4.7	4.13
M8	2	8	86.5	7.6	5.8	4.43
M12	2	12	82.0	12.4	5.6	4.50
M17	2	17	77.8	17.0	5.2	3.94
M25	2	25	71.7	23.4	4.8	3.65
C8	6	8	86.0	8.2	5.8	4.51
C12	6	12	81.5	13.0	5.4	4.09
C17	6	17	76.9	17.7	5.3	3.71
C25	6	25	71.0	24.2	4.7	3.61

To understand the effect of Co content on coating microstructure and mechanical properties, it was noted that the particles surface temperature is decreased (from 1680° to 1580 °C) with increasing Co content, while the particles velocity almost remained constant (Figure 2-13).

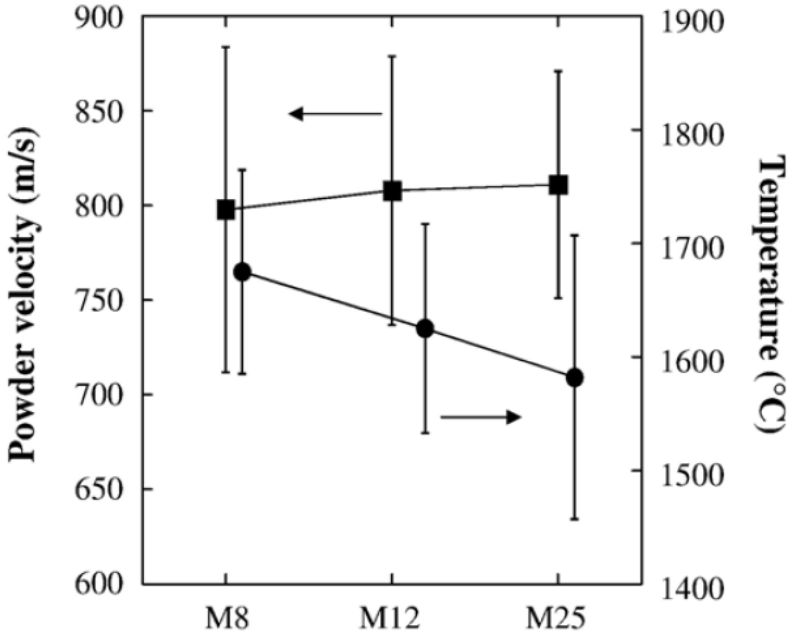

Figure 2-13: Effect of Co content on thermal spray particles velocity and temperature (Chivavibul et al. 2007).

Moreover, as the powder temperature upon impact is higher than the melting point of Co (1495 °C), the latent heat needed to melt the Co is higher when Co content is higher. Increasing Co contents lead to reduced coatings porosity since Co has lower melting point compared to WC and is easier to be melted and fill the pores in the coating. Furthermore, the mean free path of binder matrix is increased with increasing Co content. The coating hardness also decreased with increasing Co content for all the carbide sizes. Also, Young's moduli of the coatings with fine and medium carbides decreased with increasing Co content, and the fracture toughness is slightly increased with increasing Co.

2.2.4 Previous studies of scratch testing

The scratch test was first suggested for coating adhesion measurements by Perry (1981; 1983) and Steinmann and Hintermann (1985). Scratch testing consists on the whole of moving a stylus on the surface of a material with an increasing normal load.

Critical load, in scratch testing, can be identified as the load as a result of which a particular failure mechanism is detected and repeated regularly with increasing the load over the critical load. Based on this definition of critical load, Laukkanen et al. (2006) introduced first observable crack on the surface of material under scratch testing to extract the fracture toughness of coated surfaces.

The failures which happen in scratch testing tend to be complicated and a function of multiple simultaneously factors. However, the test helps for creating failure mode maps as described by Bull (1997) when studying failure mode maps in the thin film scratch adhesion test. The obtained map shows various failure modes happening throughout the scratch testing.

Bull (1999) investigated whether scratch testing can be used as a model for the abrasive wear of hard coatings. The correlation between abrasive wear rate measured by the Taber test and hardness and scratch testing parameters for TiN coatings on 304 stainless-steel deposited by three various deposition technologies was investigated. The relationship between abrasive wear resistance and hardness is found to be inadequate compared to the correlation with interfacial shear strength determined in the scratch test which is found to be slightly better. On the whole, when increasing the interfacial shear strength, the abrasive wear rate of the system diminished. Nevertheless, the equilibrium between the deformation mechanisms, plasticity and coating detachment changes as the coating depth and substrate hardness raise. Tests showed that choosing a suitable scratch test load to impersonate this is not achievable. The study illustrated that the scratch test in form of testing period can be used to create the same damage mechanisms as are experienced in abrasive wear but cannot be used in simple terms to provide a quantitative calculation of wear rate.

Borrero-López et al. (2010) investigated the use of the scratch test to measure the fracture strength of brittle thin films. The possibility of using the scratch test to measure the fracture strength of brittle thin films was proved. Weibull analysis of the strength data shows that the SiC film possesses higher strength and reliability compared with DLC and TiO2 films.

Holmberg et al. (2003) developed a 3D finite element model to investigate stresses, crack propagation and fracture toughness in scratched TiN coated steel substrates. The contact situation in a scratch test is examined in the case of sliding a spherical rigid diamond tip with an increasing load over an elastic–plastic steel plate deposited with a 2 μm thick hard ceramic TiN coating. They report that the highest first principal tensile stress is created in the contact area tail part. After sliding of nearly 1 mm, a peak area of maximum first principal stress take shape in the back tail area at the edge of the scratch channel. This generates the first noticeable angular cracks in the coating. With considerable plastic deformation of the substrate, the maximum tensile stresses were positioned behind the contact at a gap of 0.5–1 times the contact length from the back edge of the contact. Such stresses have a "horseshoe shaped ridge of maximum values with an opening in the sliding direction". Changing the situation of deformation from sliding mode on the coating to ploughing mode describes the loss of load carrying capacity of the layered surface system. The model is used for finding out the fracture toughness of the coating. In the case of the crack spacing being less than the crack length, the critical fracture toughness is equivalent to the tensile stress multiplied by the square root of half of the crack spacing. To find out the fracture toughness in the case of a 2 μm thick TiN coating on steel substrate, an opposite crack field turned out to be the transversal tensile cracks in the scratched channel. Tests showed that the fracture toughness of the TiN coating was determined to be 7 MPa $m^{1/2}$.

Assessing wear performance together with the explanation of associated mechanisms is a demanding attempt for thick films and overlay coatings, where the majority of the wear testing methods depend on measuring of volume or mass loss of the materials under testing. This provides quantitative instead of mechanistic comprehension of the wear of material which requires careful and widespread post-facto inspection on traces of wear event (Ghabchi et al. 2014).

Other researches, (such as Choi et al. 2009; Gouldstone et al. 2007; Oliver and Pharr 1992) have studied static indentation reaction of cermet materials without translation of the contact bodies. The instrumented indentation technique is considered as one of the methods for controlled loading of material with known geometry which provides practical information related to elasto-plastic properties of materials that can be used in material design. The instrumented indentation technique is principally a static test and not designs for describing the collaboration of material surface with moving indenter tip. As a consequence, and according to Zum Gahr (1998) and Ghabchi et al. (2014), hardness or elastic modulus measured by indentation technique as individual parameters are incapable to absolutely explain the wear performance of material.

The conception of instrumented indentation has been extended via controlled scratch testing where synchronised load applying and sliding in lateral direction in respect to contacting material surfaces are allowed. A careful evaluation of the damage area caused by the test affords important information on the load reactions and dynamic sliding influences. Therefore, there is an opportunity to clarify the dynamic contact problem of the thick coatings using controlled scratch tests, which was the focus of the study carried out by Ghabchi et al. (2014).

Ghabchi et al. (2014) studied the damage mechanisms and cracking behaviour of thermal sprayed WC–CoCr coating under scratch testing. Detailed evaluation of the resulting damage area offered repeatable cracking patterns. These last were classified into five categories, namely: localized collapsing of material, angular cracks, primary semi-circular and developed semi-circular cracks, and splat delamination. Linking observed damage mechanisms with the process induced microstructural explanations (such as carbide grain size and residual stresses) was investigated to find out any correlation between delamination load for cracking and the process induced variable. Quantitative correlations were found between particle properties as defined by non-dimensional melting index idea and residual stresses. Melting index takes the collective influence of particles thermal and moving history and accordingly coating porosity and the process induced decomposition. The tests illustrate the significant role of coating density and stress evolution throughout the coating creation. Crack patterns categorized as localized collapsing of material and splat delamination are precisely detected in thick

thermally sprayed composite coatings whereas angular cracks and primary semi-circular and developed semi-circular cracks are common and comparable to those observed for PVD and CVD thin coatings.

The tests, (Ghabchi et al. 2014), showed the significant role of stresses and modulus on scratch resistance. Coatings with higher advancing stress and modulus resulting from improved melting (quantified through melting index parameter) display higher critical load for delamination. The methodology provides a strategy for using theistic process monitoring as a tool for describing coating behaviour under contact load situations. Moreover, achieving quantitative values such as different critical loads tends to have inferences in the assessment of performance related properties of the coating. An example of that is the critical load for splat delaminating which showed clear correlation with growing stress. This can be used as a clear indication of splat cohesion strength. Fracture toughness can be determined via the critical load for the formation of angular or semi-circular cracks. The study introduces the scratch testing as an influential assessment technique to describe contact reaction of thick thermal spray cermet coatings comprising operative mechanisms. However, more efforts are required to show a relationship between each critical load and developed stresses and mechanical properties of coating. This can open the doors for the scratch testing to be used as performance and reliability assessment tool for thick coatings.

Jaworski et al. (2008) used scratch test to characterise mechanical properties of suspension plasma sprayed TiO_2 coatings. Thickness of the coatings has been determined using optical microscope measurements of metallographic cross sections. The coatings morphology and the phase composition have been measured with SEM and X-ray diffraction method, respectively. Scratch test allowed for describing the adhesion of coatings by finding out the critical force required to “peel off” the coatings from the substrate as well as estimating their cohesion by the observations of the scratch hardness. The hardness has been determined using the thickness of the coating and the value of force applied. The design of experiments allowed for finding out the effects of three principal parameters, namely: inputted electric power to plasma, spray distance, and suspension feed rate onto coating adhesion speeded by critical force.

Xie and Hawthorne (1999) studied the damage mechanisms of Al_2O_3, Al_2O_3–TiO_2 and Cr_2O_3 ceramic thermal spray coatings with single point scratch tests using diamond indenters. In the tests, three scratching types were studied, namely: single scratching on fine virgin surface, repetitive scratching and parallel interacting scratching. Furthermore, coatings surface and subsurface damage patterns by reason of the scratching, microstructures of the coatings, and the prototypes of wear remains were evaluated. Xie and Hawthorne found that the unique microstructure of the coatings determined their wear and correlated damage mechanisms. The main mechanism of material removal in the scratching of Al_2O_3 and Al_2O_3r 13% TiO_2 coatings was micro fracture within the plastic area, which happens preferentially at the existed micro cracks. The mechanism of material removal in the scratching of the Cr_2O_3 coating is function of contact load and geometry. When the contact load is smaller than a critical load, the main mechanism of material removal is the same as that of Al_2O_3 and Al_2O_3r13% TiO_2 coatings. However, when overcoming the critical value, the predominant mechanism of material removal is macro-fracture controlled by lateral cracking. The study found out that major damage mechanism is micro-fracture started from already existing cracks in the microstructure.

Vencl et al. (2011) used the scratch testing on cross section of thick ceramic coating to evaluate the adhesion/cohesion of coatings. The possibility of adhesion/cohesion bond strength assessment of thick plasma spray coatings with scratch tester using the ISO working draft (ISO/WD 27307) was investigated compared to the standard test method (ASTM C 633). Four different coatings deposited with atmospheric plasma spraying were studied. They reported that scratch testing can be utilized as an effective tool for the assessment of thick plasma spray coatings cohesion. Using scratch testing in this matter is a comparatively simple and fast test method. The test for practical application can also be used as a complement of standard test methods such as a coating characterization and quality control technique.

Nohava et al. (2010) worked to enhance the understanding of using two methods for the description of the mechanical properties of thermally-sprayed coatings, namely: instrumented indentation and scratch tests. Although these two methods are relatively famous, they are rarely used in the thermal spray area where their use is quite

complicated. The mechanical properties of thermally sprayed coatings are known as scale dependent where they possess a heterogeneous microstructure. The continuous multi cycle (CMC) indentation method tends to be used with a wide range of thermally sprayed coatings. This method established the subsistence of scale effects on thermally sprayed coatings mechanical properties. Such effects are hard to be referred to the recognised indentation size influence mechanism associated with strain gradient plasticity. These effects point towards the lamellar structure of the coatings. Tests illustrated also that the majority of the used coatings demonstrate a stable hardness value at depths above ~2000 nm. Such threshold should be taking into account when describing measurement criteria for the mechanical properties of thermally sprayed coatings. In the case of cross section, the scratch testing introduces an easy and quick qualified method for cohesion characterization. The study showed that the scratch method can provide important data about the quality of the coating as well as the mechanisms of cohesive failure.

The literature survey shows that, except the work done by Ghabchi et al. (2014), there is no systematic study focusing as main task on using scratch test to evaluate thermal spray thick coatings and if the scratch test could be used to predict the thick coatings wear behaviour.

Therefore, this gap can be fulfilled during this research by studying the coating fracture during scratch test and find the correlation between the scratch test critical load, (where the coating failure occurs), and the coating wear behaviour.

CHAPTER 3 Experimental Procedures

In this chapter, the specific materials and techniques used to produce the coatings will be explained in details. The tests used to characterise the coatings will be also described.

3.1 HVOF Sprayed cermet Coatings

Four types of WC-M feedstock powders have been deposited by HVOF spray systems. These powders have been produced through an agglomeration and sintering process with a similar nominal size (-45+15μm). The starting powders and coatings have been characterised by XRD and SEM techniques as described in the following sections.

3.1.1 Materials

Two types of starting powders, Amperit 518.074 (WC-12wt%Co) and Amperit 547.074 (WC-12wt%Ni), denoted through this study as WC-12Co and WC-12Ni, respectively, have been used to examine the effect of metal binder type on coating microstructure, mechanical properties and dry sliding wear behaviour. Both powders have been produced by H. C. Starck GmbH. The starting feedstock powders Woka 3202 (WC-17wt%Co) with coarse WC grain size, and Woka 3202 FC (WC-17wt%Co) with fine WC grain size, which labelled in this study as WC-17CoC and WC-17CoF signifying fine and coarse carbide size, respectively, have been used to study the effect of WC grain size on coating microstructure, mechanical properties and dry sliding wear behaviour. These powders have been manufactured by Sulzer Metco and their chemical compositions are illustrated in Table 3-1. All the powders used during this study are produced through an agglomeration and sintering process and have the same particle size, -45+15. Substrates of mild steel, rectangular plates (60 mm x 12 mm x2 mm in size), for microstructural analysis, and discs (Φ 38 mm x6 mm in thickness), for scratch and wear testing, have been used for coating deposition.

Table 3-1: Chemical Composition of the feedstock powders

Powder	Composition (wt. %)				
	Co	Ni	C	Fe	W
WC-12Co	12	-	5	0.2	Balance
WC-12Ni	-	12	5	0.2	Balance
WC-17CoC	17	-	5	0.04	Balance
WC-17CoF	17	-	5	0.04	Balance

3.1.2 Deposition Procedure

In order to provide a roughened surface, on which the coating will be deposited, the substrates had been grit-blasted with Al_2O_3 before spraying has been applied. Coatings have been sprayed using a Metallisation MET-JET 4L (Figure 3-1), which is the latest development of kerosene fuelled HVOF system. The fuel and oxygen are burnt in a combustion chamber, before emerging as a free jet. The resultant hot gas passes through a converging-diverging throat along a 100 mm nozzle, and the powder is radially injected downstream of the throat. The gun vertical velocity was 5 mm s^{-1}.

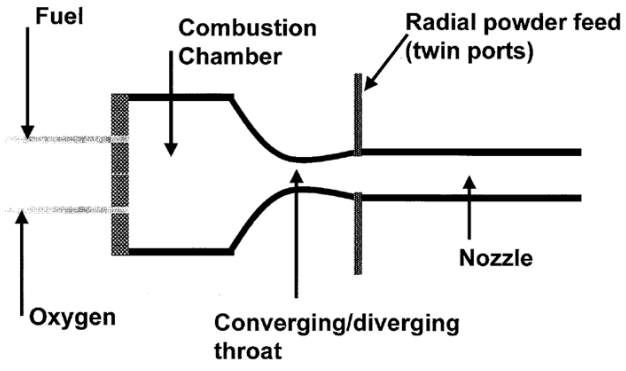

Figure 3-1: Schematic illustration of the HVOF kerosene liquid fuel spray gun, adapted from (Zhang et al. 2003).

The substrates were fixed on the circumference of a horizontally-rotating turn-table with a radius of 120mm, giving a surface velocity of 1 m s^{-1}. A compressed air jet has been used to cool specimens during and after spraying. The coating parameters are shown in Table 3-2 and the average thickness of all coatings with these parameters has been about 350 µm as-sprayed coating.

Table 3-2: Coating parameters

Spraying Parameter	Value
Oxygen flow rate (l min^{-1})	950
Fuel (Kerosene) flow rate (l min^{-1})	0.4
Nozzle length (mm)	100
Spray distance (mm)	300
Powder ports	2
Carrier gas (N_2) flow rate (l min^{-1})	6
Powder feed rate (g min^{-1})	70
Number of passes	30
Substrate velocity (m s^{-1})	1
Gun traverse speed (mm s^{-1})	5

3.1.3 Microstructure Characterisation

Coating microstructure is an essential factor which affects its mechanical properties, such as hardness, fracture toughness, and the coating wear behaviour. Powders and coatings microstructure have been examined by the X-Ray Diffraction (XRD) and the Scanning Electron Microscope (SEM) during this study as will be explained in the next two sections.

3.1.3.1 X-Ray Diffraction (XRD)

In order to identify the phases present in the powders and coatings, the Bruker D500 Diffractometer has been used for X-ray diffraction (XRD) with CuK∝ (λ=0.15406 nm) radiation. The diffractometer has been operated at 40 kV and 25 mA, with diffraction angles (2θ) between 30º to 90º and a 0.02° step size where the dwell time has been 2 sec per step. Three disc samples of each coating have been scanned as-coated. The same samples have been rescanned after they had been grinded and polished. The International Centre for Diffraction Data - Powder Diffraction File (ICDD-PDF) has been used to identify the phases presented in the spectra (Appendix A).

Quantitative X-ray diffraction analysis (Appendix B) is used to measure the level of decomposition during the coating process. Although, the accuracy of this method is not so precise since it does not account for the fraction of the metal binder (Co/Ni) and amorphous phases. However, it still gives an idea about the weight percentage of the crystalline tungsten-containing phases in the coatings.

3.1.3.2 Scanning Electron Microscopy (SEM)

Environmental scanning electron microscopy - field emission gun (ESEM-FEG, FEI-XL30) - which provides a high resolution has been used to investigate the microstructure of powders and coatings. Powders have been sprinkled on a carbon tab, which attached to an aluminium stub, to examine its morphology. Powders cross sections have been prepared by mixing the powder with hot-mounting resin. In contrast, the cross sections of the coatings have been prepared by sectioning normal to the coating by a precision diamond blade. To this end, an automatic cut- off machine (Accutom-5) has been performed, with a cutting rate of 0.005-0.02 mm s^{-1} and cutting speed 3000 rpm. After cutting, the specimens have been cleaned with acetone and mounted in hot-mounting resin. Grinding is used to prepare samples for microscopic evaluation. The cutting process results in mechanical deformation below the sample surface. This deformation must be removed by consequent grinding with silicon carbide papers. In this study carbide papers with four different grit size (240, 400, 800 and

1200) have been used on rotating discs with continuous water flushing to reduce frictional heat, dust formation and wash away abrasion debris. The sample has been turned 90 degrees after each stage, until the grinding marks from the previous step disappeared. The samples were then polished with 6 µm and 1 µm diamond paste to remove any remaining surface scratches. The microstructures of both powders and coating cross sections have been observed by SEM utilizing secondary (SE) and backscattered electron imaging (BSE). All SEM investigations on powders and coatings have been performed at 20 kV.

3.1.4 Mechanical properties characterisation

Coating mechanical properties play an important role in coating applications. These properties can be used to predict the coating wear behaviour. In the present study, microhardness, fracture toughness and scratch test are the mechanical properties which have been used to investigate the coatings.

3.1.4.1 Microhardness

Using a BUEHLER microhardness tester, the microhardness test has been performed on polished cross-sections of all coatings employing a 0.3 kgf load and a dwell time of 15 s. During this process, forty Vickers indentations have been taken along the mid-plane of the coating section on each specimen and average hardness has been quoted, along with standard error in mean.

3.1.4.2 Fracture Toughness

The fracture toughness of coatings has been determined by using an indentation method. A Vickers indenter has been used on polished cross-sections of coatings with a 10 kg load and, in total; thirty indentations from each coating have been examined. Indentations have been made along the mid-plane of the coating. Following indentation no cracking has been seen in the plane perpendicular to the coating–substrate interface. However, in most of the cases, these cracks have been seen parallel to the coating–substrate interface. The lengths of the latter cracks have been measured by using SEM

imaged in SE mode. Cracks parallel to the substrate–coating interface have been used in order to calculate the fracture toughness (K_{IC}) of the coatings. The Evans and Wilshaw equation (3-1) has been employed. The recommended $^{c}/_{a}$ ratio for the use of this equation is ($0.6 < {}^{c}/_{a} < 4.5$). The Evans and Wilshaw equation has been selected because of its applicability to systems generating short cracks.

$$K_{IC} = 0.079 \left(\frac{P}{a^{3/2}}\right) \log\left(\frac{4.5\,a}{c}\right) \qquad 3\text{-}1$$

Niihara equation (3-2) for Palmqvist cracks has been also employed to compare the coating fracture toughness results. The recommended $^{l}/_{a}$ ratio for the use of this equation is ($0.25 \leq {}^{l}/_{a} \leq 2.5$).

$$K_{IC} = \frac{0.035 \left(\frac{l}{a}\right)^{-1/2}}{\left(\frac{\emptyset}{H\,a^{1/2}}\right) \cdot \left(\frac{H}{E\,\emptyset}\right)^{2/5}} \qquad 3\text{-}2$$

Where:

K_{IC}: Fracture Toughness

P: The applied indentation load

a: The indentation half diagonal

l: The length of the crack

c: The length of the crack from the centre of the indent

H: The coating hardness

E: The coating Young's modulus, which is taken 200 GPa according to Bansal et.al. (2006).

$\emptyset$: The constraint factor ($\approx H/\sigma_y \approx 3$, where σ_y is the yield stress)

The geometries of Palmqvist and median cracks around Vickers indentation are shown in Figure 3-2 where a, l and c are illustrated.

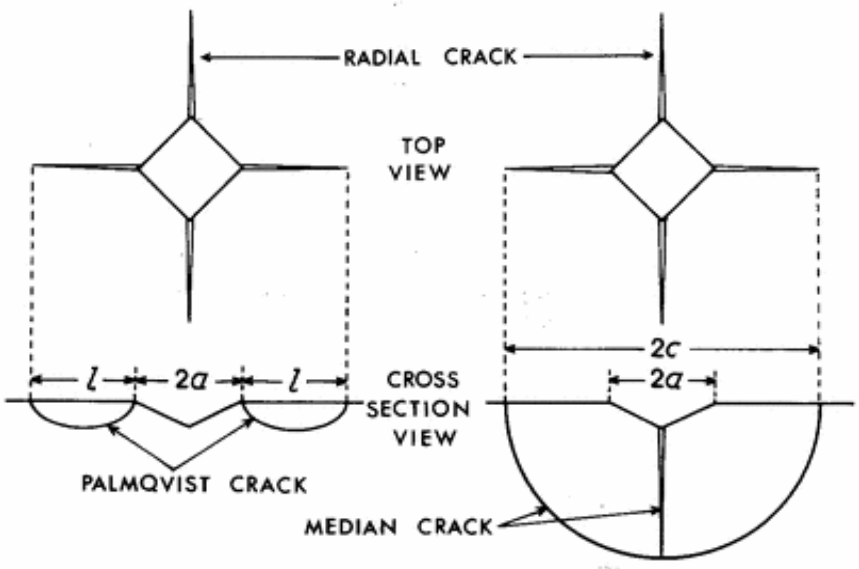

Figure 3-2: A fracture mechanics analysis of indentation induced Palmqvist crack. Adapted from K. Niihara (1983).

3.1.4.3 Scratch test

Scratch testing has been performed on polished disc samples (Ra=0.04 µm), using a diamond stylus with a spherical tip of 200 µm radius. The normal load continuously increased from 5 N preload to 50 N during scratching. The loading rate has been 50 $Nmin^{-1}$ and the sliding speed has been 10 mm min^{-1}. Three scratches have been undertaken on one sample for each coating, where the measured scratch length for all samples has been about 8 mm. During scratching, the tangential force representing the friction force has been continuously measured. Scratch test apparatus is shown in Figure 3-3. The optical profilometry (using a Bruker ContourGT Optical Profiler) and the SEM have been used to study the coatings fracture mechanism during the scratch test.

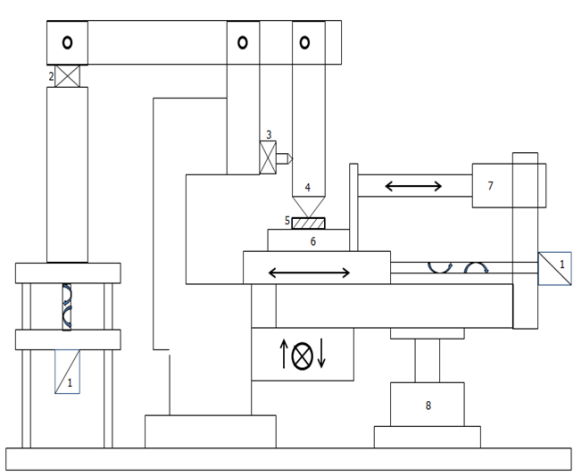

Figure 3-3: Schematic shows the scratch test apparatus

3.2 Dry Sliding Wear Testing

The sliding wear test has been performed using the conventional ball-on-disc apparatus, as displayed in Figure 3-4.

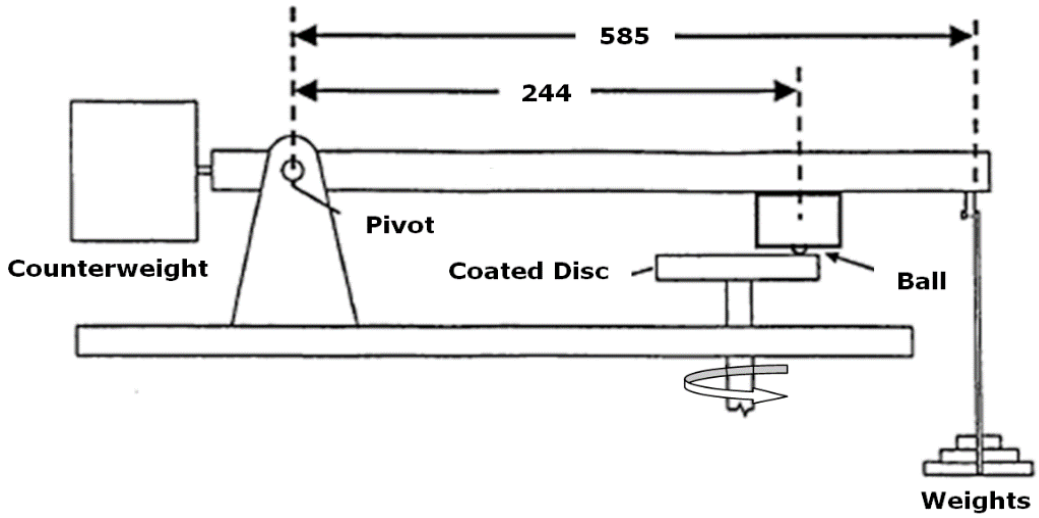

Figure 3-4: Schematic exhibited the Ball-on-disc sliding wear test apparatus.

$$\text{Load (N)} = \frac{\text{Weight (kg)} * 585 \text{ mm} * 9.81 \text{ m}s^{-2}}{244 \text{ mm}}$$

Coated disc samples of 38 mm in diameter and 6 mm in thickness have been prepared for wear testing by grinding them with a diamond discs (with grit sizes of 120, 220 and 1200). These samples have been then polished with 9 μm and 3 μm diamond discs. Struer's LabForce3 machine has been used in the grinding and polishing processes by applying load of 30 N and a rotation speed of 300 rpm during grinding and 150 rpm during the polishing process. The average roughness of polished coated discs has been about (Ra ≈ 0.04 μm). To obtain the transition load between mild and severe wear, the ball-on-disc wear test has been performed under different loads, (three samples have been run with each load). The wear track diameter has been 26 mm, the sliding speed has been 60 rpm (0.082 m s^{-1}) and the sliding distance has been 1500 m in most of the cases. The test has been performed at room temperature without lubrication. Due to its high hardness, (1610 kgf mm^{-2}), sintered WC-6wt%Co ball with 9.525 mm diameter (Spheric-Trafalgar Ltd., Ashington, UK) has been employed as the counterface, with a new ball being used for each test. The friction force has been monitored during the wear test by a linear variable differential transformer (LVDT) connected to a data logger. After the wear test had been done, the volume loss of the disc has been measured by stylus profilometry (Mitutoyo, Surftest SV. 600). Sixteen single-line traces have been made across the wear track in case of mild wear. However, in case of severe wear only eight single-line traces have been made across the wear track. In both mentioned cases the cross-sectional area of wear scar has been measured, using area under curve Cyber Solutions software. The wear volume has been calculated by multiplying the cross-section area of wear scar by the track circumference. The specific wear rate (mm^3 $N^{-1}m^{-1}$) (Stachowiak 2006) is given by the following expression:

$$w_s = \frac{V}{W.L} \qquad 3\text{-}3$$

Where: $w_{s=}$ Specific wear rate

V= Wear volume

W= Normal load

L= Total sliding distance

The wear of the ball has been assumed to represent the removal of a spherical cap of material. The worn surface of the ball has been scanned by SEM to measure the

spherical cap diameter. The volume of ball material loss has been calculated by the following equations, (Polyanin and Manzhirov 2006), Appendix C.

$$V = \pi h^2 \left(R - \frac{h}{3}\right) \quad 3\text{-}4$$

$$h = R - \sqrt{(R^2 - a^2)} \quad 3\text{-}5$$

Where: R= The radius of the ball

h= The height of a spherical cap

a= The radius of the spherical cap

The specific wear rate of the ball has been calculated by dividing the total volume loss (mm^3) by the normal load (N) and the sliding distance (m), (see Appendix C).

The SEM has been used to inspect the plan-view of wear track on coated discs and counterface balls. Cross sections, through the wear scar of the worn surfaces of discs, have been made parallel to the sliding direction. These samples have been prepared by cutting them with a precision diamond blade, mounting in hot-mounting resin, grinding and polishing (as explained in section 3.1.3.2). The cross-sections of the worn surfaces of coated discs have been examined by SEM. Energy dispersive spectroscopy (EDX) has been employed for quantitative analysis in the wear scar cross-section. The optical profilometry (using a Bruker ContourGT Optical Profiler) has been used to investigate the wear scars of coated discs through mild and severe wear to understand coating wear behaviour.

CHAPTER 4 Effect of Metal Binder Type on Microstructure and Properties of WC-Metal Coatings: Results and Discussion

In this chapter the results and discussion of WC-12Co and WC-12Ni powders and their coatings sprayed by high velocity oxy fuel (HVOF) spraying are investigated to study the effect of metal binder type on the microstructure, mechanical properties and dry sliding wear behaviour of these WC-metal coatings.

4.1 Experimental Results

4.1.1 Powder Characterisation

Feedstock powders are crucial for the thermally sprayed coatings and their properties. To examine the effect of metal binder type on coating microstructure, mechanical properties and dry sliding wear behaviour two powders, Amperit 518.074 (WC-12wt%Co) and Amperit 547.074 (WC-12wt%Ni), which denoted through this study as WC-12Co and WC-12Ni, respectively, have been used. Both powders have been produced through an agglomeration and sintering process with a similar nominal size (-45+15µm) by H. C. Starck GmbH. The XRD and SEM have been used to investigate starting powders (WC-12Co and WC-12Ni), and their characterisation is discussed in the next two sections.

4.1.1.1 X-Ray Diffraction (XRD)

The XRD pattern of the starting powders (WC-12Co and WC-12Ni) is shown in Figure 4-1. From this figure, it can be seen that both powders consist of WC hexagonal close-packed (hcp) crystal structure and metal binder (cobalt or nickel) with face-centred-cubic (fcc) crystal structure. Appendix A presents the International Centre for Diffraction Data – Powder Diffraction File (ICDD-PDF) of all phases appearing in this study.

4.1.1.2 Scanning Electron Microscopy (SEM)

The microstructure of WC-12Co and WC-12Ni powders are shown respectively in Figure 4-2 and Figure 4-3. Both powders had a spherical morphology, with high levels of porosity (typical agglomeration and sintering powder morphology), Figure 4-2a, and Figure 4-3a. The high magnification in these last figures (top right corner) shows both powders consist of angular WC grains embedded in metallic binder. The cross sections of WC-12Co and WC-12Ni powders are seen in SEM-BSE high magnification images illustrated respectively in Figure 4-2b and Figure 4-3b. Angular particles of WC embedded in metallic (Co/Ni) binder can be seen in the cross-section microstructure of both powders. Cracks in the WC particles and porosity can also be seen in both powders. The WC grains size is in the same range (0.8 - 3 μm) for both powders (WC-12Co & WC-12Ni). Table 4-1 shows the range of WC grain size change between powders and coatings.

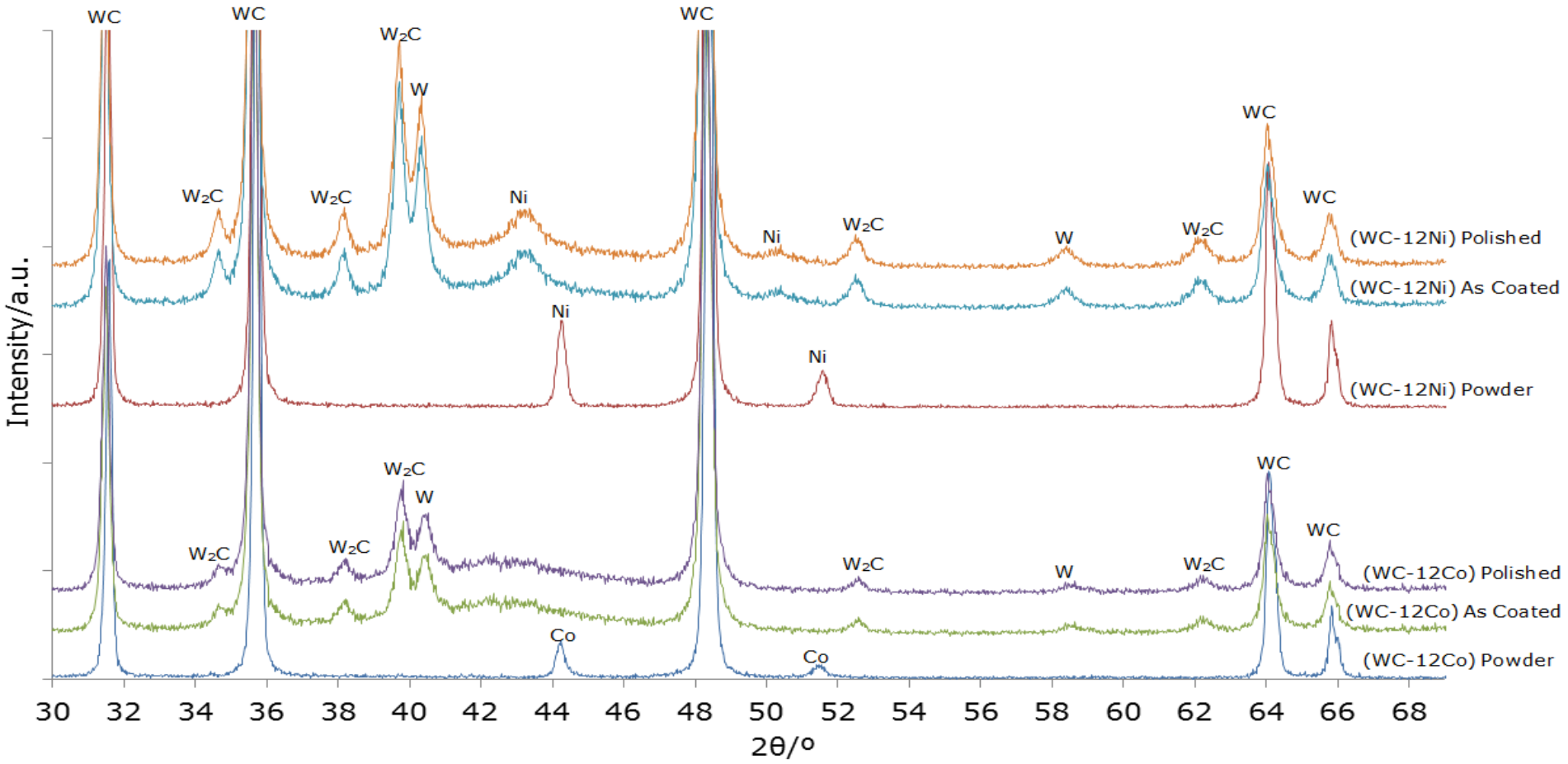

Figure 4-1: XRD pattern of WC-12Co and WC-12Ni powders and coatings. (ICDD-PDF for all phases is presented in appendix A).

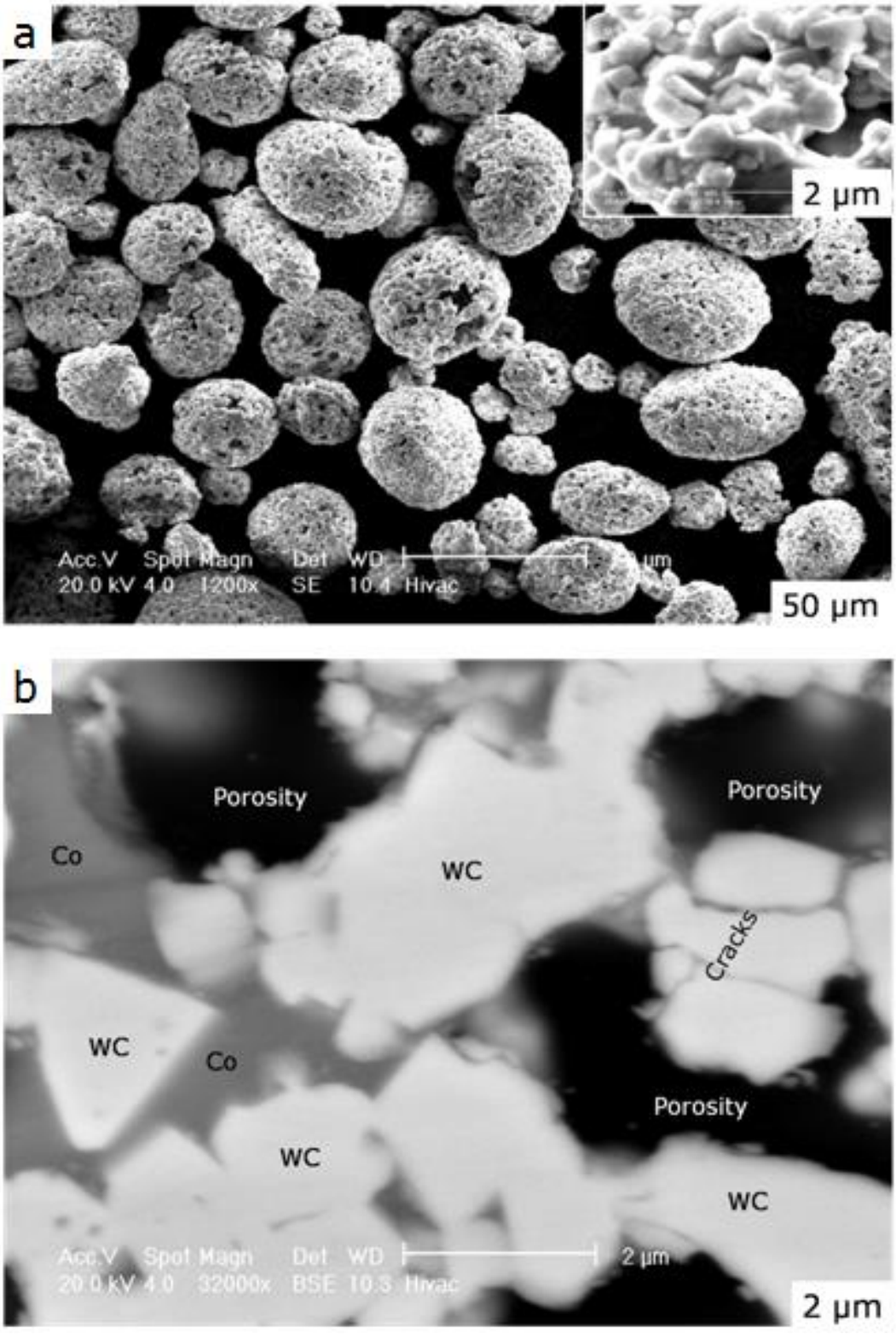

Figure 4-2: The microstructure of WC-12Co powder (a) Low magnification SEM-SE image shows spherical morphology. The high magnification on right top corner shows angular WC particles. (b) High magnification SEM-BSE image of the powder cross-section shows angular WC embedded on Co matrix.

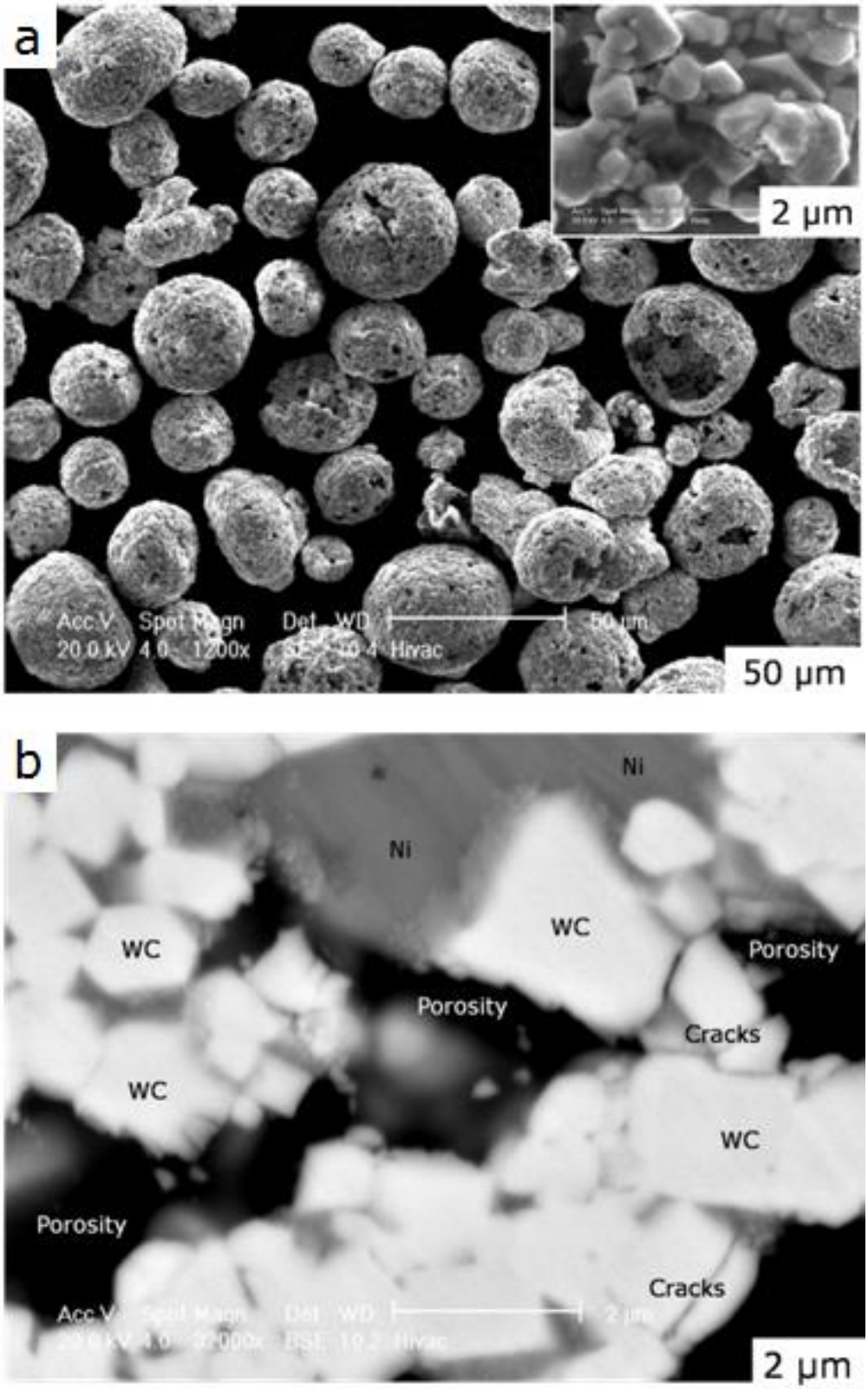

Figure 4-3: The microstructure of WC-12Ni powder (a) Low magnification SEM-SE image shows spherical morphology of the powder. The high magnification on right top corner shows an angular WC grains. (b) High magnification SEM-BSE image of the powder cross-section show angular WC embedded on Ni binder.

Table 4-1: WC grain size change between the powders and the coatings of WC-12Co and WC-12Ni

Coating material	WC grain size range of powder / µm	WC grain size range of coating / µm
WC-12Co	0.8 – 2.3	0.7 – 2.1
WC-12Ni	0.8 – 2.9	0.7 – 2.7

4.1.2 Characterisation of HVOF Sprayed Coatings

Improvement of the coating for specific application requires finding suitable combination of properties. One of the vital factors influencing the thermal spray coating properties is the coating microstructure. The next two sections represent the microstructure characterisation of WC-12Co and WC-12Ni coatings as determined from the XRD and the SEM techniques.

4.1.2.1 X-Ray Diffraction (XRD)

Since the scratch test and sliding wear will be performed on polished samples, the coated samples were scanned two times, as coated and after the polishing to make sure that coating phases are same on the top surface and underneath (about 50 µm of the coating was grinded and polished). The as coated and polished X-ray patterns are very identical in both WC-12Co and WC-12Ni coatings, as shown in Figure 4-1.

It has been feasible to observe the main peaks indexed to WC (hcp). The peaks are obvious in the XRD pattern of WC-12Co and WC-12Ni as-sprayed and after polishing coatings, (Figure 4-1). Furthermore, a number of microstructure changes can be seen in both coatings. These changes are found in peaks related to W_2C (hcp), and metallic tungsten peaks (bcc), in both traces. In the XRD pattern of WC-12Ni coating, the nickel crystal structure (fcc) is very apparent, despite the fact that it shifted slightly from its position in the powder, and the peaks of the coating sample became broader. In contrast, the cobalt peaks (fcc) do not appear in the XRD pattern of the WC-12Co coating.

Nevertheless, the WC-12Co coating has a diffuse diffraction halo centred at about $2\theta=43^{\circ}$, indicating an amorphous or nanocrystalline material. The ICDD-PDF of all phases is present in Appendix A.

Table 4-2 shows the quantitative X-ray diffraction analysis, (Appendix B), of WC-12Co and WC-12Ni coatings phases. Even though, there is some limitation of this method, however, it provides useful information about relative portions of crystalline tungsten-containing phases. These measurements provide evidence of the higher level of decomposition of the WC-12Co coating, because there is a decrease in the WC content and higher weight percent of metallic tungsten and W_2C phases comparing with WC-12Ni coating.

4.1.2.2 Scanning electron microscopy (SEM)

The microstructure of both WC-12Co and WC-12Ni coatings are demonstrated in Figure 4-4 and Figure 4-5, respectively. Low magnification images of SEM-BSE in Figure 4-4a, and Figure 4-5a shows common lamellar structure of HVOF thermally sprayed coatings in both WC-12Co and WC-12Ni coatings, which exhibit different features. Molten and semi-molten matrix areas are presented in both coatings. Porosity can be seen in both coatings along with a homogeneous distribution of carbide particles, some of which have rounded edges. Table 4-1 shows there is no significant reduction in WC grain size after coating for both materials. The selected areas "b" in Figure 4-4a, and Figure 4-5a, for WC-12Co and WC-12Ni coatings respectively are demonstrated by high magnification images of SEM-BSE in Figure 4-4b and Figure 4-5b in order. In these last figures, WC core surrounded with a thin brighter spotty rings and clusters of small particles which related to W_2C and metallic tungsten have been found. Some intergranular cracks and cracks in WC grains in both WC-12Co and WC-12Ni coatings exist and they are depicted in Figure 4-4c and Figure 4-5c respectively.

Quantitative X-ray diffraction analysis in Table 4-2, (see Appendix B), represent the relative portions of phases weight percentage excluding cobalt and nickel phases. This method is not so accurate since it does not account the fraction of amorphous phase and the metal binder (Co/Ni) phase as well. However, it still gives an idea about the

weight percentage of carbide phases. It shows that the W_2C and metallic tungsten phases are higher in WC-12Co coating comparing to WC-12Ni coating. This means that WC-12Co coating experience higher decomposition than WC-12Ni coating.

Table 4-2: Quantitative X-ray diffraction analysis of the crystalline tungsten-containing phases in WC-12Co and WC-12Ni coatings.

Coating	WC (wt %)	W_2C (wt %)	W (wt %)
WC-12Co	87	10	4
WC-12Ni	91	7	3

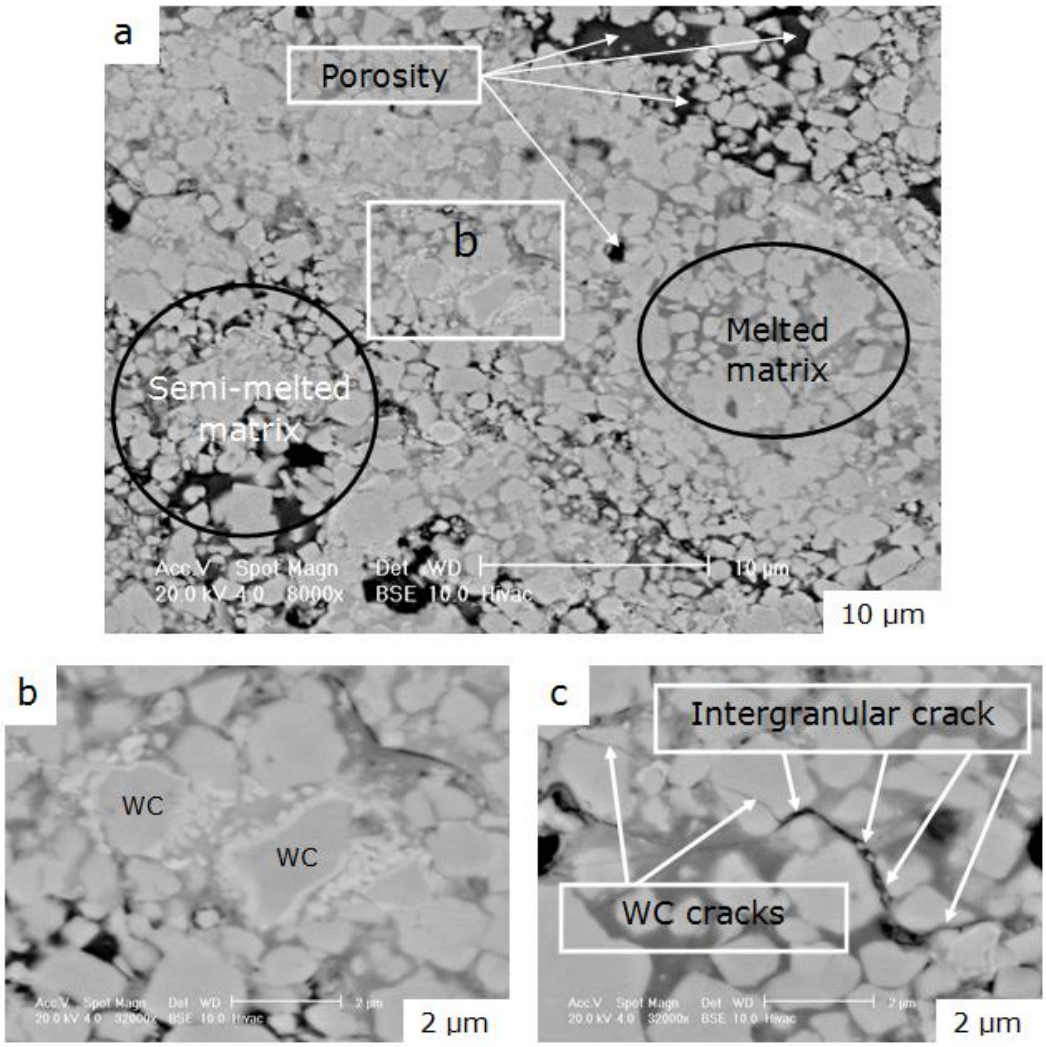

Figure 4-4: The microstructure of WC-12Co coatings. (a) SEM-BSE low magnification image shows different features. (b) Shows WC particles surrounded by brighter rings of W2C and/or metallic W particles. (c) Represent an intergranular cracks and cracks in WC grains.

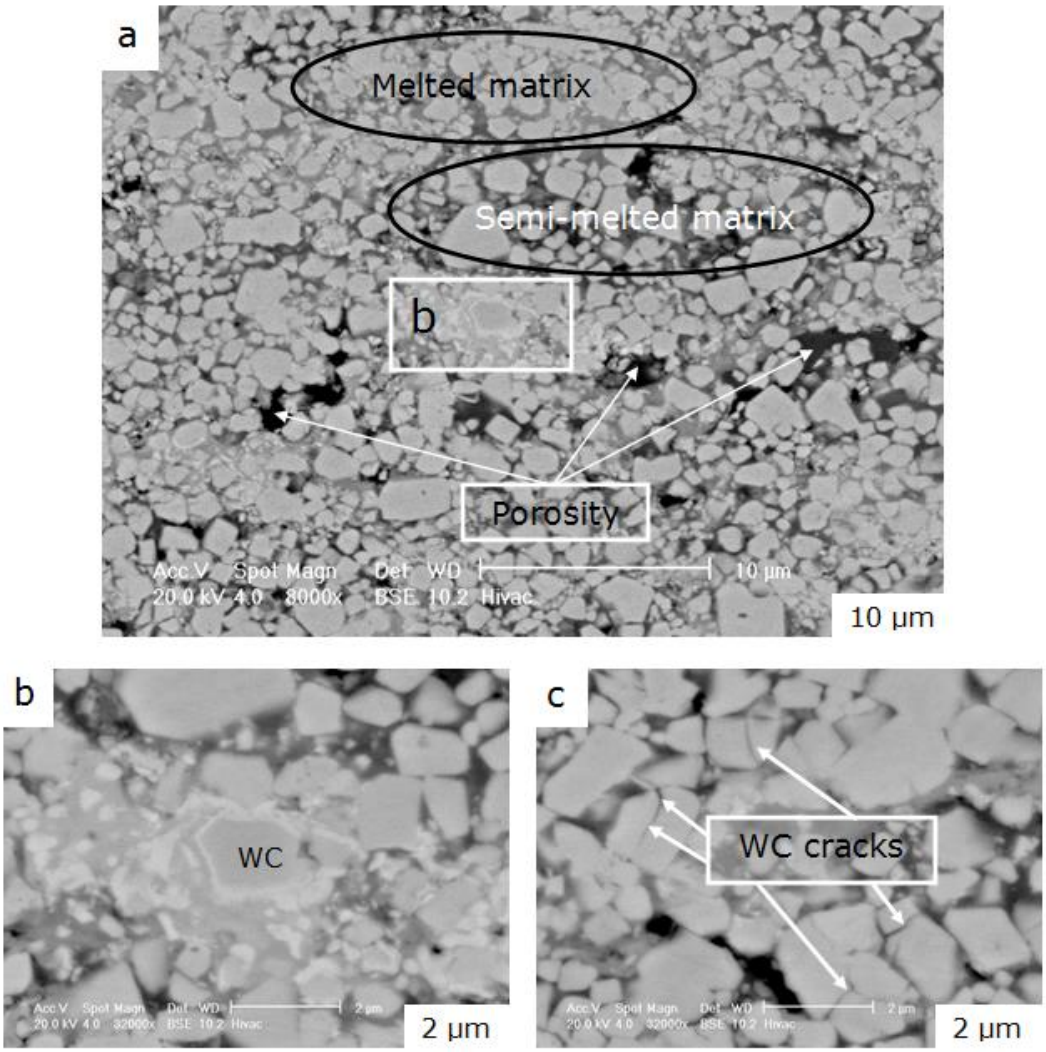

Figure 4-5: The microstructure of WC-12Ni coatings. (a) SEM-BSE low magnification image shows different characteristics. (b) Shows bright spotty rings and clusters particles related to W_2C and/or metallic W surrounding WC grains. (c) Illustrates cracks in WC grains.

4.1.3 Mechanical properties of coatings

The performance of cermet coatings depends mainly on its mechanical properties, such as hardness and fracture toughness. The following three sections represent the results of mechanical properties of WC-12Co and WC-12Ni coatings, including microhardness, fracture toughness and scratch test. However, the focus in this section will be largely on scratch test as it is represented as an innovative method to predict the wear behaviour of thick thermally sprayed coatings.

4.1.3.1 Microhardness

In order to assess the mechanical properties of the coatings, forty Vickers indentations have been taken along the mid-plane of the coating cross-section to measure the microhardness. The results showed an average value of $HV_{0.3/15}$ =1257 ± 27kgf mm^{-2} for the WC-12Co coating and $HV_{0.3/15}$ =1010 ± 20 kgf mm^{-2} for the WC-12Ni coating, Table 4-3. The ± values represent the standard error in the mean. Figure 4-6 illustrates the cumulative distribution of microhardness where the median values are equal to 1256 kgf mm^{-2} for the WC-12Co coating and 1005 kgf mm^{-2} for the WC-12Ni coating.

4.1.3.2 Fracture toughness

In order to measure the coatings fracture toughness, indentations have been performed by using the Vickers hardness method, the indentation load has been 10 kg. It is worth mentioning that the same load has been applied on both WC-12Co and WC-12Ni coatings.

Figure 4-7 demonstrates intergranular cracks formed parallel to the coating/substrate interface, with the majority of cracks formed at the corner of the indent (although several formed some distance from the corner).

Table 4-3: Microhardness and fracture toughness of WC-12Co and WC-12Ni coatings

Coating powder	Microhardness $HV_{0.3/15}$ $kgfmm^{-2}$	Fracture toughness K_{IC} (Evans & Wilshaw) $MPam^{1/2}$	Fracture toughness K_{IC} (Niihara) $MPam^{1/2}$
WC-12Co	1257 ± 27	5.6 ± 0.2	5.4 ± 0.2
WC-12Ni	1010 ± 20	4.6 ± 0.2	5.0 ± 0.2

Fracture toughness equations, (Evans and Wilshaw) and (Niihara), explained in details in section 3.1.4.2 (±values represent the standard error in the mean i.e. $\sigma/\sqrt{n}$).

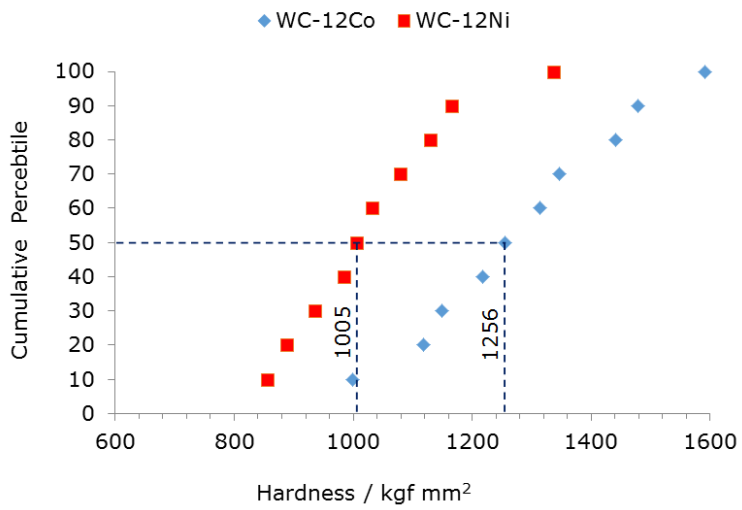

Figure 4-6: Cumulative distribution plot of WC-12Co and WC-12Ni coatings microhardness shows the median values for both coatings.

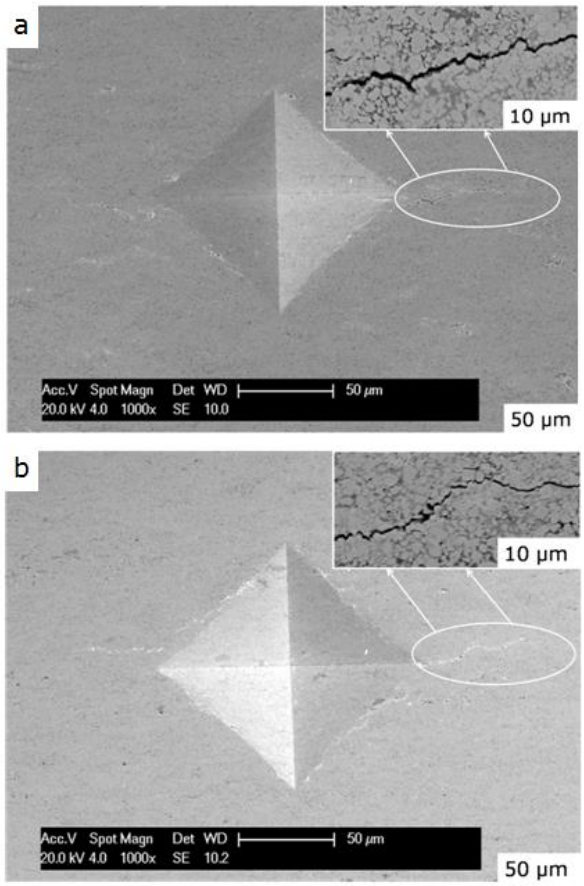

Figure 4-7: Indentation of fracture toughness with load 10 kg of (a) WC-12Co coating and (b) WC-12Ni coating, show intergranular cracks generated parallel to the coating/substrate interface formed at the corner of the indent.

Fracture toughness values have been calculated from measurements of the indentations and the associated cracks on cross-sections of the coating. It has been found that the c/a values always matched the range of $0.6 \leq c/a < 4.5$, for which the Evans and Wilshaw equation is valid. In order to achieve comparative results, the fracture toughness for both WC-12Co and WC-12Ni coatings has been calculated by employing the Niihara equation. The results of coating fracture toughness are presented in Table 4-3, where the ± values represent the standard error in the mean. The plot of cumulative distributions of these data is shown in Figure 4-8 (Evans and Wilshaw equation) and Figure 4-9 (Niihara equation). The median fracture toughness values are presented in both last figures.

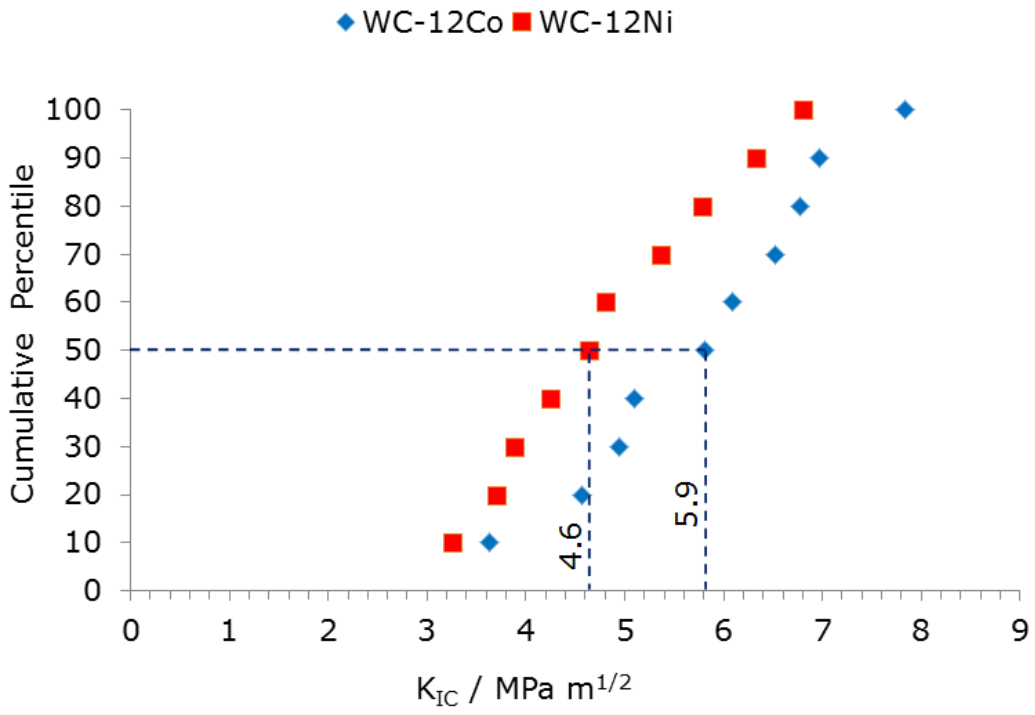

Figure 4-8: Cumulative distribution plot of WC-12Co and WC-12Ni coatings fracture toughness, calculated by Evans and Wilshaw equation shows the median values for both coatings.

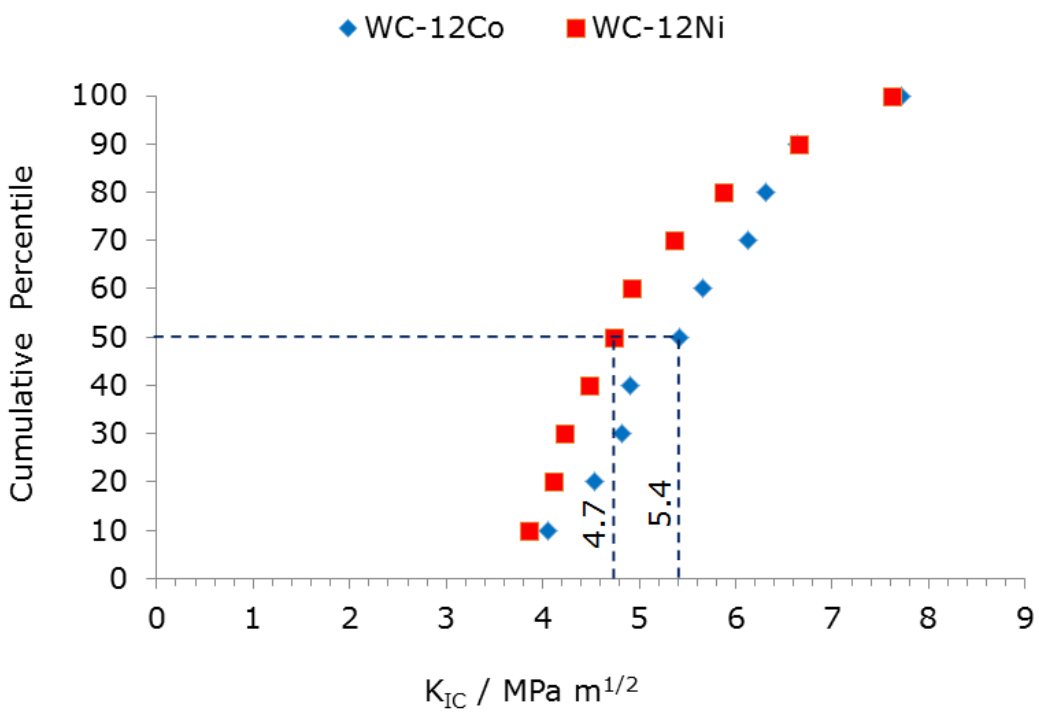

Figure 4-9: Cumulative distribution plot of WC-12Co and WC-12Ni coatings fracture toughness, calculated by Niihara equation shows the median values for both coatings.

4.1.3.3 Scratch test

The scratch test has been performed on polished disc samples with surface roughness Ra ≈ 0.04 µm of both WC-12Co and WC-12Ni coatings. In order to understand the coating failure mechanism during the scratch test, related to the loading conditions, three scratches were produced on the polished sample. Scratch grooves have been examined using the optical profilometry (using a Bruker ContourGT Optical Profiler) and the SEM. The parameters of the scratch setup have been a preload of 5 N and the load increased continually up to 50 N. The total sliding distance has been approximately 8 mm for both coatings. The loading rate has been 50 N min^{-1} and the sliding speed has been 10 mm min^{-1}. According to coating fracture, the total length of scratch can be divided into five sectors. In the two following sections the coating failure mechanism of WC-12Co and WC-12Ni coatings will be discussed in details.

Figure 4-10 and Figure 4-11 depicted the schematic of coating fracture mechanism map along the scratch track of both WC-12Co and WC-12Ni coatings

respectively depending on the progressive of the normal load and the distance where these failures appears. The graphs in Figure 4-10 and Figure 4-11 illustrated the changes of scratch depth and width according to the progressive load, with a critical load starting at 17 N for WC-12Co coating and at 11 N for WC-12Ni coating.

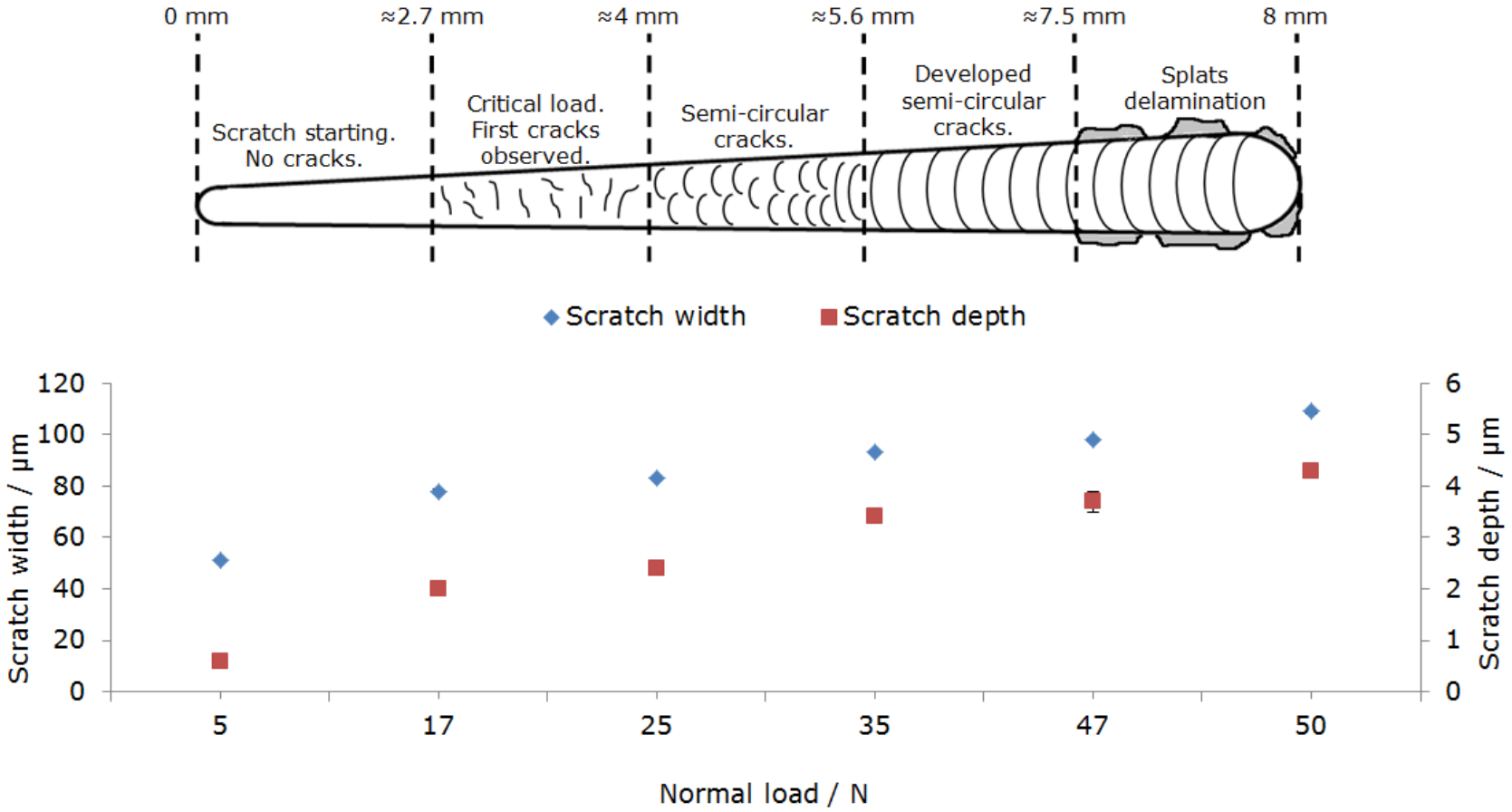

Figure 4-10: Schematic of scratch fracture mechanism map of WC-12Co coating, (note: non-linear scale).

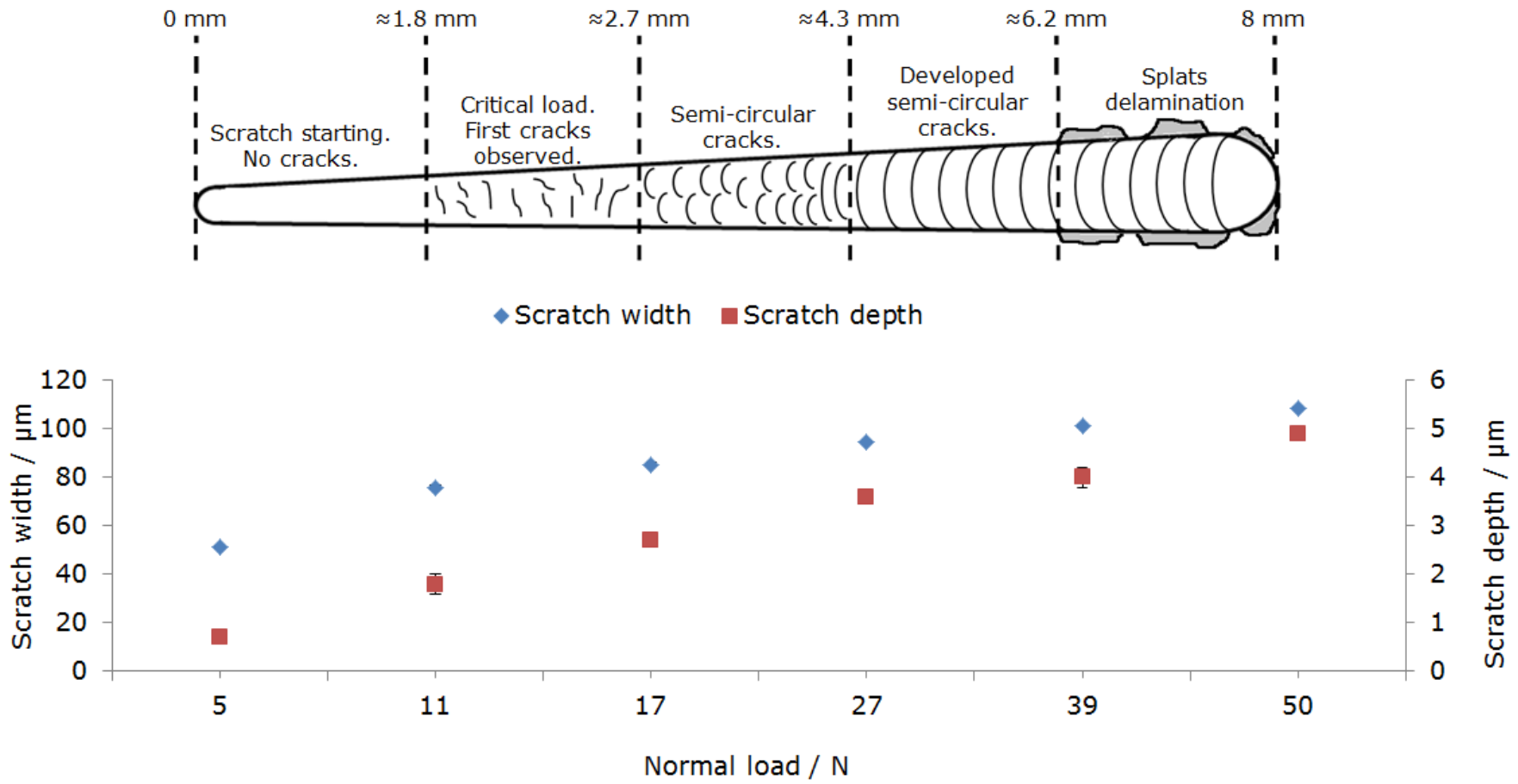

Figure 4-11: Schematic of scratch fracture mechanism map of WC-12Ni coating, (note: non-linear scale).

Starting section

The scratch starting section commences at the starting point of the scratch with preload 5 N and continues until observation of the first crack on the coating. The high magnification SEM-BSE image taken from the middle of the scratch track of this section, Figure 4-12, proves that there are no cracks in both WC-12Co and WC-12Ni coatings at this stage. The scratch width and depth were about 50μm and 0.6 μm respectively for both coatings in this section.

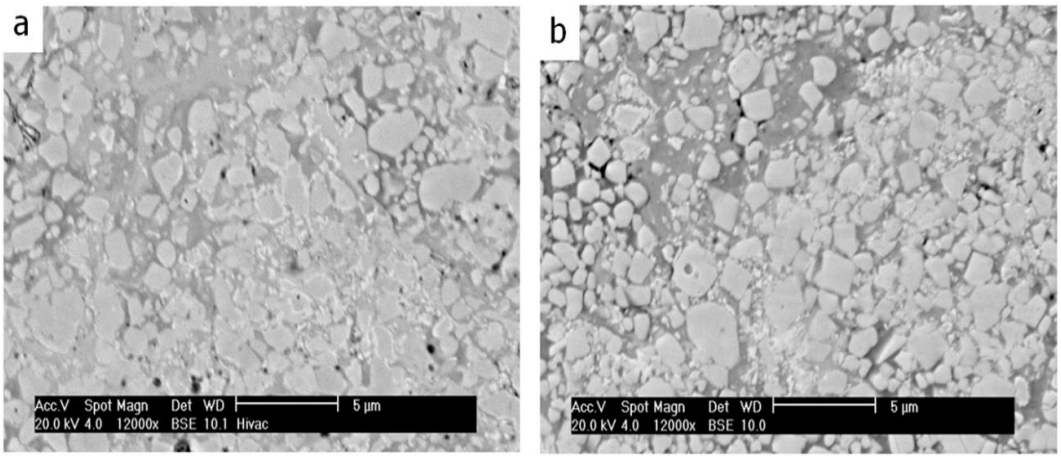

Figure 4-12: SEM-BSE images taken from the middle of the scratch track at starting section. (a) WC-12Co coating and (b) WC-12Nicoating.

Critical load section

The normal load at which the initial cracks of the coating can be observed is termed as the critical load. For the WC-12Co coating, the initial cracks have appeared at approximately 2.7 mm from the starting point with normal load around 17 N, (Figure 4-10), where for the WC-12Ni coating these cracks appeared at about 1.8 mm from the starting point with normal load about 11 N, (Figure 4-11).

The average width of the scratch track for both WC-12Co and WC-12Ni coatings in this segment have been approximately 78 μm and 76 μm respectively, where the average depth of the scratch groove for both WC-12Co and WC-12Ni coatings were about 2 μm and 1.8 μm in order.

Low magnification images of SEM-BSE in Figure 4-13 demonstrate the mode of these initial cracks which are short and have no specific shape. SEM-BSE high magnification images in Figure 4-14 represent these narrow primary intergranular cracks in the matrix. There have been few noted cracks in the WC grains in WC-12Co coating. However, there no cracks in the WC grains have been noticed in WC-12Ni coating.

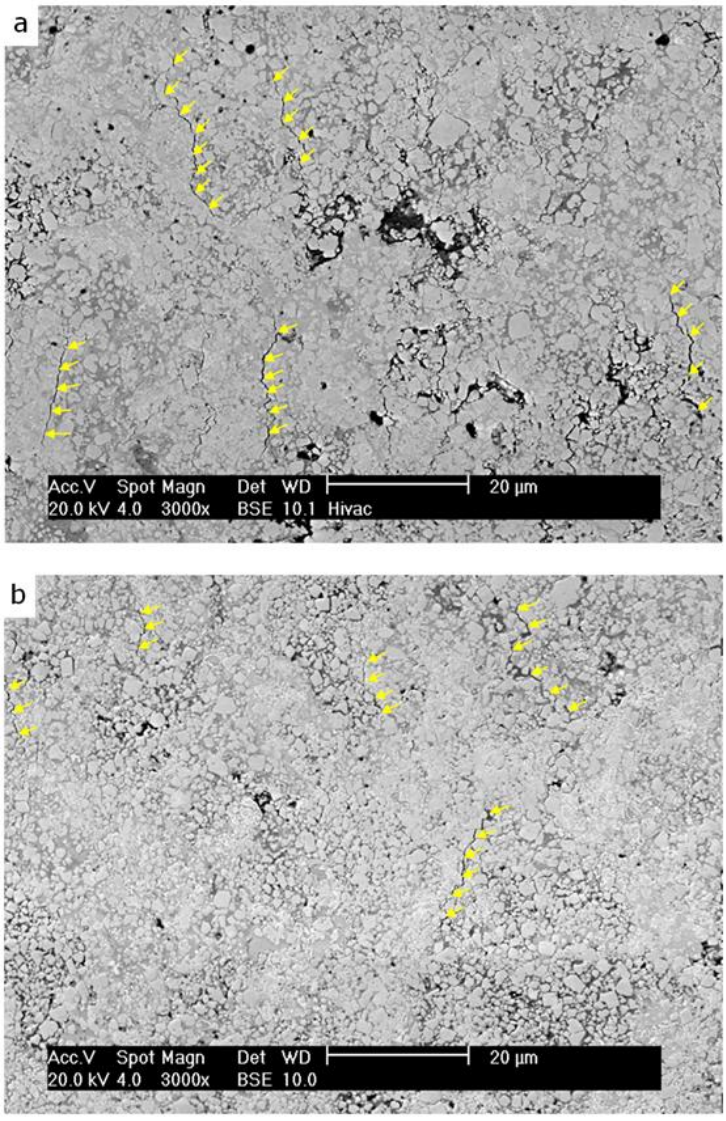

Figure 4-13: The critical load section of scratch track. The low magnification images of SEM-BSE show the mode of the cracks (arrows). (a) WC-12Co coating and (b) WC-12Ni coating.

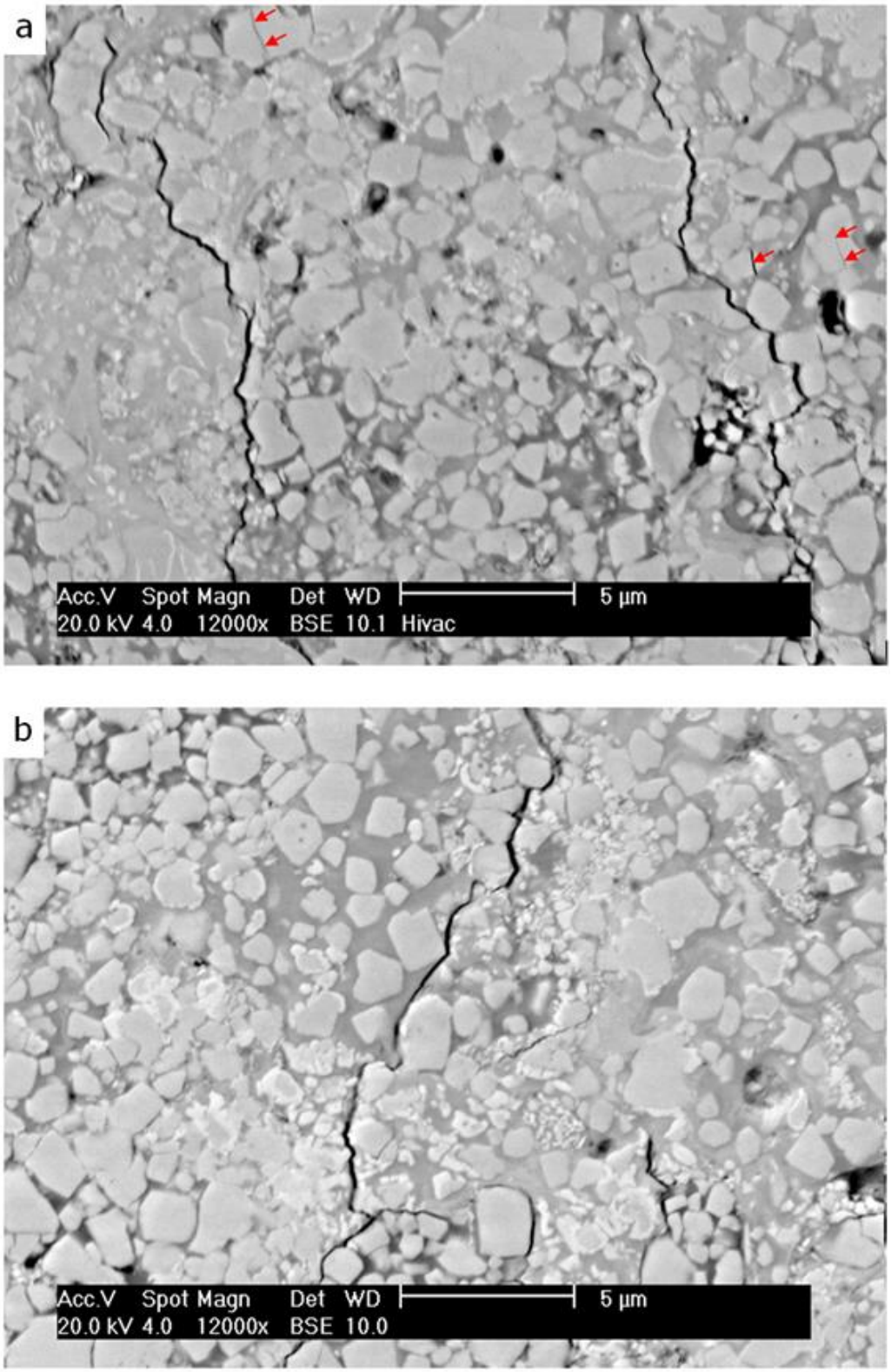

Figure 4-14: The critical load section of the scratch. SEM-BSE high magnification images represent the narrow initial matrix cracks. (a) WC-12Co coating, few cracks in WC grains observed (red arrows), and (b) WC-12Ni coating, no cracks in WC grains seen.

Semi-circular cracks section

As the normal load increased, the cracks in the coating increased. About 4 mm from the starting point of the scratch of WC-12Co coating, where the normal load exceeds 25 N; the cracks take semi-circular shape. This happens with WC-12Ni coating as the normal load exceeds 17 N, about 2.7 mm from the starting point of the scratch.

The 2D Bruker ContourGT Optical Profiler images in Figure 4-15 represent these semi-circular cracks in both coatings (arrows). The average width and depth of the scratch in this sector have been approximately 83 µm and 2.4 µm respectively in WC-12Co coating. These values within the WC-12Ni coating were 85 µm and 2.7 µm respectively.

The scratch width increased compared to the previous section. The high magnification SEM-BSE images in Figure 4-16 exhibited that these semi-circular cracks still follow the boundaries of the coating grains, (i. e. travel through the matrix) in both coatings. However, in WC-12Co coating these cracks start to break the WC grains in their path. Few cracks appear in the WC grains in both WC-12Co and WC-12Ni coatings.

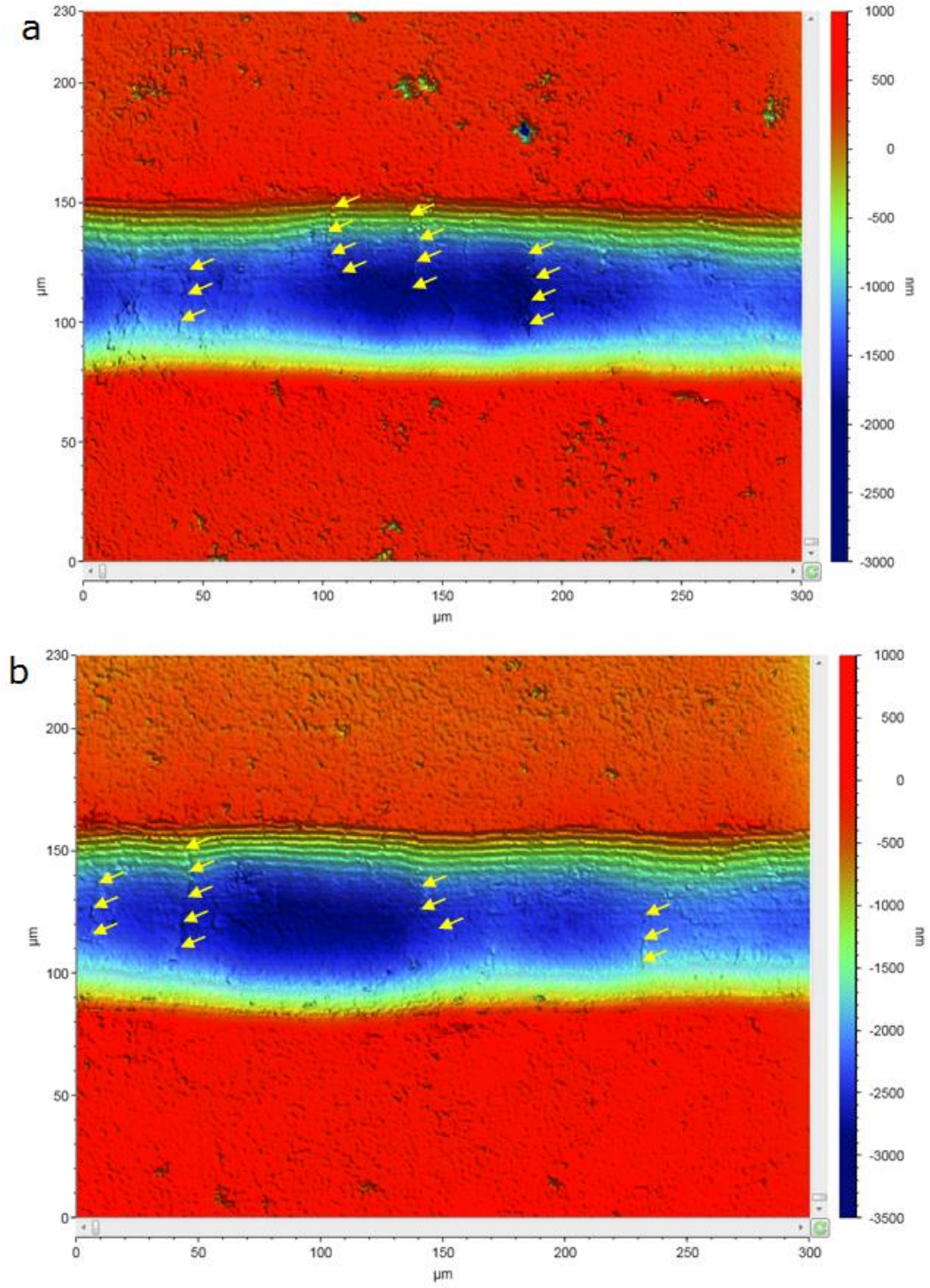

Figure 4-15: The 2D Bruker ContourGT Optical Profiler images represent the semi-circular cracks (arrows). (a) WC-12Co coating and (b) WC-12Ni coating.

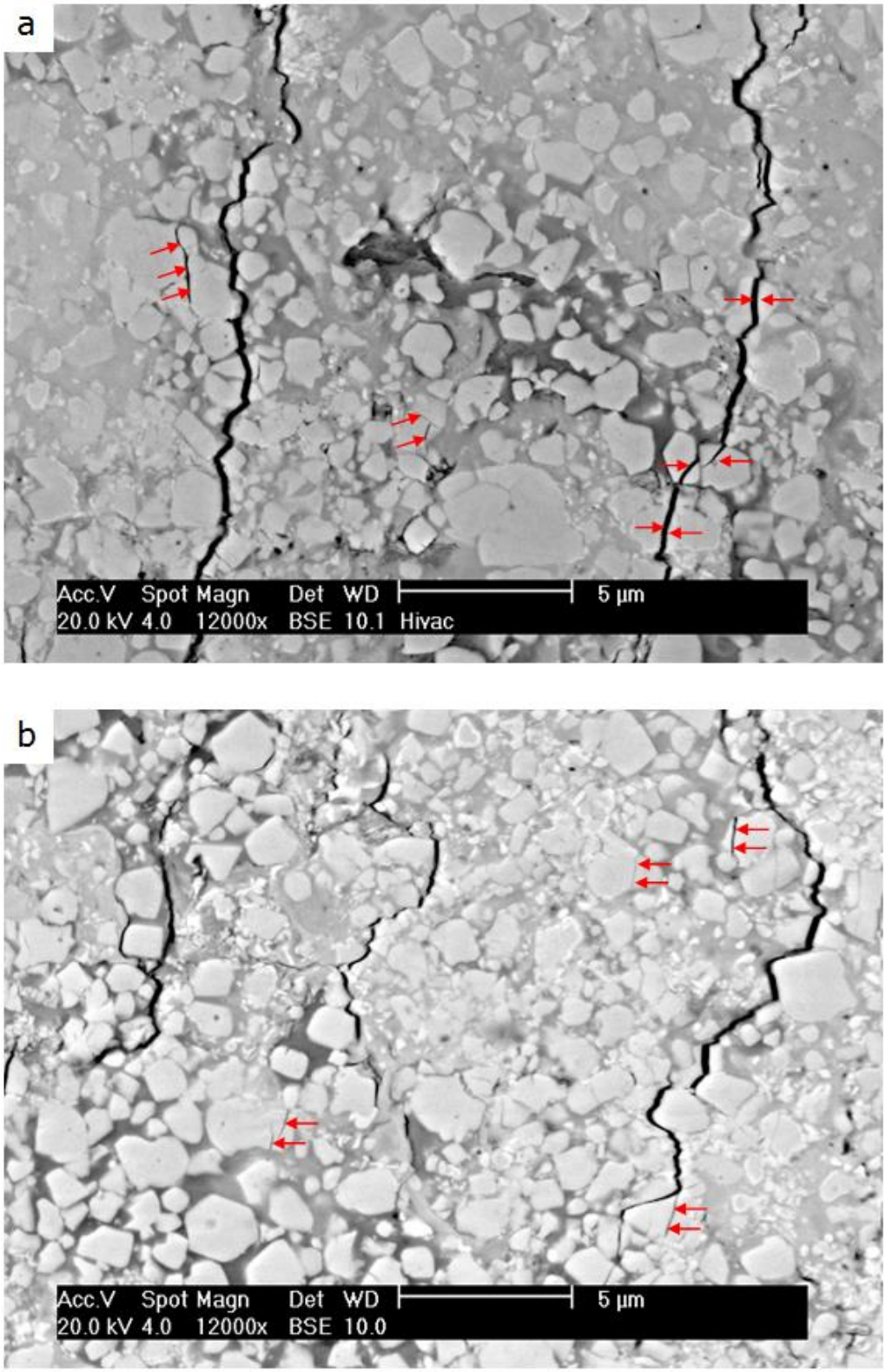

Figure 4-16: The SEM-BSE high magnification images exhibited the semi-circular cracks. (a) WC-12Co coating, the semi-circular cracks go through the matrix and WC grains as well (arrows) and (b) WC-12Ni coating, the cracks still travel through the matrix and few cracks appears in WC grains (arrows).

Developed semi-circular cracks section

As the normal load increases, the semi-circular cracks developed to cover (approximately) the whole scratch width and the intensity of these cracks increased until the end of the scratch. These developed semi-circular cracks have been seen with WC-12Co coating when the normal load is exceeds 35 N and this occurs at approximately 5.6 mm from the starting point of the scratch (see Figure 4-10). However, with WC-12Ni coating these cracks appear when the normal load is above only 27 N and this seen at about 4.3 mm from the starting point of the scratch of this coating (see Figure 4-11).

The average scratch width and depth at this section for WC-12Co coating were approximately 93 µm and 3.4 µm respectively, while with WC-12Ni coating the average scratch depth and width at this section were about 95 µm and 3.6 µm, respectively. The WC-12Ni coating scratch shows slightly wider scratch track and deeper scratch groove through in this section; although the normal load with this coating (WC-12Ni) here is less than that of WC-12Co coating, Figure 4-17. The high magnification SEM-BSE images in Figure 4-18 illustrated these developed semi-circular cracks for both WC-12Co and WC-12Ni coatings travelling through the matrix and the carbide grains. These scratch cracks become wider than the cracks in previous section. The cracks in the WC grains are very obvious in this section in both WC-12Co and WC-12Ni coatings.

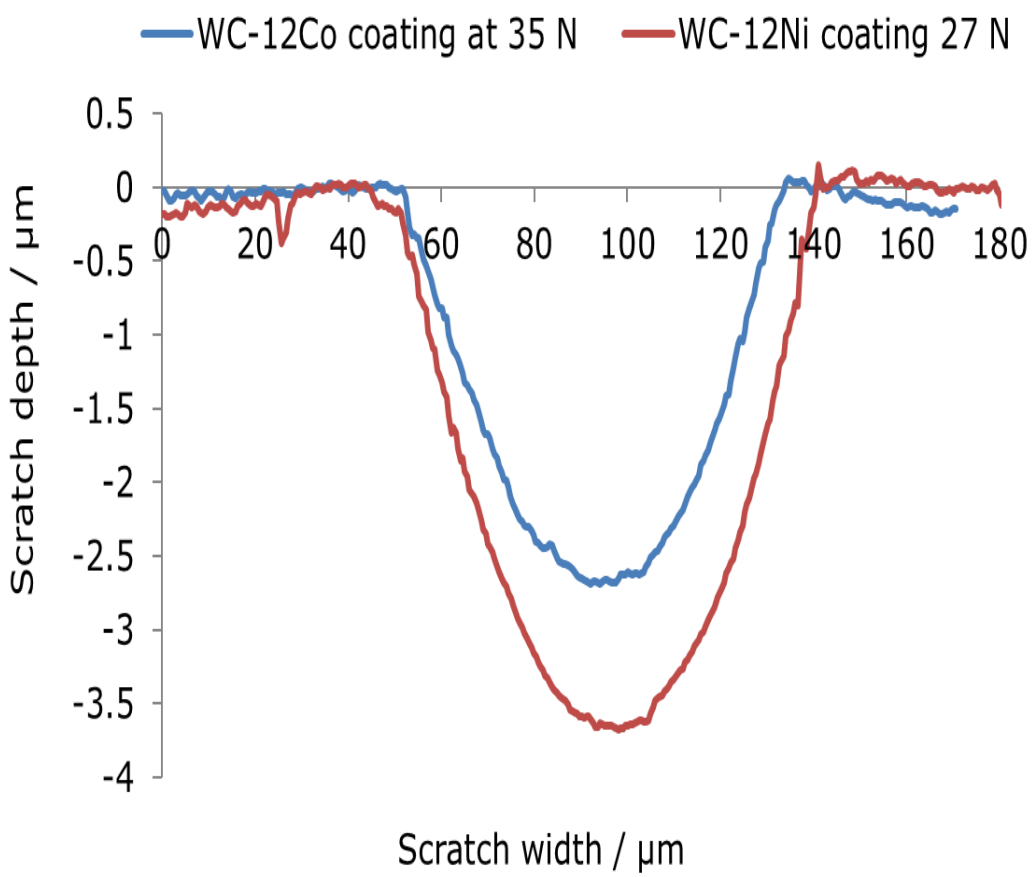

Figure 4-17: The plot of scratch profile of WC-12Co and WC-12Ni coatings at the developed semi-circular cracks section. WC-12Ni coating shows slightly wider scratch track and deeper scratch groove with lower normal load.

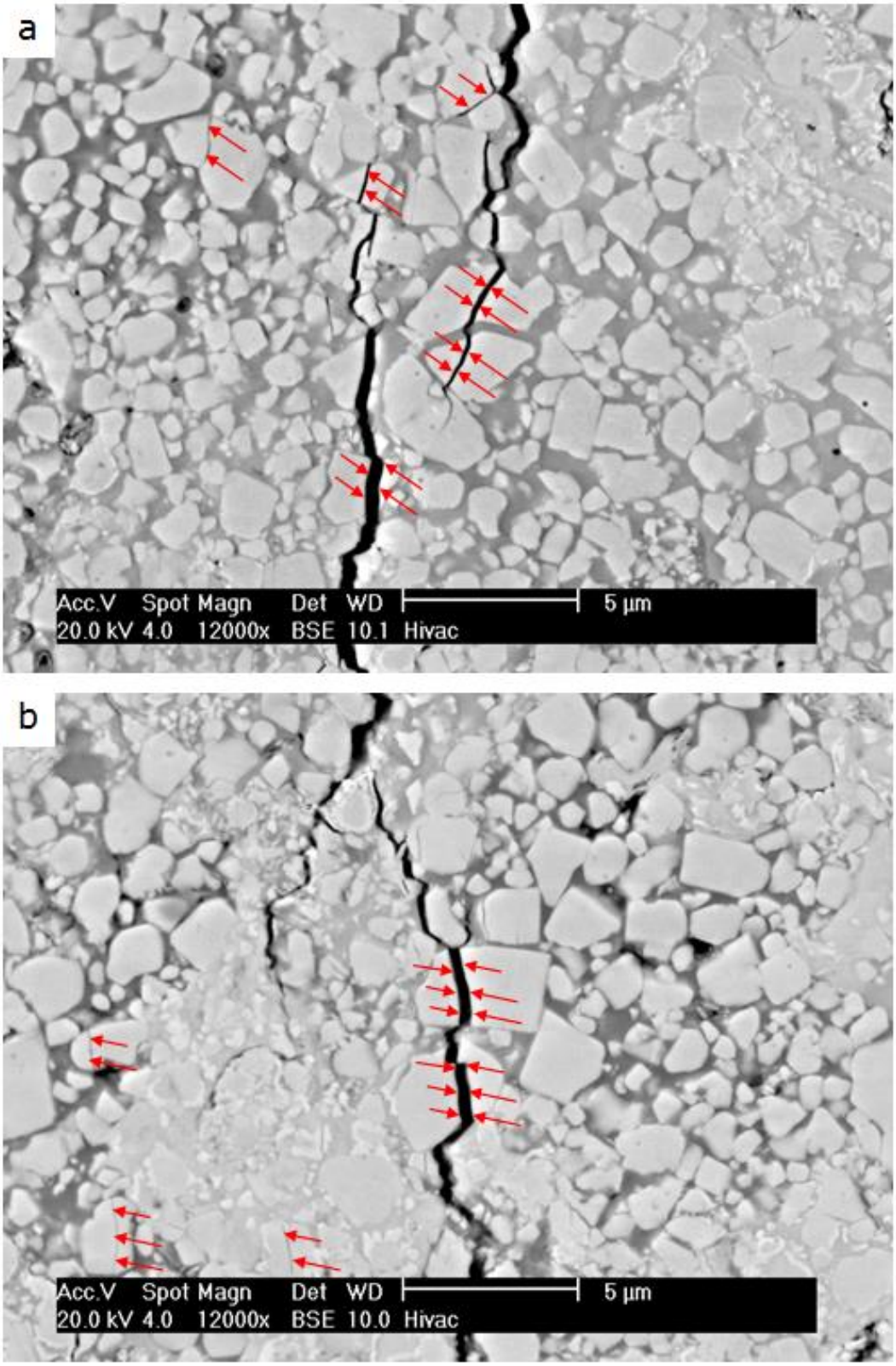

Figure 4-18: The high magnification SEM-BSE images show the developed semi-circular cracks going through the matrix and the WC grains. The cracks in the WC grains are very obvious in both coatings. (a) WC-12Co coating and (b) WC-12Ni coating.

Coating splats delamination section

The coating splats begin to delaminate at the edges of the scratch track when the normal load exceeds 47 N, about 7.5 mm from the starting point of the scratch of WC-12Co coating. The same thing is happen with WC-12Ni coating when the normal load goes above 39 N, approximately 6.2 mm from the starting point of the scratch.

The 3D Bruker ContourGT Optical Profiler images in Figure 4-19 illustrates the scratch profile at this section shows the coating splats delamination at the scratch edges. The average scratch width and depth at the end of the WC-12Co coating scratch have been about 109 µm and 4.3 µm, in order. These values with the WC-12Ni coating scratch were about 109 µm and 4.9 µm respectively.

The SEM images in Figure 4-20 represent the delamination of coating splats at the edges of the scratch and the cracks at this sector. The SEM high magnification images detailed the coating fracture behaviour of both WC-12Co and WC-12Ni coatings. The developed semi-circular cracks travel through the matrix and the carbide grains on both coatings. The cracks in WC grains have been seen in this section of the scratch with both of WC-12Co and WC-12Ni coatings.

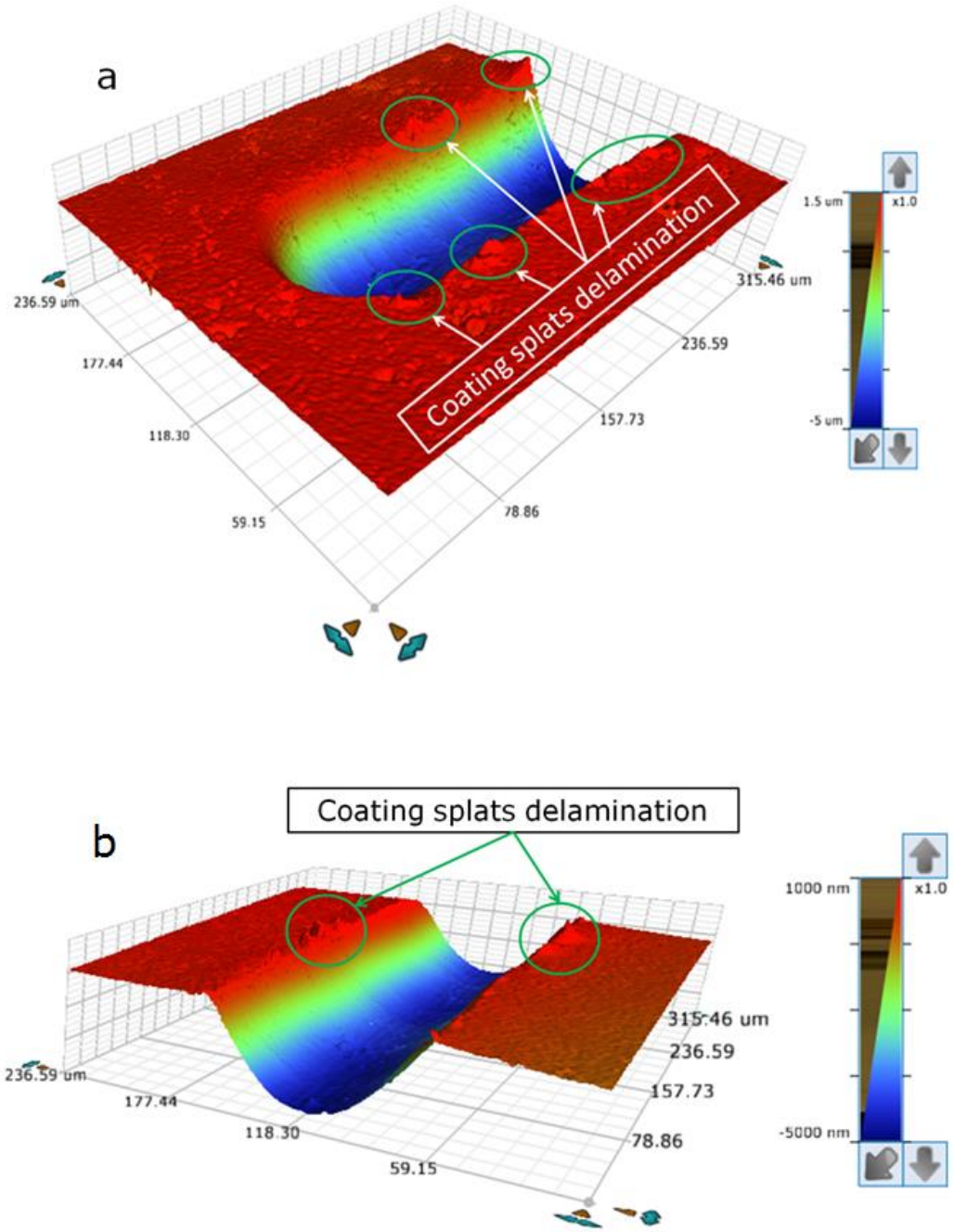

Figure 4-19: The 3D Bruker ContourGT Optical Profiler images exhibited the coating splats delamination at the scratch edges. (a) WC-12Co coating and (b) WC-12Ni coating.

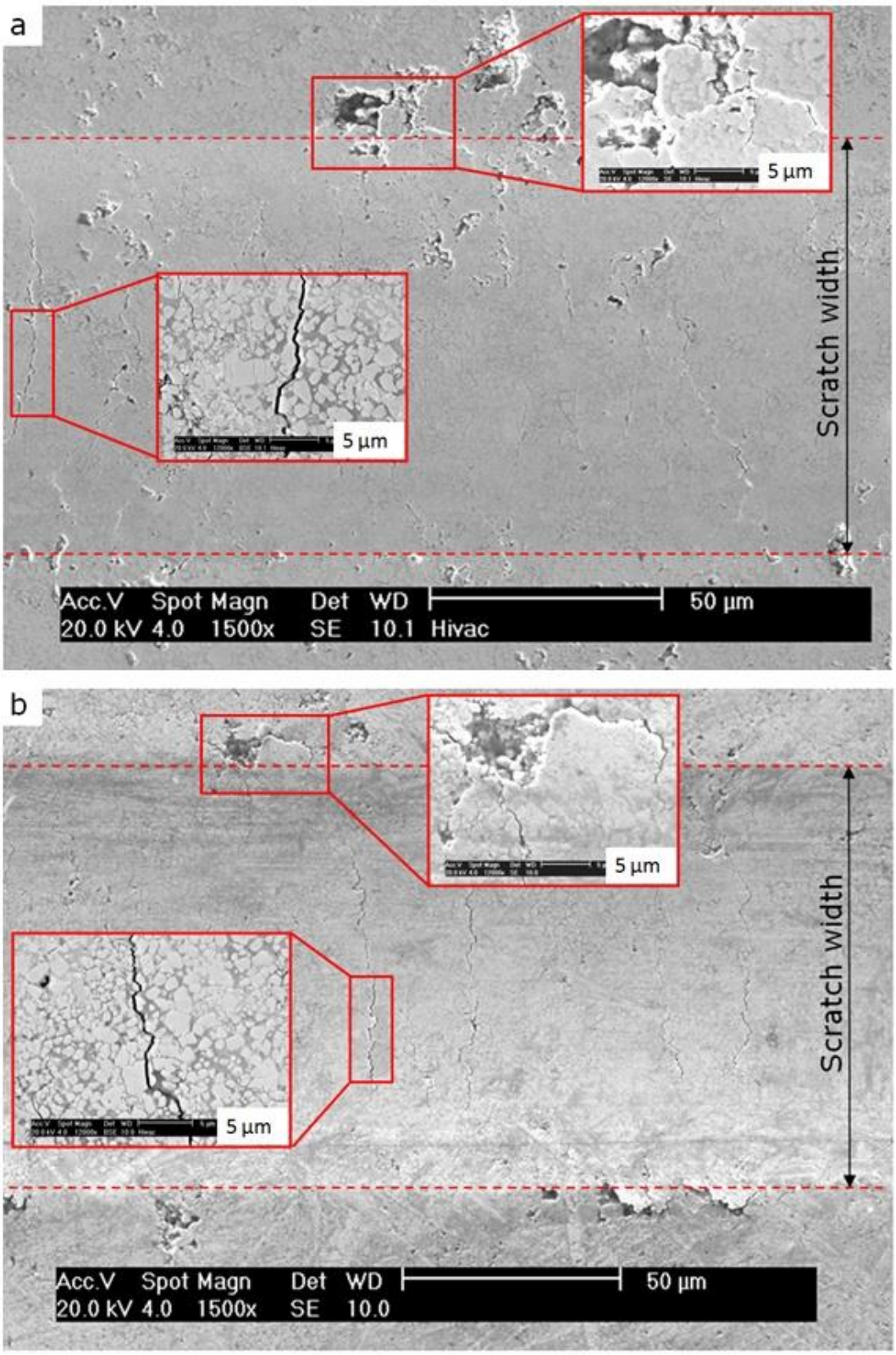

Figure 4-20: The SEM images illustrated the coating splats delamination at the edges of the scratch and the cracks at this section. The high magnification SEM images show the coating fracture behaviour and the cracks modes. (a) WC-12Co coating and (b) WC-12Ni coating.

4.1.4 Sliding wear behaviour

A dry sliding wear test has been employed on polished disc samples with surface roughness Ra = 0.04 μm, and the results obtained from the ball-on-disc dry sliding wear test of both coatings, WC-12Co and WC-12Ni, under different loads, are summarised in Table 4-4, ± values represent the standard error in the mean. Figure 4-21 shows the wear rate of the WC-12Co and WC-12Ni coated discs (plotted on a log scale) versus the applied loads. The wear rate of the counterface sintered WC-6Co ball sliding on coated discs (also plotted on a log scale) versus the applied loads is shown in Figure 4-22. An investigation on wear scars has been performed using the SEM and the optical profilometry (using a Bruker ContourGT Optical Profiler), in order to gain an understanding of wear behaviour. This investigation shows that the difference in the wear mechanism of both coatings is insignificant. However, the WC-12Co coating, as shown in Table 4-4, can withstand a higher applied load in the sliding wear test before the transition from mild to severe wear occurs.

Table 4-4: Results of dry sliding wear test of WC-12Co and WC-12Ni coated discs and WC-6Co sintered balls.

Coating	Normal load N	Sliding distance m	Disc wear 10^{-6} mm^3	Disc wear rate 10^{-6} mm^3/N.m	Disc wear scar depth µm	Friction coefficient µ	Ball wear rate 10^{-6} mm^3/N.m
WC-12Co	141	1500	139	0.0007±0.00001	0.13	0.17	0.15±0.03
	212	1500	1187	0.004±0.0007	0.15	0.27	0.2±0.04
	282	1500	327310	0.8±0.1	2.50	0.59	0.9±0.2
	353	100	392736	11±2	4.60	0.08	16±3
WC-12Ni	71	1500	430	0.004±0.0005	0.08	0.18	0.035±0.005
	118	1500	723	0.004±0.0003	0.10	0.19	0.01±0.001
	141	1500	66821	0.32±0.02	14.00	0.62	0.045±0.004
	212	100	2350017	111±9	31.40	0.16	2.3±0.2

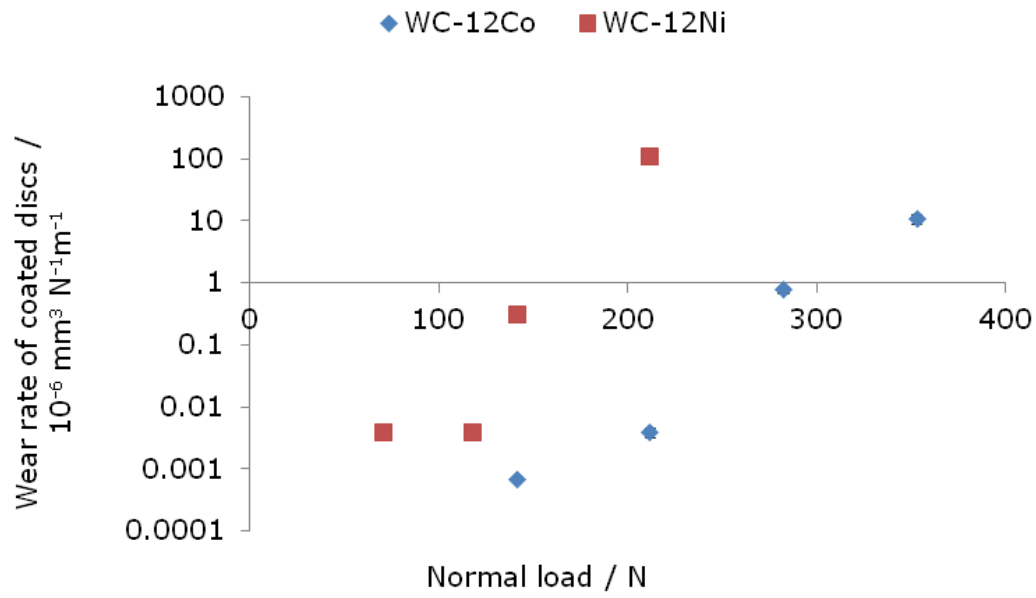

Figure 4-21: Plot of wear rate of WC-12Co and WC-12Ni coatings. The error bars represent the standard error in the mean.

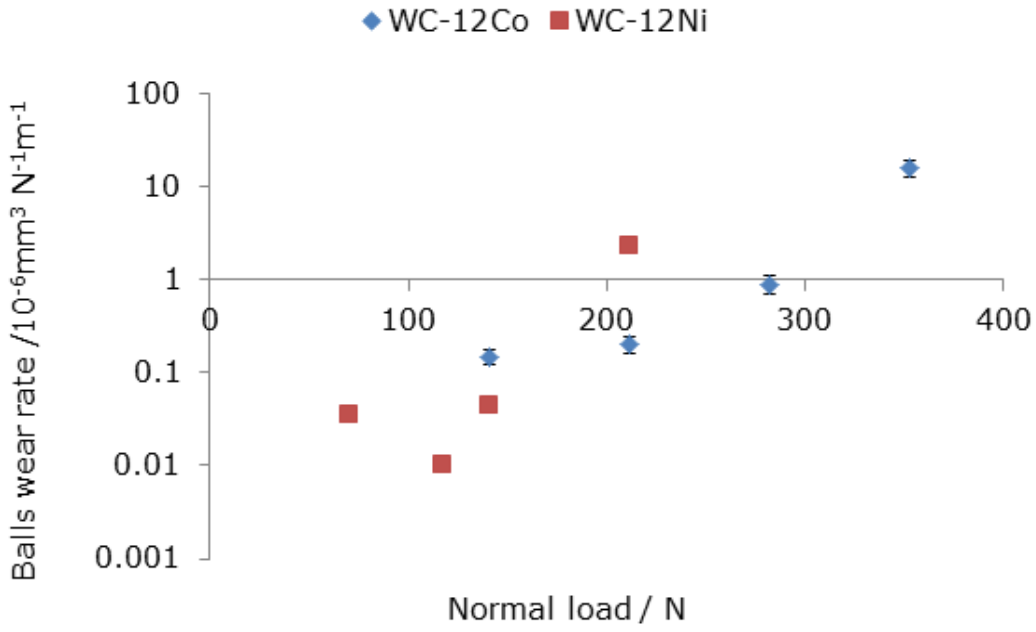

Figure 4-22: Plot of wear rate of sintered balls WC-6Co sliding against WC-12Co and WC-12Ni coated discs. The error bars represent the standard error in the mean.

4.1.4.1 Wear behaviour of WC-12Co coating

In order to assess the wear behaviour of the WC-12Co coating, a plan view of worn surfaces of WC-12Co coating under loads of 212 N and 282 N has been captured and demonstrated in Figure 4-23 and Figure 4-24 respectively. The reason behind choosing these particular loads is referred to the fact that the transition from mild to severe wear takes place somewhere in between these two loads.

The plan view of the surface of the WC-12Co coating worn under a load of 212 N (below the transition load) is illustrated in Figure 4-23. The worn surface of the coating shows a smooth surface with a number of pits as illustrated in low magnification SEM-SE image in Figure 4-23a. The wear track has been around 1.5 mm in width; this is after a sliding distance of 1500 m. Figure 4-23b shows a SEM-BSE image from the middle of the wear track. It has been found that a number of localised transfer layers had been generated during the dry sliding test. Selected area "c" from previous figure is demonstrated in high magnification SEM-SE image in Figure 4-23c which shows the fracture of some of the brittle oxide layers. The selected area "d" in Figure 4-23b is illustrated in high magnification SEM-BSE image in Figure 4-23d shows narrow intergranular cracks (indicated by red arrows) propagate in the coating layer during the mild wear of WC-12Co coating.

Cross-section has been made through the mild wear track to investigate the wear behaviour of WC-12Co coating in this stage. Figure 4-23e shows the wear scar cross-section below the transition load (212 N) which shows thick localised transfer layer on the top. Narrow intergranular subsurface cracks are propagating in the WC-12Co coating during mild wear (red arrows in Figure 4-23e).

The energy dispersive X-ray analysis (EDX) of the transferred layer, shown in Figure 4-23f demonstrates the presence of tungsten, cobalt, and oxygen. The increase of the weight percent of the oxygen in the transferred layer made it clear that this layer is an oxide layer.

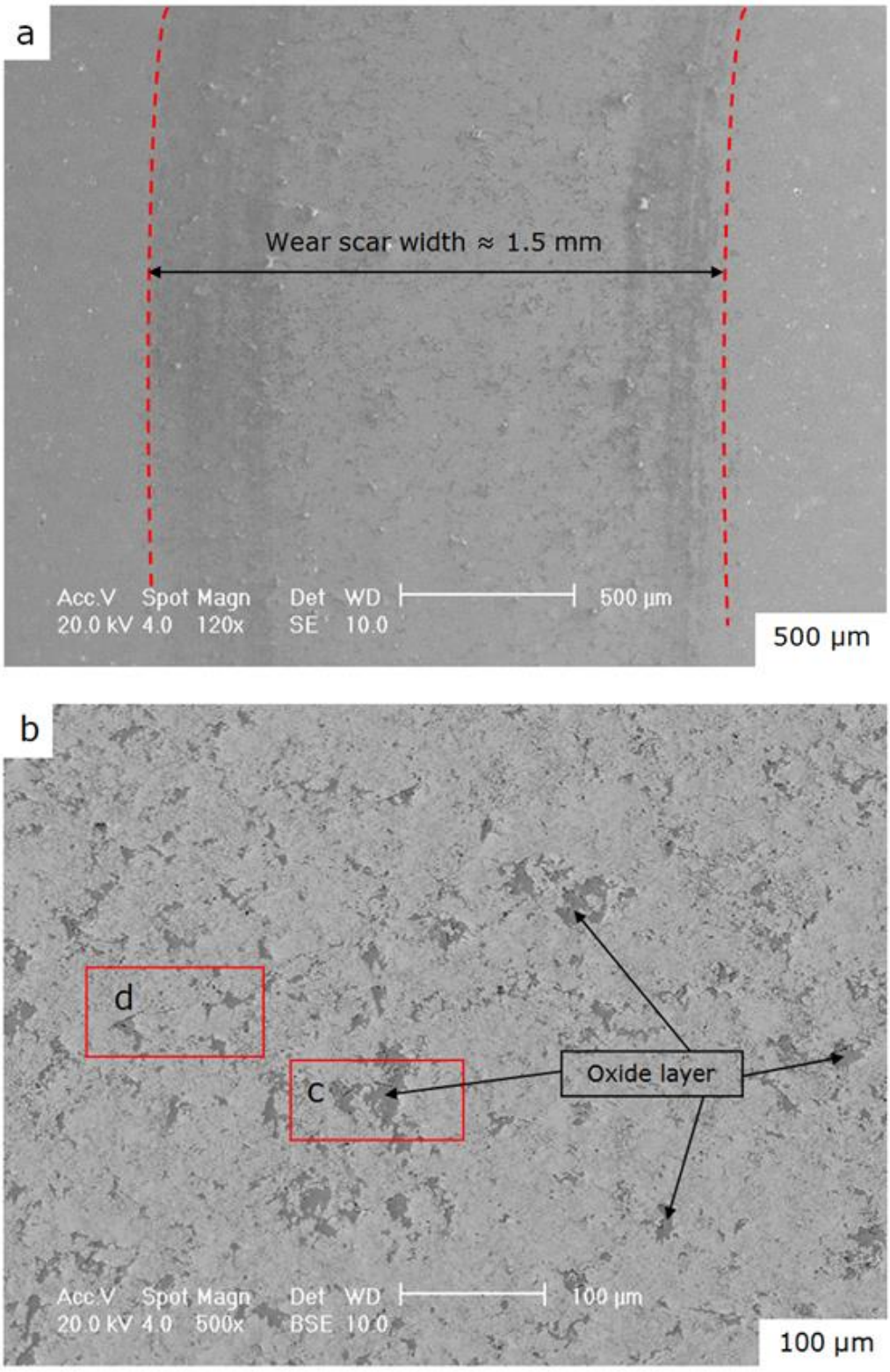

Figure 4-23: Mild wear behaviour of WC-12Co coating. (a) Top view of wear scar of WC-12Co coating worn under normal load 212 N. (b) SEM-BSE image taken from the middle of the wear track shows the localised oxide layers, selected areas c & d are shown in next figures, respectively. (Sliding direction is from top to bottom).

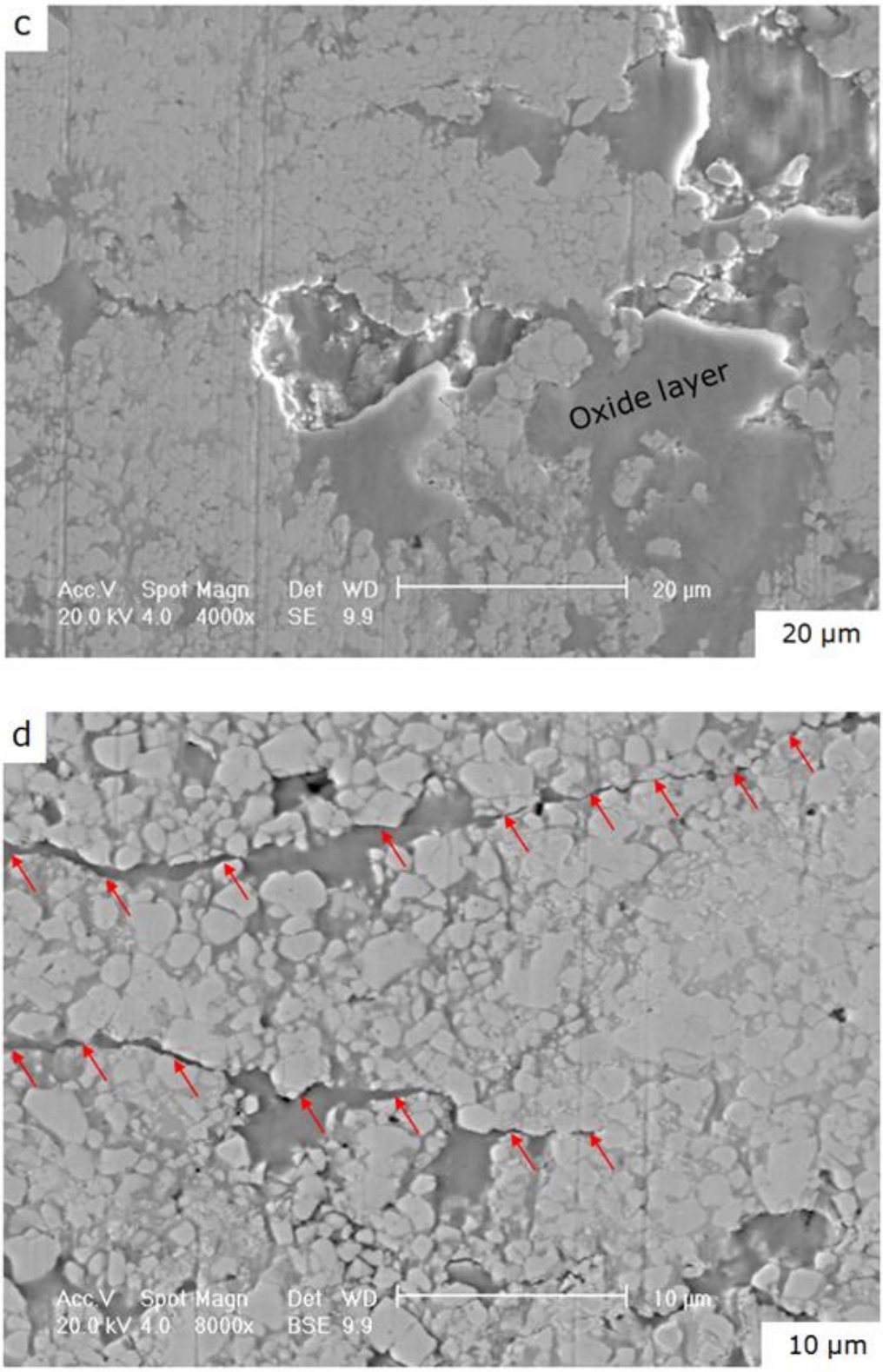

Figure 4-23 (Cont.): Mild wear behaviour of WC-12Co coating. (c) SEM-SE image shows the fracture of some of the brittle oxide layers during the mild wear. (d) SEM-BSE high magnification shows narrow intergranular cracks generated in the coating surface during the mild wear (red arrows).

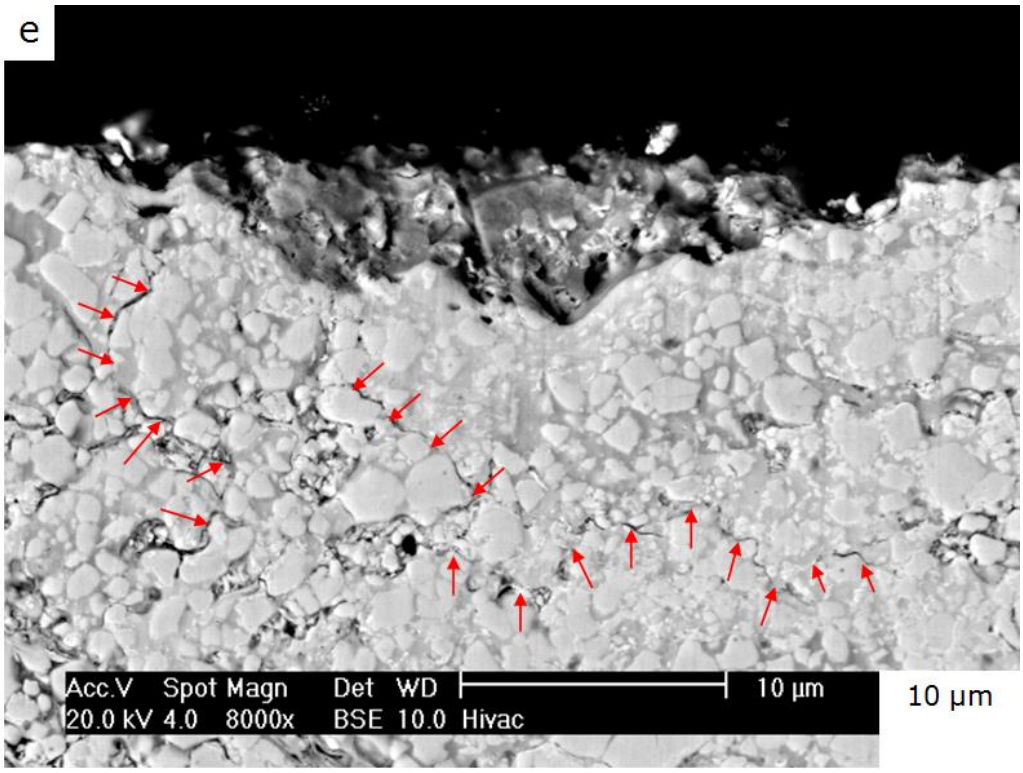

Figure 4-23 (Cont.): Mild wear behaviour of WC-12Co coating. (e) Cross-section through the wear track of WC-12Co coating during mild wear (normal load = 212 N) shows the localised oxide layer and very narrow intergranular subsurface cracks (red arrows).

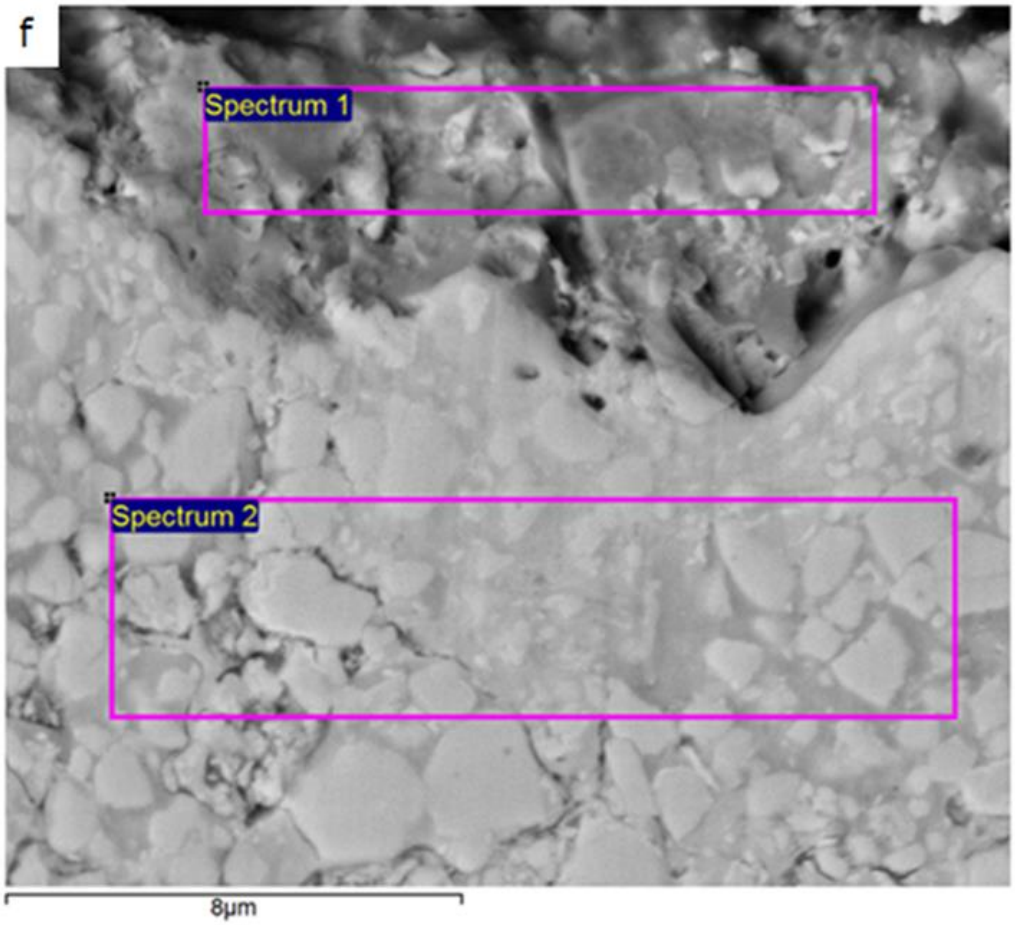

Spectrum	O wt%	Co wt%	W wt%
Spectrum 1	7	16	77
Spectrum 2	1	11	88

Figure 4-23 (Cont.): Mild wear behaviour of WC-12Co coating. (f) EDX analysis of transfer layer (spectrum 1). The increase in the oxygen weight percent proves that this transfer layer is an oxide layer.

In contrast, the surface of the same coating (WC-12Co) worn under a load of 282 N (above the transition load) shows more severe wear as can be clearly seen in Figure 4-24.

The surface of the WC-12Co coated disc worn under the load of 282 N reveals more severe wear as exhibited in low magnification SEM-SE image in Figure 4-24a. The wear track has been about 2 mm in width, this is after a sliding distance of 1500 m. Selected area "b" in previous figure from the middle of the wear track is presented in SEM-SE image in Figure 4-24b. It shows very severe wear and approximately the whole wear track is covered by the transfer layer. The selected area "c" in Figure 4-24b is illustrated in high magnification SEM-SE image in Figure 4-24c shows the fracture of the brittle oxide layer during the wear test. The angular WC grains in high magnification SEM-BSE in Figure 4-24d are indication that the top coating layer (which means the brittle oxide layer in this stage) has been fractured. Wider cracks have been seen in the transfer layer presented in Figure 4-24d.

Cross-section was made in the severe wear track to examine the wear behaviour of WC-12Co coating during severe wear. The wear scar cross-section above the transition load (282 N) is depicted in Figure 4-24e and shows a thin transfer layer covering the top surface of the worn coating surface. Wider intergranular subsurface cracks are propagating in the WC-12Co coating through severe wear. In this case, cracks in WC grains are observed.

The energy dispersive X-ray analysis (EDX) of the transferred layer during severe wear is illustrated in Figure 4-24f reveals the existence of tungsten, cobalt, and oxygen. The increase of the weight percent of the oxygen in the transferred layer made it clear that this layer is an oxide layer.

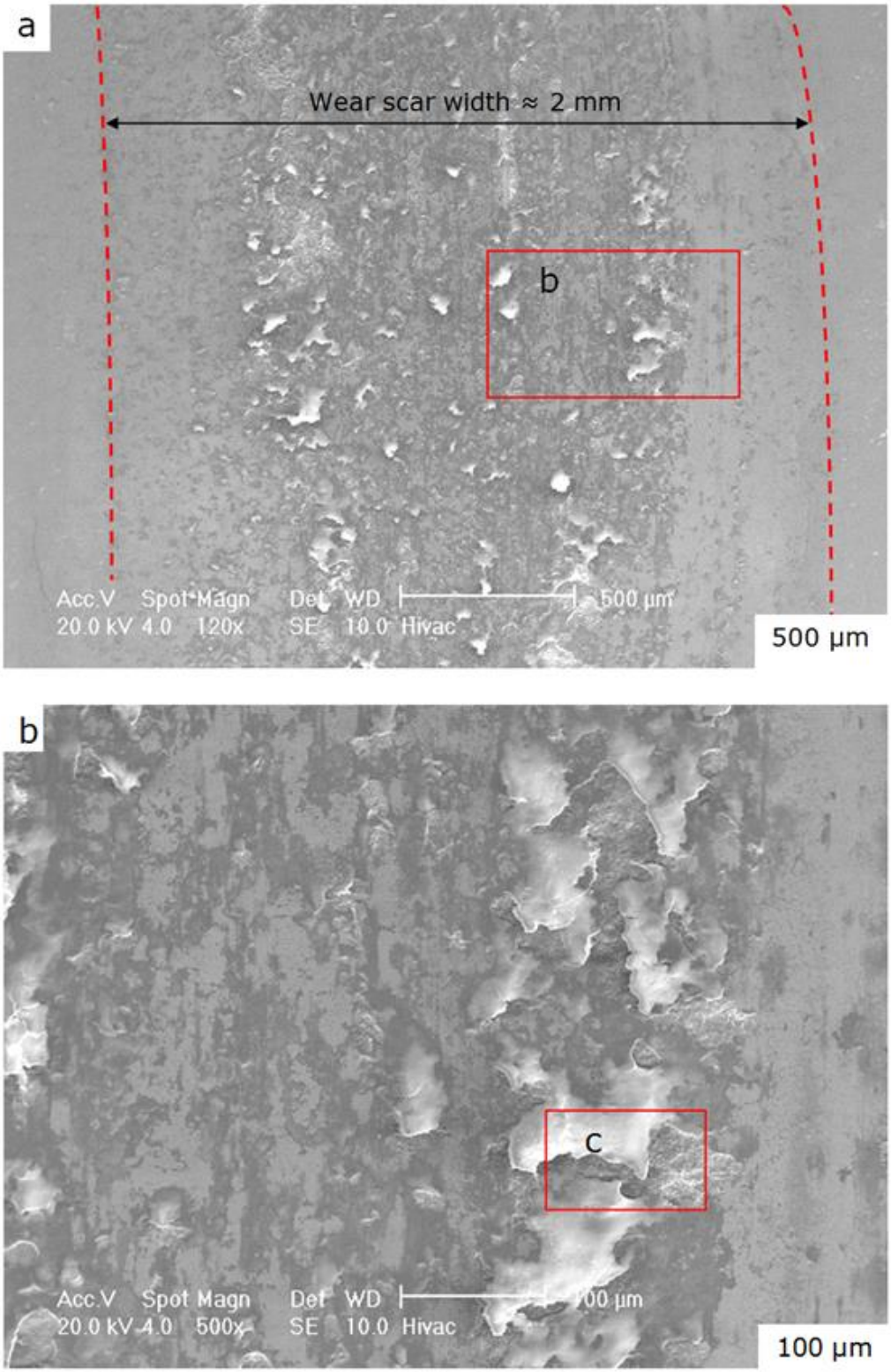

Figure 4-24: Severe wear behaviour of WC-12Co coating. (a) Top view of wear scar of WC-12Co coating worn under normal load 282 N. (b) SEM-SE image taken from the middle of the wear track shows very severe wear. The transfer layer is about to cover the whole wear track. Selected areas c is shown in next figure. (Sliding direction is from top to bottom).

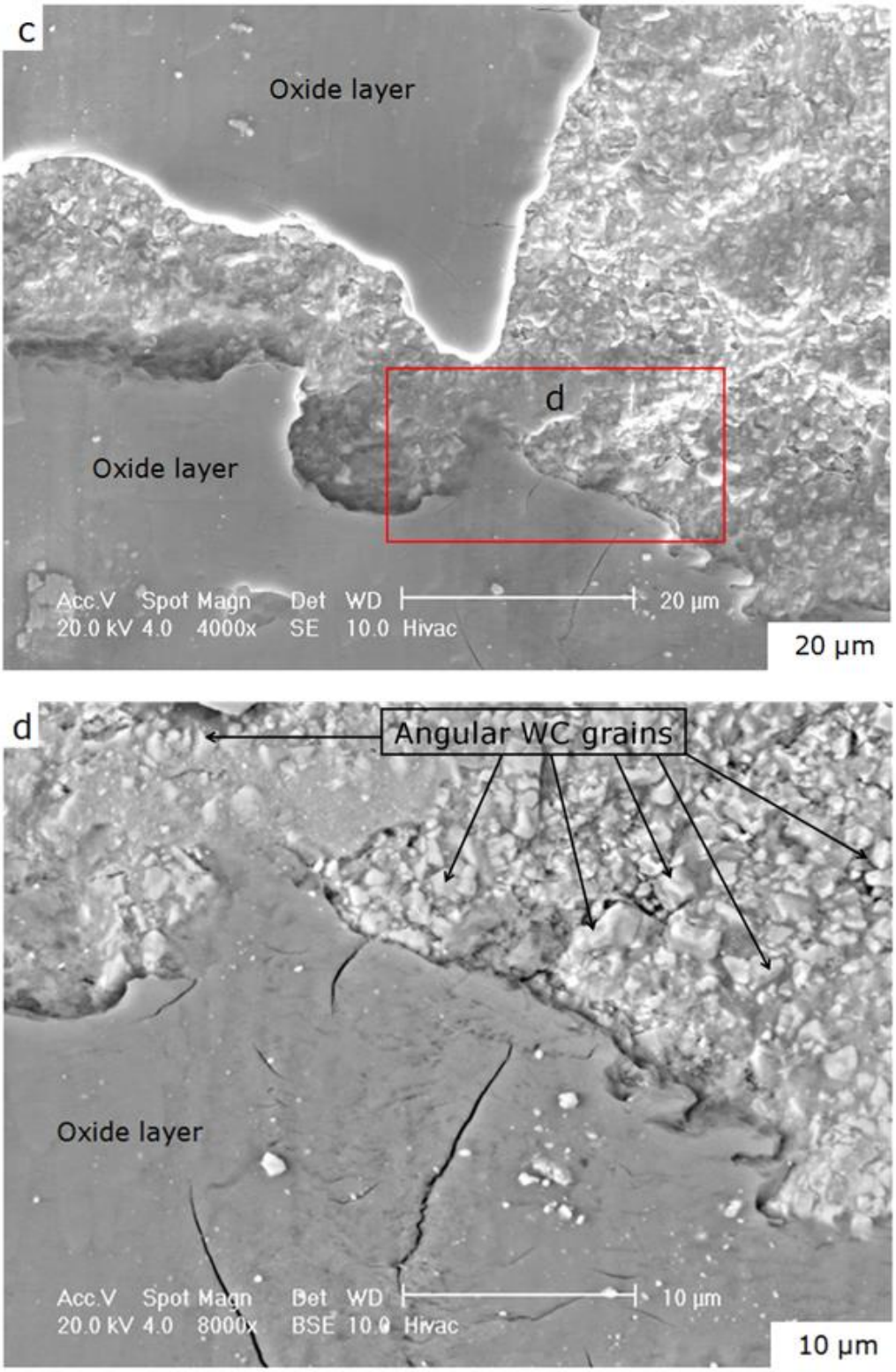

Figure 4-24 (Cont.): Severe wear behaviour of WC-12Co coating. (c) SEM-SE image illustrates the fracture of the brittle oxide layer. (d) SEM-BSE high magnification image if selected area "d" shows the angular WC grains which indicates the fracture of the top oxide layer.

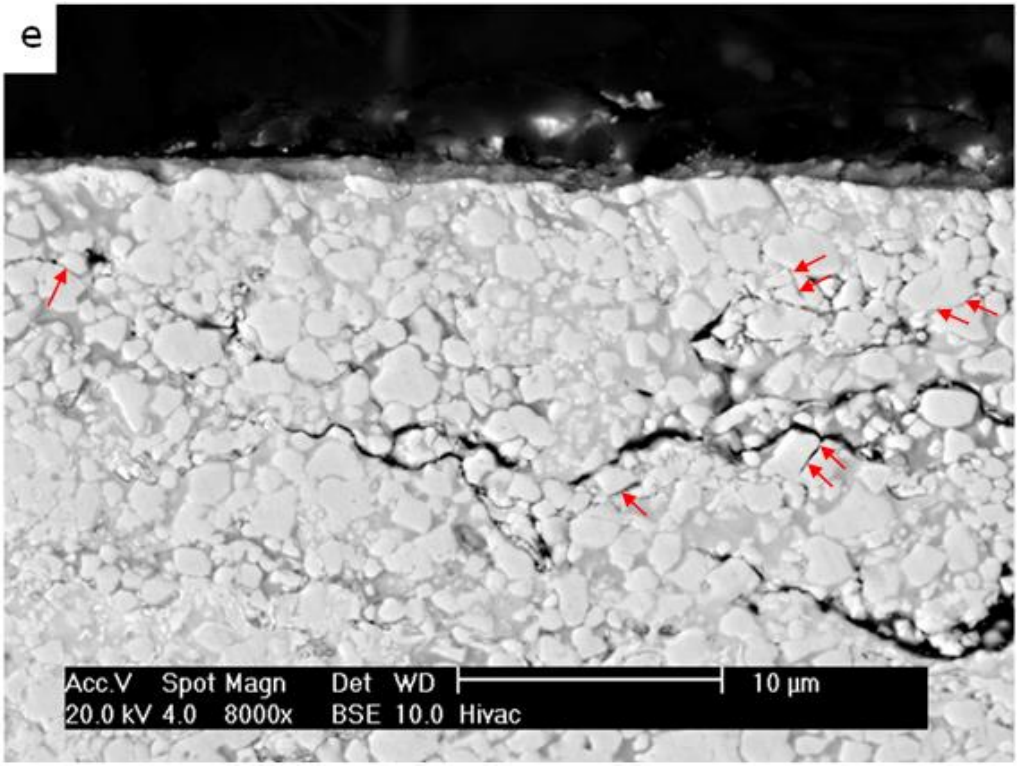

Figure 4-24 (Cont.): Severe wear behaviour of WC-12Co coating. (e) Cross-section in the severe wear scar of WC-12Co coating (normal load = 282 N) shows thin transfer layer covering the whole top surface and wider intergranular subsurface cracks. Cracks are seen in the WC grains (red arrows).

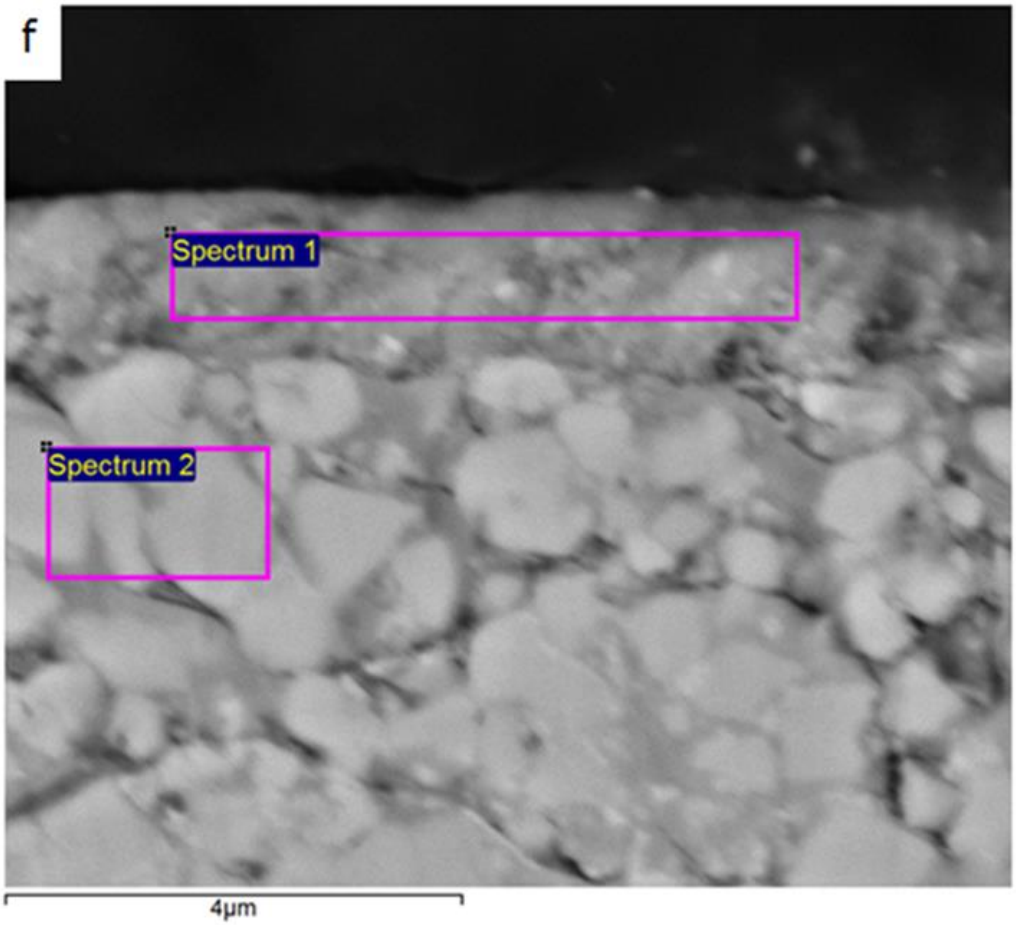

Spectrum	O wt%	Co wt%	W wt%
Spectrum 1	17	7	76
Spectrum 2	1	7	92

Figure 4-24 (Cont.): Severe wear behaviour of WC-12Co coating. (f) EDX analysis of transfer layer (spectrum 1). The increase in the oxygen weight percent indicates that this transfer layer is an oxide layer.

The morphology of the wear debris of WC-12Co coating worn with severe wear, (282 N), is demonstrated in Figure 4-25. The wear debris consists of plate-like debris which has resulted from the delamination of the transferred layer. Agglomerated fine particles can also be seen. The wear debris during mild wear has been extremely little, which cannot be collected for investigation.

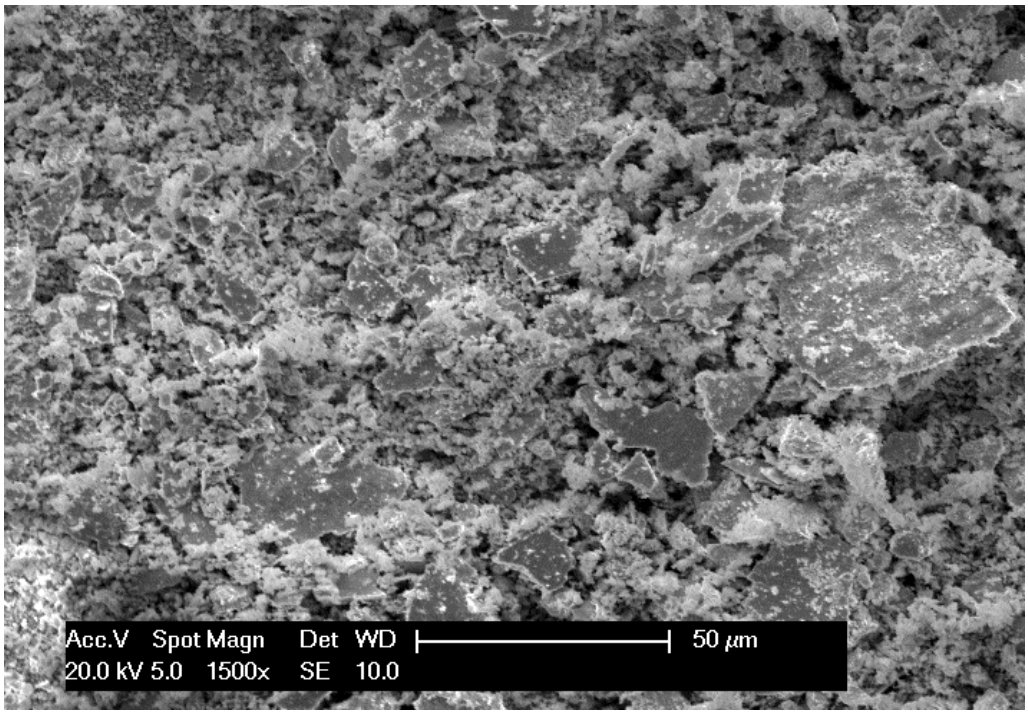

Figure 4-25: The wear debris of WC-12Co coated disc worn with a severe wear shows the plate like debris.

The optical profilometry (using a Bruker ContourGT Optical Profiler) has been used to investigate the wear scar of WC-12Co coating. The 2D Bruker ContourGT Optical Profiler image of mild wear sample, below the transition load (212N), is illustrated in Figure 4-26a, that shows low wear. However, the 2D Bruker ContourGT Optical Profiler image of severe wear, above the transition load (282 N), is exhibited in Figure 4-26b that shows high wear. Figure 4-26c represents the wear scar profile of WC-12Co coating with mild wear, below the transition load (212 N), where the wear scar depth is about 0.15 µm and the scar width is around 1.5 mm. The wear scar profile with severe wear, above the transition load (282 N), is illustrated in Figure 4-26f with a wear scar depth of about 2.5 µm and wear scar width of nearly 2 mm.

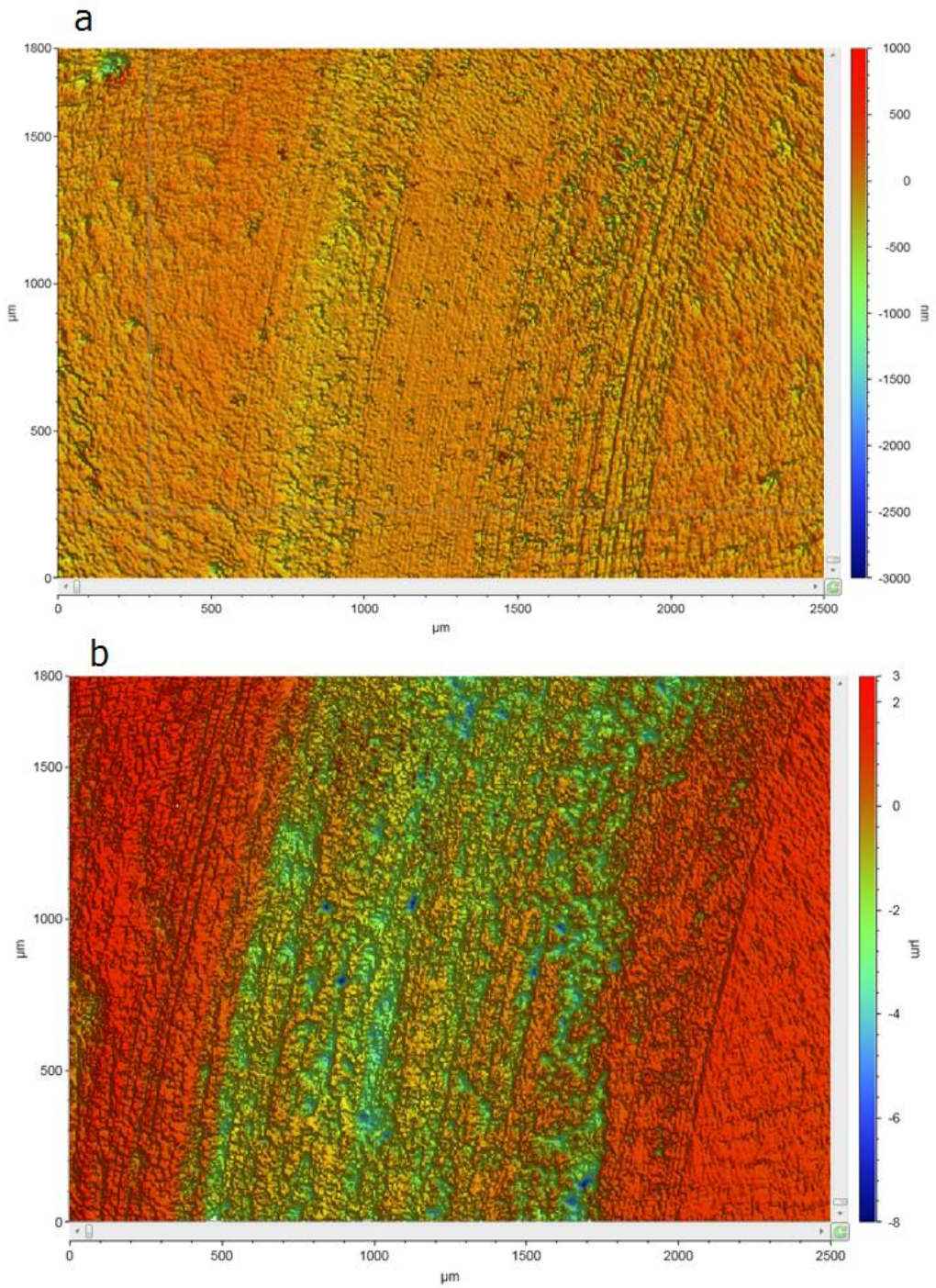

Figure 4-26: Bruker ContourGT Optical Profiler investigation of wear scar of WC-12Co coating. (a) 2D Bruker ContourGT Optical Profiler image during mild wear (normal load = 212 N) shows low wear. (b) 2D Bruker ContourGT Optical Profiler image during severe wear (normal load = 282 N) shows high wear.

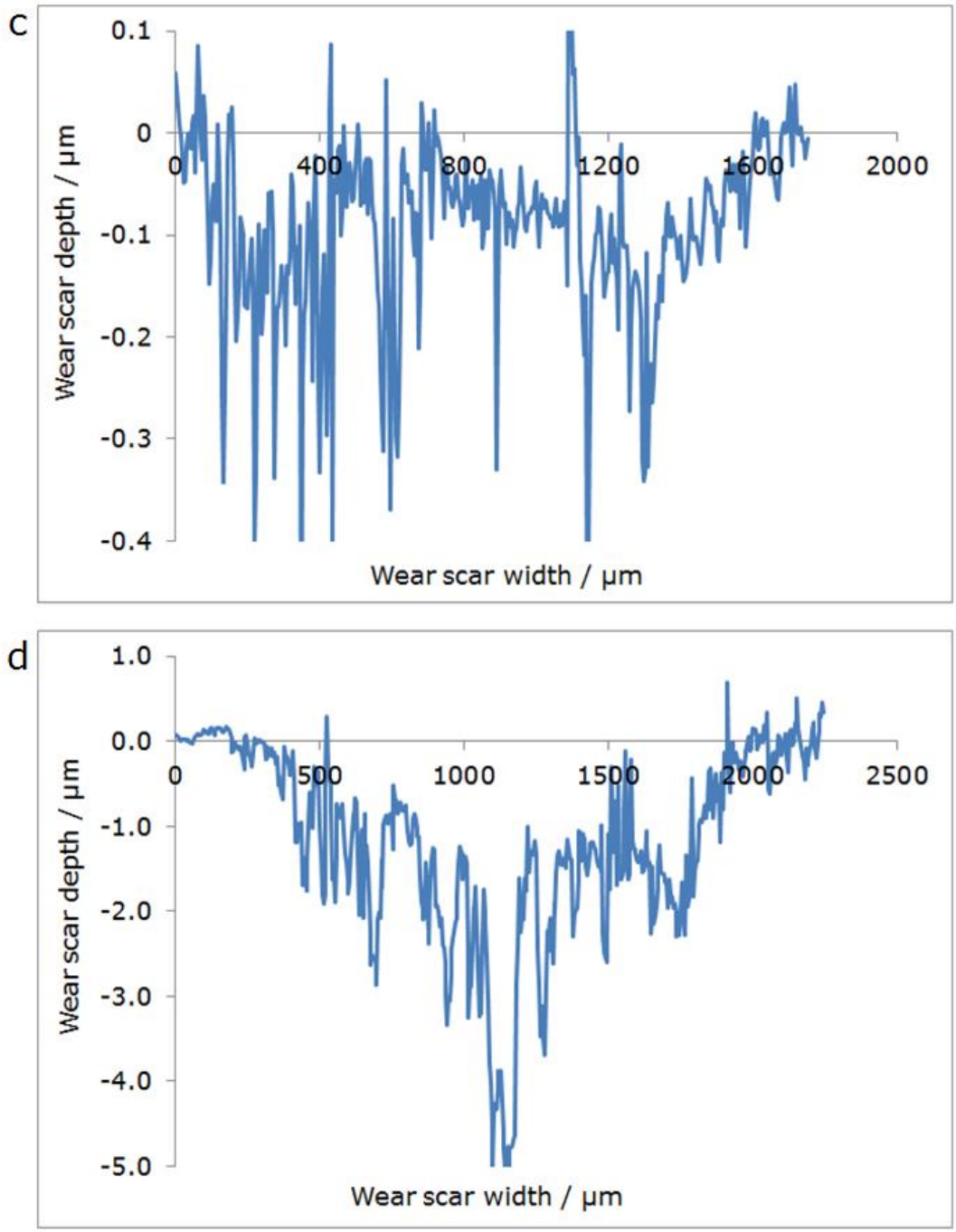

Figure 4-26 (Cont.): Bruker ContourGT Optical Profiler investigation of wear scar of WC-12Co coating. (c) The plot of mild wear profile shows the width and the depth of wear scar. (d) The plot of severe wear profile shows the width and the depth of wear scar.

The variation of the friction coefficient with sliding distance for WC-12Co coating during mild and severe wear is demonstrated in Figure 4-27. During the mild wear (normal load = 212 N), through the running-in period from starting to about 250 m the friction coefficient increased to µ=0.2. The curve then start to increase gradually

until the friction coefficient has been about μ = 0.35 at 1100 m, where it becomes steady state.

The friction coefficient increased sharply during running-in period with the severe wear (normal load = 282 N) to reach around μ = 0.74. Then the curve start to decrease gradually until the μ = 0.56 about 1100 m, where the steady state start.

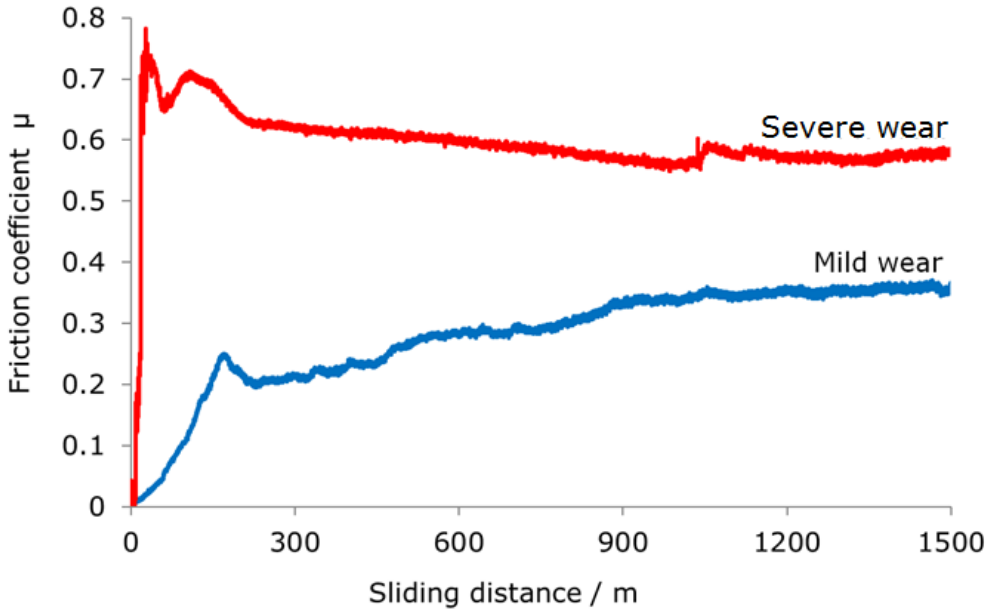

Figure 4-27: Variation of the friction coefficient with sliding distances for WC-12Co coating during wear test.

The worn surface of the counterface sintered WC-6Co ball which sliding against the WC-12Co coated disc during the mild wear, (below the transition load, 212 N), has been examined by the SEM. Figure 4-28a shows a very smooth worn surface with a little debris stuck on it. Figure 4-28b is the high magnification SEM-BSE image of selected area "b" which illustrates the small amount of wear debris transformed from the coated disc and stuck on the worn surface of the ball. Figure 4-28c is the high magnification SEM image which illustrates the selected area "c" from the middle of the ball worn surface proving that there has been no significant change in the microstructure of the ball worn surface through the mild wear.

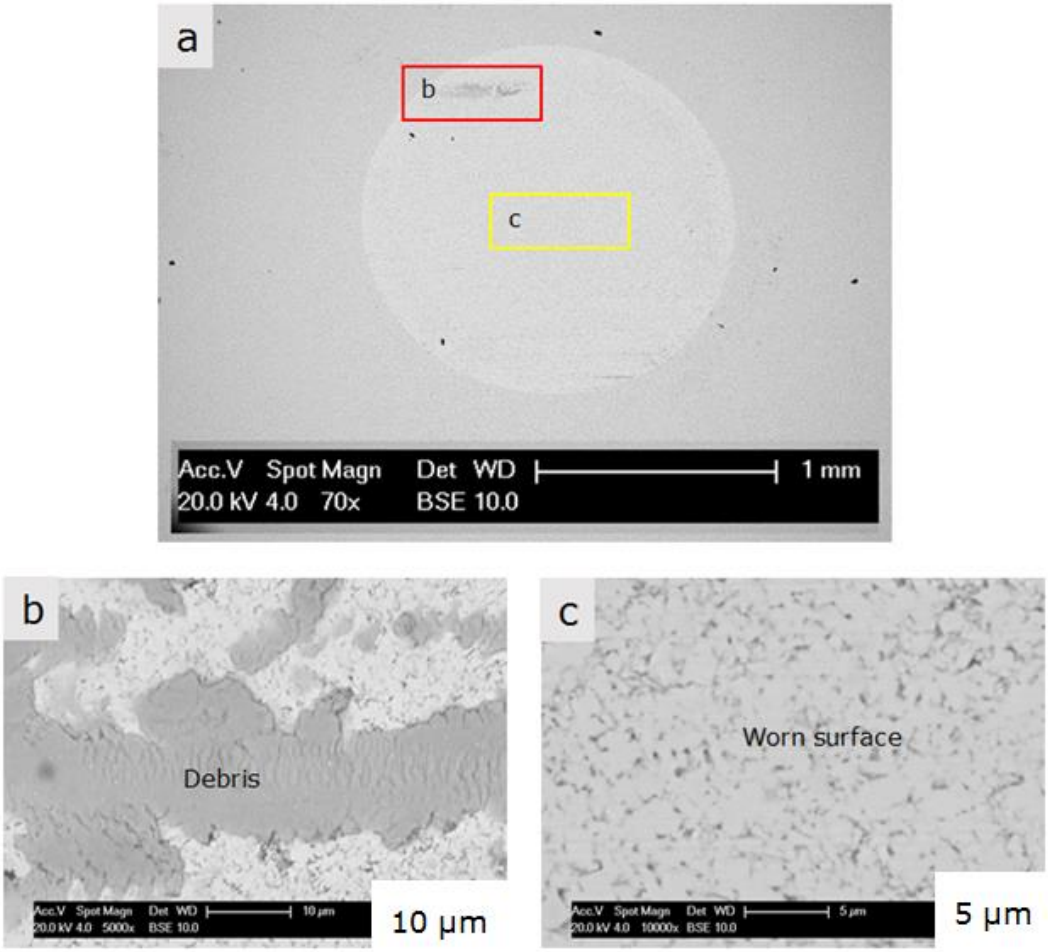

Figure 4-28: Mid wear behaviour of sintered WC-6Co ball sliding against WC-12Co coated disc. (a) Low magnification SEM-BSE of the ball worn surface. (b) SEM-BSE image of elected area "b" shows the debris stuck on the ball worn surface. (c) High magnification SEM-BSE image of selected area "c" from the middle of ball worn surface shows smooth surface.

The wear behaviour of the sintered WC-6Co ball sliding counter to the WC-12Co coated disc through the severe wear is illustrated in Figure 4-29. The selected area "b" in Figure 4-29a, is exhibited in SEM-BSE image in Figure 4-29b. This last shows unworn ball surface, the debris generated during sliding wear and the worn surface with some dislocated WC grains. Figure 4-29c represents the high magnification SEM image of wear debris morphology which shows the mix of tribofilm matrix (grey colour) with fine WC particles (bright colour). Furthermore, Figure 4-29d shows the high magnification SEM image of the ball worn surface where the dislocation of some WC grains is very obvious (arrows).

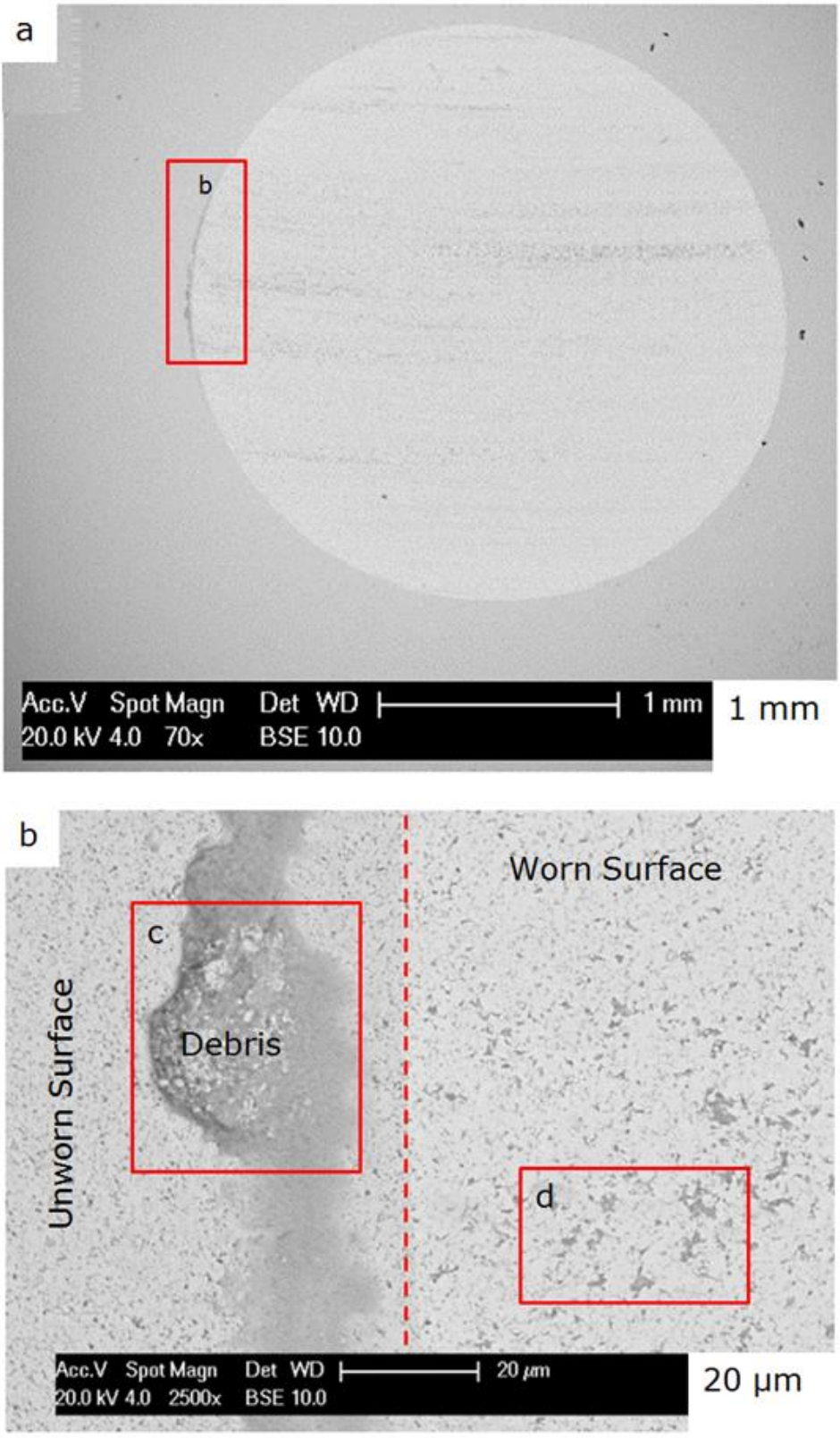

Figure 4-29: Severe wear behaviour of sintered WC-6Co ball sliding against WC-12Co coated disc. (a) Low magnification SEM-BSE image of ball worn surface. (b) SEM-BSE image of selected area "b" shows worn and unworn surface of the ball.

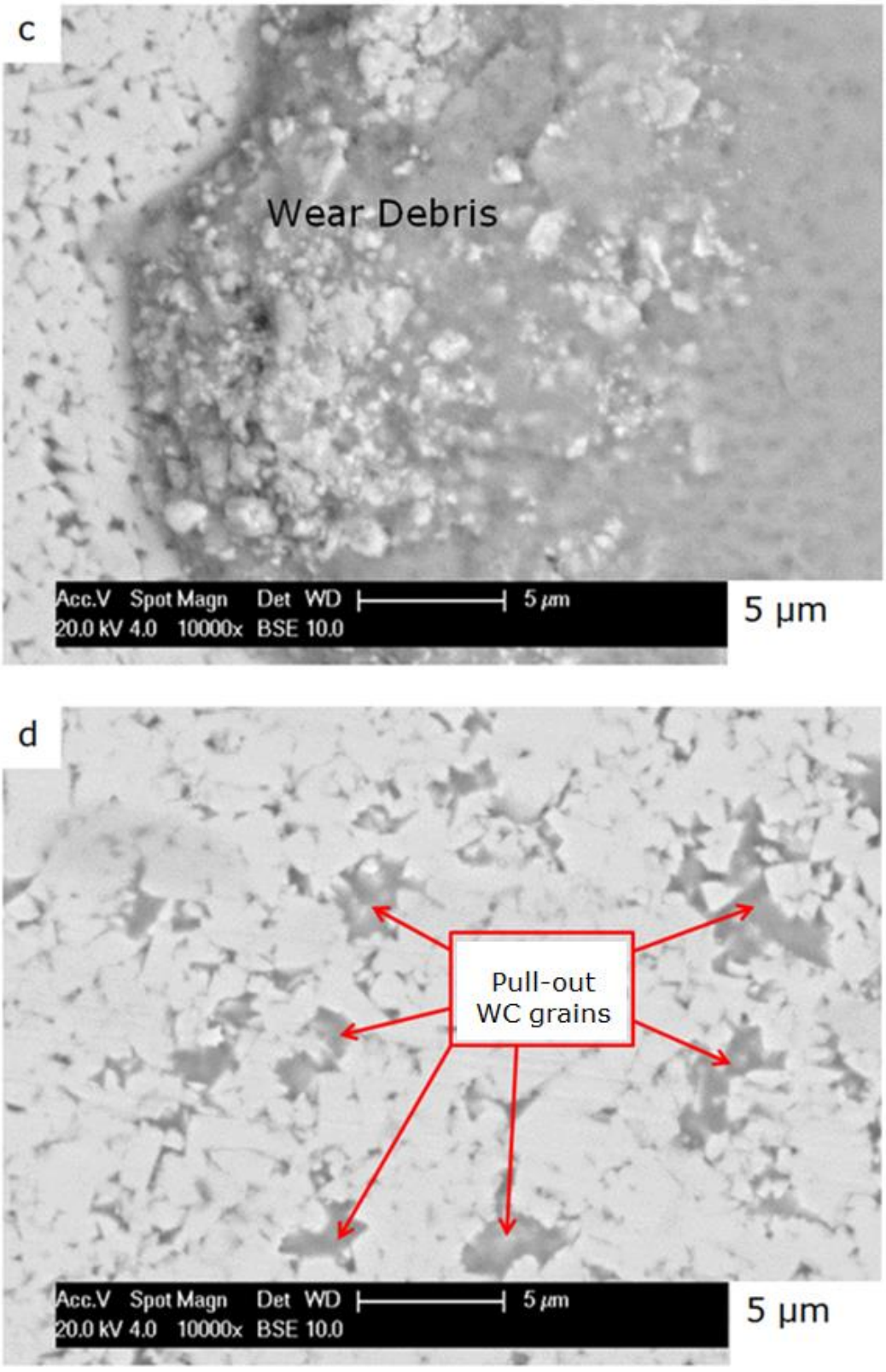

Figure 4-29 (Cont.): Severe wear behaviour of sintered WC-6Co ball sliding against WC-12Co coated disc. (c) The morphology of the wear debris shows fine WC particles embedded in oxide matrix. (d) High magnification SEM-BSE of ball worn surface shows bull-out of WC grains.

4.1.4.2 Wear behaviour of WC-12Ni coating

To examine the dry sliding wear behaviour of WC-12Ni coating, the worn surface of WC-12Ni coating below and above the transition load (118 N and 141 N, respectively) has been captured and shown in Figure 4-30 and Figure 4-31 in order. These loads have been selected because the transition from mild to severe wear takes place somewhere in between.

The plan view of the WC-12Ni coating worn under a load of 118 N (below the transition load) is illustrated in Figure 4-30. It shows a smooth surface with a number of pits as illustrated in low magnification SEM-SE image in Figure 4-30a. The wear track width has been about 0.6 mm; this is after a sliding distance of 1500 m. Figure 4-30b shows a SEM-BSE image from the middle of the wear track. It has been found that a number of localised transfer layers had been generated during the dry sliding test. Narrow intergranular cracks propagate in the coating top surface are observed. Selected area "c" in Figure 4-30b is demonstrated in high magnification SEM-SE image in Figure 4-30c which illustrates the narrow crack propagating through the coating grain boundaries (noted by red arrows). The polished surface of WC grains (flat WC grains) proves there is no fracture in the coating yet.

Cross-section has been made through the mild wear track to investigate the wear behaviour of WC-12Ni coating in this stage. Figure 4-30d shows the wear scar cross-section below the transition load (118 N) which shows thick localised transfer layer on the coating top surface. There are no subsurface cracks observed in this stage.

The energy dispersive X-ray analysis (EDX) of the transferred layer is shown in Figure 4-30e and indicates the presence of tungsten, nickel, and oxygen. The increase of the weight percent of the oxygen in the transferred layer made it clear that this layer is an oxide layer.

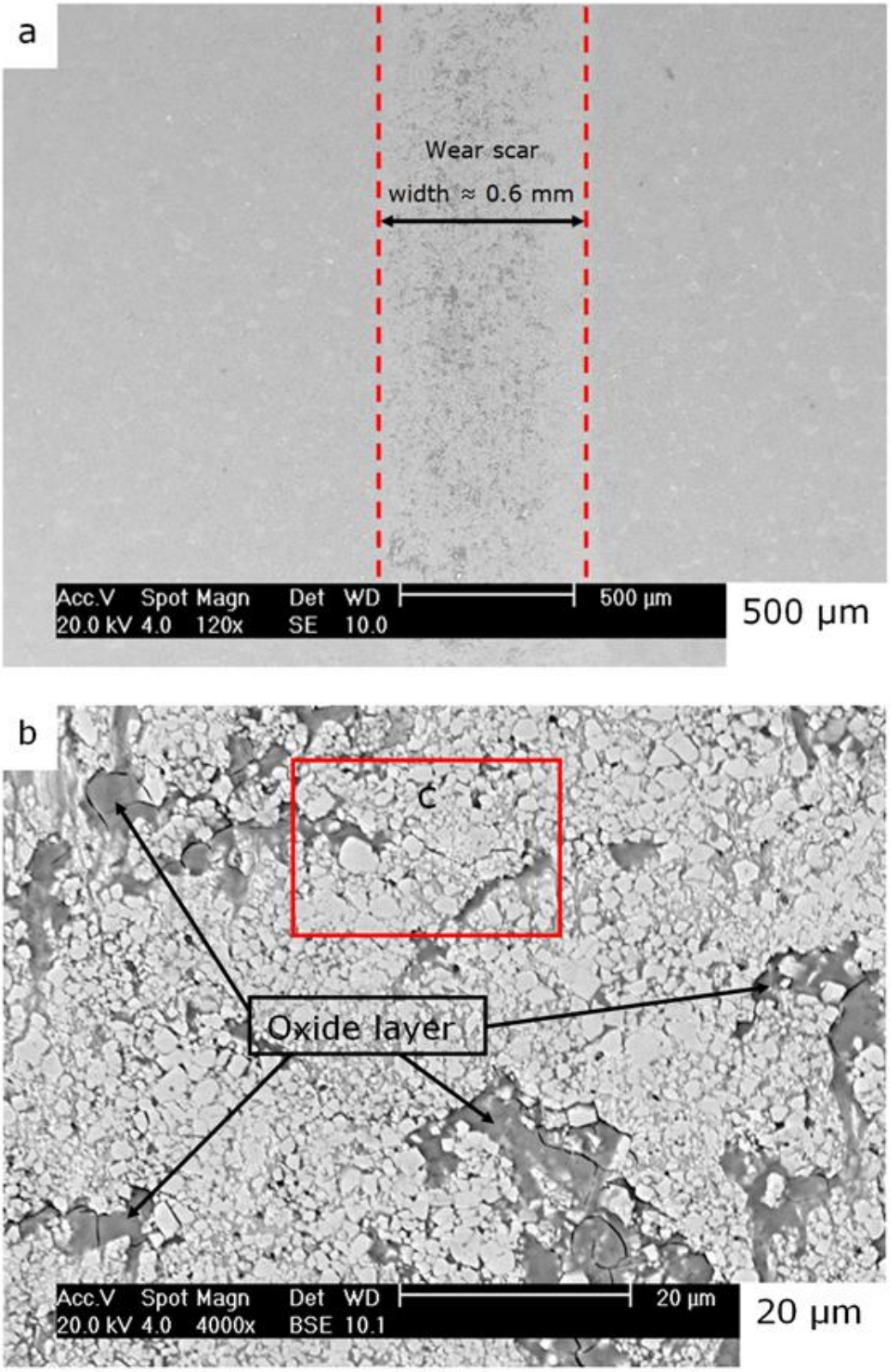

Figure 4-30: Mild wear behaviour of WC-12Ni coating. (a) Top view of wear scar of WC-12Ni coating worn under normal load 118 N. (b) SEM-BSE image taken from the middle of the wear track shows the localised oxide layers, selected area c shows in next figure. (Sliding direction is from top to bottom).

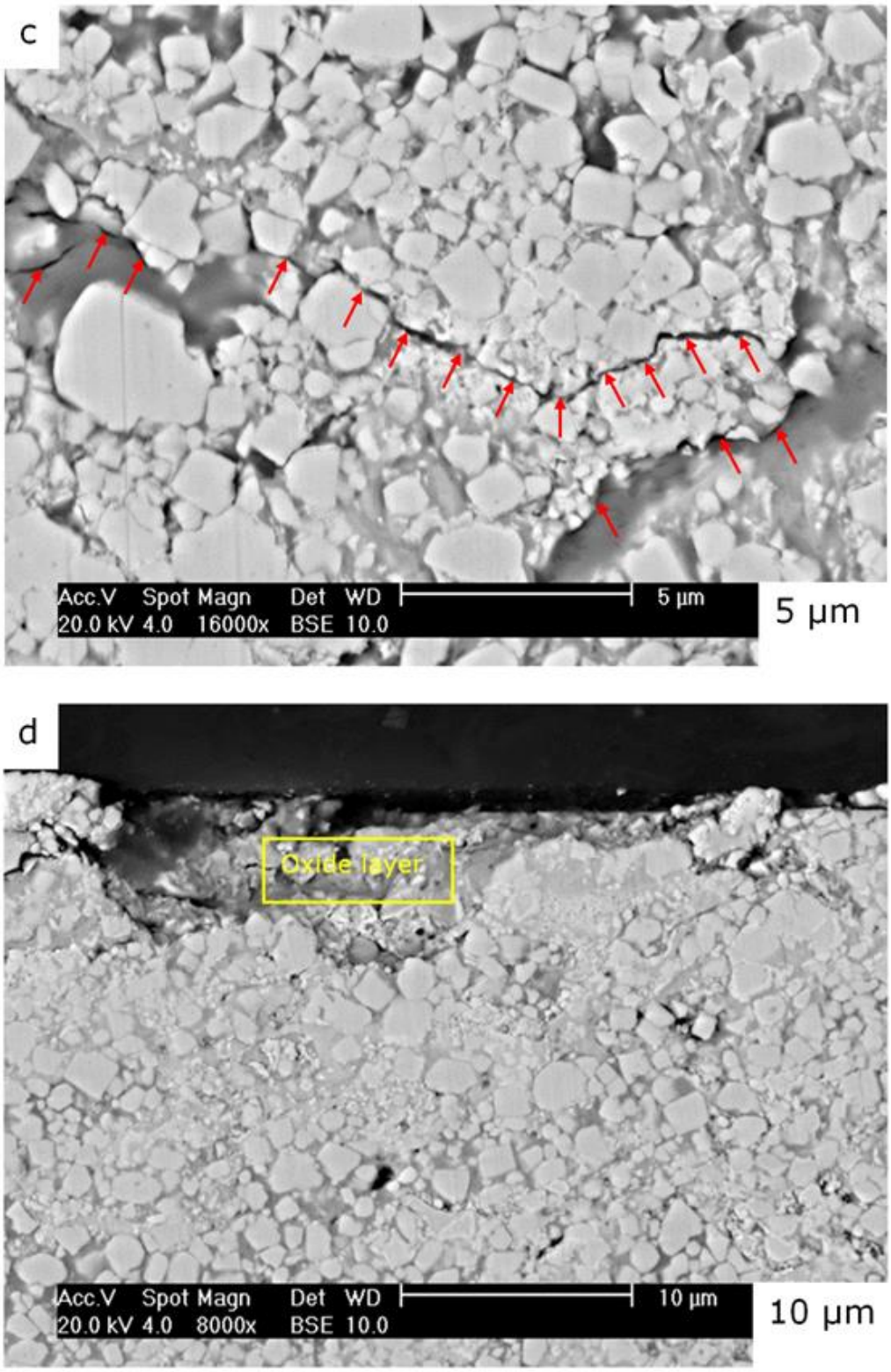

Figure 4-30 (Cont.): Mild wear behaviour of WC-12Ni coating. (c) SEM-BSE high magnification shows narrow intergranular cracks propagate in the WC-12Ni coating surface during mild wear (red arrows). (d) Cross-section in the mild wear scar of WC-12Ni coating (normal load = 118 N) shows localised oxide layer on the top surface.

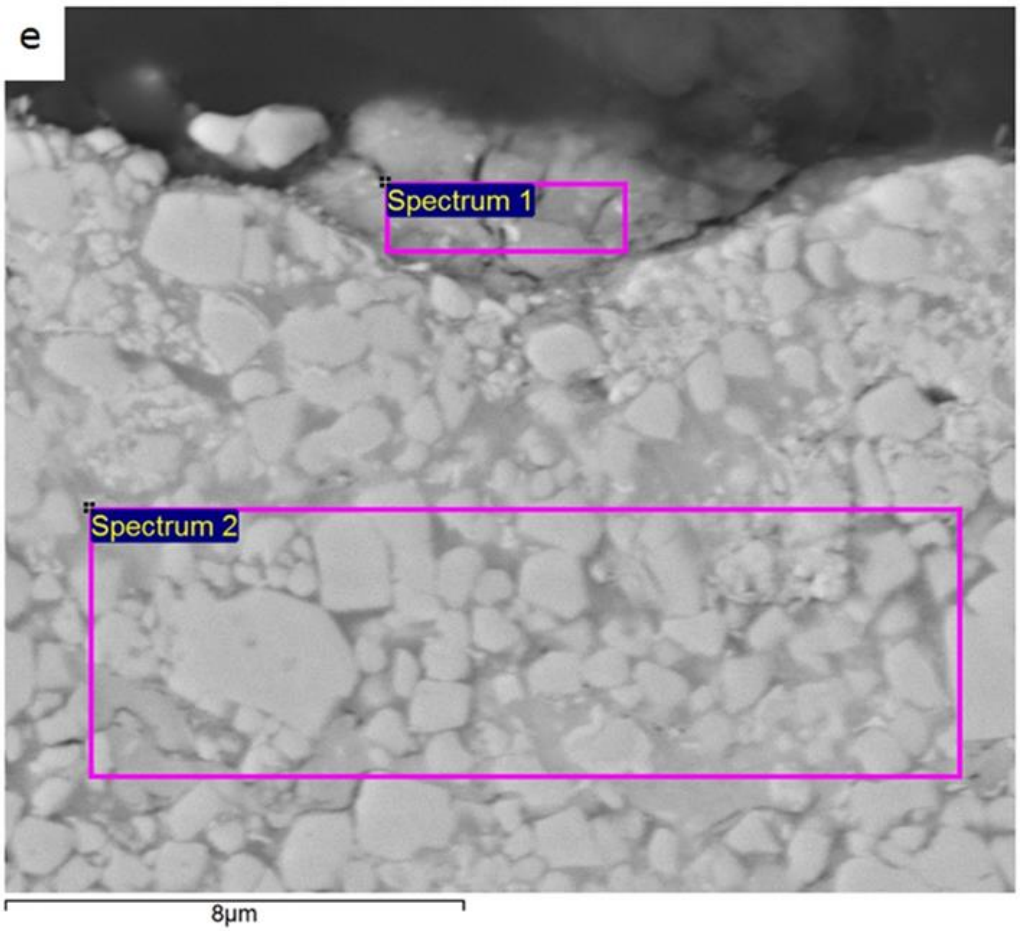

Spectrum	O wt%	Co wt%	W wt%
Spectrum 1	20	12	68
Spectrum 2	1	16	83

Figure 4-30 (Cont.): Mild wear behaviour of WC-12Ni coating. (e) EDX analysis of transfer layer (spectrum 1). The increase in the oxygen weight percent indicates that this layer is an oxide layer.

In contrast, the surface of the same coating (WC-12Ni) worn under a load of 141 N (above the transition load) shows more severe wear as can be clearly seen in Figure 4-31.

The surface of the WC-12Ni coating worn under the load of 141 N shows more severe wear as demonstrated in low magnification SEM-SE image in Figure 4-31a. The wear track has been about 1 mm in width; this is after a sliding distance of 1500 m. Selected area from the middle of the wear track is presented in SEM-BSE image in Figure 4-31b. It shows very severe wear and almost the whole wear track is covered by the transfer layer (grey colour areas). The WC grains crushed during severe wear of WC-12Ni coating. The selected area "c" in previous figure is illustrated in SEM-SE image in Figure 4-31c shows wide transgranular cracks on the brittle transfer layer which lead to the fracture of this layer during the wear test. The angular WC grains in high magnification SEM-BSE in Figure 4-31d are proving that the top coating surface (which meanly the brittle oxide layer) has been fractured.

Cross-section made in the severe wear track to investigate the wear behaviour of WC-12Ni coating during severe wear. The wear scar cross-section above the transition load (141 N) is shown in Figure 4-31e and shows a thin transfer layer covering the entire wear track top surface. It can be seen that a significant amount of fine tungsten carbide particles embedded in the transferred layer exists, and there is a large amount of fine debris stuck in the wear track. There are no subsurface cracks and no cracks in WC grains are observed in this cross-section.

The energy dispersive X-ray analysis (EDX) of the transferred layer during severe wear of WC-12Ni coating is illustrated in Figure 4-31f and reveals the presence of tungsten, nickel, and oxygen. The increase of the oxygen weight percent in the transferred layer made it clear that this layer is an oxide layer.

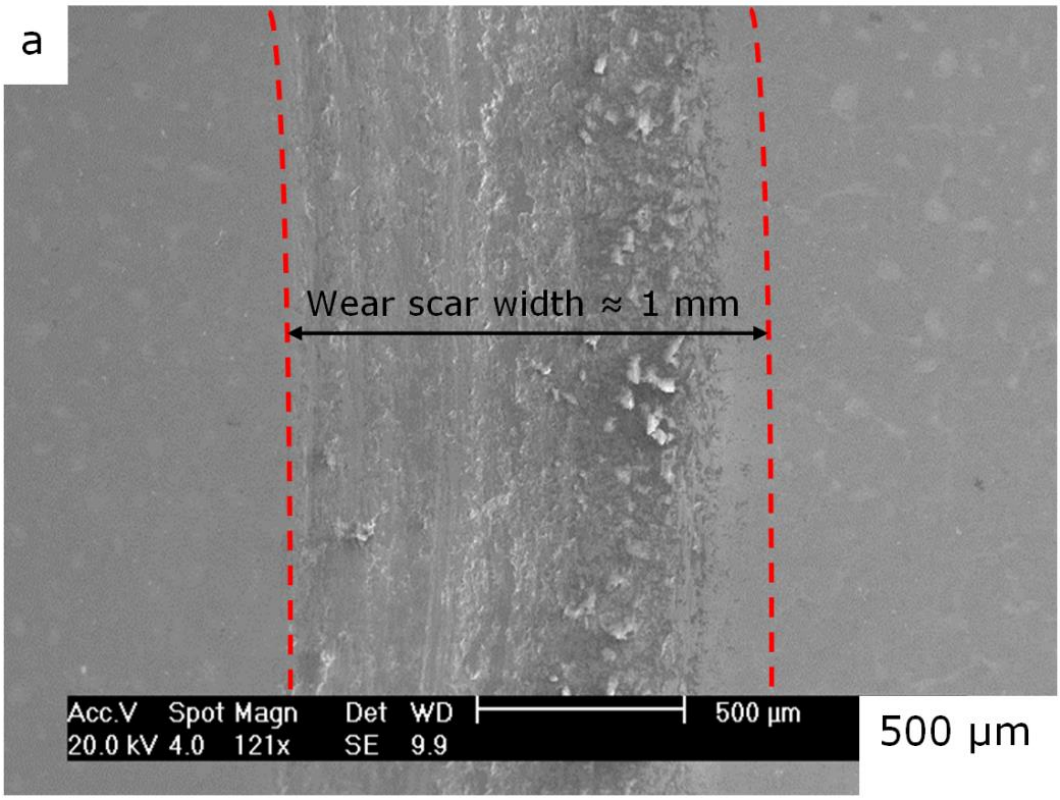

Figure 4-31: Severe wear behaviour of WC-12Ni coating. (a) Top view of wear scar of WC-12Ni coating worn under normal load 141 N. (Sliding direction is from top to bottom).

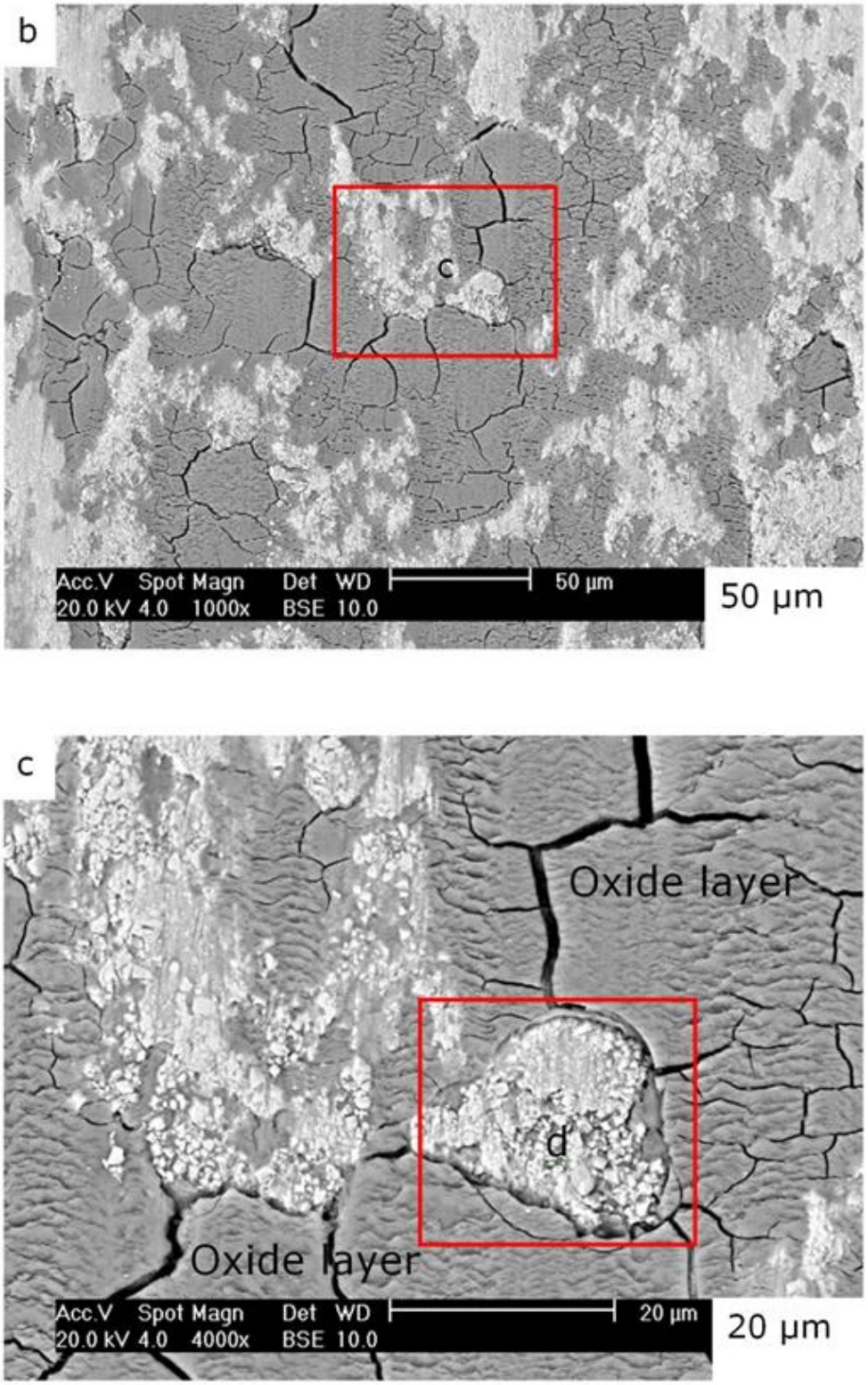

Figure 4-31 (Cont.): Severe wear behaviour of WC-12Ni coating. (b) SEM-BSE image taken from the middle of the wear track shows very severe wear. The transfer layer is approximately covering the whole wear scar. (c) SEM-BSE image shows the fracture of the brittle transfer layer. The wide transgranular cracks are very obvious in this layer.

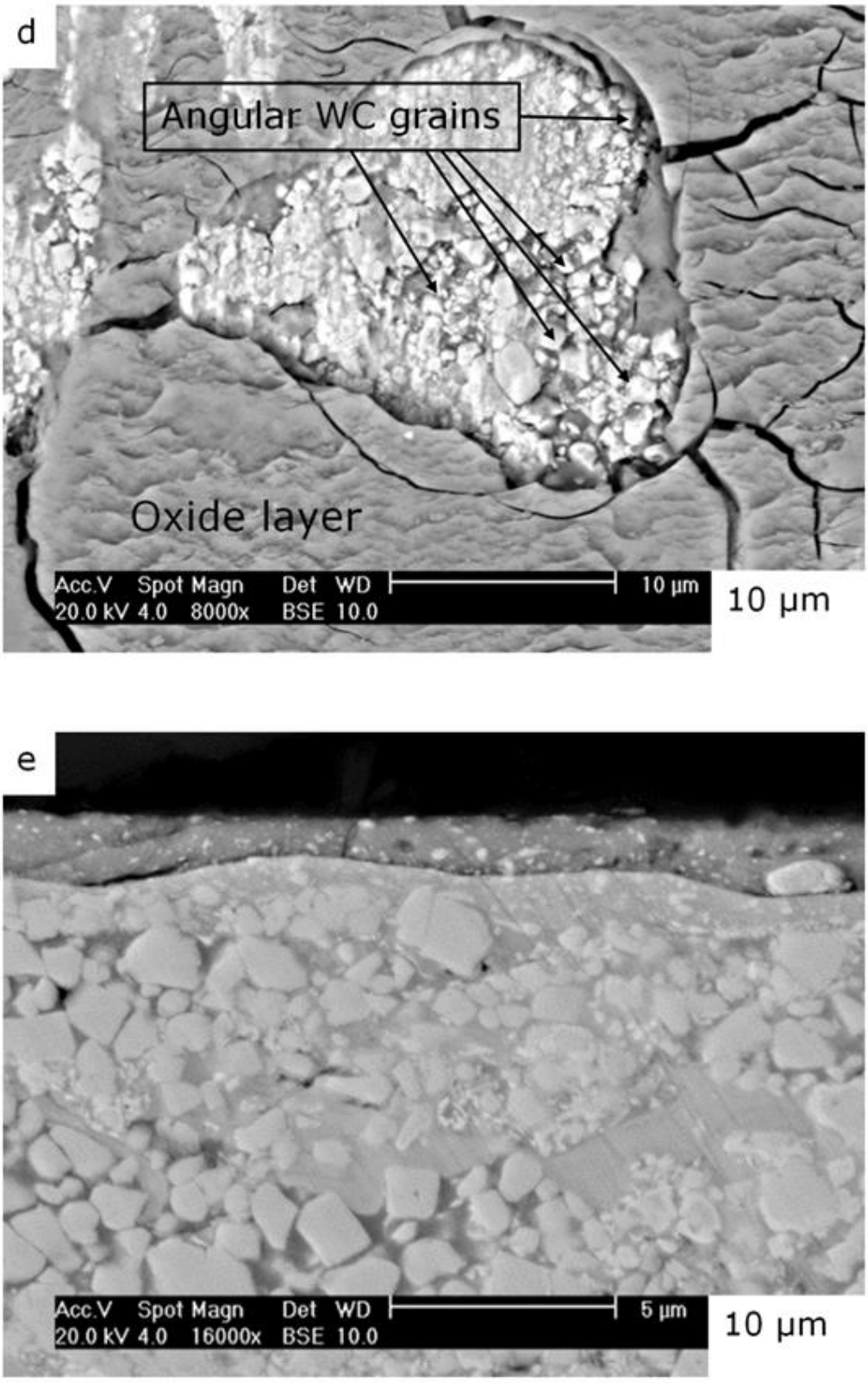

Figure 4-31 (Cont.): Severe wear behaviour of WC-12Ni coating. (d) SEM-BSE image shows the angular WC grains prove the fracture of the top oxide layer. (e) Cross-section in the severe wear scar of WC-12Ni coating (normal load = 141 N) shows thin transfer layer covering the top surface.

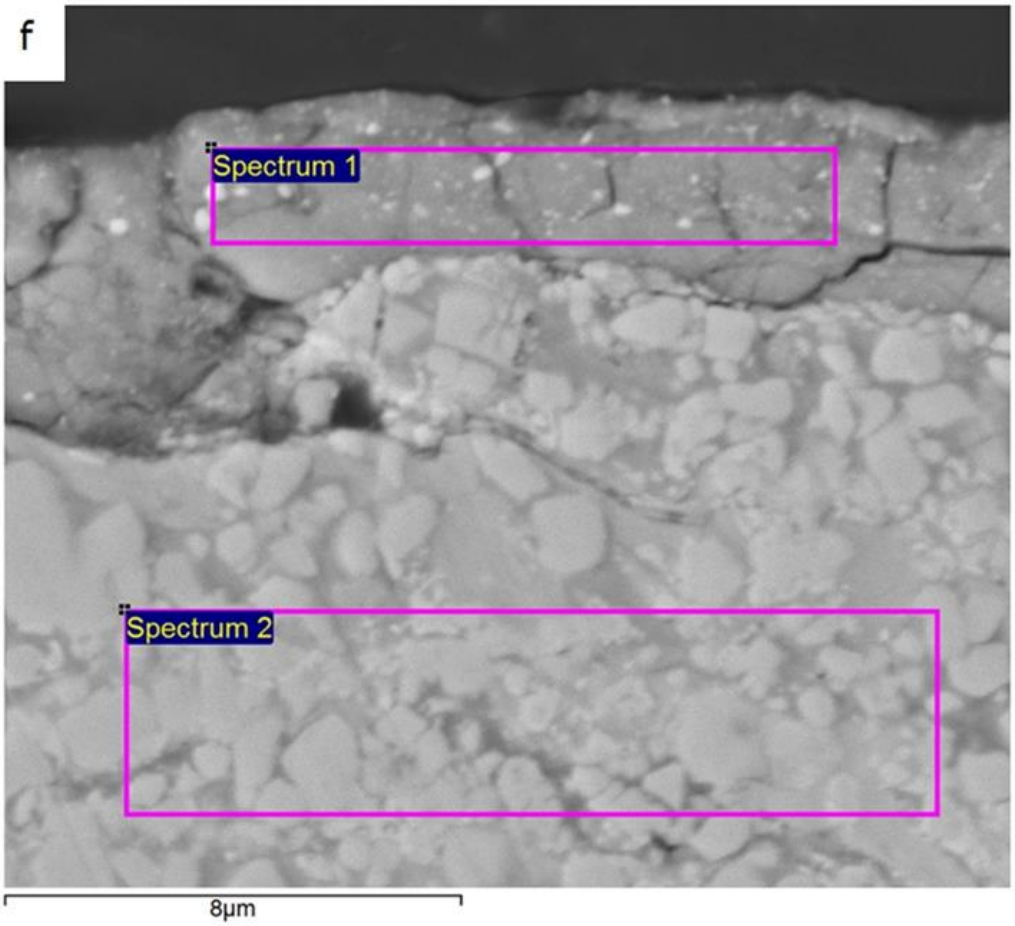

Spectrum	O wt%	Co wt%	W wt%
Spectrum 1	19	12	69
Spectrum 2	1	15	84

Figure 4-31 (Cont.): Severe wear behaviour of WC-12Ni coating. (f) EDX analysis of transfer layer (spectrum 1). The increase in the oxygen weight percent indicates that this layer is an oxide layer.

The wear debris during mild wear has been extremely little, which cannot be collected for investigation. The morphology of the wear debris of WC-12Ni coating worn with severe wear, (141 N), is demonstrated in Figure 4-32. The wear debris consists of plate-like debris which has resulted from the delamination of the transferred layer. Agglomerated fine particles can also be seen.

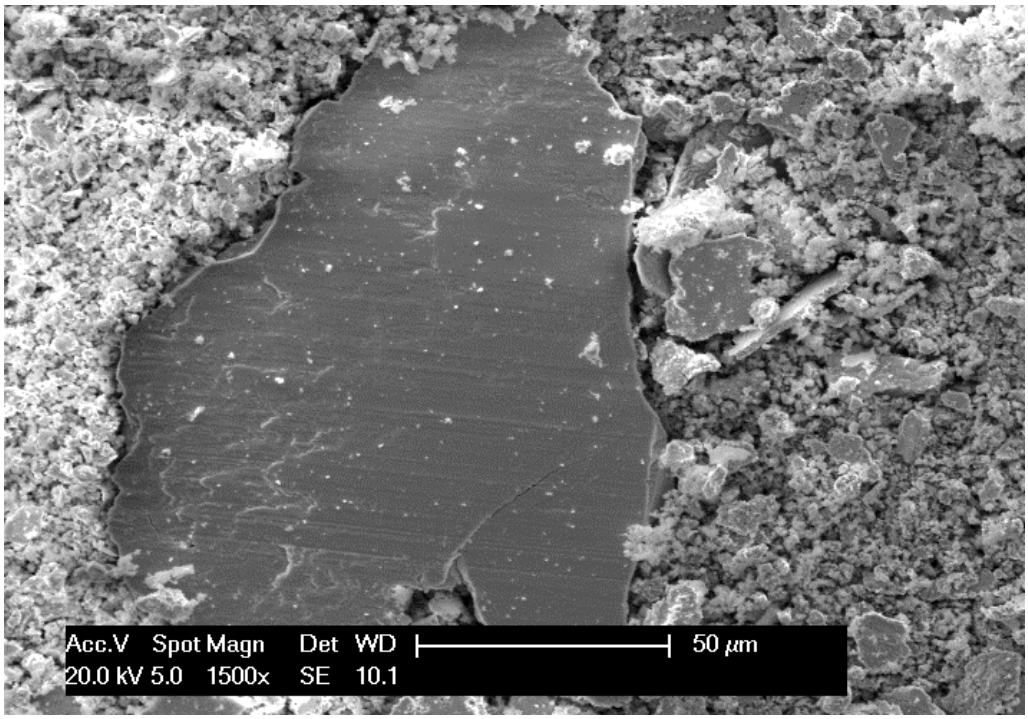

Figure 4-32: The wear debris of WC-12Ni coated disc worn with a severe wear (normal load = 141 N) shows the plate like debris.

To inspect the wear scar of WC-12Ni coating the optical profilometry (using a Bruker ContourGT Optical Profiler) has been used. The 2D Bruker ContourGT Optical Profiler image of mild wear sample, below the transition load (118 N), is illustrated in Figure 4-33a shows low wear. However, the 2D Bruker ContourGT Optical Profiler image of severe wear, above the transition load (141 N), is shown in Figure 4-33b which represents high wear. Figure 4-33c illustrates the wear scar profile of WC-12Ni coating with mild wear, below the transition load (118 N), where the wear scar depth and scar width of approximately 0.1 µm and 0.6 mm, respectively. The wear scar profile with severe wear, above the transition load (141 N), is illustrated in Figure 4-33d with a wear scar depth and width of almost 14 µm and 1 mm, respectively.

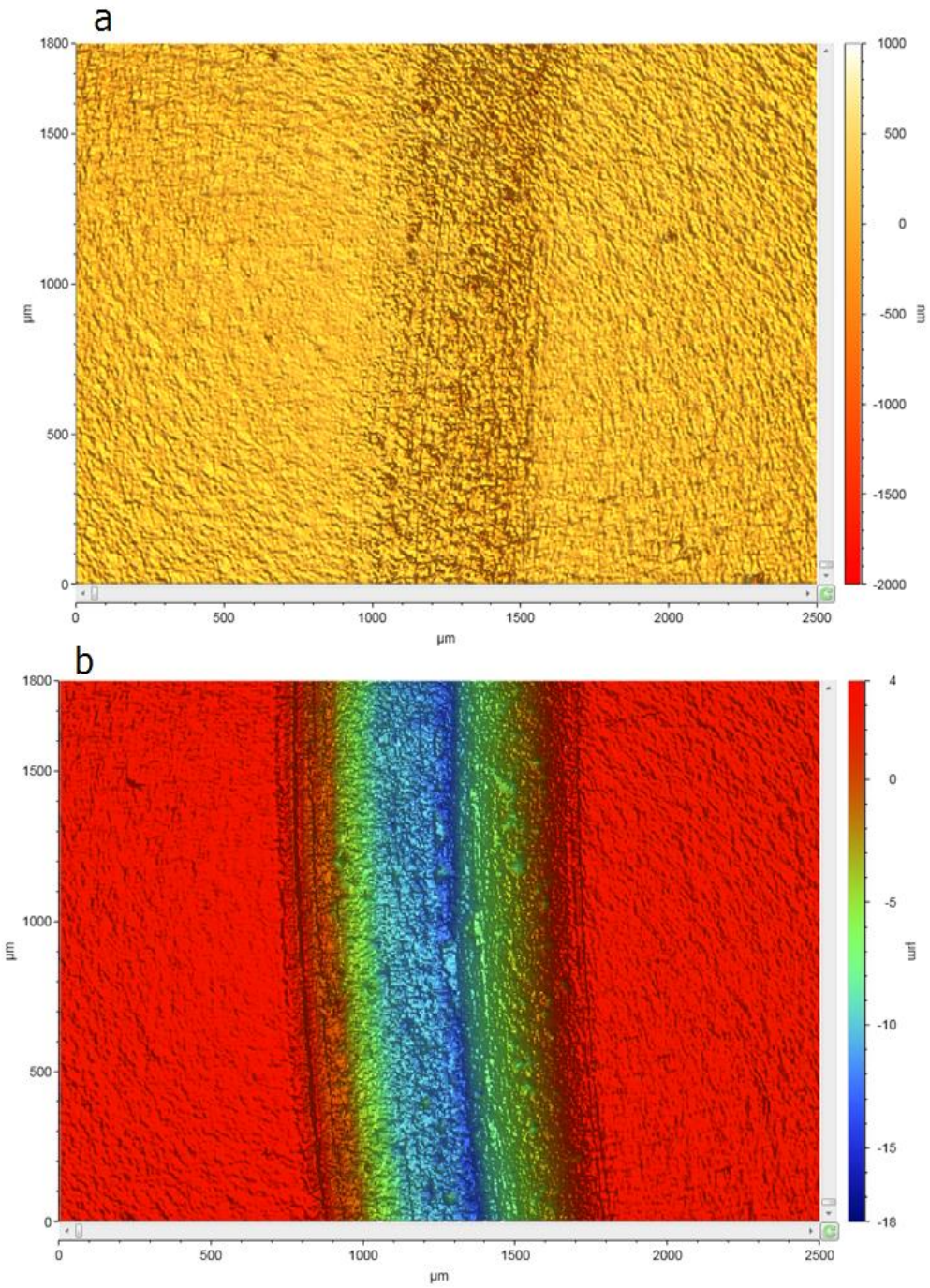

Figure 4-33: Bruker ContourGT Optical Profiler investigation of wear scar of WC-12Ni coating. (a) 2D Bruker ContourGT Optical Profiler image during mild wear (normal load = 118 N) shows low wear. (b) 2D Bruker optical image during severe wear (normal load = 141 N) shows high wear.

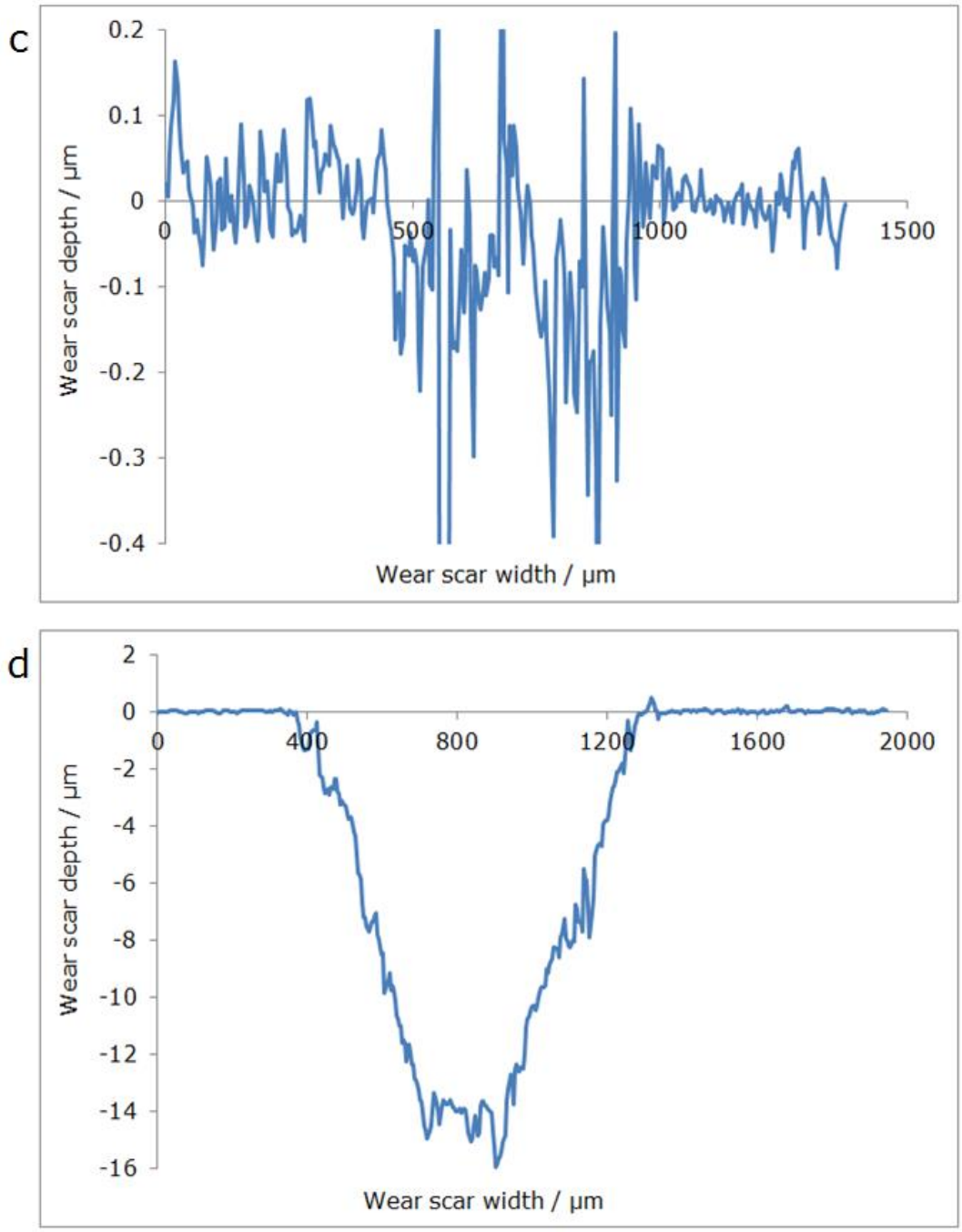

Figure 4-33 (Cont.): Bruker ContourGT Optical Profiler investigation of wear scar of WC-12Ni coating. (c) The plot of mild wear profile shows the width and the depth of wear scar. (d) The plot of severe wear profile shows the width and the depth of wear scar.

The changing of the friction coefficient with the sliding distance for WC-12Ni coating through mild and severe wear is illustrated in Figure 4-34. Throughout the mild wear (normal load = 118 N), the friction coefficient curve increased gradually until the friction coefficient has been about μ = 0.19 at 1200 m, where it become approximately

steady state. The friction coefficient increased sharply during running-in period with the severe wear (normal load = 141 N) seen to reach around μ = 0.7 at about 300 m. Then the curve start to decrease gradually until the μ = 0.6 about 700 m, then the curve increase gradually to reach μ = 0.7 at 1200 m where the steady state starts.

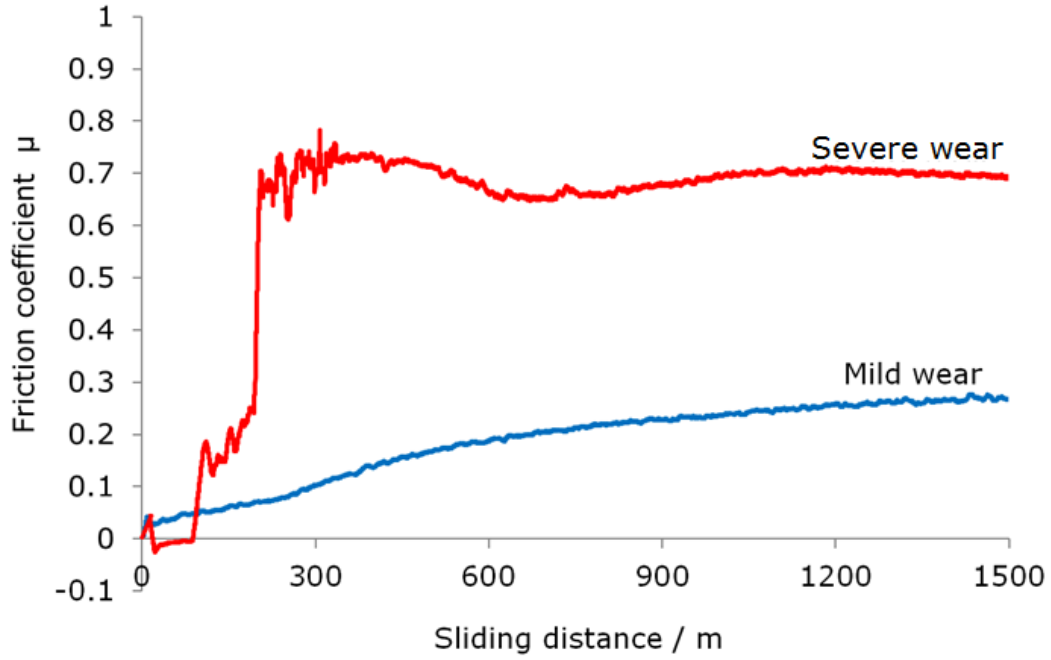

Figure 4-34: Variation of the friction coefficient with sliding distances for WC-12Ni coating through wear test.

The SEM has been used to examine the worn surface of the sintered WC-6Co ball sliding against the WC-12Ni coated disc during the mild and severe wear. Figure 4-35 represents the wear behaviour of the sintered ball during the mild wear of WC-12Ni coating. Figure 4-35a, illustrates the SEM low magnification of ball worn surface. The selected area b is exhibited in Figure 4-35b which shows unworn and worn surfaces and the little debris transformed from the coated disc, and stuck on the ball surface. Figure 4-35c is the high magnification SEM image of worn surface of counterface ball. The last figure shows a very smooth surface proving that there has been insignificant change in the ball microstructure.

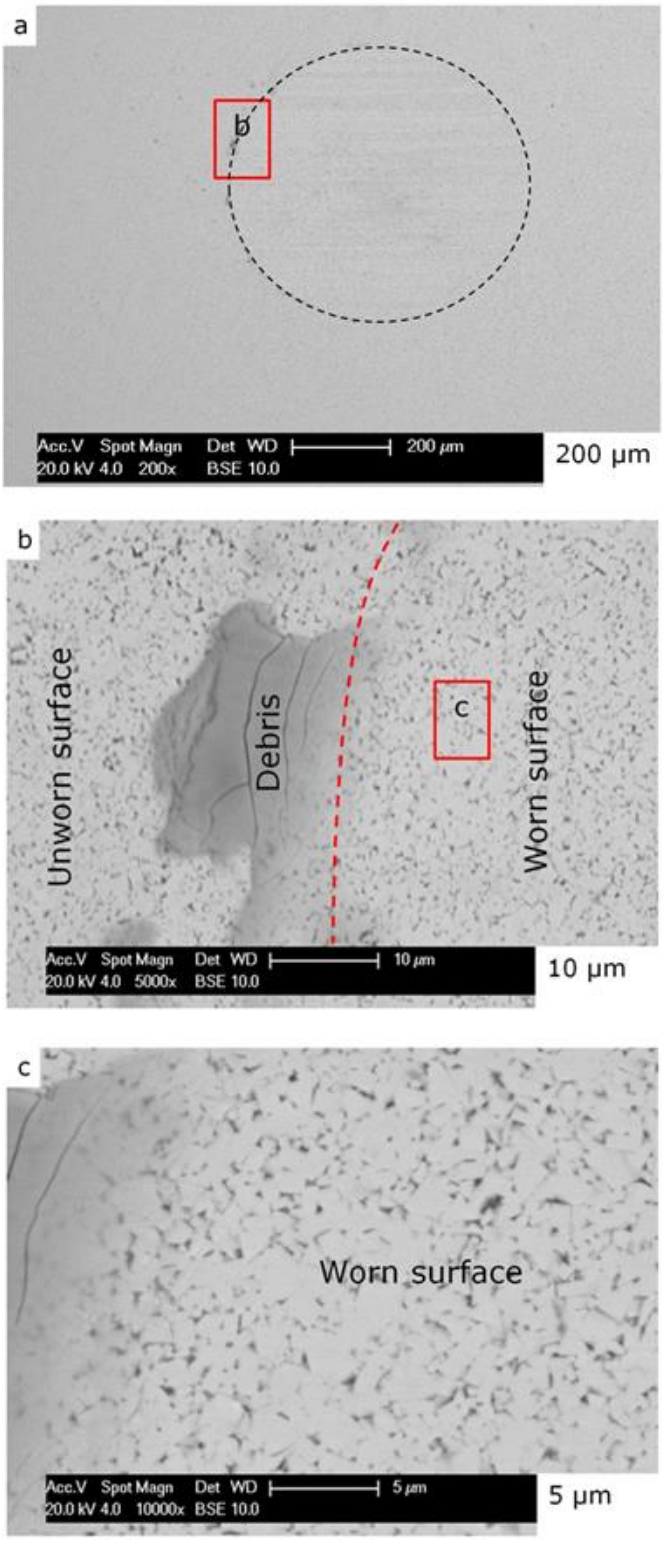

Figure 4-35: Mid wear behaviour of sintered WC-6Co ball sliding against WC-12Ni coated disc. (a) Low magnification SEM-BSE image of the ball worn surface (sliding direction from right to left). (b) SEM-BSE image shows worn and unworn ball surfaces and the debris stuck on the ball surface. (c) High magnification SEM-BSE from the middle of ball worn surface shows smooth ball surface.

The wear performance of the sintered WC-6Co ball sliding against the WC-12Ni coated disc during the severe wear is demonstrated in Figure 4-36. The selected area "b" from the middle of the ball in Figure 4-36a, is exhibited in SEM-BSE image in Figure 4-36b. This figure shows high severe wear of ball worn surface which approximately covered by brittle oxide layer. The fracture of the brittle oxide layer is very obvious. The selected area "c" in Figure 4-36b is presented in high magnification SEM-BSE image in Figure 4-36c which demonstrates the brittle oxide layer. The angular WC grains prove the fracture of the outer layer of the ball during the severe wear.

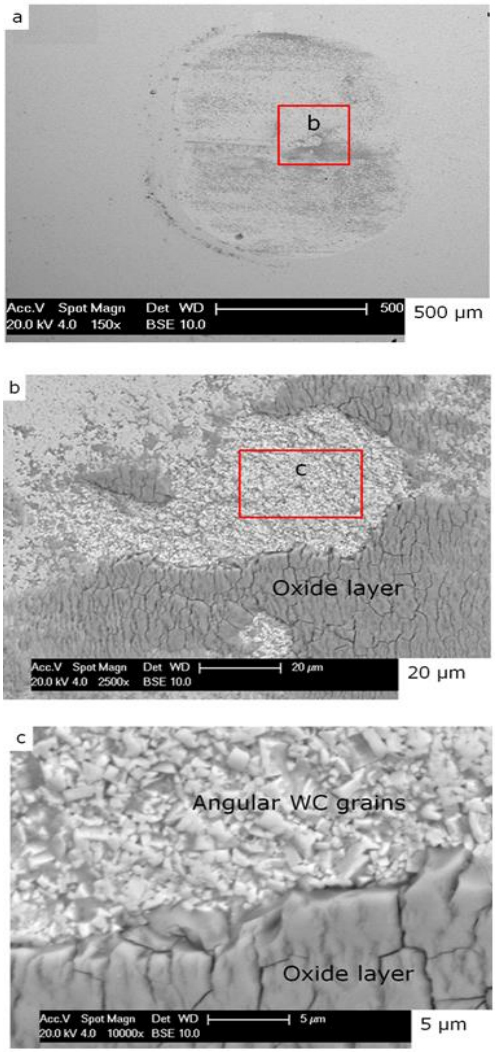

Figure 4-36: Severe wear behaviour of sintered WC-6Co ball sliding against WC-12Ni coated disc. (a) Low magnification SEM-BSE image of the ball worn surface (sliding direction from right to left). (b) SEM-BSE image of selected area "b". The brittle oxide layer is about covering the entire ball worn surface. (c) High magnification SEM-BSE image of selected area "c". The angular WC grains indicate the fracture of the brittle oxide layer during the wear test.

4.2 Discussion

The main aim of this section is to discuss the results of the tests carried out in this chapter to investigate the effect of the metal binder type (Co/Ni) of both WC-12Co and WC-12Ni coatings on the coating microstructure and their mechanical properties. This will also include discussing the influence of coating microstructure and the mechanical properties of these two coatings on the dry sliding wear behaviour. The section will start with the coatings microstructure, including: brief description of the thermal spray coating mechanism, discussing the results of X-Ray diffraction and Scanning Electron Microscopy (SEM), and final conclusion reflecting the differences between the two metal binders (Co/Ni). Then, the mechanical properties of both WC-12Co and WC-12Ni coatings will be discussed, including the microhardness, fracture toughness, scratch test and a conclusion of these mechanical properties will be given. After that, the dry sliding wear behaviour of the corresponding coatings will investigated and discussed in the light of coating microstructure and their mechanical properties, followed by related conclusions. Finally, general conclusions for the whole tests will give by the end of the section reflecting the main aim behind this section.

4.2.1 Coating Microstructure

Coating microstructure is an essential factor that affects its mechanical properties, such as hardness, fracture toughness, and the coating wear behaviour. The coating microstructure is mainly affected by the deposition process and process parameters. The starting powder type and its size range are also very essential. For the specific application, the right powder and process control are required to guarantee the production of a coating with the suitable microstructure and the needed properties. In this study, to investigate the metal binder effect, two powders of similar types and size range are selected (see section 4.1.1).

Microstructure formation mechanism

During HVOF thermal spraying process, the starting powder is injected into a flame, where it melts or semi-melted and is accelerated toward the component surface to

create the coating layers. The microstructure formation of HVOF thermally sprayed WC-M coating mechanism is described as follows:

As a WC–M powder particle enters the hot gas, its temperature increases and the metal binder will begin to melt. WC will begin to dissolve in the metal binder when this latter is molten. Moreover, more WC will dissolve as the temperature of particles continues to rise. The decomposition of a powder particle expected to proceed as follows. The metal binder will melt and WC will dissolve into the liquid as the temperature increases. Carbon removed from the melt both by reaction with oxygen at the melt/gas interface or during oxygen diffusion into the rim of the molten particle, resulting CO formation. The reduction of carbon from the melt will consequently be controlled to a shell area, the depth of which is affected by carbon movements, oxygen and the reaction kinetics. Conversely, additional dissolution of WC grains in this shell area will be driven by reduction of carbon from the melt as the system tries to recreate local equilibrium in the WC–melt system. Because of dissolution, the general outcome will be WC grains, which are significantly less angular in the outer rim of a powder particle. The other results are a reduced WC volume fraction compared with the central areas of the particles and a W:C atomic percentage in the melt greater than unity. During rapid solidification of the splat, W_2C, W and the M(W, C) nanocrystalline/amorphous phase are generated, where M in this case is Co/Ni. Nevertheless, carbon loss leads to the melt composition much closer to the phase of M_2C (W_2C), on rapid cooling, nucleation of W_2C and consequent W_2C growth could be kinetically preferred mostly if WC acted as an effective nucleation substrate for W_2C. The M(W, C) liquid phase will be under cooled under the liquids temperature due to the high cooling rates. It is expected that the liquid can transform to an amorphous phase where the nucleation kinetics of the complex crystalline phases M_6C and $M_{12}C$ are probable to be inactive. The nanocrystallinity might be attributed to crystallization of an originally amorphous matrix as a result of reheating throughout successive gun passes to create a thick coating (Stewart et al. 2000).

This proposed mechanism is supported by the XRD results. From the powders patterns (Figure 4-1), it is very clear that the WC-12Co and WC-12Ni powders are similar. Both of them contained only hexagonal close-packed (hcp) WC and face-

centred-cubic (fcc) metal binder peaks (cobalt in WC-12Co powder, and nickel in WC-12Ni powder). The cobalt and nickel peaks are approximately at the same position ($2\theta = 44.2^{\circ}$ for Co and $2\theta = 44.8^{\circ}$ for Ni). Also, both WC-12Co and WC-12Ni powders have a similar particles size (-45+15μm), both produced by agglomeration and sintering process and have similar WC grains size range (0.8-2.5 μm). This similarity in starting powders will ensure that there is no effect driven from the difference in starting powders structure.

The high magnification SEM-BSE images of both powders cross-section in Figure 4-2b and Figure 4-3b shows only two phases. Angular WC grains (bright colour) are surrounded by metallic binder which is cobalt in WC-12Co powder and nickel in WC-12Ni powder (grey colour). This fact is supported by the results of x-ray scan of these powders, Figure 4-1; where only WC and cobalt/nickel are appear.

The broadening of the diffracted beams of metal binders in both coatings, (Figure 4-1), is a result of their very small crystals plus micro strain, i.e., the thickness of the crystal is inversely proportional to the width of the diffraction curve, (Cullity and Stock 2001). The XRD results of WC-12Ni coating show a retained nickel phase, which is in good agreement with the published results of WC-Ni thermally sprayed coatings (Berger et al. 2008; Celik et al. 2006; Guilemany et al. 1995; Stachowiak 2006).

Furthermore, patterns of WC-12Co coating (Figure 4-1) show a broad diffraction halo centred at about $2\theta=43^{\circ}$ which indicates the presence of amorphous or nanocrystalline phase in this coating. This has been identified previously by many researchers such as (Karimi et al. 1993; Stewart et al. 2000; Verdon et al. 1998) and can be related to a nano-crystalline phase containing cobalt, tungsten and carbon, Co(W, C), which corresponds to the matrix. The fact that the cobalt peaks are detected in the powder and not in the coating, suggests that most of the cobalt is present as nano-crystalline binder phase.

The main difference between the XRD scans for both of WC-12Co and WC-12Ni coatings is that the Ni crystalline phase is still exist where the Co crystalline phase does

not appear clearly. This could be attributed to the higher WC solubility in a Co based liquid than in a Ni based one, and the temperature at which liquid forms in the W-Co-C system is lower than that in the W-Ni-C system, Figure 4-37, (Gapriel et al. 1986). The WC solubility in liquid Co is high and strongly varies depending upon the temperature. With decreasing carbon content, the solubility of tungsten in cobalt increases and has been reported to vary between 2 and 15 wt.% at about 1250 °C. The tungsten solubility in cobalt binder at ambient temperature has been reported to be 3.5 wt.%. The solubility of cobalt in tungsten carbide is very small and can be neglected. With regard to the solid solubility of carbon in the binder, a typical range reported for WC–Co was 0–0.2 wt.% at elevated temperatures, with the higher values at the lower tungsten levels. Solid solubility of tungsten and carbon in cobalt binders are inversely related. The solubility of W and C in the liquid Ni of the W–C–Ni system were reported to be about 5.0 and 2.0 wt.%, respectively at 1350 °C. The solubility of tungsten in Ni at ambient temperature has been reported to be 5.4 wt.% (Fernandes and Senos 2011; Tracey 1992; Uhrenius et al. 1995).

The knowledge of the phase diagrams for WC and different binders will be extremely useful and opportune regarding the need to choose initial compositions. Using Thermo-Calc software, with SSOL5 database, Figure 4-37 depicts two vertical sections through ternary systems; one for the Co–W–C system (Figure 4-37a), the other for the Ni–W–C system (Figure 4-37b). Both phase diagrams calculated at 12 wt% Co/Ni, 5 wt% C and 83 wt% W which are the powders stoichiometric composition. Figure 4-37 represents the effect of substitutions of the Co binder by Ni in the WC-based cermet coatings, focusing on important two phase range WC + fcc region, where the fcc is representing the metal binder phase which is cobalt or nickel in this case. The solid red denoted by “p” and “q′” with vertical dashed lines are indicating the favourable carbon composition and minimum and maximum melting temperature of the metal binder in the system.

From Figure 4-37, two significant concepts can be seen: The two phase range (fcc + WC) is significantly enlarged and moved to higher temperature in a WC-Ni coating as compared to the WC-Co coating (both contain 12 wt% metal binder). The narrow carbon window is more difficult to avoiding either eta-phases ($M_6C/M_{12}C$) or graphite.

Furthermore, the overlapping of the two-phase (WC + fcc) field by the three phase area (liq.+M_6C+WC) also narrows the carbon window in practice. This is due to the fact that for compositions within this overlap, the M_6C that is formed at temperatures needs to transform back to WC+ binder upon cooling to yield a two phase system, (Guillermet 1989; Schubert et al. 2015; Upadhyaya 1998). The similar finding for both Co-W-C and Ni-W-C with 10 wt% metal binder was given by other researchers (Wang et al. 2014).

Although, the quantitative X-ray diffraction analysis, (Table 4-2), is not so accurate since it does not account for the fraction of the metal binder (Co/Ni) and amorphous phases. Nevertheless, it could be supporting this result. It shows less weight percent of WC and higher percent of metallic tungsten and W_2C phases with WC-12Co coating compared to WC-12Ni coating, which mean more decomposition of WC grains with WC-12Co coating.

In the Met-Jet 4L HVOLF system, (Figure 3-1), kerosene and oxygen are burnt in a combustion chamber. Hot gas passes through a converging–diverging throat along a 100 mm nozzle before emerging as a free jet. Powder is injected downstream of the throat. The microstructure of both WC-12Co and WC-12Ni coatings are demonstrated respectively in Figure 4-4 and Figure 4-5. Both coatings approximately show similar features, Figure 4-4a and Figure 4-5a show some porosity in both coatings and melted and semi-melted matrix, (metal binder), areas. These clear differences in melted and semi-melted areas in both WC-12Co and WC-12Ni coatings related to the coating system, where the spraying with HVOLF shows less degree of decomposition compared to spraying with HVOGF as mentioned by several researchers in this subject such as Schwetzke et.al.(1999) and Sudaprasert et.al.(2003). This low degree of decomposition could be attributed to the low temperature of HVOLF coating process, and the high particle velocity during this process leading to decrease the dwelling times of the particles in the hot gas. This leads to low degree of melted metal binder. The kerosene-fuelled HVOF thermal spray coating process was modelled by Kamnis et.al. (2006) who reported that the gas temperature and velocity are about 2300 K and 1700 m s^{-1} respectively, Figure 4-38. The HVOGF gas temperature and velocity are approximately 2700 K and 1500 m s^{-1} respectively, (Gu 2000). A full discussion of the mechanism of

microstructure development in HVOF thermal spray coating is given by Stewart et.al. (2000), as summarised in the starting of this section.

Decomposition is shown in the XRD pattern in Figure 4-1 by the formation of W_2C and W, and an amorphous hump in WC-12Co coating, and by the broadening of Ni peaks and formation of W_2C and W, in WC-12Ni coating. In the SEM images, decomposition is indicated by the variation in contrast in the binder phase and the existence of bright phases. Decomposition is occurring more in melted binder areas, due to that the WC grains takes rounded shape, while these WC grains are still angular in semi-melted binder areas due to the low decomposition. However, the decomposition is higher in WC-12Co coating than WC-12Ni coating. The greater decomposition in WC-12Co coating could be related to the high solubility of WC in cobalt based liquid than in nickel based liquid (Gapriel et al. 1986). This is due to the lower temperature at which liquid forms in the W-Co-C system comparing to W-Ni-C system, Figure 4-37.

In BSE images, the areas with bright and dark contrast represent the elements with higher and lower mean atomic number respectively. Therefore, it can be concluded that the main component for the bright areas in the WC-12Co and WC-12Ni coatings is tungsten. Figure 4-4b and Figure 4-5b show almost complete shells around WC particles and some bright clusters. The colour of these clusters and shells is lighter than that of the WC particles. It is very possible that the outer shell around WC particles and the bright particles are metallic tungsten and W_2C developed directly from the decomposition of WC.

In conclusion, higher solubility of WC during WC-12Co coating is attributed to the lower temperature at which liquid forms in the W-Co-C system comparing to W-Ni-C system, (Figure 4-37). This means more decomposition of WC through WC-12Co coating compared with the WC-12Ni coating.

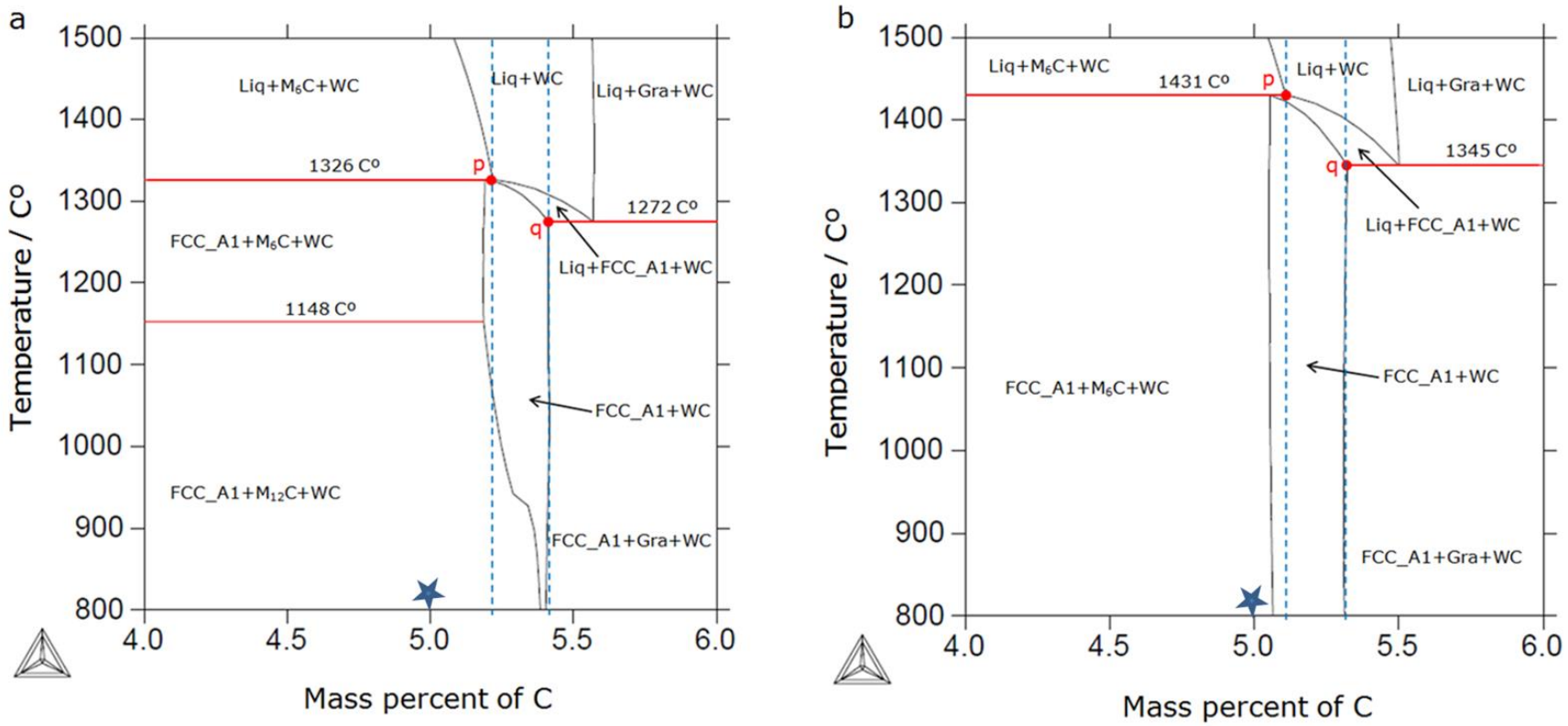

Figure 4-37: Vertical section phase diagram of (a) the Co–W–C, calculated at 12 wt% Co and (b) the Ni–W–C, calculated at 12 wt% Ni, shows the effect of complete substitution of Co by Ni. The p and q red circles define, respectively, minimum and maximum carbon contents, which are in a two phase state of FCC (metal binder) + WC just after equilibrium solidification. The blue asterisk on the baseline indicates the stoichiometric carbon value. Phase diagrams calculated by thermo-Calc software, with SSOL5 database.

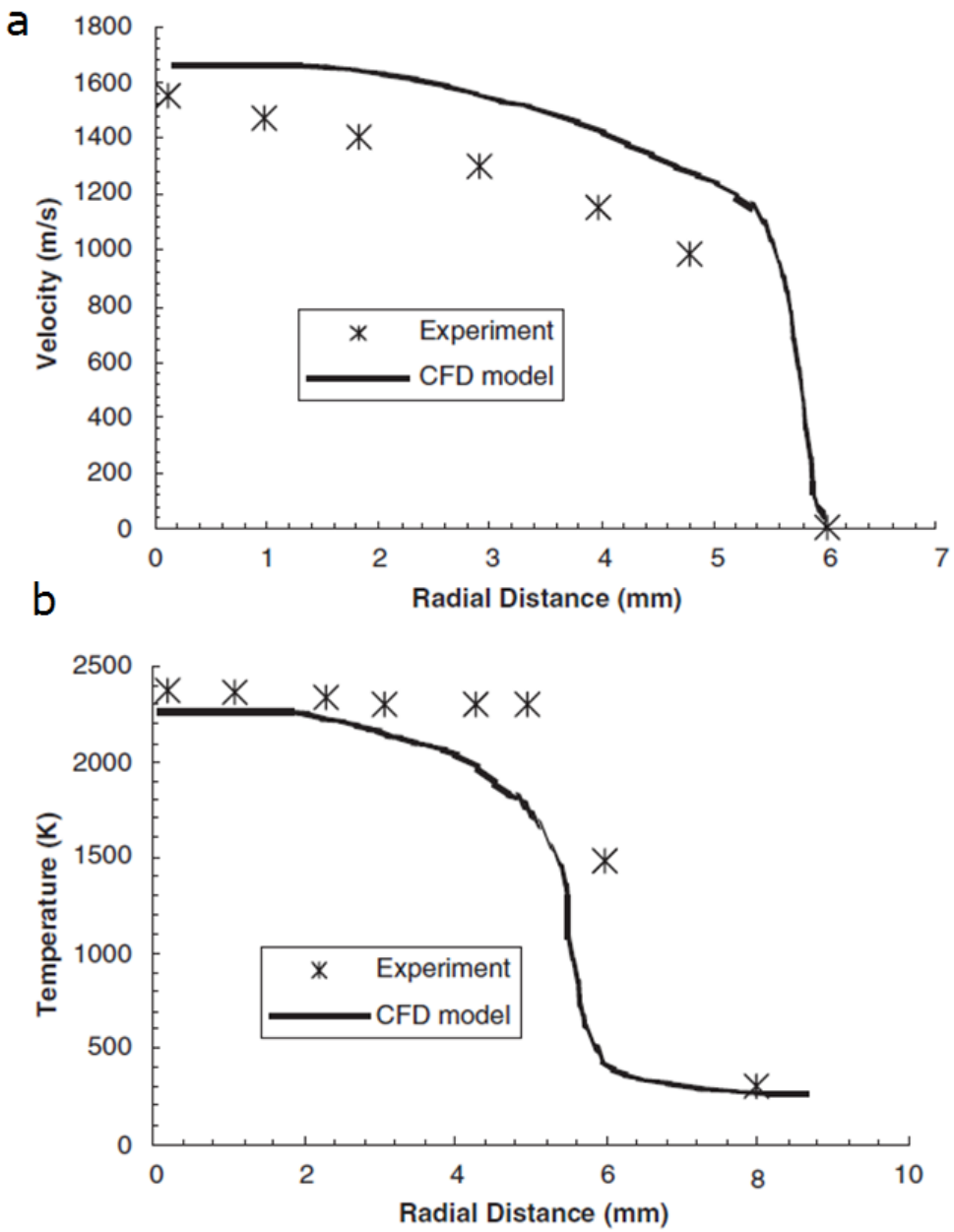

Figure 4-38: Comparison of modelling prediction with gas flow measurement (a) Gas velocity at the exit of the gun. (b) Gas temperature at the exit of the gun, adapted from (Kamnis and Gu 2006).

4.2.2 Mechanical Properties

The mechanical properties of cermet coatings play an essential role in their performance. Cermet coatings are usually used when high hardness and wear resistance are required (Lekatou et al. 2015). In this section, results of mechanical properties including microhardness, fracture toughness and scratch test of WC-12Co and WC-12Ni coatings are discussed in detail.

Microhardness

From the early stage of development of the hard coatings, hardness has been often used as a reference value to characterise the coating properties. Hardness is most often performed on polished coating cross section. Vickers hardness test is frequently used, the most common load being 2.94 N (300 g). Coatings hardness can be considered as the resultant of coating microstructure, phase composition, porosity, hardening of the binder phase, etc. (Berger 2015).

Table 4-3 represent the microhardness and fracture toughness of both WC-12Co and WC-12Ni coatings. It is obvious that WC-12Co coating ($H_{V\,300}$ 1257±27 kg mm^{-2}) is harder than WC-12Ni coating ($H_{V\,300}$ 1010±20 kg mm^{-2}), where the ± values represent the standard errors in mean.

In general, coating hardness is affected by its porosity, which is significant dependent on the temperature of the particles (He and Schoenung 2002; Lee et al. 2010). The porosity of both WC-12Co and WC-12Ni coatings are similar, (1.2%). However, the higher hardness of WC-12Co coating can be attributed to the greater W_2C content compared to WC-12Ni coating, as discussed in the previous section, (microstructure section).

Since W_2C phase (H_V 3000 kgf/mm^2) is harder than WC phase (H_V 2400 kgf/mm^2), previous studies concluded that increase in hardness is due to the increase of W_2C content in the coatings. The hardness of the coatings increased extensively with an increase in W_2C phase content, and this increases more when the nanocrystalline or

amorphous phase substitutes metallic binder as the matrix phase (Rajinikanth and Venkateswarlu 2011; Vinayo et al. 1985; Xie et al. 2013). This is matching the case of WC-12Co coating, since this coating show higher degree of decomposition and therefore contain more W_2C compared to WC-12Ni coating.

Although, there is not enough literature for WC-Ni thermally sprayed coatings, the published works reported that the hardness values of WC-Ni are 100 to 200 H_V less than the hardness of WC-Co coatings (Berger et al. 2008; Tracey 1992; Voyer and Marple 1999).

Fracture toughness

Preferable fracture toughness can be achieved with more binder content at the expense of hardness and wear resistance (Kenny 1971; Wu et al. 2011). Fracture toughness linearly decreased with hardness, and increased with increasing WC grain size, which leads to increasing the free mean path of matrix, (Ingelstrom and Nordberg 1974). Although this has been the basic understanding of fracture toughness behaviour for several decades, many new studies have suggested otherwise (Jia et al. 2005; Maizza et al. 2007; Michalski and Siemiaszko 2007; Sivaprahasam et al. 2007; Yingfang et al. 2006).

Table 4-3 represent the values of fracture toughness of both WC-12Co and WC-12Ni coatings. Even though, WC-12Co coating shows higher hardness than WC-12Ni coating, it shows higher fracture toughness also. The high solubility of WC in Co was taken as a major cause for the good toughness of WC-12Co coating, (Exner 1979). Higher solubility of WC in Co leads to generation of amorphous/nanocrystalline phase, which improves the coating cohesion and consequently increases the coating fracture toughness. Most of the cracks propagated in the coating layer under the indentation load of 10 kg were in the direction parallel to the coating/substrate interface.

Figure 4-7(a & b) are the SEM images of the indentation cracks generated in both coatings. They show the anisotropic fracture behaviour usually found in thermal spray coatings, which is based on the microstructure and composition of the coatings. Crack

propagation is affected by the porosity, the shape, size, and distribution of the WC carbide particle. Such anisotropy has been reported for cermet coatings in previous studies (Cantera and Mellor 1998; De Palo et al. 2000; Usmani et al. 1997; Wayne and Sampath 1992). The cracks in both coatings are propagating through the matrix, mostly in the direction parallel to the coating/substrate interface.

Scratch test

During scratch test coating fractures are following similar a mechanism in both WC-12Co and WC-12Ni coatings. Five general fracture sections were recognised; Figure 4-39 shows the schematic developed as a map of the fracture failure mechanism. Detailed damage mechanism maps for WC-12Co and WC-12Ni coatings are demonstrated in Figure 4-10 and Figure 4-11 respectively.

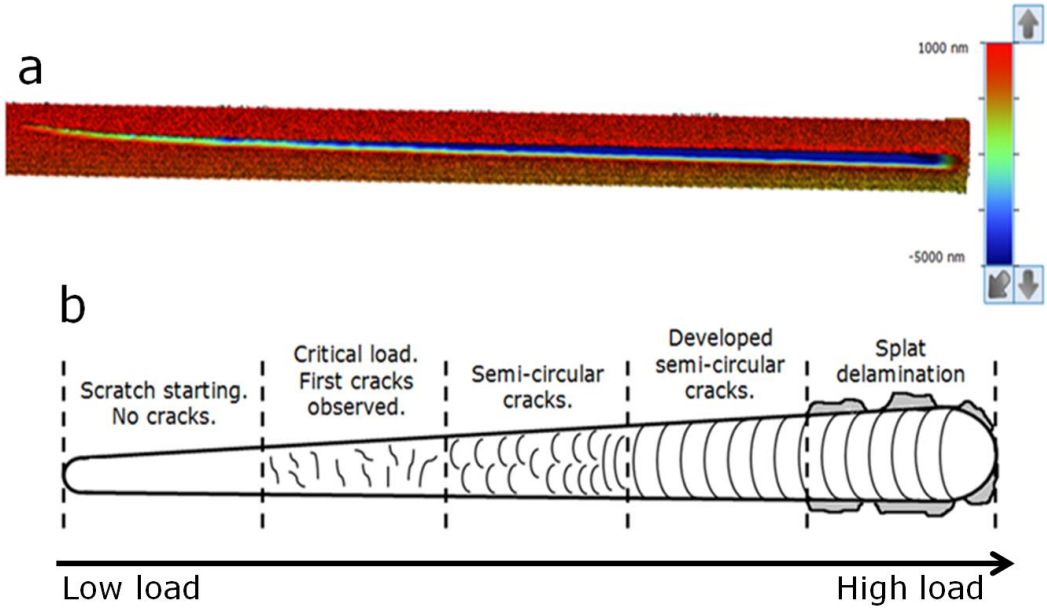

Figure 4-39: Scratch of WC-based thermally sprayed coatings. (a) Bruker image of entire scratch length. (b) Schematic of fracture mechanism map shows different fracture modes developed with progressive load.

Scratch starting sector

In the starting section of the scratch track there are no cracks seen in both coatings. In the starting of the scratch test the indenter tip works as a pure indentation to apply the preload without lateral movement. The material underneath the indenter deforms plastically and/or elastically at this stage. Ghabchi et al. (2014) reports local collapsing of material in this section which was not observed in this study. This could be attributed to the low porosity of both WC-12Co and WC-12Ni coatings (1.2%).

Critical load section

Figure 4-40 represents the critical loads at different sections of scratch test of both of WC-12Co and WC-12Ni coatings. It is very obvious that WC-12Co coating shows higher critical loads at all scratch test stages. This might be related to the higher hardness and fracture toughness of this coating.

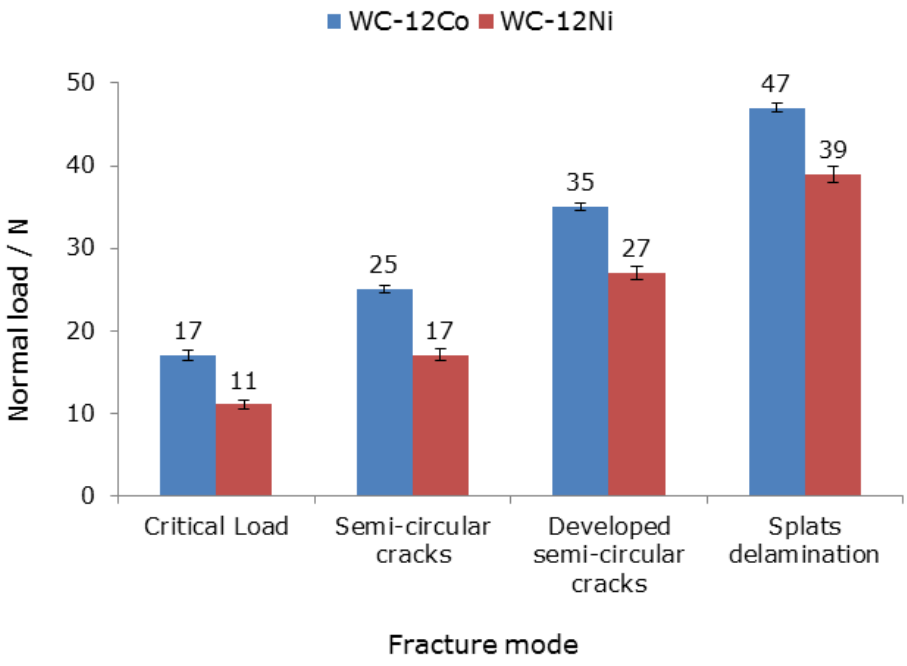

Figure 4-40: Critical loads of scratch test of WC-12Co and WC-12Ni coatings at different fracture modes.

The critical load is the normal load at which the initial cracks of the coating can be observed. The critical load has been about 17 N for WC-12Co coating and about 11 N for WC-12Ni coating. Higher critical load of WC-12Co coating could be related to its higher hardness and fracture toughness. Cracks in this section propagate through the matrix, and the mode of these initial narrow intergranular cracks is short and has no specific shape in both coatings. There have been few cracks observed in the WC grains in this section with WC-12Co coating, while no cracks have been noticed in the WC grains with WC-12Ni coating, and this could be attributed to higher load with WC-12Co coating. Ghabchi et al. (2014) reports angular cracks at the scratch edges in this section, which not observed here. This could be due to different coating material, (WC-CoCr), and different coating process, (HVOF, Diamond Jet-2600 system using hydrogen as fuel gas), used.

The scratch depth and width are increasing as the stylus tip moves and the load is increased. Due to friction force, compressive stresses are generated in front side of the moving style tip. Pile-up of the coating material is formed by pushing this material upward due to the friction force between the front side of the style tip and the coating material surface. Tensile stresses will be created at the top of the highest pile-up point. Furthermore, this friction force causes the material to sink-in at the trail of the stylus tip and tensile stress is generated behind the tip. The pile-up and sink-in generated in front and behind the moving tip are due to friction forces. Nevertheless, it is more related to material hardness (Alcala et al. 2000).

Semi-circular cracks

Intergranular semi-circular cracks are observed in both WC-12Co and WC-12Ni coatings scratch track (Figure 4-16). Few cracks appeared in the WC grains in this section of both coatings. The maximum tensile stress tends to appear at the contact surface as the friction force is increased. Semi-circular cracks might follow the maximum tensile stress on the coating surface which developed in the tail of moving stylus tip (Ghabchi et al. 2014). Similar semi-circular cracks have been reported with scratch test of thin coatings (Bull 1997; Holmberg et al. 2006).

Developed semi-circular cracks

The developed semi-circular cracks appear on the scratch track of WC-12Co and WC-12Ni coatings when the normal load exceeds 35 N and 27 N respectively. This difference could be related to the higher hardness and fracture toughness of WC-12Co coating compared to the WC-12Ni coating (see Table 4-4). The cracks in the WC grains are very obvious in this section in both coatings.

Figure 4-41 illustrates the scratch profile of WC-12Co and WC-12Ni coatings at this section. WC-12Co coating shows lower scratch depth, despite the higher load on this coating comparing to WC-12Ni coating at this section. This could be due to the higher hardness and fracture toughness of WC-12Co coating.

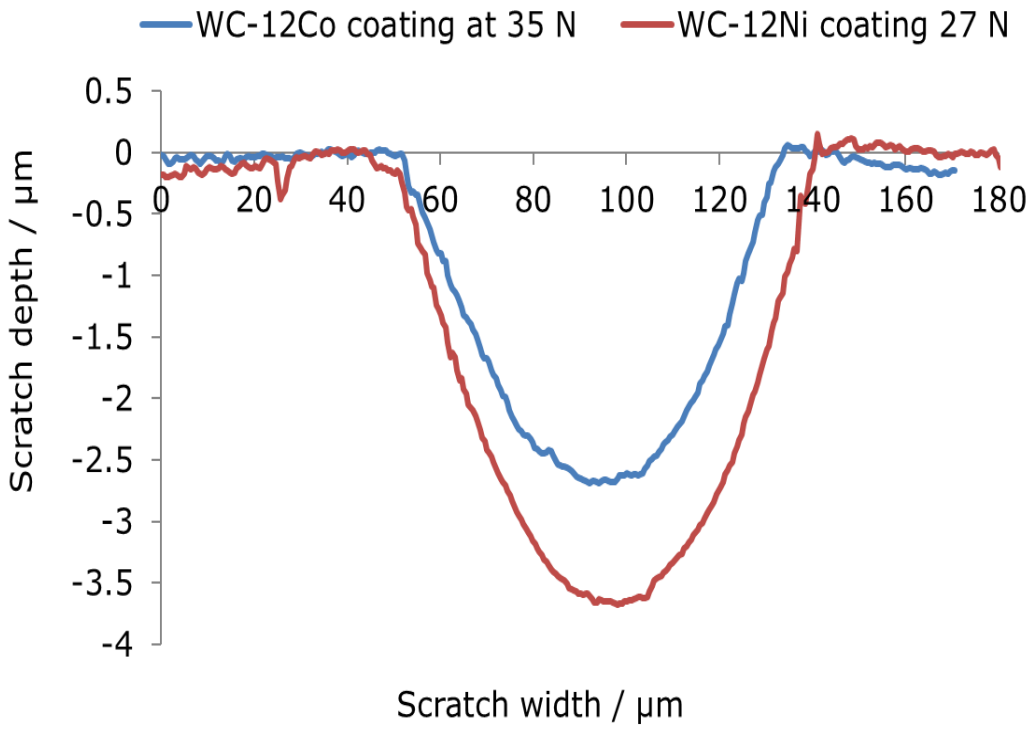

Figure 4-41: The plot of scratch profile of WC-12Co and WC-12Ni coatings at the developed semi-circular cracks section. WC-12Ni coating shows deeper scratch groove with lower normal load.

The major difference between semi-circular cracks observed in thermal sprayed thick coatings and thin coatings is that cracks penetration depth in thermal sprayed thick coatings will be limited to few splats thickness, whereas in thin coatings cracks penetration depth can be down to the substrate/coating interface. In general, the semi-circular cracks are propagating parallel to the coating surface (Ghabchi et al. 2014).

Coating splats delamination

Attributable to formation of tensile stress at higher point of pile-up, it is assumed that splat delamination might occur in front of moving tip (Figure 4-19). Coating splats delamination in thick coating is considered as partial or full detachment of one splat from the coating layer. However, in thin coatings, the detachment of the whole coating from the substrate would be considered (Ghabchi 2011).

The splat boundaries are considered as the weak regions in the coating layer. As the normal load is increased, the scratch depth and width are increased. The developed semi-circular cracks interact with the coating splat boundaries, leading to delamination of the coating splats at the edge of the scratch track (Figure 4-20). Delamination critical load could be used as an indication of quality of splat/splat cohesion.

In summary, WC-12Co coating shows a better mechanical properties comparing to WC-12Ni coating. According to microhardness results WC-12Co coating shows higher hardness, and this could be attributed to the higher decomposition and the generation of hard phase of W_2C as discussed in microstructure section. However, the WC-12Co coating exhibited a higher fracture toughness as well compared to WC-12Ni coating, and this could be related to the higher solubility of WC in the liquid cobalt binder compared to the nickel binder. This improves coating cohesion which consequently enhances coating fracture toughness. Through scratch test both WC-12Co and WC-12Ni coatings are following the same mechanism of coating failure during scratch test. However, WC-12Ni coating shows lower critical loads in all fracture sections through the scratch test, which could be attributed to higher hardness and fracture toughness of WC-12Co coating. The scratch test could be used to characterise thick coatings and to predict the wear behaviour of these coatings. Nevertheless, more

work should be done with this test for thick coatings to confirm it as an investigation tool.

4.2.3 Sliding Wear Behaviour

In this section the dry sliding wear behaviour of both WC-12Co and WC-12Ni coatings will be discussed and compared during mild and severe wear in the light of their microstructure and mechanical properties. Staring with the sliding wear mechanism, this discussion will highlight the effect of the metal binder type on the sliding wear behaviour.

Many researchers investigated the sliding wear behaviour of WC-base thermally sprayed coatings, such as Shipway et al (2005); Wood (2010) and Yang et al. (2003). However, most of these studies assessed the sliding wear behaviour due to specific issues like the coating microstructure, carbide grain size or during the elevated temperatures. Also, all these studies draw the wear behaviour mechanism from the investigation of the wear track by the end of the wear test, and from that they suggest what is going on during the wear test.

Recently, Luo et al. (2015) developed an online wear test (investigated in situ in a large SEM chamber) on the thermally sprayed coatings. In this work, the wear behaviour of these coatings was investigated using a pin-on-disc wear test. According this study the sliding wear mechanism of WC-Co coating can be summarised as follow:

A small channel with a round smooth bottom was generated, after few rotations of the coated disc sample, by the contact with the counterface ball. This channel became a little broader and deeper after some rotations. There are many loose particles (wear debris), which were separated from the surface of the coated disc due to abrasive wear and adhered onto the surface of the counterface ball. These loose particles contain many sharp-edged WC grains, and thus scratched the surface of the coated disc. More rotations led to the increase of loose particles which separated from the coated disc and adhered onto the worn surface of the ball.

Due to the high contact pressure between the coating surface and the wear counterpart, a local ‘‘cold welding’’ occurred between the adherent materials and the coating. Some big particles were torn out of the adherent coating material on the counterface ball and reattached onto the coating surface, generating some protrusions on the coating surface. This is a typical characteristic of adhesive wear. These protrusions were again ground away from the surface of the coating due to the abrasive wear, after some more rotations.

The grinding and polishing process to prepare the coated disc for wear test always leads to some pits in the top surface, which are due to opening of the pores in the top surface of the coated disc. In the wear process, loose coating particles (wear debris) gathered and adhered into these pits. Thus, the pits are completely filled with the wear debris and some protrusions were formed. After more rotations, these protrusions broke off from the wear track.

Due to of the existence of interlaminar micro-cracks in the coating, a stress concentration occurred at the opening of the micro-crack under a high normal force and friction force. This micro-crack propagated due to repeated application of these two forces. Thus, the adherent material, together with some coating material, was again torn out of the coating and the pit became even bigger than before. Hence, it can be concluded that the wear between the coating and counterface ball did not only occur at the interface between the coating and the counterface ball, but also between the coating and the adherent coating material on the counterface ball.

In this study, both WC-12Co and WC-12Ni coatings show a similar wear mechanism. However, the WC-12Co coating withstands a higher applied load before the transition from mild to severe wear occurs.

The higher wear resistance of WC-12Co coating could be attributed to its higher hardness and fracture toughness as well. These mechanical properties affected strongly by the coating microstructure. As mentioned during the coatings microstructure discussion, the WC-12Co coating contains higher W_2C phase fraction comparing to

WC-12Ni coating. Also, the nanocrystalline/amorphous phase is appearing with the WC-12Co coating. It is reasonable that the hardness increases with increasing content of W_2C in the coating, since W_2C phase (HV = 29.4 GPa) is harder than the WC phase (HV = 23.5 GPa). Furthermore, nanocrystalline/amorphous Co–W–C phase is not only harder than metal binder phase, but also results in an increase of the cohesion between tungsten carbide particles and the matrix (Jacobs et al. 1999; Vinayo et al. 1985; Yang et al. 2003b). Whereas, the high fracture toughness of the WC-12Co coating could be related to the high solubility of WC in the liquid Co metal binder comparing to the solubility of WC in liquid Ni metal binder (Exner 1979).

During the mild wear, both coatings showing approximately the same low wear rate, Table 4-4 (0.004×10^{-6} $mm^3/N.m$), after same sliding distance of 1500 m for both coatings. Although, the normal load with WC-12Co coating (212 N) is higher than the normal load with the WC-12Ni coating (118 N). However, the wear rate of the counterface ball (sintered WC-6wt%Co ball with 9.5 mm diameter and HV = 1610 kgf mm^{-2}) with WC-12Co coating is higher than the wear rate of same ball sliding against WC-12Ni coated disc; this is very obvious in Table 4-4, where the wear rate of the ball sliding against WC-12Co coated disc (0.2×10^{-6} $mm^3/N.m$) is about 20 times higher than the wear rate of the same ball sliding against WC-12Ni coated disc (0.01×10^{-6} $mm^3/N.m$). Also, this can be confirmed from the wear scar width of both coatings, it was only about 0.6 mm with WC-12Ni coating, Figure 4-30a, where it was doubled with WC-12Co coating to be about 1.5 mm, Figure 4-23a, on the other hand, the radius of the ball worn surface sliding against WC-12Co coated disc is two times more than that of the same ball sliding against WC-12Ni coated disc. This higher wear of counterface ball sliding over WC-12Co coated sample could be attributed to the high hardness of WC-12Co coating (see Table 4-3).

Figure 4-23(a-d) and Figure 4-30(a-c) show the coated disc worn surface of WC-12Co and WC-12Ni coatings during mild wear respectively. As mentioned above, both coatings show the same wear mechanism. Some localised pits which filled by the tribofilm layer (oxide layer/wear debris), and these can be explained as stated in the sliding wear mechanism as follows:

During the grinding and polishing of the coated samples to prepare for wear test, some pits were generated on the top surface, which in fact is due to the opening of porosity in the top surface of the coating, Figure 4-42. After some rotations of the sliding wear test, the wear debris starts to generate and it contains hard chips from the coating particles which increase the abrasive wear between the coated disc and the counterface ball. This is leading to increase the wear debris as well, which moved through the test motion and adhered into these pits (Guilemany et al. 2001), when the pits are completely filled with the wear debris, some protrusions were formed. However, these protrusions, due to the abrasive wear, were again ground away from the surface of the coating, (Luo et al. 2015). This transfer of tribofilm material is continued through the wear test between the coating and the counter ball, which in some cases lead to enlarged pits in the coating surface, as can be seen in Figure 4-23c which shows the fracture of the tribofilm layer (oxide layer) from the worn surface of WC-12Co coating. Figure 4-28b is showing these loss particles, (wear debris), adherent on the worn surface of the ball sliding against WC-12Co coating. However, during the mild wear the wear debris particles are very fine, and it works as a solid lubricant between the coating and the counter ball, where it is leading to low wear rate, (Yang et al. 2003b; Zhao et al. 2006).

Furthermore, narrow intergranular cracks were observed in the coating worn surface with both WC-12Co and WC-12Ni coatings during mild wear as can be seen in Figure 4-23d and Figure 4-30c respectively. These cracks often start from the localised pits and propagate through the brittle oxide layer and between the grains boundaries. These cracks could be attributed to the existence of interlaminar micro-cracks in the coating and the concentration of the stresses at the opening of the micro-crack under normal and friction force. The repeatedly applied forces lead to plastic deformation in the coating layer and propagation of these cracks, (Celik et al. 2006; Luo et al. 2015; Shipway et al. 2005).

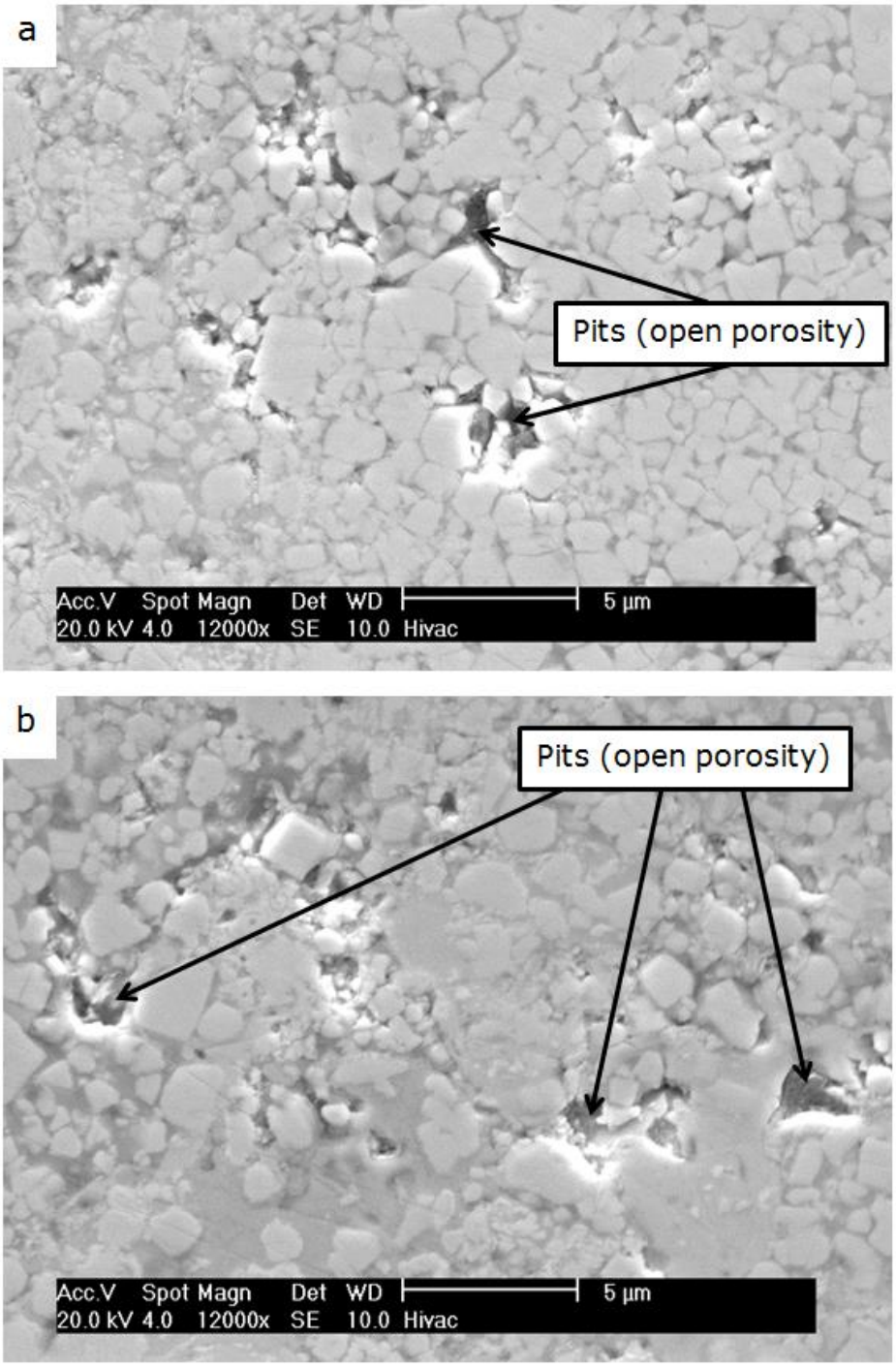

Figure 4-42: The SEM images of grinded and polished coated samples before the wear test show the pits on the top surface of the coating. (a) WC-12Co coating, and (b) WC-12Ni coating.

With the release of wear debris, the process of sliding wear becomes a case of three-body abrasion rather than two-body sliding (Mohanty et al. 1996). This abrasive wear mode is scratching of the coated surface which can increase the wear rate. However, during the mild wear and due to the low load and fine wear debris particles,

this phenomenon does not effect wear rate so much. Figure 4-26 and Figure 4-33 show the Bruker ContourGT Optical Profiler images of both WC-12Co and WC-12Ni coatings respectively. The scratches on the top coated surfaces are very obvious in both coatings.

Figure 4-23e and Figure 4-30d show the cross-section in the worn surface of both WC-12Co and WC-12Ni coatings during mild wear respectively. In both coatings, a localised thick tribofilm layer is seen on the top of worn surface. Other researchers report that on conventional cemented carbides, mild wear tests resulted in a few μm thick tribofilm (Engqvist et al. 2000; Yang et al. 2003b). The EDX analysis of this tribofilm layers indicate that it is an oxide layer. Other researchers investigate this oxide layer and they report that it consist of WO_3 and M-WO_x where M is the metal binder (Co/Ni), (e.g. $CoWO_4$), (Bolelli et al. 2014; Engqvist et al. 2000).

Furthermore, in case of WC-12Co coating narrow intergranular subsurface cracks are observed in the worn surface cross-section, where these cracks do not appear with WC-12Ni coating. These subsurface cracks appearing through WC-12Co coating cross-section could be attributed to the high load with this coating and/or due to the higher decomposition of this coating compared to WC-12Ni coating. Whereas, these cracks run mostly in the brittle regions of the coating where there has been the most extensive decomposition (Shipway et al. 2005).

When a certain level of load is exceeded, the transition from mild to severe wear suddenly occurs. This critical transition load depends on the properties of the material subjected to wear and also on the mechanical and thermal properties of the coating and the counterface. Severe wear involves enormous surface damage and large scale material transfer to the counterface (Zhang and Alpas 1997).

Experimental results of the sliding wear of WC-12Co coatings show that, wear under normal load $\leq$ 212 N is "mild" while under normal load $\geq$ 282 N the wear is "severe". In between these two normal load values there is a transition from mild to severe wear. However, with WC-12Ni coating the experimental results show that, the

transition load from mild to severe wear is somewhere between 118 N and 141 N (see Table 4-4).

Even though, the WC-12Ni coating transit to severe wear with low load, (compared to WC-12Co coating), the wear scar depth of this coating during severe wear, Figure 4-33d, is about six times higher than the WC-12Co coating wear scar depth during severe wear, Figure 4-26d. In contrast, the wear rate of counterface ball, (WC-6Co), sliding against WC-12Co coating during severe wear (0.9×10^{-6} $mm^3/N.m$) is twenty times higher than wear rate of the same ball sliding against WC-12Ni coating (0.045×10^{-6} $mm^3/N.m$), Table 4-4. The high wear of the ball sliding against WC-12Co coating is confirmed by the wear scar width with this coating, Figure 4-24a, which is double of the wear scar depth of WC-12Ni coating, Figure 4-31a. This high wear rate of the counterface ball and low wear scar depth with WC-12Co coating could be attributed to the higher hardness and fracture toughness of this coating, which related to the coating microstructure (see section 4.2.2).

Both WC-12Co and WC-12Ni coatings show severe wear mechanism when worn with normal load above the transition load, as can be seen in Figure 4-24 and Figure 4-31 respectively. With high loads, the fragmentation of the WC grains led to severe wear and the fractured grains work as abrasives and cause three-body abrasion (Zhu et al. 2001a). The cross-section in the worn surface of both coatings show thin tribofilm layer covering entire wear track, Figure 4-24e and Figure 4-31e respectively. Severe wear test gave thinner tribofilm layer, most probably the higher surface temperatures generated in the severe wear test due to the high load made the tribofilm softer and therefore thinner (Engqvist et al. 2000). Plate-like chips of severe wear debris that formed due to the delamination of the brittle transfer layer of both WC-12Co and WC-12Ni coatings are illustrated in Figure 4-25 and Figure 4-32 respectively.

In conclusion, both WC-12Co and WC-12Ni coatings show similar wear mechanism. However, WC-12Co coating withstand higher load to transit from mild to severe wear. During mild wear both coatings show a similar wear rate. The high wear resistance of WC-12Co coating could be attributed to its favourable hardness and fracture toughness compared with WC-12Ni coating. These good mechanical properties

of WC-12Co coating can be related to the coating microstructure. WC-12Co coating shows higher decomposition and also higher solubility of WC in liquid cobalt compared to WC-12Ni coating.

4.3 Conclusion

In this chapter, the effect of metal binder type on the coating microstructure, mechanical properties and dry sliding wear behaviour of WC-M thermally sprayed coatings has been investigated. Two identical feedstock powders have been used, Amperit 518.074 (WC-12wt%Co) and Amperit 547.074 (WC-12wt%Ni). These powders are denoted through this study as WC-12Co and WC-12Ni, respectively. Both powders are agglomerated and sintered with a similar nominal size (-45+15µm), both powders were manufactured by H. C. Starck GmbH. Table 3-1 shows the chemical composition of these powders. Coatings have been sprayed using a Metallisation MET-JET 4L (Figure 3-1), which is the latest development of kerosene fuelled HVOF system.

According to the coating microstructure, the W-Co-C system shows low temperature at which liquid forms compared to the W-Ni-C system, (Figure 4-37). This leads to higher solubility of WC during WC-12Co coating, which means more decomposition of WC through WC-12Co coating compared with WC-12Ni coating. From the XRD diffraction (Figure 4-1), the cobalt peaks are detected in the powder and not in the coating, this suggests that most of the cobalt is present as amorphous/nanocrystalline binder phase. This amorphous/nanocrystalline phase is due to the solid solution phase formed by dissolution of decomposition products such as W_2C, W and C in metallic binder, (cobalt), during spraying process, whereas, nickel phase is retained in the WC-12Ni coating, (Figure 4-1). In spite of limitation of the quantitative X-ray diffraction analysis, however, it is expected to provide some useful information related to the degree of decomposition. It shows that WC-12Co coating represents a high degree of decomposition compared to the WC-12Ni coating.

Regarding the mechanical properties, WC-12Co coating shows higher hardness compared to the WC-12Ni coating. This could be attributed to the higher degree of decomposition and more hard phase W_2C generated with WC-12Co coating. Also, WC-

12Co coating exhibited a higher fracture toughness compared to WC-12Ni coating, which could be related to the higher solubility of WC in the liquid cobalt binder than the nickel binder, which improves coating cohesion and consequently increase coating fracture toughness. Through the scratch test, both WC-12Co and WC-12Ni coatings are following the same mechanism of coating failure. However, WC-12Co coating withstands higher critical loads in all fracture sections through the scratch test. This could be related to the higher hardness and fracture toughness of this coating. The scratch test could be used to characterise thick coatings fracture mechanism. Delamination critical load might be indicating the splat/splat cohesion. Furthermore, scratch test can be used to predict the wear behaviour of thermally sprayed coatings. Coatings with higher critical load show higher wear resistance. However, more work should be done with this test for thick coatings to confirm it as an investigation tool.

Due to the sliding wear behaviour, both WC-12Co and WC-12Ni coatings show similar wear mechanisms. However, WC-12Co coating endures higher load before the transition from mild to severe wear. During mild wear both coatings show a similar wear rate. The high wear resistance of WC-12Co coating could be attributed to its favourable hardness and fracture toughness compared with WC-12Ni coating. These good mechanical properties of WC-12Co coating can be related to the coating microstructure. WC-12Co coating show higher decomposition and also higher solubility of WC in liquid cobalt compared to WC-12Ni coating.

CHAPTER 5 The Effect of the WC Grain Size on Microstructure and Properties of WC-Co Coatings: Results and Discussion

This chapter is to describe the characterisation of WC-17CoF powder (with fine WC grain size) and WC-17CoC powder (with coarse WC grain size) and their HVOF coatings. This is to study the effect of WC grain size on the microstructure, mechanical properties, and dry sliding wear behaviour of WC-Co coatings.

5.1 Experimental Results

5.1.1 Powder Characterisation

Starting powders are essential for the thermally sprayed coatings and their properties. To study the effect of WC grain size on the coating microstructure, mechanical properties and dry sliding wear behaviour two powders, Woka 3202 (WC-17wt%Co) with coarse WC grain size, and Woka 3202 FC (WC-17wt%Co) with fine WC grain size, which are denoted in this study as WC-17CoC and WC-17CoF, respectively, have been used. Both powders have been manufactured by an agglomeration and sintering process with a similar nominal size (-45+15µm) by Sulzer Metco. WC-17CoF and WC-17CoC powders have been examined by the XRD and the SEM, and their characterisations are represented in the following sections.

5.1.1.1 X-Ray Diffraction (XRD)

The XRD pattern of the WC-17wt%Co F and WC-17wt%Co C starting powders is shown in Figure 5-1. Both powders look completely identical, and consist of WC and Co crystals. The Co has face-centred-cubic crystal structure (fcc), where the WC crystal structure is hexagonal close-packed (hcp) in both powders. Appendix A presents the ICDD-PDF of all phases appearing in this study.

5.1.1.2 Scanning Electron Microscopy (SEM)

The external morphologies of the WC-17CoF and WC-17CoC powders are shown in Figure 5-2. Both powders had spherical particles, with high levels of porosity. The cross sections of both powders are illustrated in Figure 5-3; the microstructure of both WC-17CoF and WC-17CoC powders consists of angular particles of WC embedded in metallic cobalt binder. The difference in WC grain size between them is very obvious. Porosity and some cracks in WC grains have been seen in both powders. The range of WC grain size of 17Co F and WC-17CoC powders and their coatings are shown in Table 5-1. From the table, there has been insignificant change in the WC grains size between the powders and their coatings. However, it shows the high difference in the WC grain size between the WC-17CoF and WC-17CoC powders.

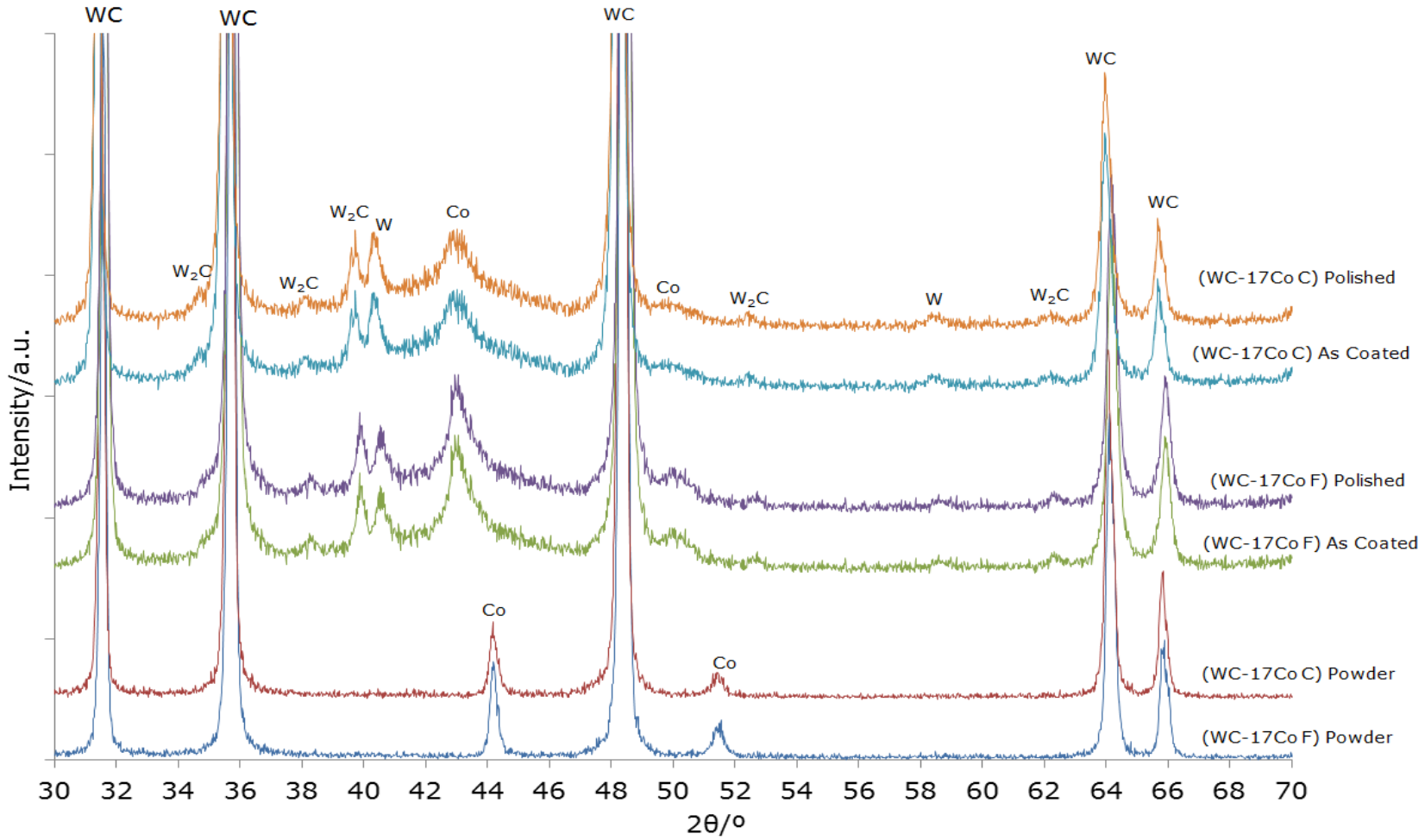

Figure 5-1: XRD pattern of WC-17CoF and WC-17CoC powders and coatings. (ICDD-PDF for all phases is presented in appendix A).

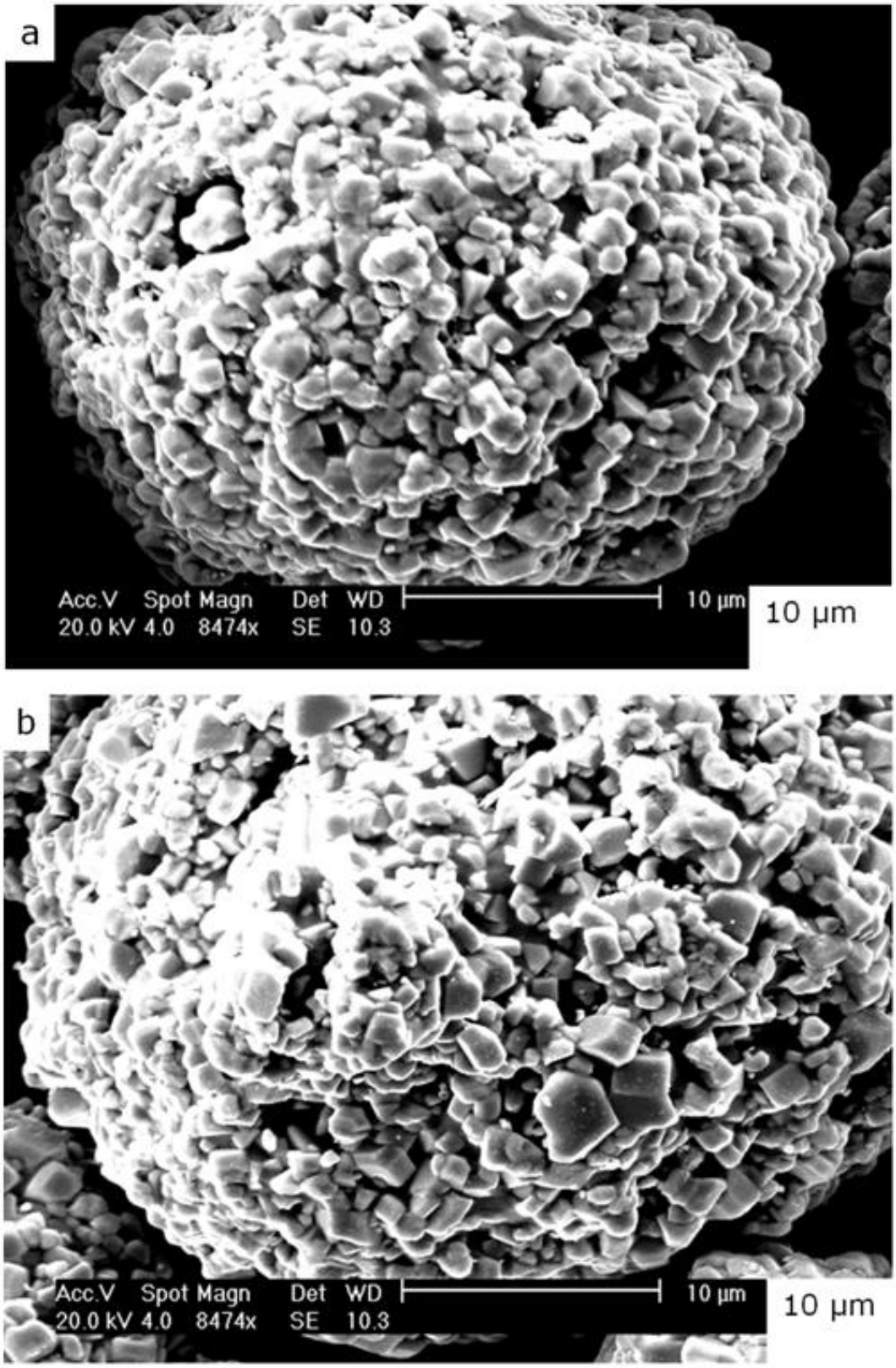

Figure 5-2: The morphology of the powders shows spherical particles with high level of porosity. (a) WC-17CoF powder. (b) WC-17CoC powder.

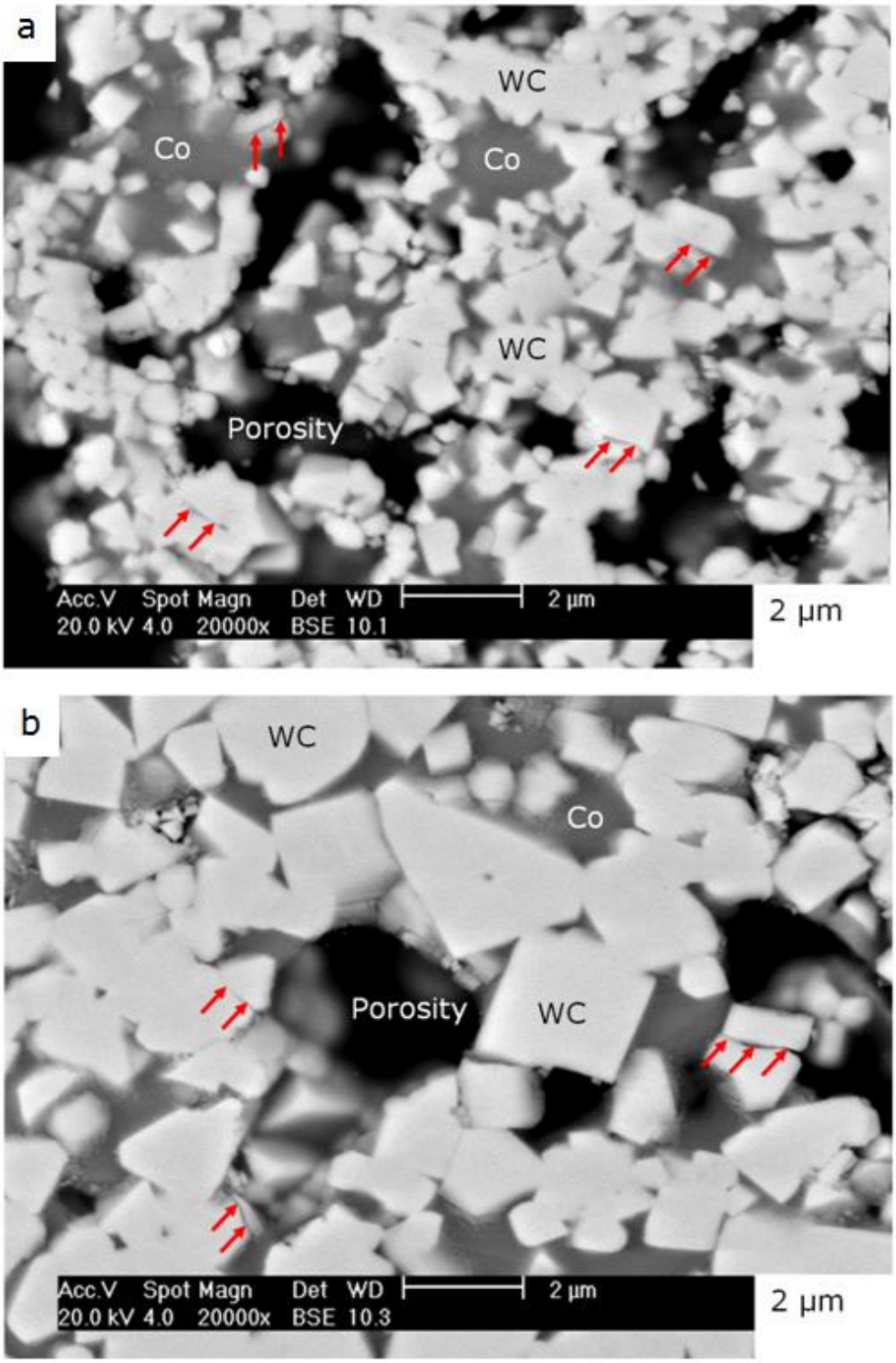

Figure 5-3: The cross-section of the powders. (a) WC-17CoF powder demonstrates fine WC grains, cobalt binder, porosity and some cracks in WC grains (red arrows). (b) WC-17CoC powder shows coarse WC grains, cobalt binder, porosity and cracks in WC grains (red arrows).

Table 5-1: WC grain size change between the powders and the coatings of WC-17CoF and WC-17CoC.

Coating material	WC grain size of powder / µm	WC grain size of coating / µm
WC-17CoF	0.4 – 1.3	0.3 – 1.3
WC-17CoC	0.8 – 2.5	0.6 – 2.1

5.1.2 Coating Characterisation

Coating microstructure is one of the important aspects affecting the thermal spray coating properties. The next two sections depict the microstructure characterisation of WC-17CoF and WC-17CoC coatings using the XRD and the SEM technique.

5.1.2.1 X-ray diffraction (XRD)

The primary peaks indexed to WC (hcp) are clearly obvious in the XRD pattern of WC-17CoF and WC-17CoC as-sprayed and after polishing coatings, Figure 5-1. A number of microstructural changes can be seen in both coatings. Peaks corresponding to W_2C (hcp), with peaks of elemental tungsten (bcc), can be seen in both traces. The Co crystal peak has been obvious; even though the coating peaks have shifted from its position in powder pattern and have been broader. The intensity of W_2C in both WC-17CoF and WC-17CoC coatings are same, which means there is no clear difference in decomposition between the fine and coarse coating. (ICDD-PDF for all phases is presented in appendix A).

5.1.2.2 Scanning electron microscopy (SEM)

The microstructure of both WC-17CoF and WC-17CoC coatings is shown in Figure 5-4 and Figure 5-5 respectively. The low magnification of the SEM-BSE images in Figure 5-4a, and Figure 5-5a, illustrates a typical lamellar structure of thermal spray coatings with different phases. In both coatings molten and semi-molten matrix (cobalt

binder) zones are seen. Some porosity is seen in both coatings microstructure, with a homogeneous distribution of carbide grains some of which are with rounded edges. There has been insignificant reduction in WC grain size after coating for both materials, Table 5-1.

The high magnification of the SEM-BSE images in Figure 5-4b and Figure 5-5b shows WC grains surrounded with a thin brighter spotty rings and clusters of small particles which are related to W_2C and/or metallic tungsten. Some cracks in WC grains in both WC-17CoF and WC-17CoC coatings are illustrated in Figure 5-4c and Figure 5-5c respectively.

Table 5-2 shows the quantitative X-ray diffraction analysis, (see Appendix B), of both WC-17CoF and WC-17CoC coatings indicating the relative portions of phases weight percentage excluding cobalt phase. The accuracy of this method is not so precise since it does not account for the fraction of the amorphous and the metal binder (Co) phases. However, it still gives an idea about the weight percentage of carbide phases. There is no significant difference in decomposition between both of fine and coarse coating. This supports the XRD results of these coatings exhibited in Figure 5-1.

Table 5-2: Quantitative X-ray diffraction analysis of the crystalline tungsten-containing phases in WC-17CoF and WC-17CoC coatings.

Coating	WC (wt %)	W_2C (wt %)	W (wt %)
WC-17CoF	94	4	3
WC-17CoC	96	3	1

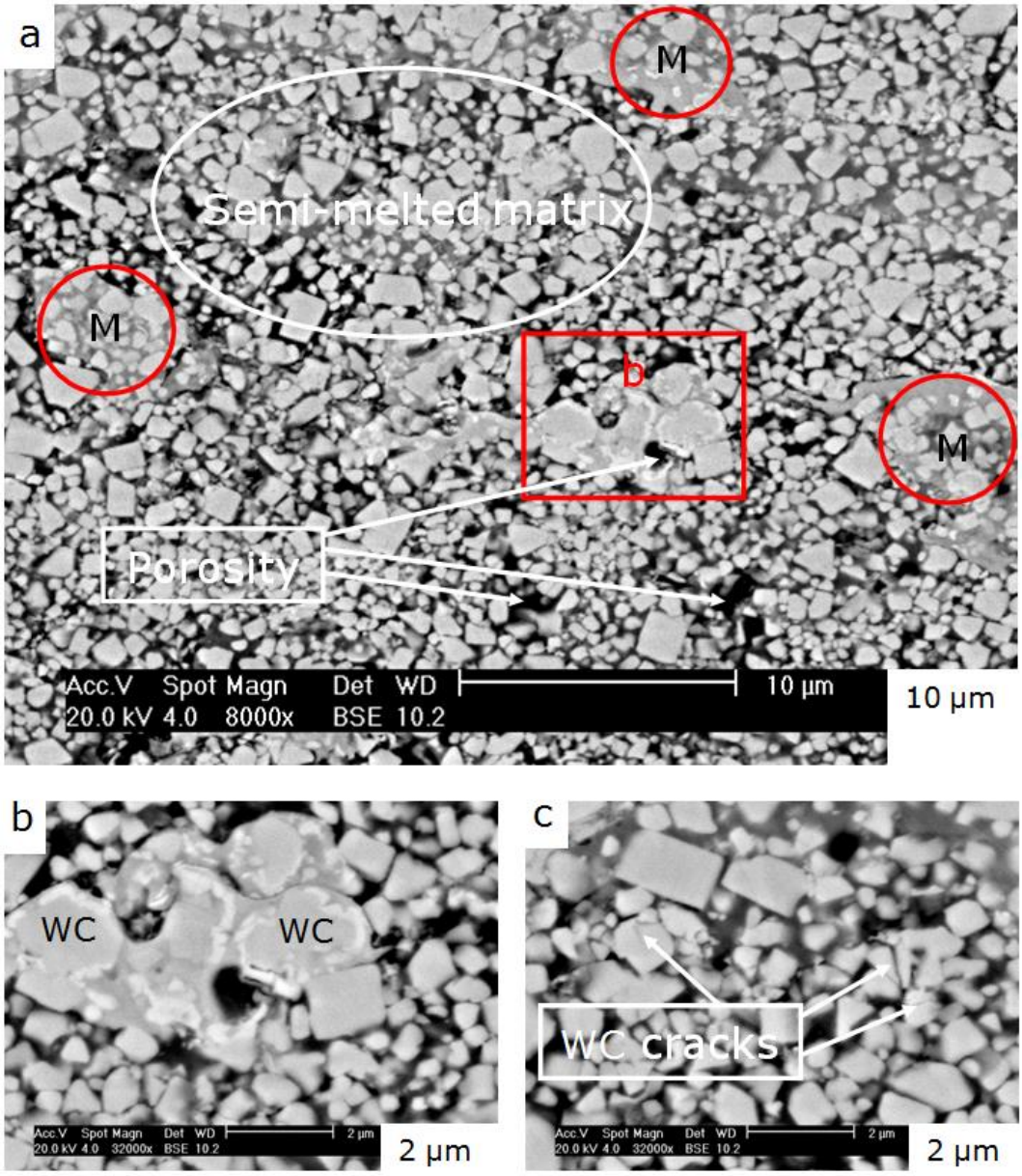

Figure 5-4: The microstructure of WC-17CoF coating. (a) The SEM-BSE image shows different features of coating microstructure. The "M" indicated to melted matrix areas. (b) The SEM-BSE image of selected area "b" illustrated the WC particles surrounded by brighter W2C rings and/or metallic tungsten particles. (c) The SEM-BSE image show cracks in WC grains.

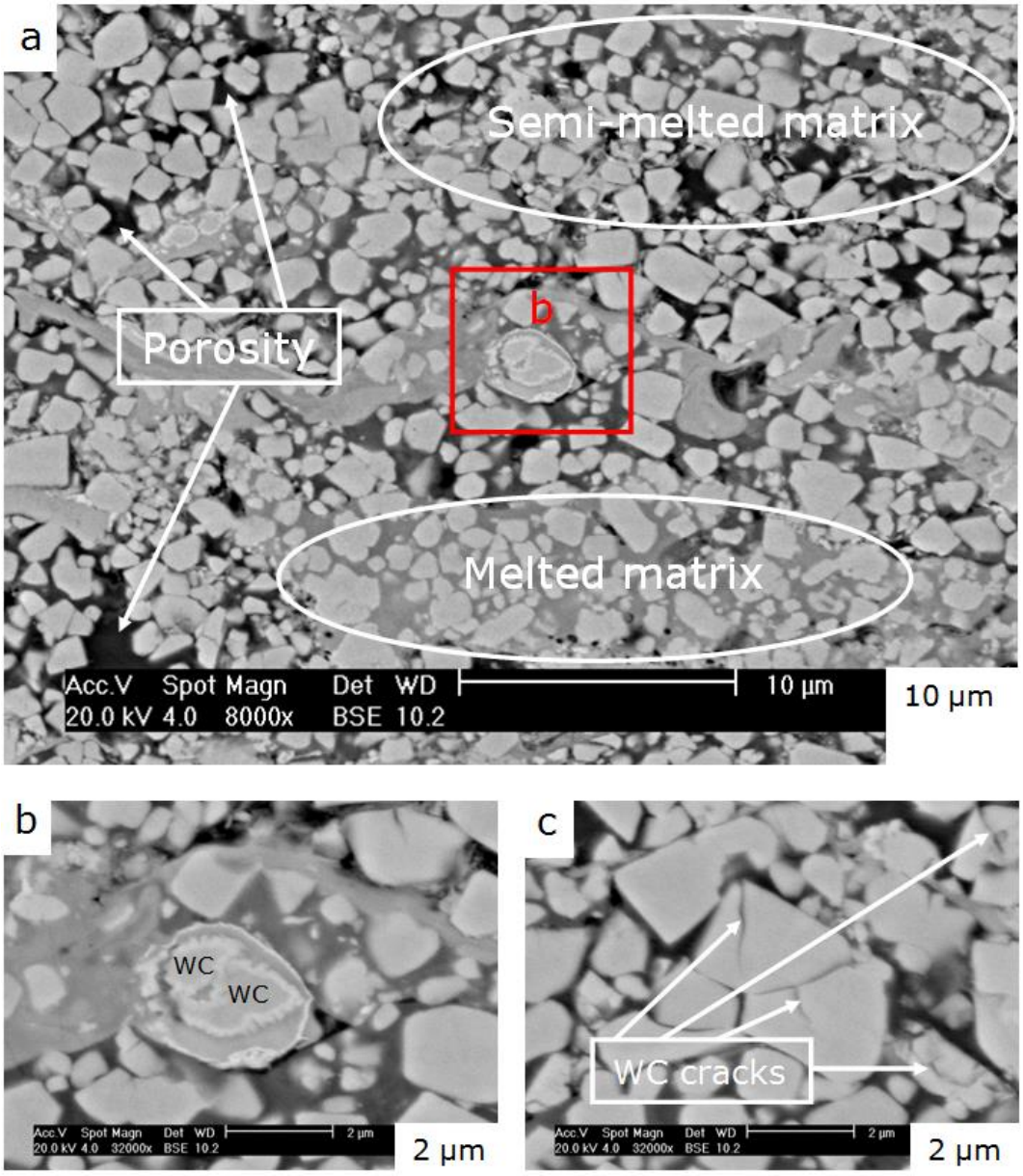

Figure 5-5: The microstructure of WC-17CoC coating. (a) The SEM-BSE image shows coating microstructure features. (b) The SEM-BSE image of selected area "b" exhibited the WC particles surrounded by W2C rings and/or metallic tungsten. (c) The SEM-BSE image demonstrates cracks in WC grains.

5.1.3 Mechanical properties of coatings

The mechanical properties, such as hardness and fracture toughness are one of the essential factors affecting the performance of cermet coatings. Next three sections depict the results of the effect of WC grain size on the mechanical properties of WC-

17Co coatings, including microhardness, fracture toughness and scratch test. Nevertheless, the scratch test as a new innovative method to predict the wear behaviour of thick coatings will be explained in more details.

5.1.3.1 Microhardness

To examine the microhardness of both WC-17CoF and WC-17CoC coatings, forty Vickers indentations have been taken along the mid-plane of the coating cross-section. The microhardness average values of WC-17CoF and WC-17CoC coatings are $HV_{0.3/15}$ = 1088 ± 33 kgf mm^{-2} and $HV_{0.3/15}$ = 1056 ± 24 kgf mm^{-2}, in order, Table 5-3. The ± values represent the standard error in the mean. The cumulative distribution of microhardness is illustrated in Figure 5-6, where the median values are equal to 1134 kgf mm^{-2} for the WC-17CoF coating and 1080 kgf mm^{-2} for the WC-17CoC coating.

5.1.3.2 Fracture toughness

Vickers hardness indentation at a 10 kg load has been carried out on both the WC-17CoF and WC-17CoC coatings, in order to evaluate their indentation fracture toughness. Figure 5-7 shows the cracks formed parallel to the coating/substrate interface, where the majority of cracks formed at the corner of the indent with several cracks on a distance from the corner. The indentation cracks have propagated between the carbides, through an anisotropic microstructure.

Fracture toughness values have been calculated from measurements of the indentations and the associated cracks on cross-sections of the coating and it has been found that the c/a values always fell within the range of $0.6 \leq c/a < 4.5$, for which the Evans and Wilshaw equation is valid. For comparison the fracture toughness for both WC-17CoF and WC-17CoC, coatings have been calculated also by the Niihara equation. Results of coating fracture toughness are presented in Table 5-3. The ± values represent the standard error in the mean. The cumulative distributions of these data are shown in Figure 5-8 (Evans and Wilshaw equation) and Figure 5-9 (Niihara equation). The median fracture toughness values are presented in both last figures.

Table 5-3: Microhardness and fracture toughness of WC-17CoF and WC-17CoC coatings

Coating powder	Microhardness $HV_{0.3/15}$ kgfmm^{-2}	Fracture toughness K_{IC} (Evans & Wilshaw) MPam$^{1/2}$	Fracture toughness K_{IC} (Niihara) MPam$^{1/2}$
WC-17CoF	1088 ± 32	6.1 ± 0.1	6.1 ± 0.1
WC-17CoC	1056 ± 24	6.6 ± 0.1	7.3 ± 0.2

Fracture toughness equations, (Evans and Wilshaw) and (Niihara), explained in details in section 3.1.4.2 (±values represent the standard error in the mean i.e. $\sigma/\sqrt{n}$).

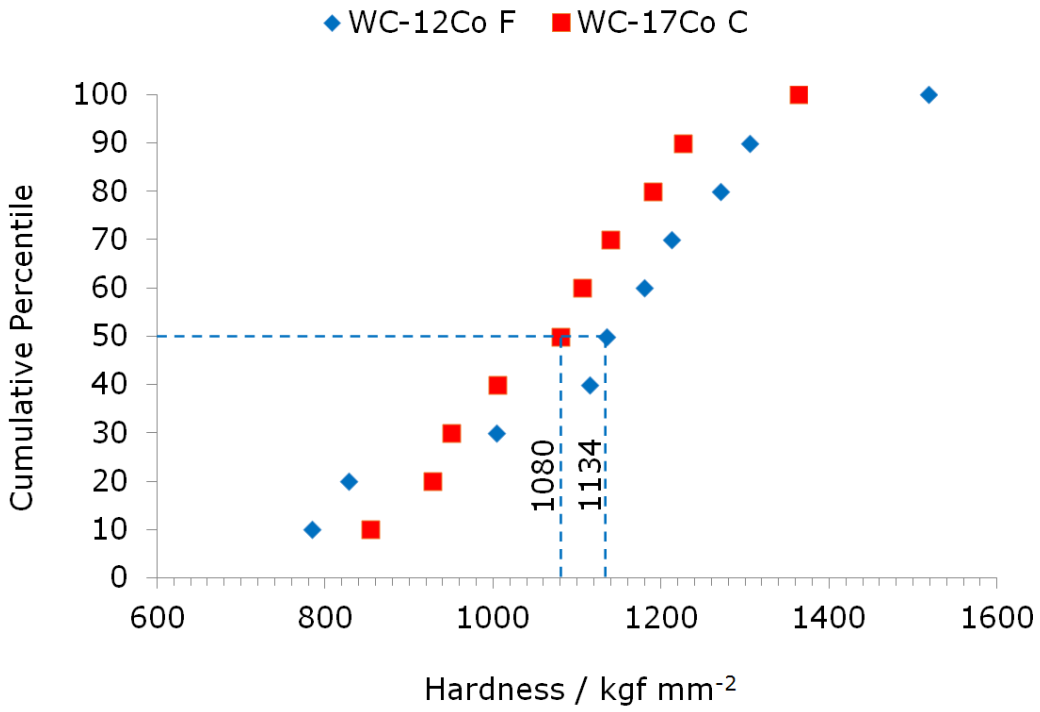

Figure 5-6: Plot of cumulative distribution of WC-17CoF and WC-17CoC coatings microhardness shows the median values for both coatings.

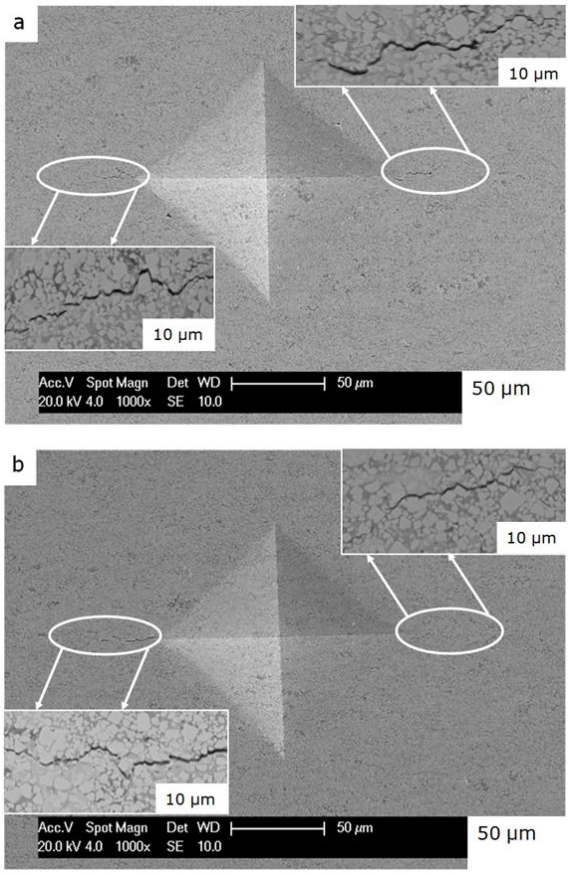

Figure 5-7: Indentation of fracture toughness with load 10 kg of (a) WC-17CoF coating and (b) WC- 17Co C coating, shows an intergranular cracks generated parallel to the coating/substrate interface formed at the corner of the indent.

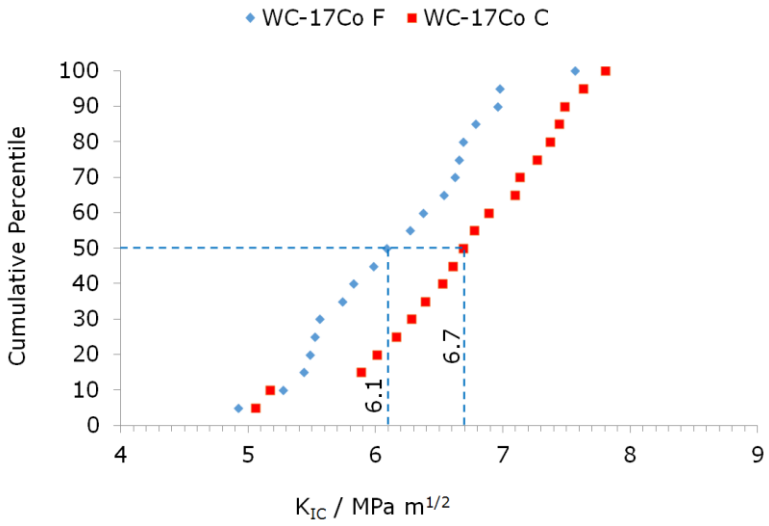

Figure 5-8: Cumulative distribution plot of WC-17CoF and WC-17CoC coatings fracture toughness, Evans and Wilshaw equation shows the median values for both coatings.

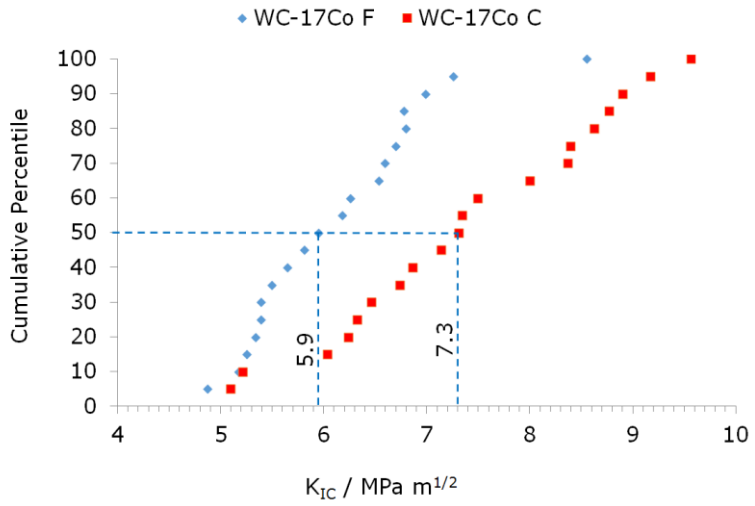

Figure 5-9: Cumulative distribution plot of WC-17CoF and WC-17CoC coatings fracture toughness, Niihara equation shows the median values for both coatings.

5.1.3.3 Scratch test

To characterise the failure behaviour of thermally sprayed WC-17CoF and WC-17CoC coatings through scratch test, three scratches have been created on the polished (Ra = 0.04 µm) sample of each coating. Scratch tracks have been inspected by the optical profilometry (using a Bruker ContourGT Optical Profiler) and the SEM, to comprehend the coating failure behaviour through the scratch test associated to the loading conditions. The scratch has started with preload of 5 N and the load has increased continually up to 50 N. The total length of the scratch has been about 8 mm for both coatings. The loading rate has been 50 N min^{-1} and the sliding speed has been 10 mm min^{-1}. Consistent with coating fracture appearing on the scratch track, the total length of scratch can be divided mainly to five segments which will be clarified in details for both WC-17CoF and WC-17CoC coatings in the following sections to investigate the failure behaviour of both coatings during the scratch test. Figure 5-10 and Figure 5-11 represent the schematic of coating fracture mechanism along the scratch track of both WC-17CoF and WC-17CoC coatings respectively, according to the progression of the normal load and the distance where these failures occur. The charts in Figure 5-10 and Figure 5-11 exhibit the variations of scratch depth and width consistent with the progressive load. The critical load is starting at 14 N for WC-17CoF coating and at 10 N for WC-17CoC coating.

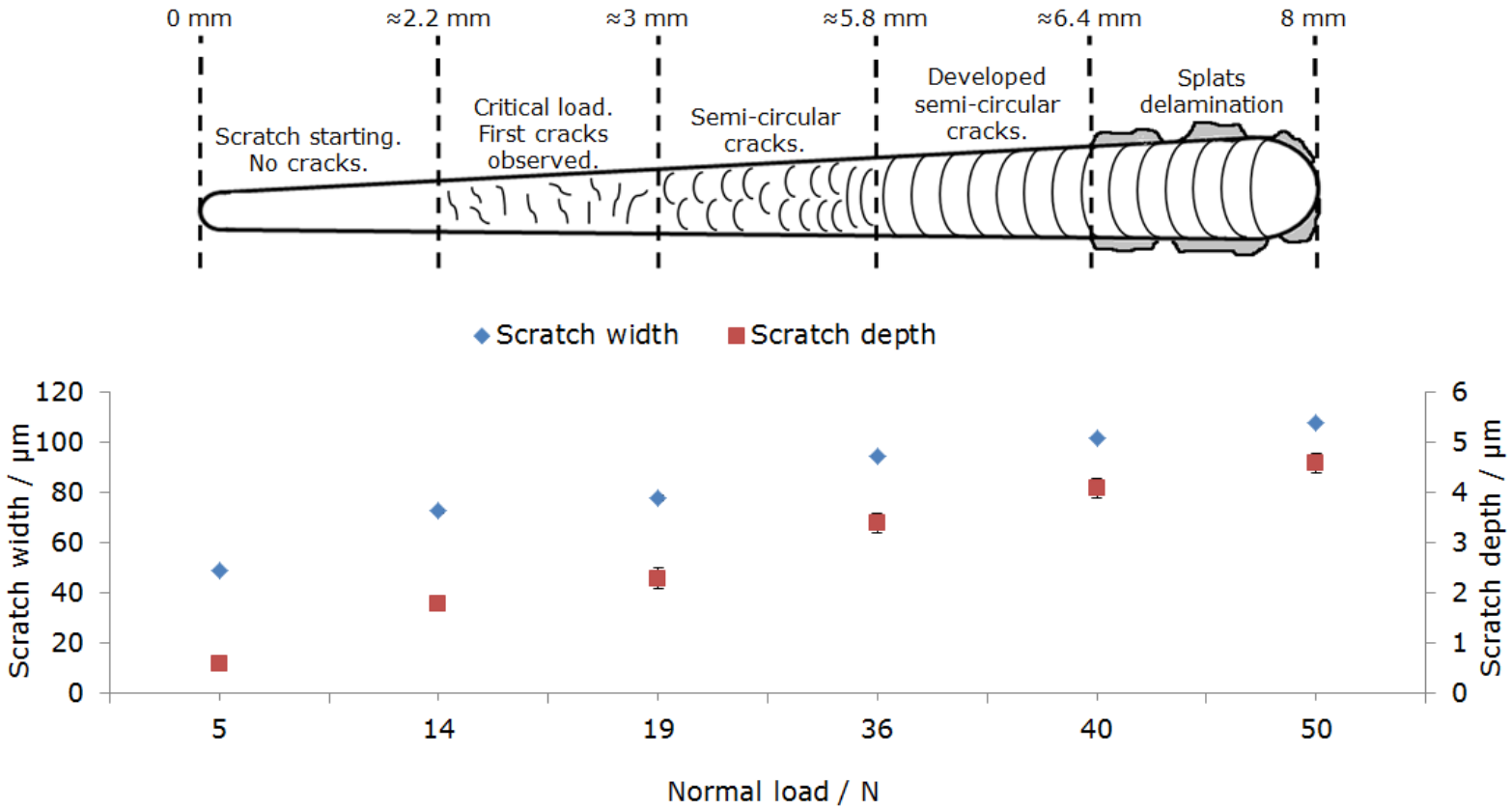

Figure 5-10: Schematic of scratch fracture mechanism map of WC-17CoF coating, (note: non-linear scale).

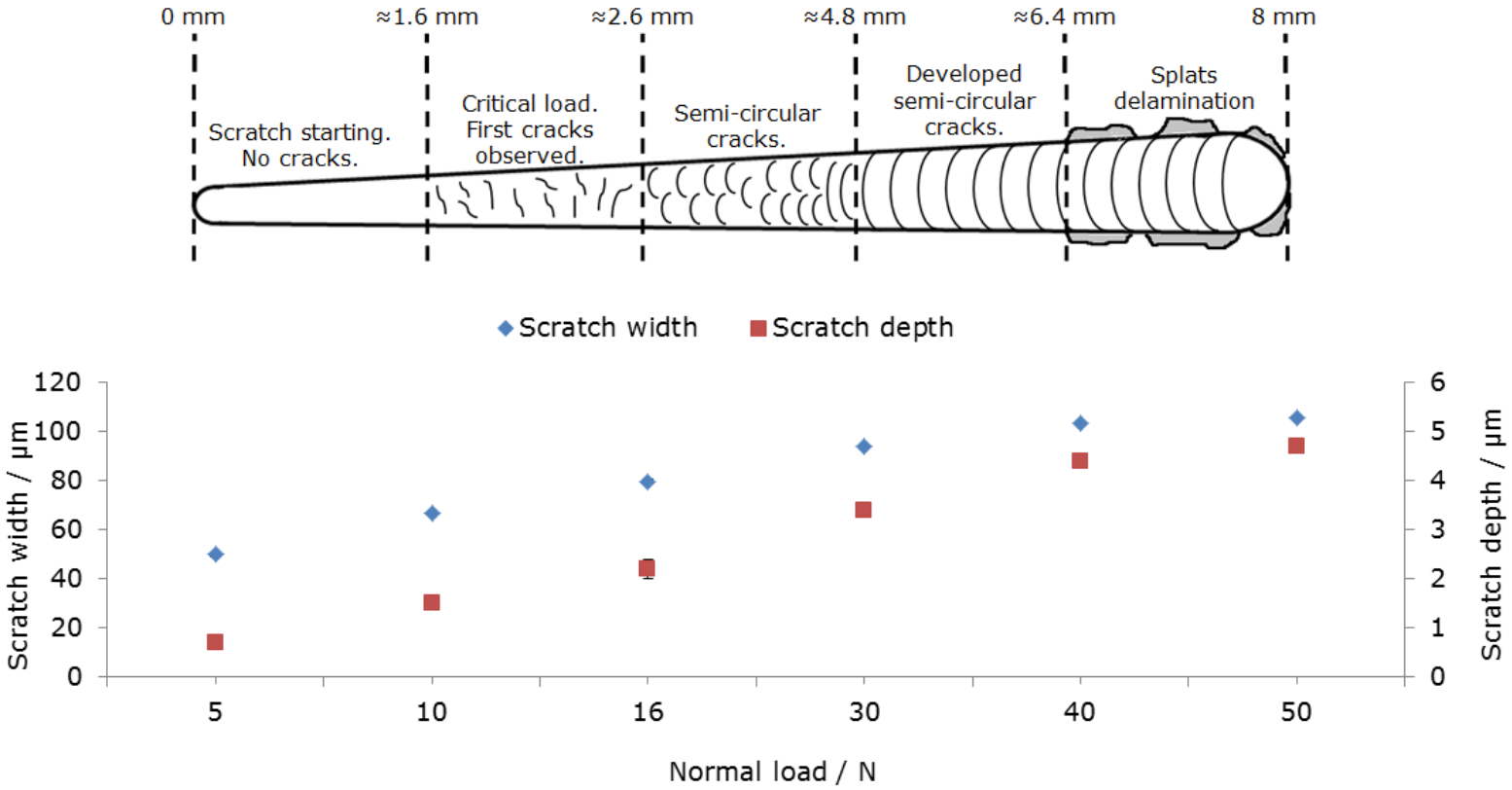

Figure 5-11: Schematic of scratch fracture mechanism map of WC-17CoC coating, (note: non-linear scale).

Starting zone

The scratch starting section is begins at the starting point of the scratch, with preload 5 N, and carrys on until observation of the first crack on the scratch track. There are no cracks observed in the scratch track in both WC-17CoF and WC-17CoC coatings at this stage. The scratch width and depth were about 50 µm and 0.6 µm respectively for both coatings. Figure 5-12 illustrates the 3D Bruker ContourGT Optical Profiler images of the scratch profile at the starting zone for both of WC-17CoF and WC-17CoC coatings.

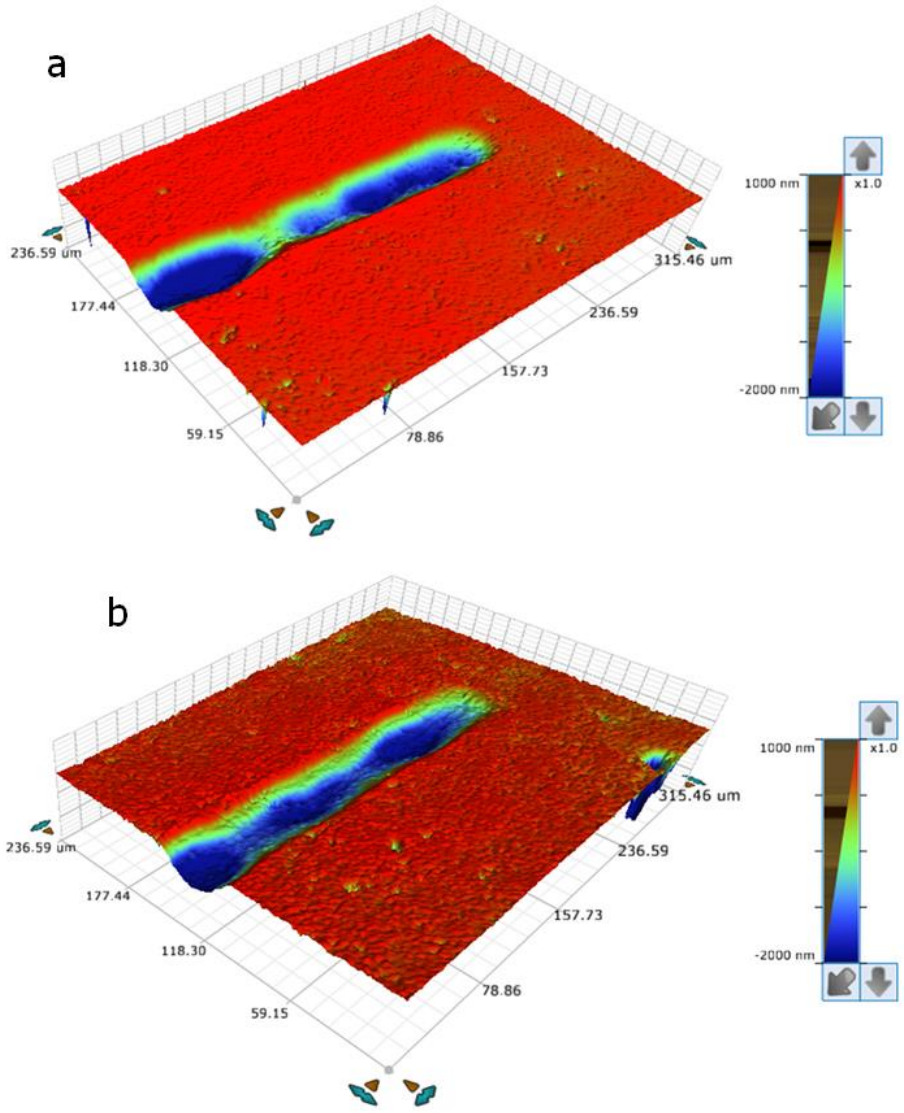

Figure 5-12: The 3D Bruker ContourGT Optical Profiler images show the profile of scratch starting zone (a) WC-17CoF coating and (b) WC-17CoC coating.

Critical load zone

Critical load is the normal load where the initial cracks in the scratch track can be observed. These primary cracks have been seen when the normal load (critical load) exceeds 14 N for WC-17CoF coating scratch, at approximately 2.2 mm from the scratch starting point (see Figure 5-10). In contrast, these initial cracks have been observed on the scratch track of the WC-17CoC coating when the normal load, (critical load), go over 10 N, around 1.6 mm from the scratch starting point (see Figure 5-11).

These primary cracks are demonstrated in the 2D Bruker ContourGT Optical Profiler images in Figure 5-13 (illustrated by the arrows). The average width and depth of the scratch through this section are nearly 73 µm and 1.8 µm, respectively for WC-17CoF coating scratch, whereas with WC-17CoC coating scratch these values were about 67 µm and 1.5 µm respectively.

The SEM-BSE images in Figure 5-14 demonstrate the mode of these initial narrow intergranular cracks which are short and have no specific shape in both coatings. Moreover, few cracks have been noted in the WC grains with WC-17CoC coating in this section.

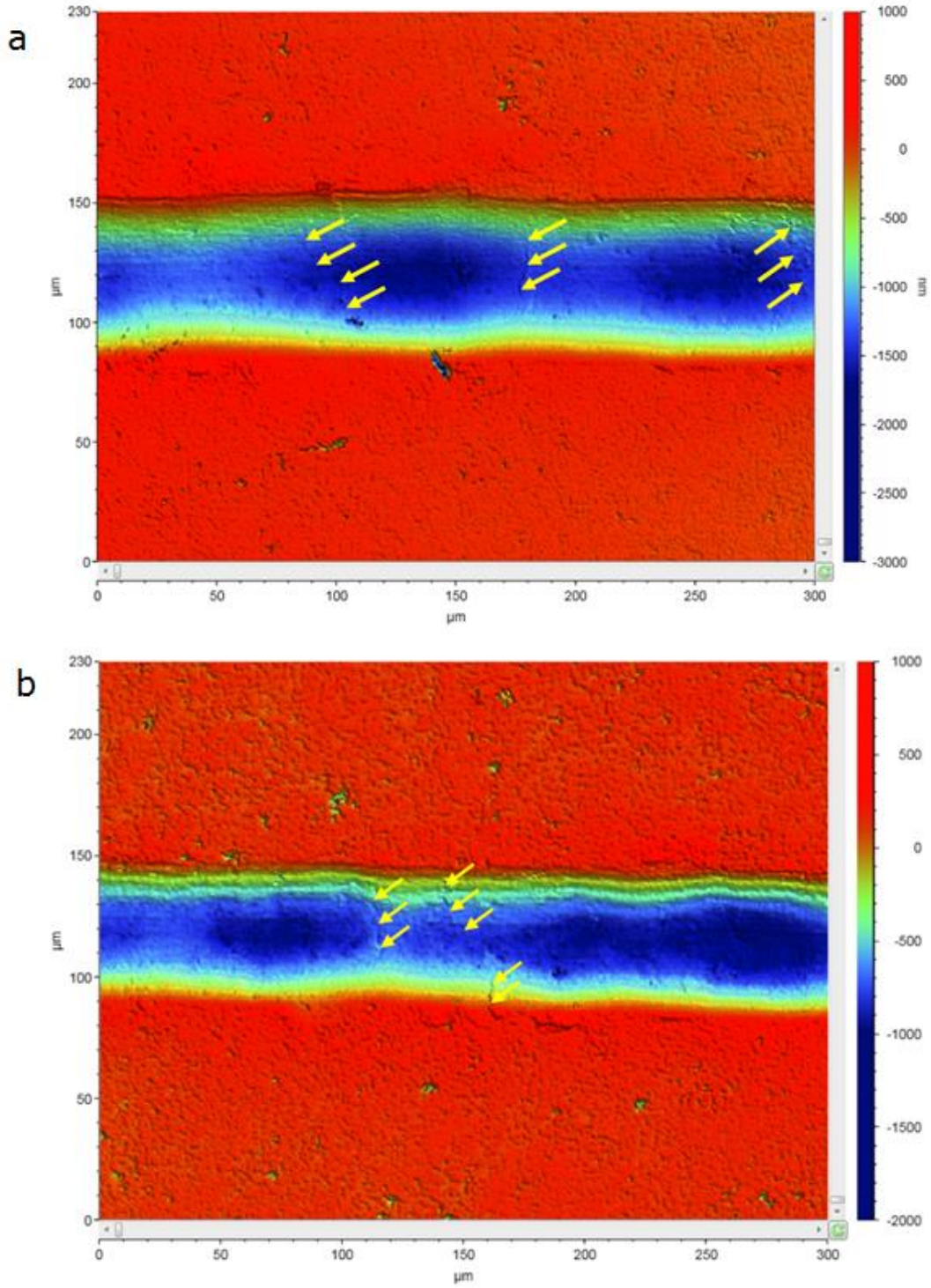

Figure 5-13: The 2D Bruker ContourGT Optical Profiler images of the critical load section illustrate the primary cracks of the scratch (arrows). (a) WC-17CoF coating scratch. (b) WC-17CoC coating scratch.

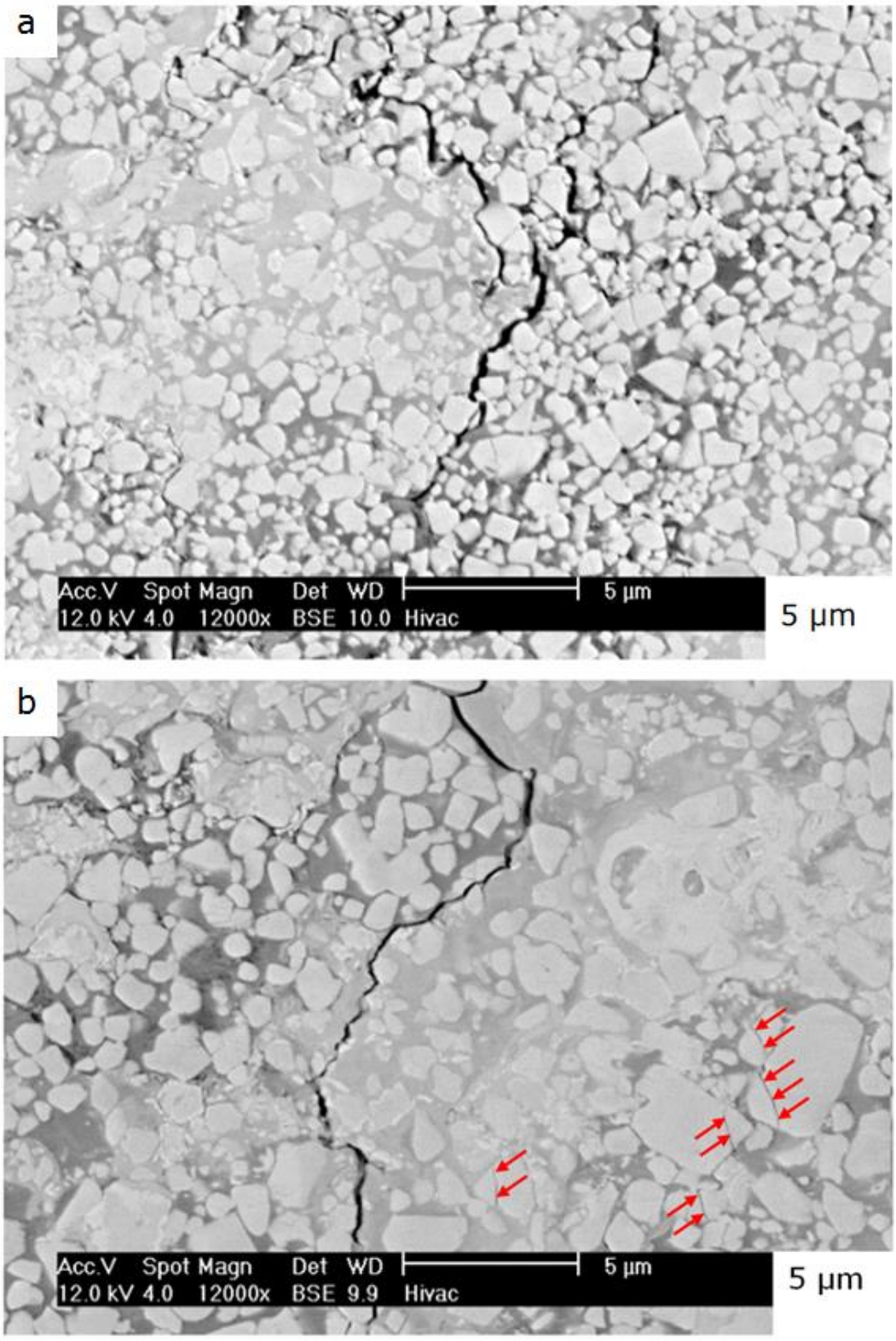

Figure 5-14: The SEM-BSE images demonstrate the mode of the initial narrow intergranular cracks. (a) WC-17CoF coating. (b) WC-17CoC coating, some cracks in the WC grains observed with this coating (red arrows).

Semi-circular cracks zone

The scratch cracks increased as the normal load is increased. These cracks take semi-circular shape almost 3 mm from the starting point of the scratch of WC-17CoF coating, where the normal load is exceed 19 N (see Figure 5-10). These semi-circular cracks are noted with the scratch of WC-17CoC coating as the normal load go over 16 N, about 2.6 mm from the starting point of this scratch (see Figure 5-11).

The average width and depth of the WC-17CoF coating scratch in this section were approximately 78 µm and 2.3 µm respectively, while with WC-17CoC coating scratch the average width and depth were about 80 µm and 2.2 µm in order.

The high magnification SEM-BSE images in Figure 5-15 exhibited that these narrow intergranular semi-circular cracks travel through the matrix in both coatings. There are no cracks observed in the WC grains in WC-17CoF coating scratch through this section. However, with WC-17CoC coating the cracks in the WC grains have been very obvious.

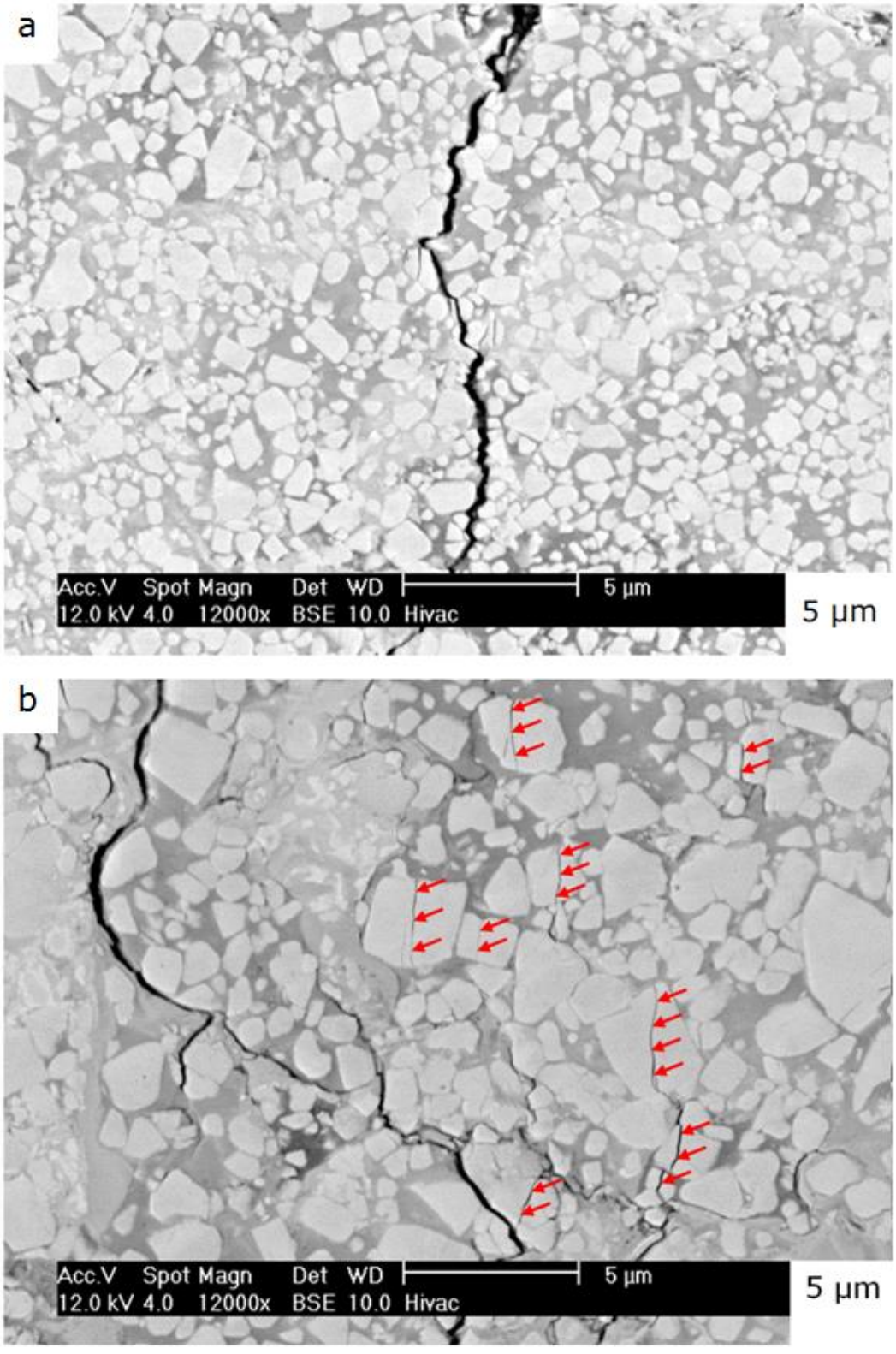

Figure 5-15: The SEM-BSE images exhibited the narrow intergranular semi-circular cracks travelling through the matrix. (a) WC-17CoF coating, no cracks observed in the WC grains. (b) WC-17CoC coating, the cracks in the WC grains are obvious (red arrows).

Developed semi-circular cracks section

The intensity of the semi-circular cracks has increased with the progressive normal load and these cracks have developed to cover the whole scratch width. When the normal load has exceed 36 N, nearly at 5.8 mm from the starting point, the developed semi-circular cracks were observed in the scratch track of the WC-17CoF coating (see Figure 5-10). While with WC-17CoC coating scratch, these developed semi-circular cracks appeared when the normal load has exceeds only 30 N, approximately 4.8 mm from the starting point of the scratch (see Figure 5-11). The average scratch width and depth at this section for WC-17CoF coating have been about 95 µm and 3.4 µm respectively. Whereas for WC-17CoC coating, they were about 94 µm and 3.4 µm on average.

The SEM-BSE images in Figure 5-16 exhibited the mode of these developed semi-circular cracks in this zone, they travel through the matrix and the carbides grains and propagated through the entire scratch width in both WC-17CoF and WC-17CoC coatings.

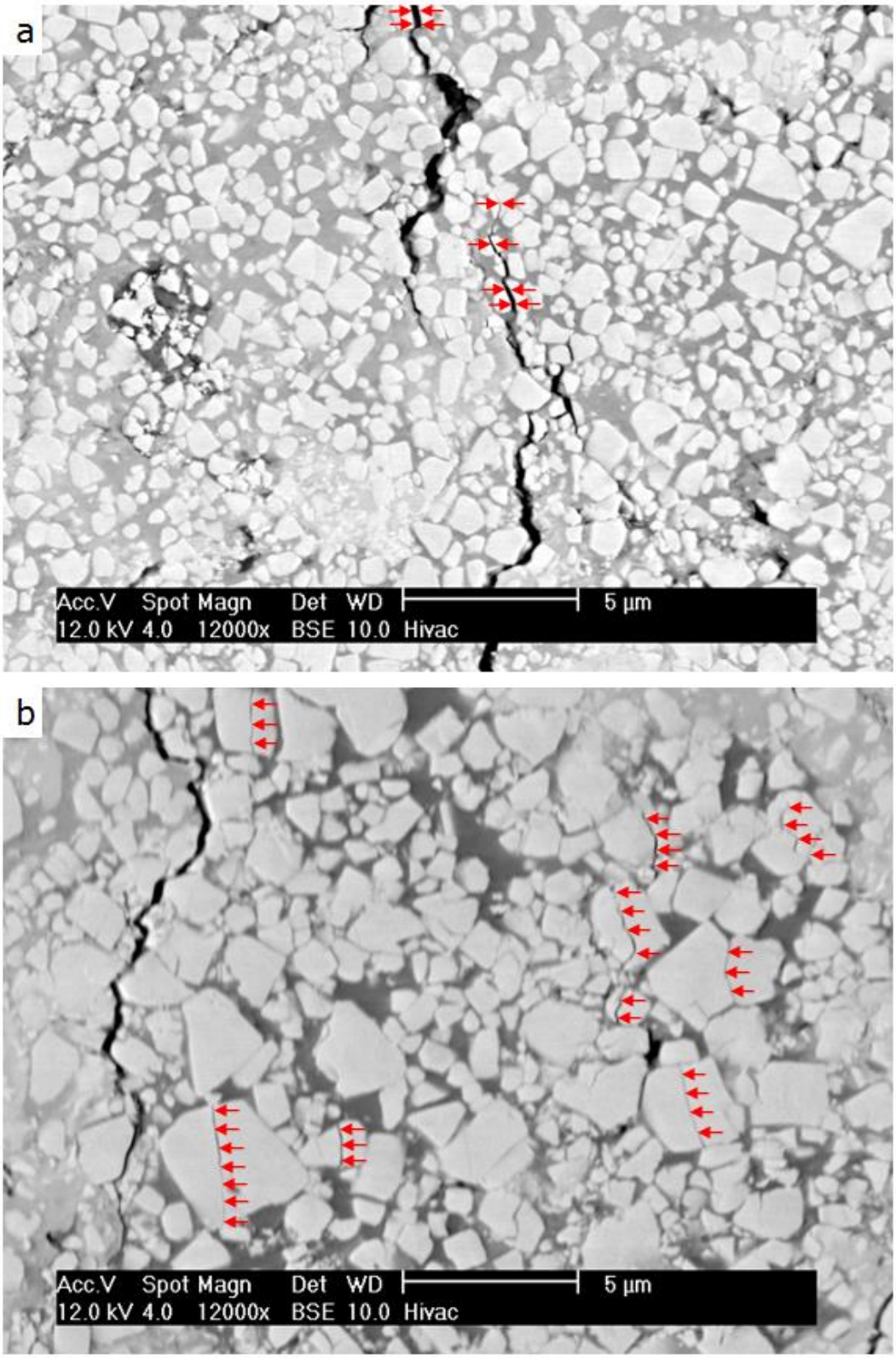

Figure 5-16: The SEM-BSE images demonstrate the developed semi-circular cracks (a) WC-17CoF coating, no cracks observed in the WC grains and (b) WC-17CoC coating, the cracks in WC grains are obvious (red arrows).

Coating splats delamination zone

The delamination of the coating splats at the edges of the scratch track of both WC-17CoF and WC-17CoC coatings have been seen when the normal load has exceeded 40 N, about 6.4 mm from the starting point of the scratch of both coatings, (see Figure 5-10 and Figure 5-11).

Coating splats delamination and the cracks at this zone of the scratch are exhibited in the 2D Bruker ContourGT Optical Profiler images in Figure 5-17 for both WC-17CoF and WC-17CoC coatings. The average scratch width and depth at the end of the WC-17CoF coating scratch were about 108 µm and 4.6 µm respectively. However, these values at the end of the WC-17CoC coating scratch were about 106 µm and 4.7 µm in order.

The SEM images in Figure 5-18 show the coating splats delamination at the edges of the scratch and the cracks at this section. Coatings fracture behaviour is exhibited in the SEM high magnification images of both WC-17CoF and WC-17Co coatings. Developed semi-circular scratch cracks are travelling through the matrix and the WC grains on both coatings. There are no cracks in WC grains in the whole scratch track of WC-17CoF coating. In contrast, the cracks in WC grains of the WC-17Co coating scratch are very obvious throughout this zone of the scratch.

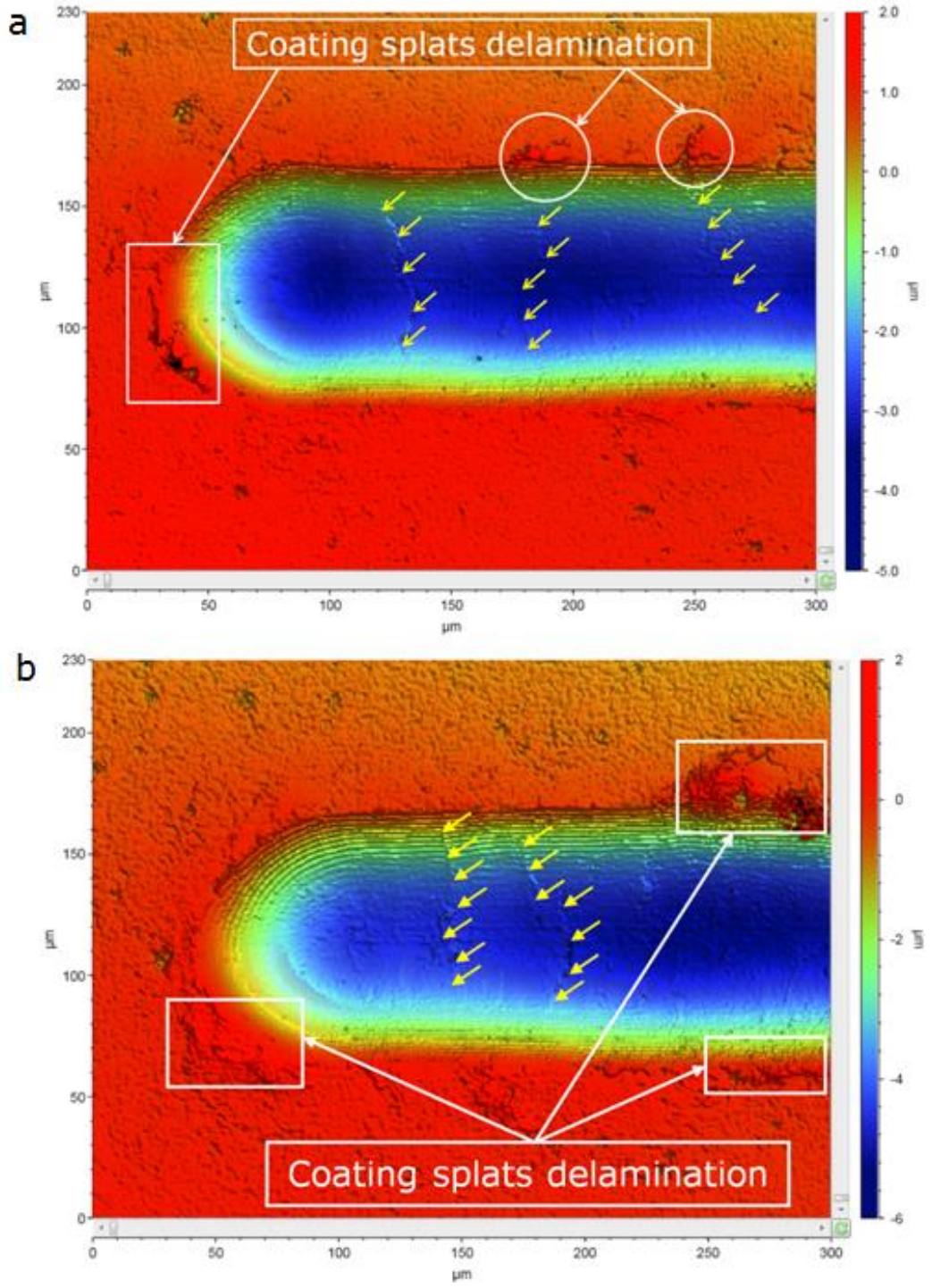

Figure 5-17: 2D Bruker ContourGT Optical Profiler images of coating splats delamination zone show the cracks at this zone and the coating splats delamination at scratch edges, (a) WC-17CoF coating and (b) WC-17CoC coating.

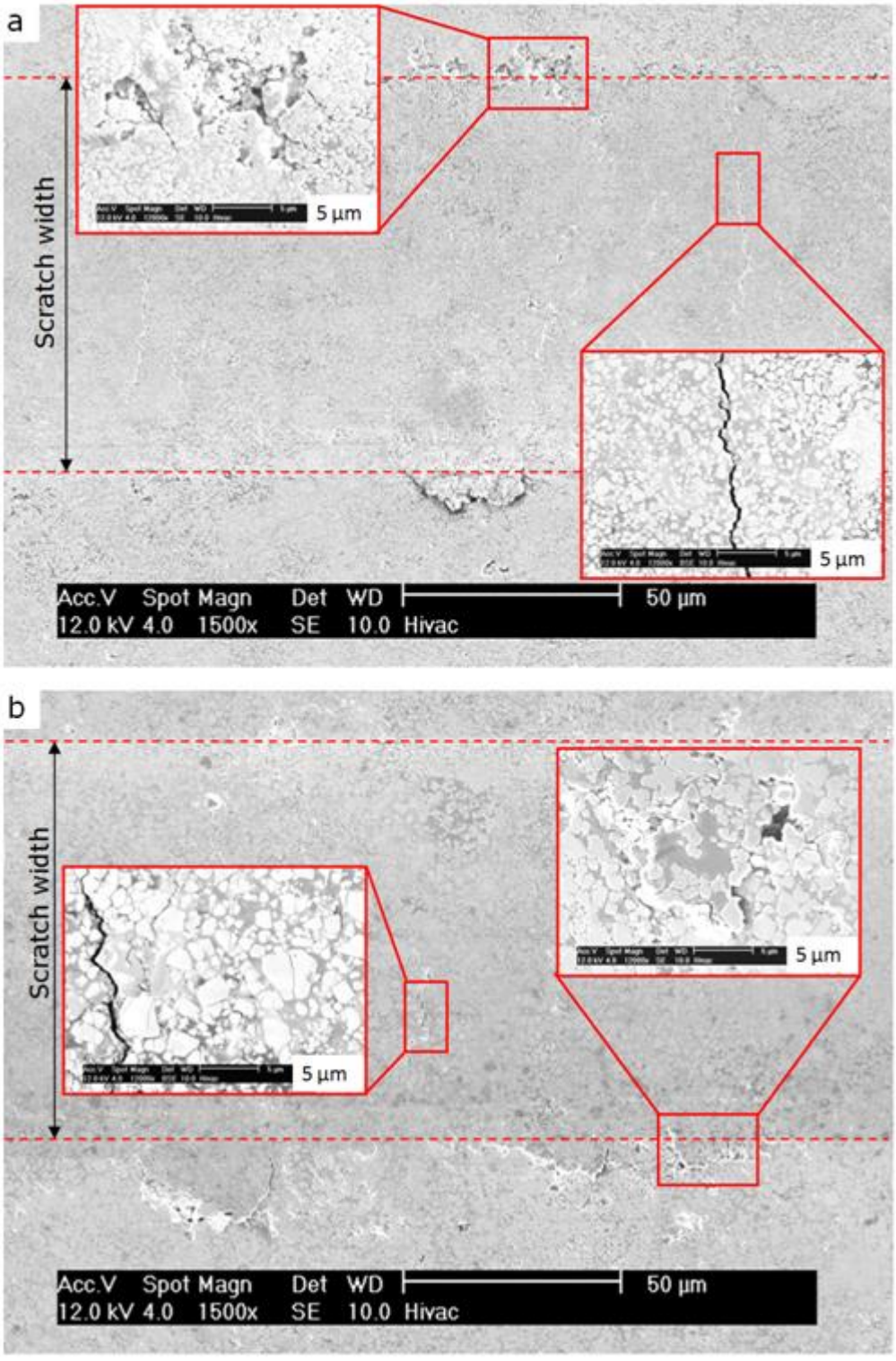

Figure 5-18: The SEM images show the coating splats delamination at the edges of the scratch and the cracks at this zone. The high magnification SEM images illustrate the coating fracture behaviour and the cracks modes. (a) WC-17CoF, no cracks in WC grains through this coating. (b) WC-17Co coating, the cracks in WC grains are very obvious.

5.1.4 Sliding wear behaviour

The results obtained from the ball-on-disc dry sliding wear test of both coatings, WC-17CoF and WC-17CoC, under different loads, are summarised in Table 5-4, ± values represent the standard error in the mean. The wear rate of both coatings WC-17CoF and WC-17CoC is illustrated in Figure 5-19 (plotted on log scale) versus the applied loads. The wear rate of the counterface WC-6Co balls sliding on coated discs (also plotted on a log scale) versus the applied loads is exhibited in Figure 5-20. Wear scars have been investigated by the SEM and by the optical profilometry (using a Bruker ContourGT Optical Profiler), to understand the wear behaviour. This investigation shows that there has been insignificant difference in the wear mechanism of both coatings. However, the WC-17CoF coating, as shown in Table 5-4, can withstand a higher applied load in the sliding wear test before the transition from mild to severe wear occurs.

Table 5-4: Results of dry sliding wear test of WC-17CoF and WC-17CoC coated discs and WC-6Co sintered balls.

Coating	Normal load N	Sliding distance m	Disc wear 10^{-6} mm^3	Disc wear rate 10^{-6} mm^3/N.m	Disc wear scar depth µm	Friction coefficient µ	Ball wear rate 10^{-6} mm^3/N.m
WC-17CoF	141	1500	707	0.0033±0.0005	0.29	0.08	0.009±0.002
	212	1500	1357	0.0043±0.0005	0.35	0.15	0.009±0.001
	282	300	3332542	52.5±3.7	35.00	0.13	5.1±0.5
	353	300	7006706	66.2±5.3	60.00	0.11	5.7±0.6
WC-17CoC	141	1500	583	0.0028±0.0002	0.25	0.08	0.009±0.001
	212	300	490526	7.7±1.5	13.40	0.11	0.7±0.2
	282	225	5926227	93.3±10.3	54.38	0.13	6.7±0.9
	353	50	1443221	81.8±8.2	21.94	0.09	3.6±0.4

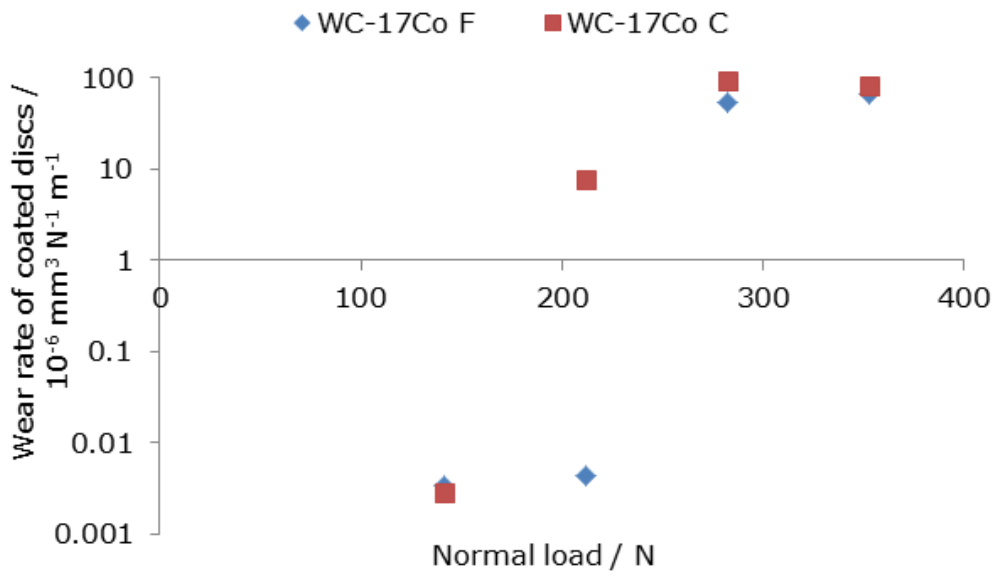

Figure 5-19: Plot of wear rate of WC-17CoF and WC-17CoC coatings. The error bars represent the standard error in the mean.

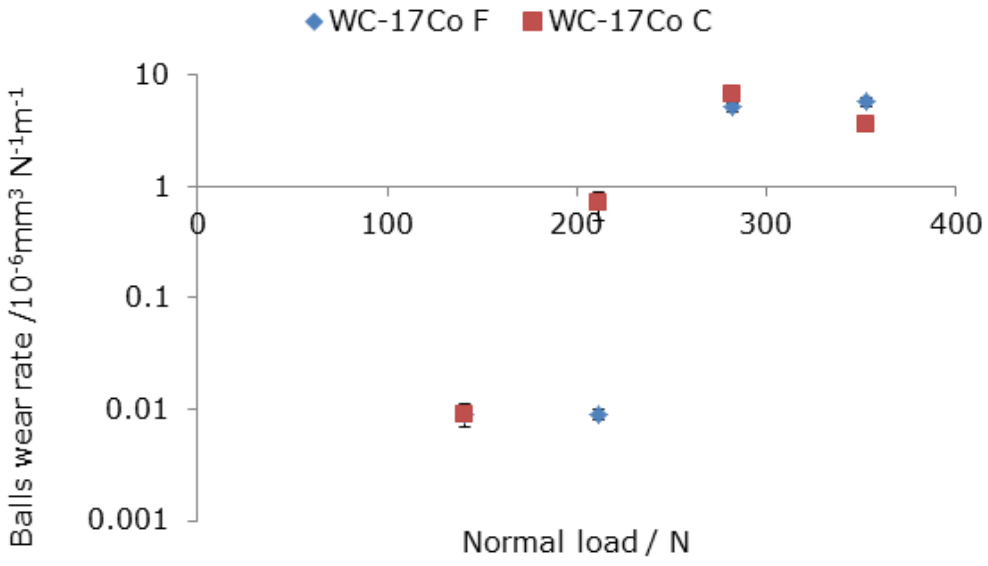

Figure 5-20: Plot of wear rate of sintered balls WC-6Co sliding against WC-17CoF and WC-17CoC coated discs. The error bars represent the standard error in the mean.

5.1.4.1 Wear behaviour of WC-17CoF coating

The plan view of WC-17CoF coating surfaces worn under loads of 212 N and 282 N are illustrated in Figure 5-21 and Figure 5-22 respectively. These loads have been selected since the transition from mild to severe wear has happened between them.

The top view of the surface of the WC-17CoF coating worn under a load below the transition load (212 N) is exhibited in Figure 5-21. The worn surface of the coating exhibits a very smooth surface as shown in low magnification SEM-SE image in Figure 5-21a. The wear track is around 0.9 mm in width after a sliding distance of 1500 m. Figure 5-21b shows a SEM-BSE image from the middle of the wear track. It is found that transfer layers had been generated during the dry sliding test (grey colour areas) and exist in a number of localised regions. Selected area "c" in Figure 5-21b is further characterised in the high magnification SEM-SE image presented in Figure 5-21c which indicates the generation of oxide layers during wear test. The selected area "d" in Figure 5-21c is illustrated in higher magnification SEM-BSE image in Figure 5-21d and indicates that very narrow intergranular cracks (indicated by red arrows) propagate in the coating layer during the mild wear of WC-17CoF coating. The polished surface of the WC grains (flat surface) indicates that during sliding of the WC-17CoF coating under mild wear conditions, the coating does not exhibit severe fracture leading to material loss. Furthermore, Figure 5-21d does not show any cracks in WC grains themselves.

A cross-section has been made through the mild wear track to investigate the wear behaviour of WC-17CoF coating. Figure 5-21e shows the wear scar cross-section following sliding wear testing below the transition load (212 N); a thick localised transfer layer can be observed on the top surface of the section. Selected area “f” in Figure 5-21e is characterised in higher magnification SEM-BSE imaging in Figure 5-21f, which shows the localised thick tribofilm layer (oxide layer) on the top surface of the worn surface of WC-17CoF following mild wear. No subsurface cracks are observed in the cross-section of WC-17CoF coating following sliding wear testing under mild conditions.

The energy dispersive X-ray analysis (EDX) of the transferred layer, shown in Figure 5-21g indicates the presence of tungsten, cobalt, and oxygen. The increase of the weight percent of the oxygen in the transferred layer provides evidence that this layer is an oxide layer.

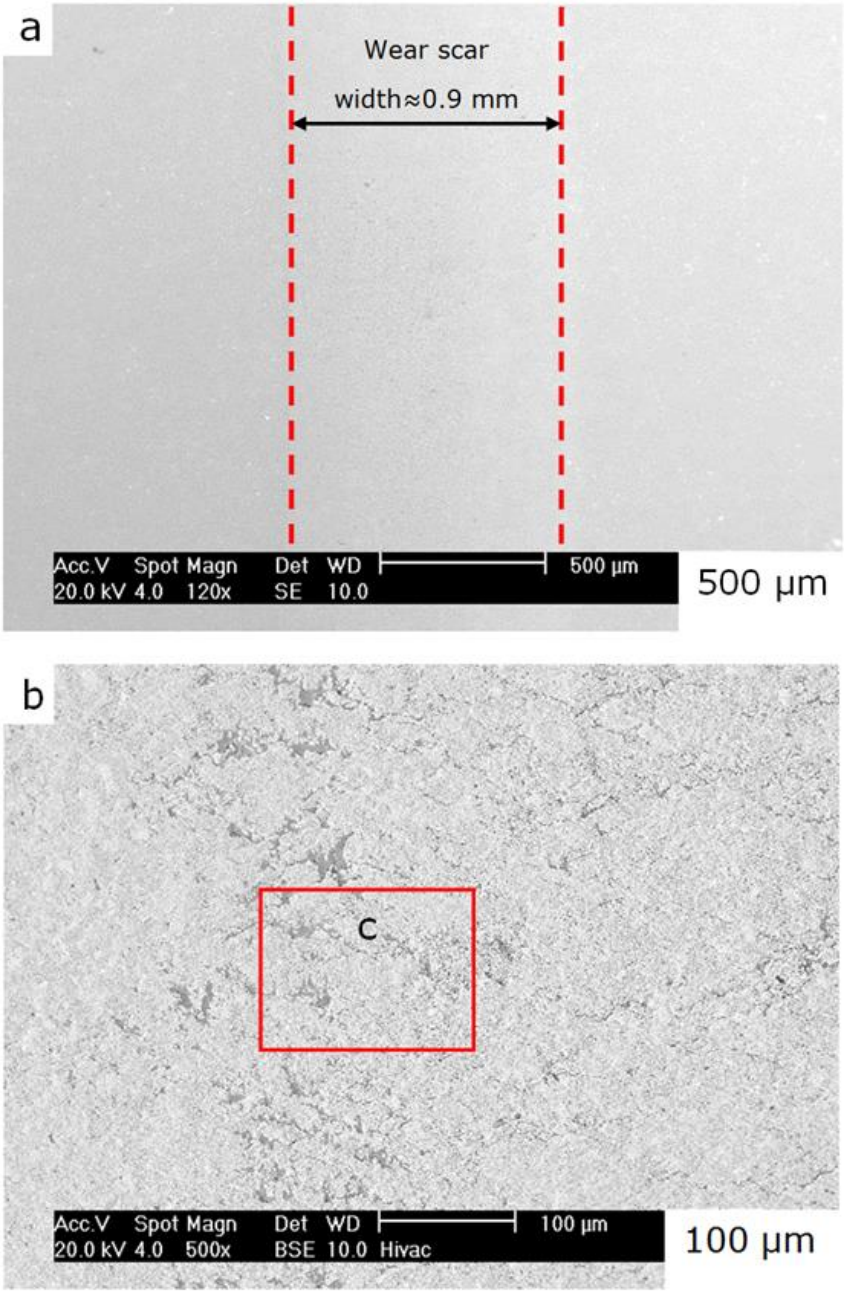

Figure 5-21: Mild wear behaviour of WC-17CoF coating. (a) Top view of wear scar of WC-17CoF coating worn under normal load of 212 N and (b) SEM-BSE image taken from the middle of the wear track shows the localised oxide layers (grey colour areas). Sliding direction is from top to bottom.

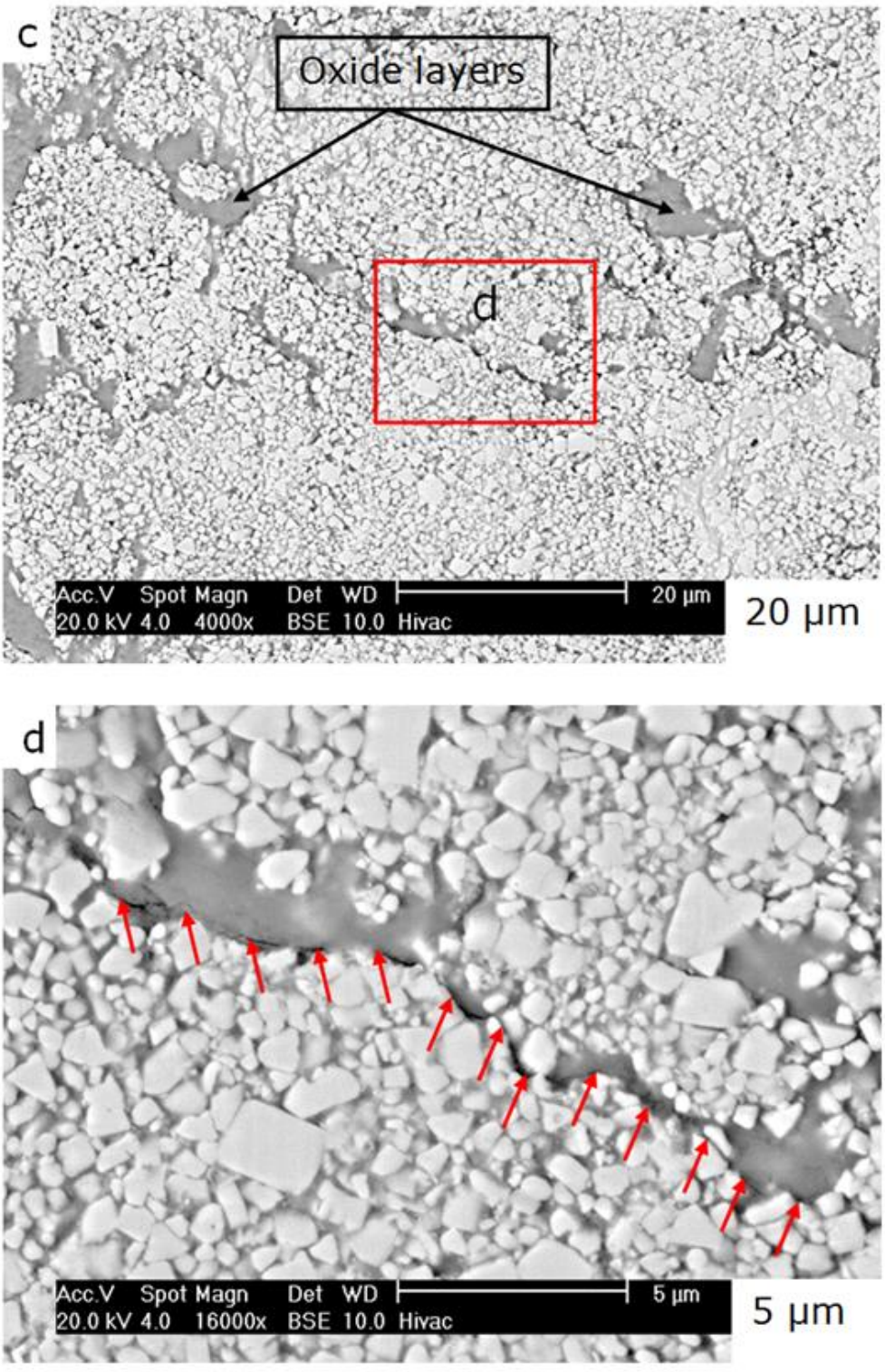

Figure 5-21 (Cont.): Mild wear behaviour of WC-17CoF coating. (c) SEM-BSE image showing the oxide layers and narrow cracks on the worn surface of WC-17CoF coating. (d) High magnification SEM-BSE of selected area "d" shows narrow intergranular crack propagated in the worn coating surface during the mild wear (red arrows). No cracks in WC grains themselves are observed.

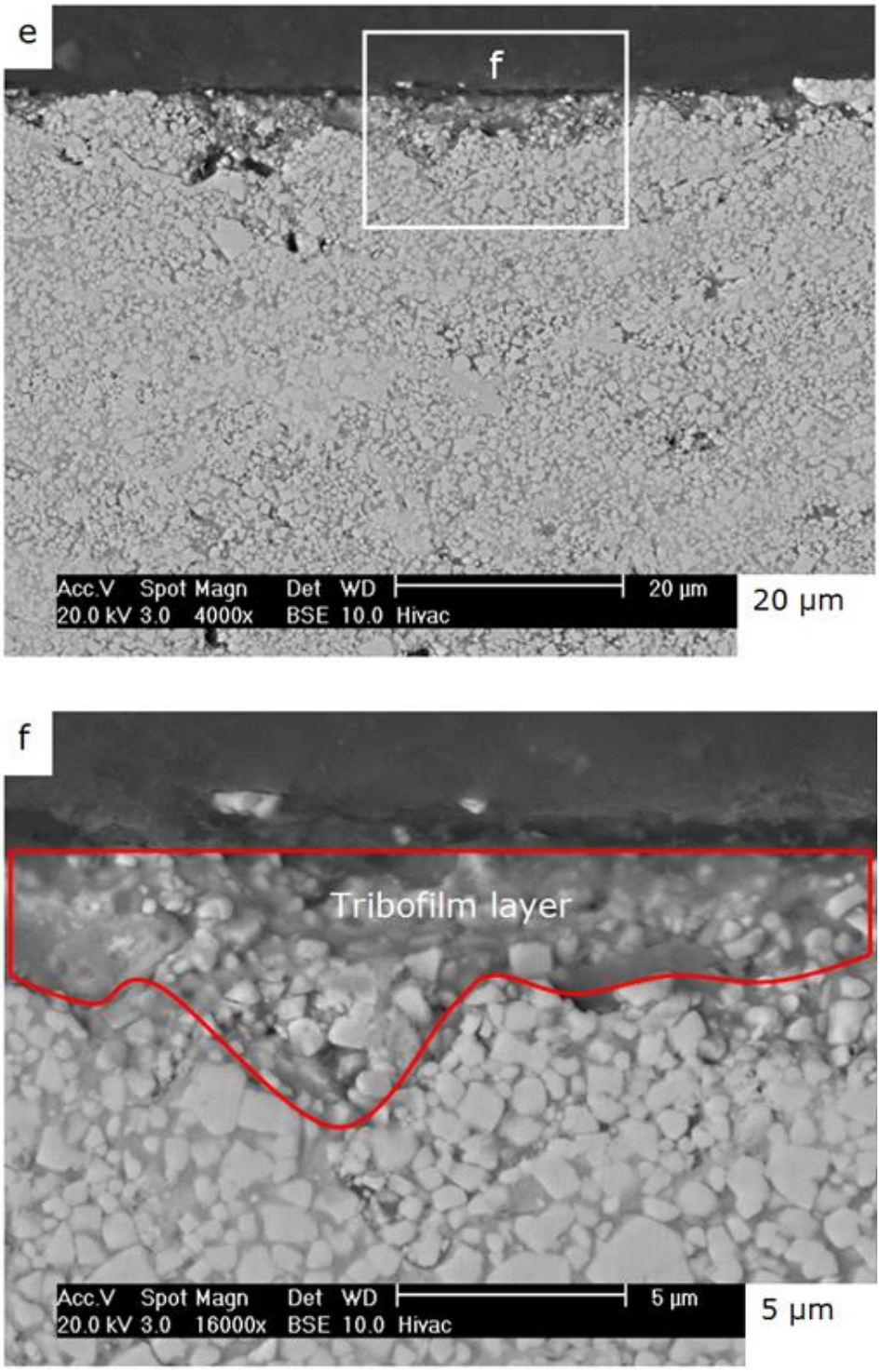

Figure 5-21 (Cont.): Mild wear behaviour of WC-17CoF coating. (e) Cross-section through the wear track of WC-17CoF coating during mild wear (normal load = 212 N) shows the localised oxide layer. There are no subsurface cracks observed. (f) High magnification SEM-BSE image of selected area "f" showing the tribofilm layer on the top worn surface of WC-17CoF coating. No cracks in WC grains themselves are observed.

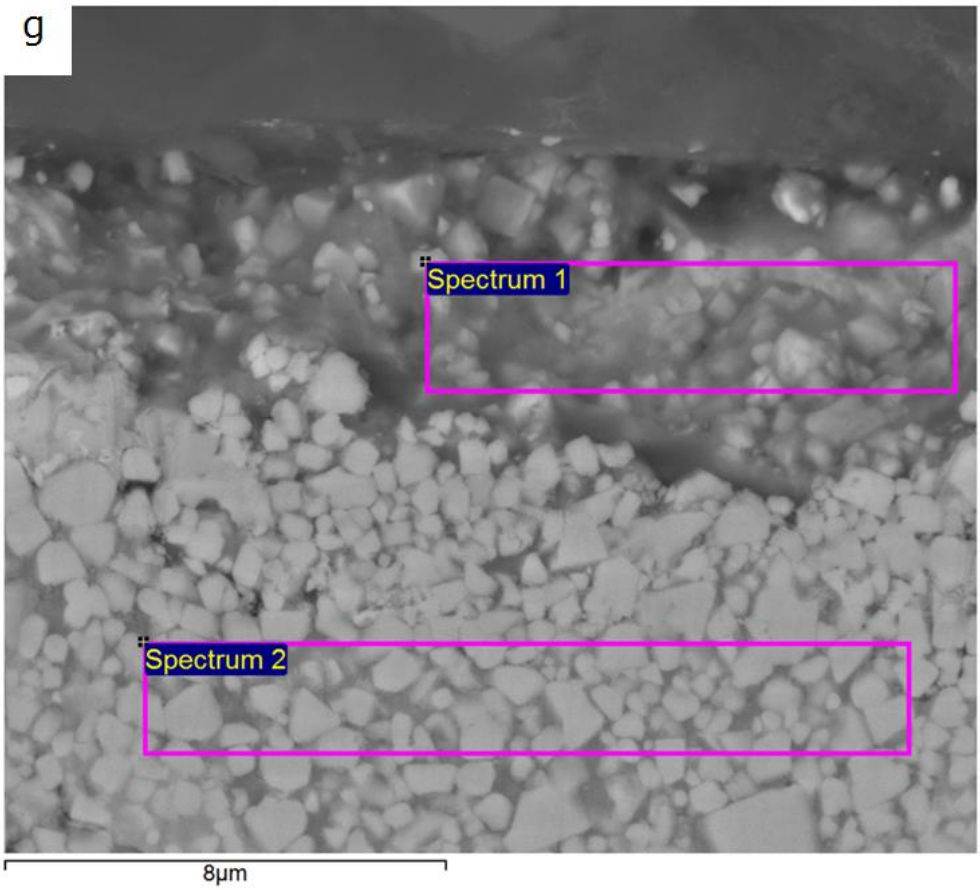

Spectrum	O wt%	Co wt%	W wt%
Spectrum 1	15	14	71
Spectrum 2	1	18	81

Figure 5-21 (Cont.): Mild wear behaviour of WC-17CoF coating. (g) EDX analysis of transfer layer (spectrum 1). The increase in the oxygen weight percent indicates that this transfer layer is an oxide-based debris layer.

The surface of the WC-17CoF coated discs worn under normal load of 282 N exhibits more severe wear as illustrated in low magnification SEM-SE image in Figure 5-22a. The wear track has developed to a width of about 2.3 mm, after a sliding distance of only 300 m. The SEM-SE image in Figure 5-22b is taken from the middle of the wear track, and indicates very severe wear, with the transfer layer having significant coverage of the overall wear scar area. The selected area "c" in Figure 5-22b is characterised in a higher magnification SEM-SE image in Figure 5-22c which shows the worn coating surface significantly covered by the brittle oxide-based debris layer. The angular WC grains in high magnification SEM-BSE in Figure 5-22d indicate that the top worn surface has experienced some fracture.

To examine the wear behaviour of WC-17CoF coating following severe wear, a cross-section has been made through the wear scar. Figure 5-22e shows the wear scar cross-section following sliding above the transition load (282 N); the figure shows thin transfer layer covering the whole top worn coating surface. Selected area “f” in Figure 5-22e is characterised in the higher magnification SEM-BSE image in Figure 5-22f which shows a thin tribofilm layer (oxide-based debris layer). There is little evidence for subsurface cracking; moreover, there is no evidence for significant cracking in the WC grains themselves.

The results from the energy dispersive X-ray analysis (EDX) of the transferred layer, presented in Figure 5-22g indicate the existence of tungsten, cobalt, and oxygen. The increase of the oxygen weight percent in the transferred layer indicates that this layer is an oxide layer.

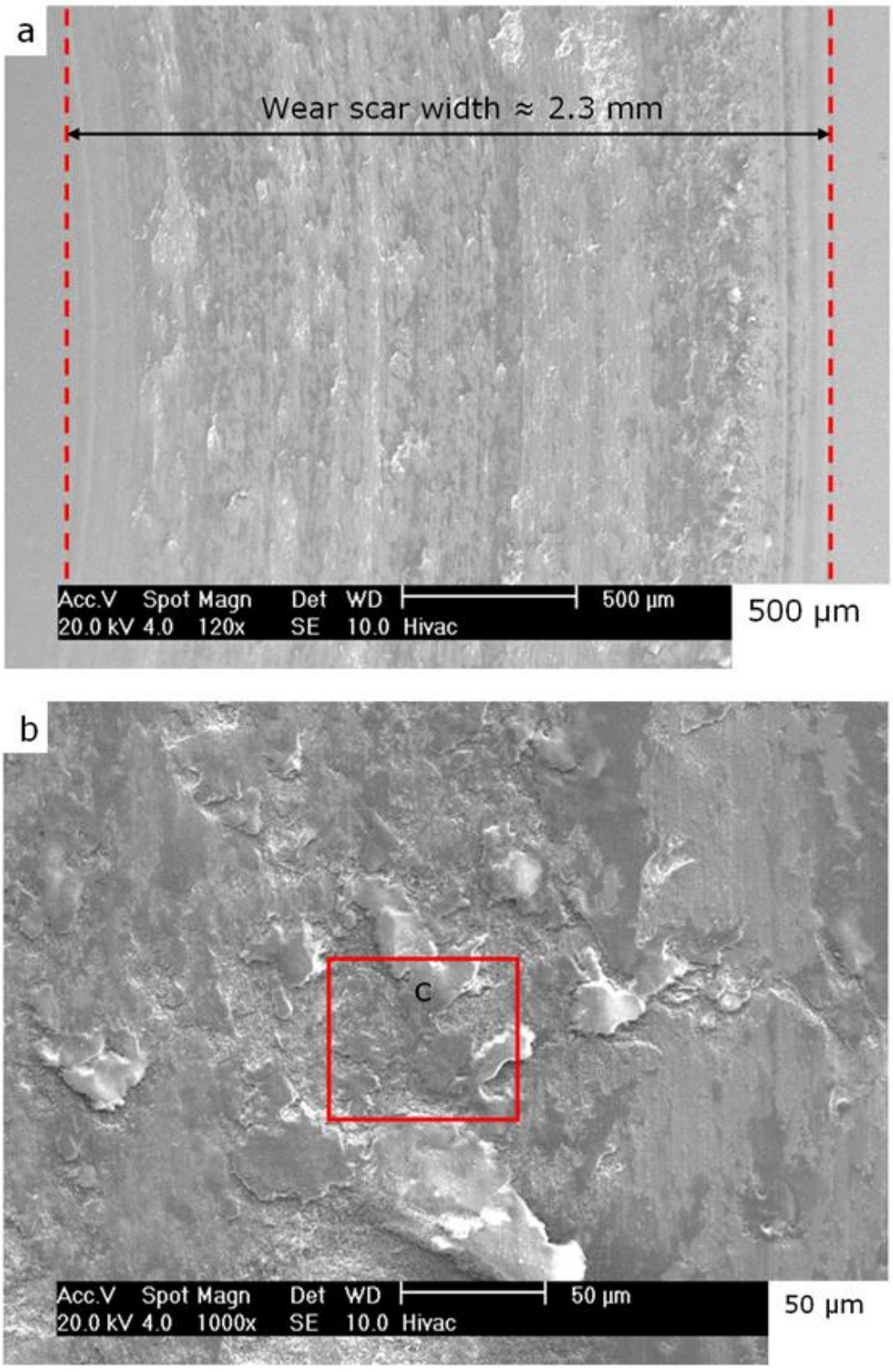

Figure 5-22: Severe wear behaviour of WC-17CoF coating. (a) Top view of wear scar of WC-17CoF coating worn under normal load 282.24 N. (b) SEM-BSE image taken from the middle of the wear track shows very severe wear. Sliding direction is from top to bottom.

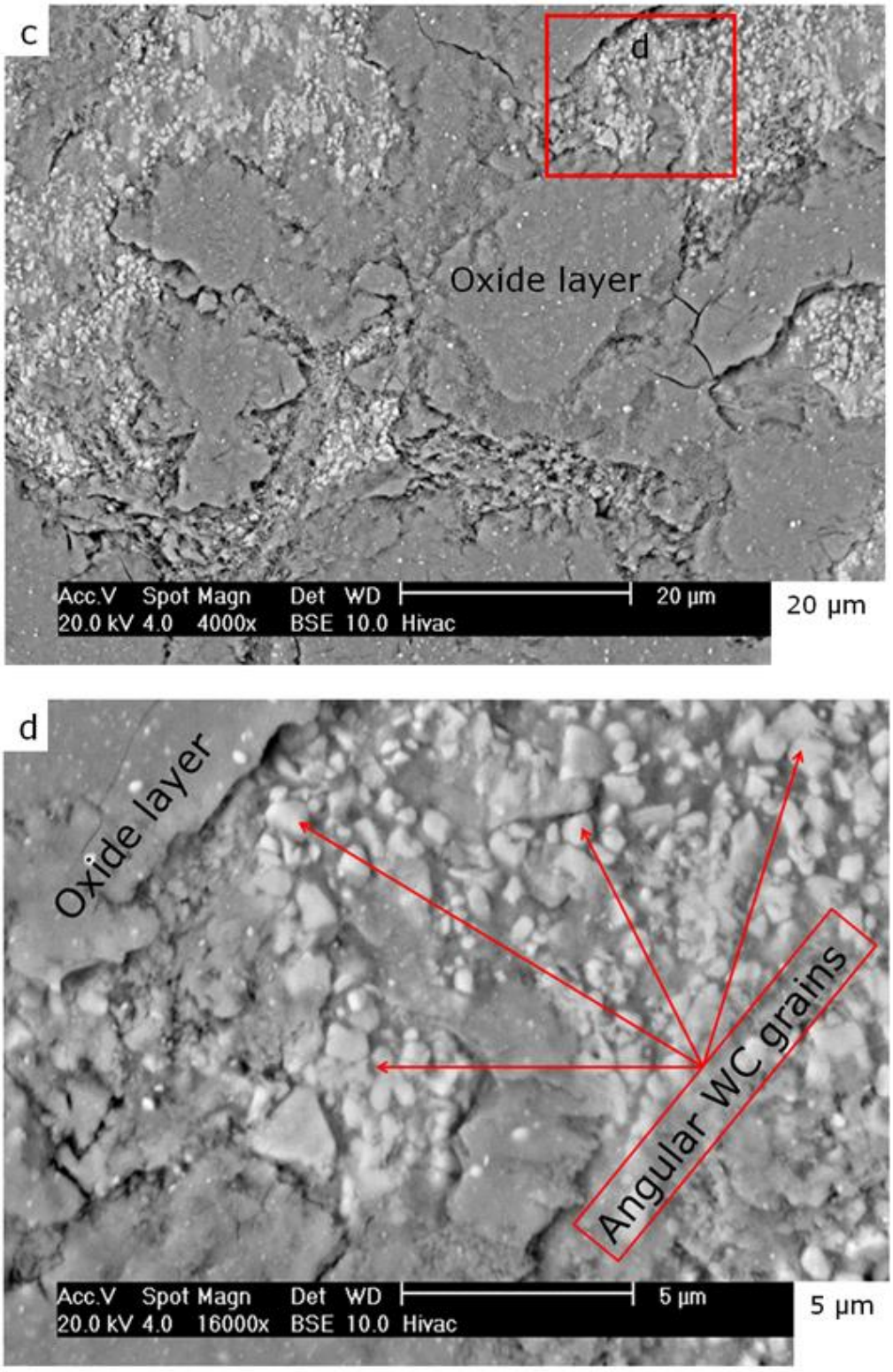

Figure 5-22 (Cont.): Severe wear behaviour of WC-17CoF coating. (c) SEM-BSE image of selected area "c" shows the worn coating surface covered by the brittle oxide layer. (d) High magnification SEM-BSE image of selected area "d" illustrates the angular WC grains which indicate the fracture of the brittle oxide layer from the top worn surface.

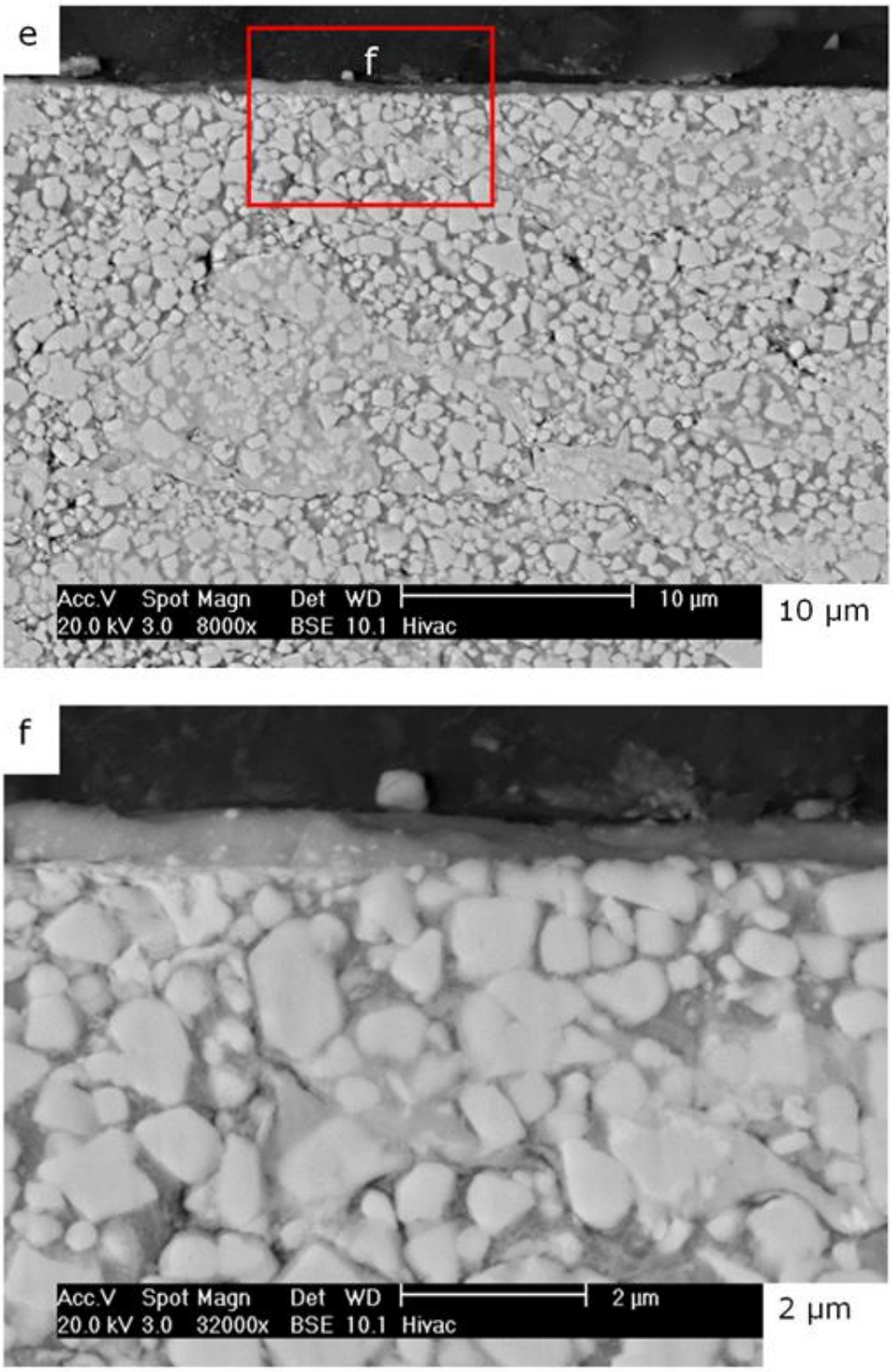

Figure 5-22 (Cont.): Severe wear behaviour of WC-17CoF coating. (e) Cross-section of wear track of the coating under normal load of 282.24 N showing a thin oxide layer covering the whole worn surface. There are no subsurface cracks observed. (f) High magnification SEM-BSE image of selected area "f" shows the thin tribofilm layer on the top worn surface of WC-17CoF coating. No cracks in the WC grains themselves are observed.

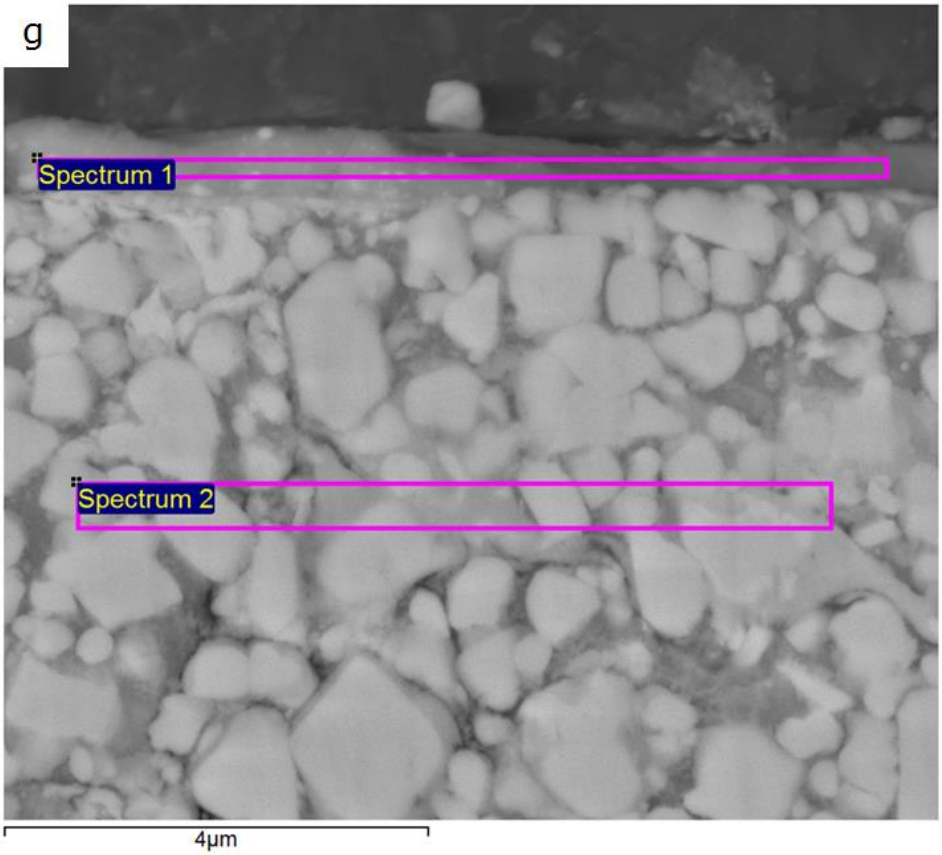

Spectrum	O wt%	Co wt%	W wt%
Spectrum 1	24	12	64
Spectrum 2	1	17	82

Figure 5-22 (Cont.): Severe wear behaviour of WC-17CoF coating. (g) EDX analysis of transfer layer. The increase in the oxygen content is indicating that this transfer layer is an oxide layer.

The morphology of the wear debris of which is formed from the WC-17CoF coating worn under normal load of 282 N (above the transition load) is illustrated in Figure 5-23. The wear debris consists of plate-like debris particles which have resulted from the delamination of the brittle oxide layer from the disc surface. Agglomerated fine particles can also be observed. The wear debris formed during mild wear of the same coating material is very small in volume, and, as such, it has not been amenable to collection and analysis.

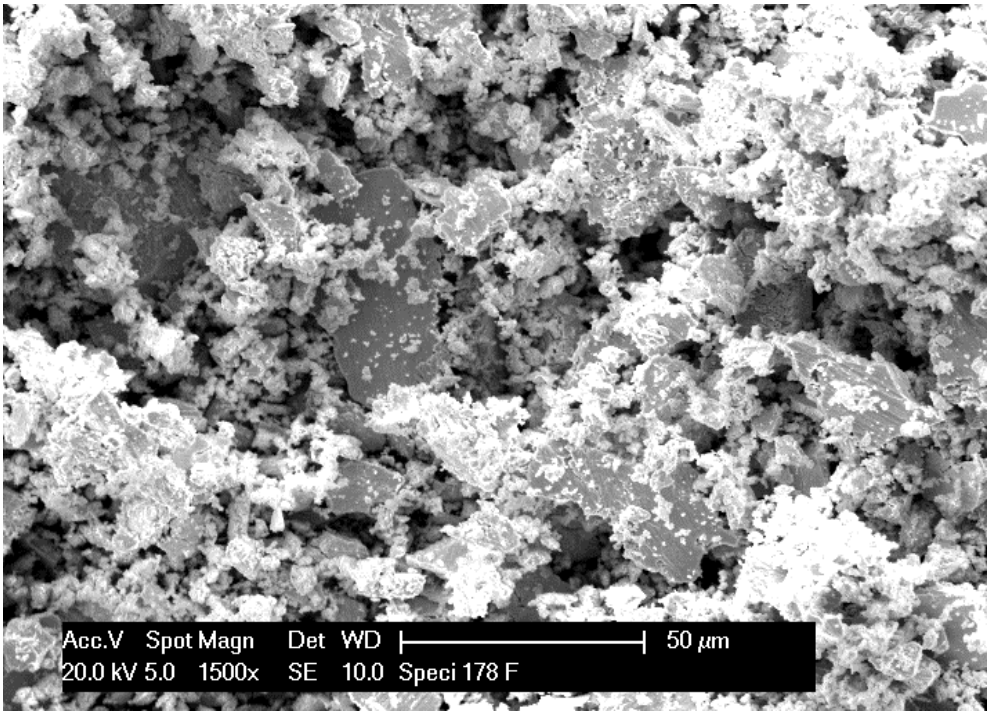

Figure 5-23: The wear debris from the WC-17CoF coated disc worn under severe wear conditions (282 N).

The wear scars on the WC-17CoF coating for both mild and severe wear have been investigated by optical profilometry (using a Bruker ContourGT Optical Profiler). The 2D Bruker image of mild wear sample, below the transition load (212 N), is exhibited in Figure 5-24a, and indicates low depths of material removal. The 2D Bruker image of the same material worn in severe conditions, (i.e. above the transition load (282 N), is illustrated in Figure 5-24b which shows high depths of material removal, of the order of tens of micro-meters. Figure 5-24c illustrates the wear scar profile of WC-17CoF coating with mild wear, below the transition load (212 N), where the wear scar depth and width are about 0.35 μm and 0.9 mm respectively. The wear scar profile with severe wear, above the transition load (282 N), is demonstrated in Figure 5-24d showing that the wear scar depth and width are about 35 μm and 2.3 mm, respectively after only 300 m sliding distance.

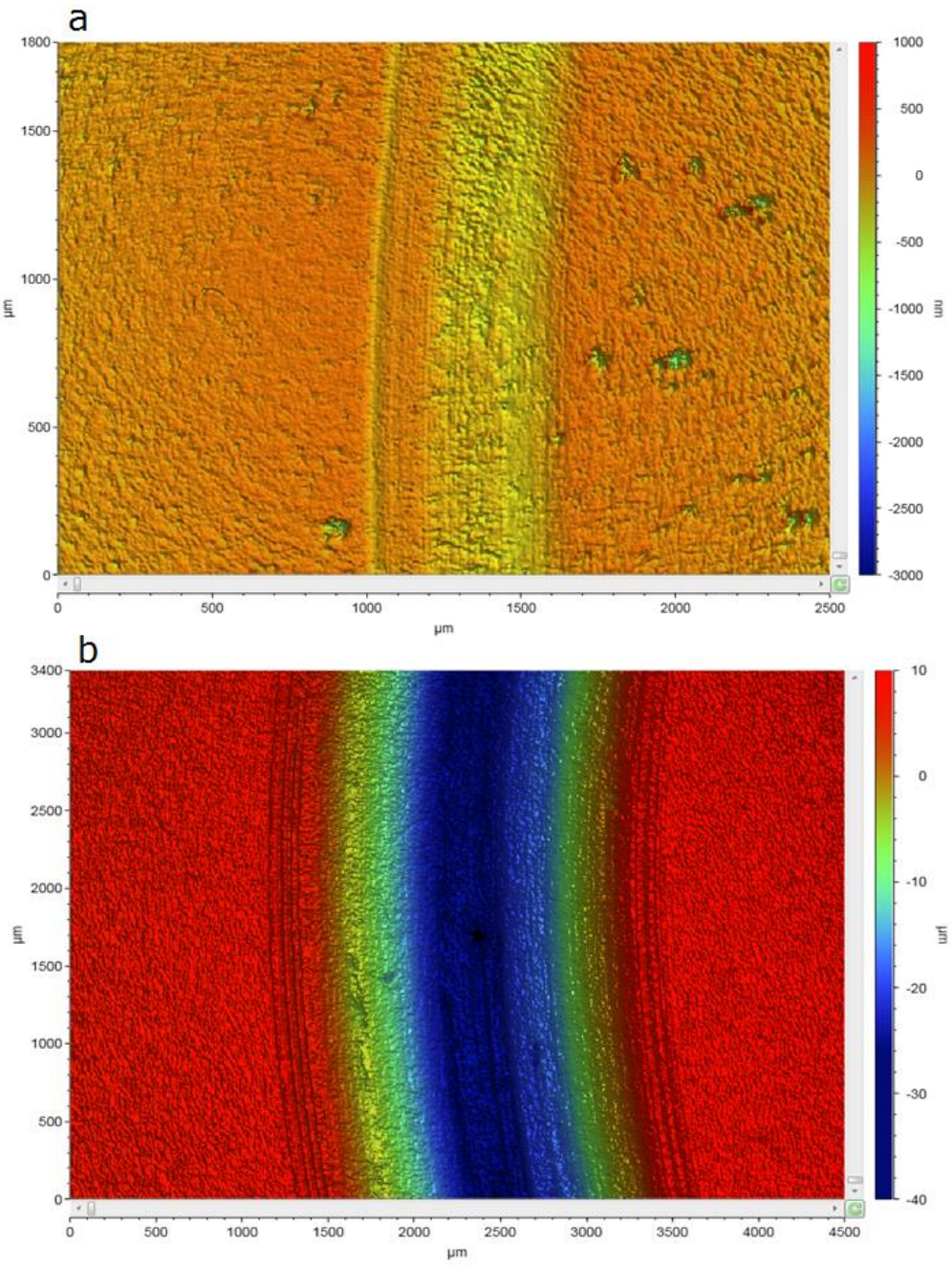

Figure 5-24: Bruker ContourGT Optical Profiler investigation of wear scar of WC-17CoF coating. (a) 2D Bruker optical image during mild wear (normal load = 212 N) indicating low wear depths. (b) 2D Bruker optical image during severe wear (normal load = 282 N) indicating high depths of wear.

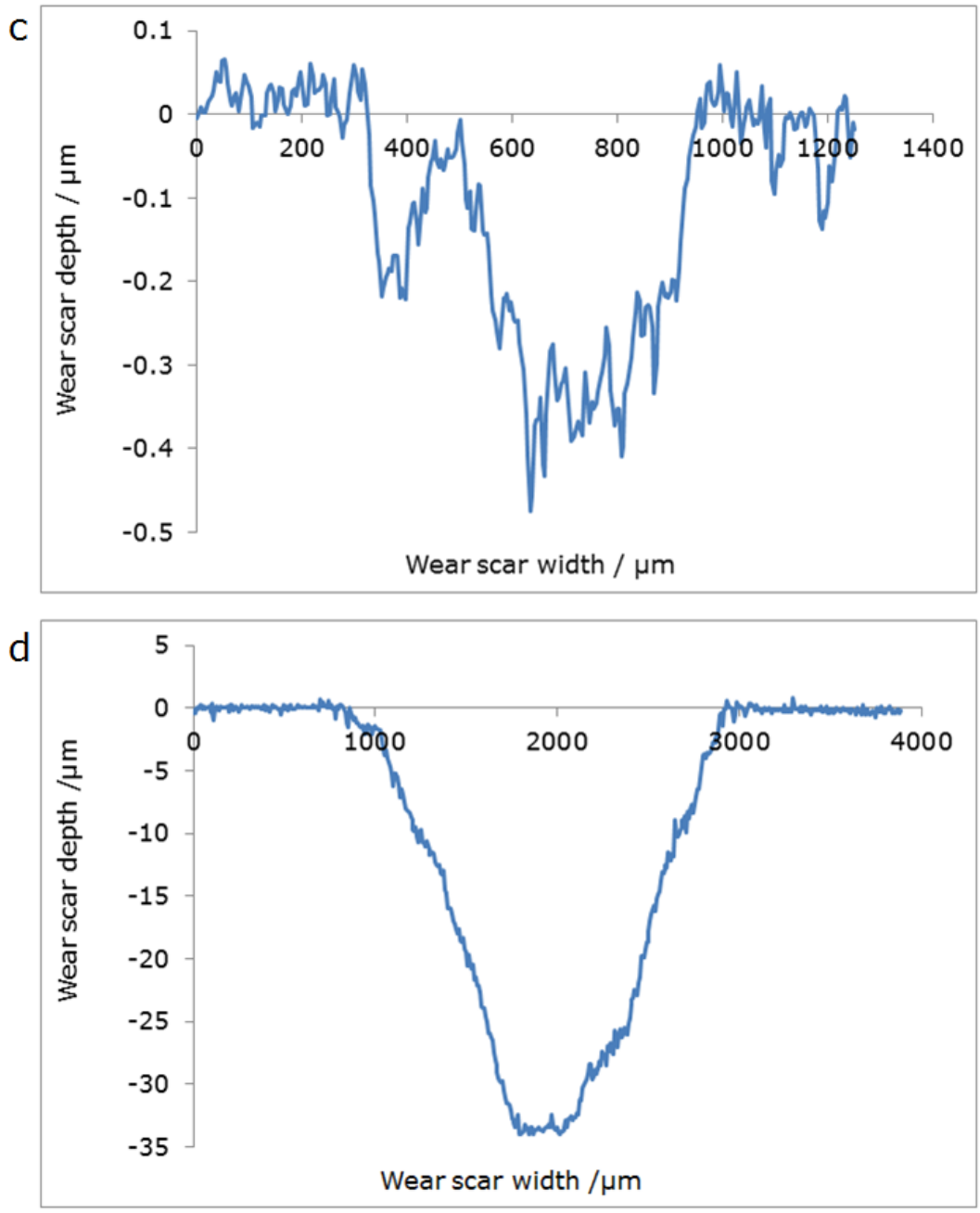

Figure 5-24 (Cont.): Bruker ContourGT Optical Profiler investigation of wear scar of WC-17CoF coating illustrating the wear scar width and depth. (c) The profile of the surface following mild wear. (d) The profile of the surface following severe wear.

The change of the friction coefficient with sliding distance for WC-17CoF coating during mild and severe wear is presented in Figure 5-25. During mild wear (normal load = 212 N), the friction coefficient curve increases gradually through the wear test towards a maximum value at the end of the test of µ = 0.19 with maximum sliding

distance 1500 m. For the severe wear test (normal load = 282 N), the wear test only ran for 300 m due to high wear in this case. The friction coefficient increased sharply during this distance to reach μ = 0.16 (running-in period), whereupon the test has been stopped.

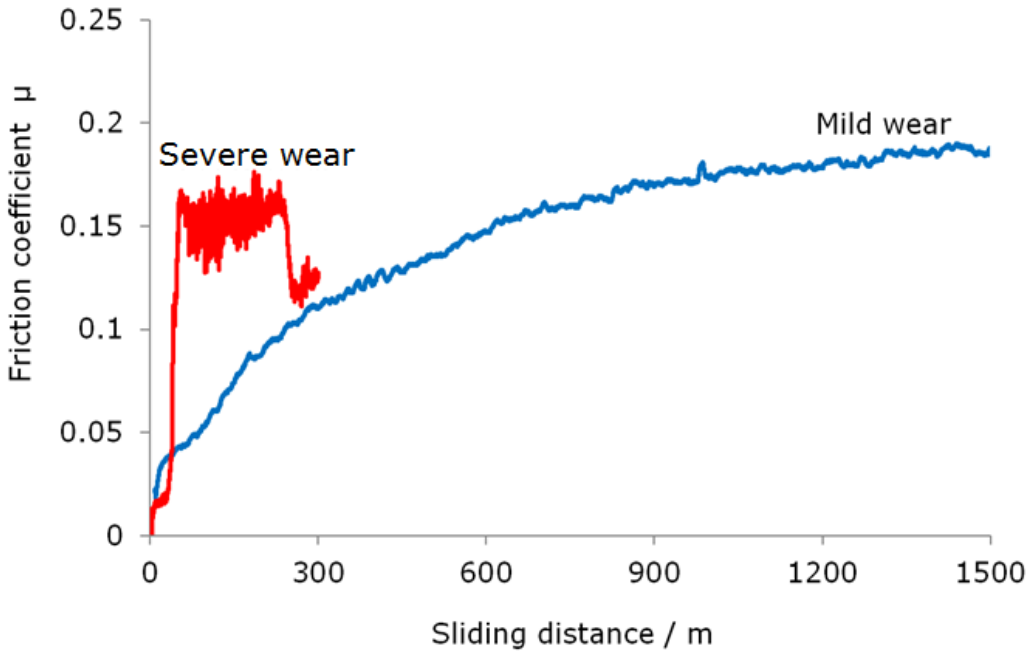

Figure 5-25: Variation of the friction coefficient with sliding distances for WC-17CoF coating throughout wear test.

The worn surface of the counterface sintered WC-6Co ball following sliding against the WC-17CoF coated disc during mild wear, (below the transition load, 212 N), has been examined by SEM. Figure 5-26a shows very smooth worn surface with a little debris attached around the edges of ball worn surface. Figure 5-26b is SEM-BSE image of selected area “b” (Figure 5-26a) which indicates that a small amount of wear debris has been transferred from the coated disc and stuck on the unworn surface of the ball. Figure 5-26c is the high magnification SEM-BSE image that characterises the selected area “c” from the middle of the ball worn surface and indicates that there has been insignificant change in the microstructure of the ball worn surface through mild wear.

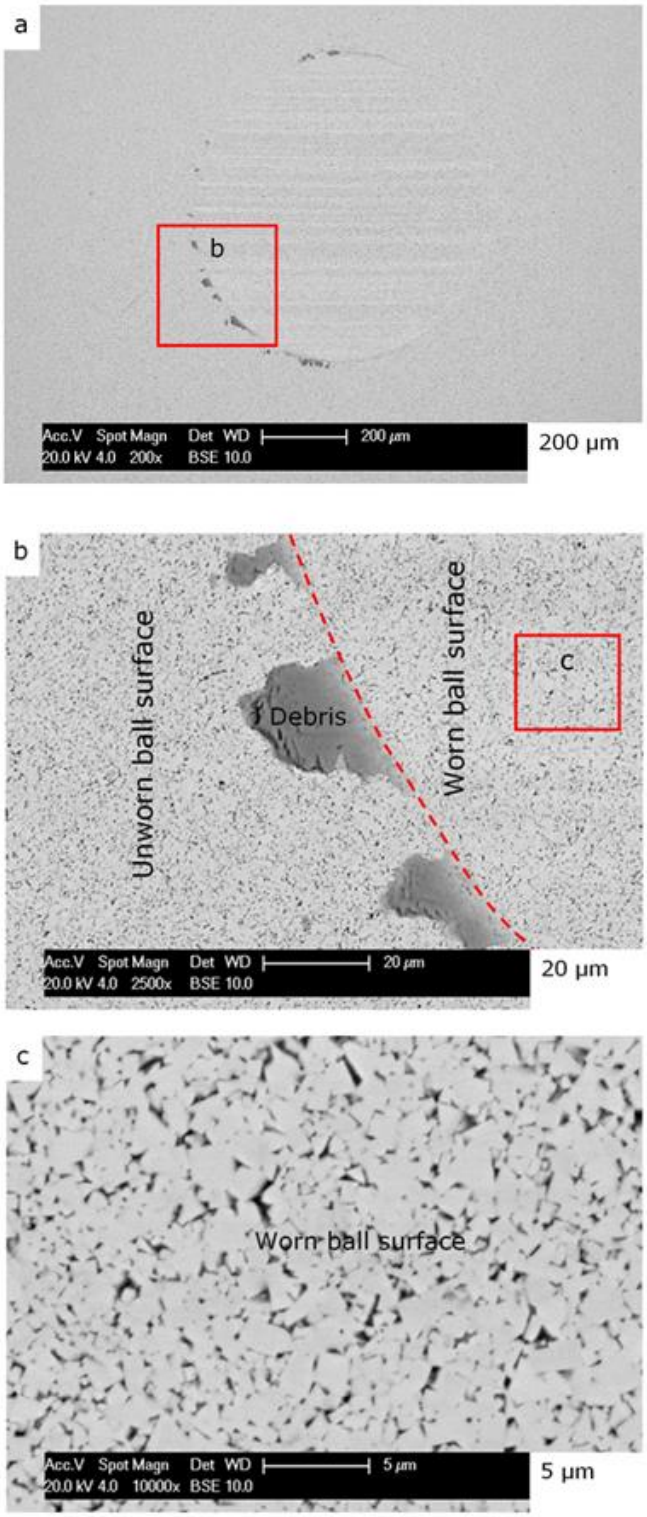

Figure 5-26: Mid wear behaviour of sintered WC-6Co ball sliding against WC-17CoF coated disc. (a) Low magnification SEM-BSE image of the ball worn surface. (b) SEM-BSE image of elected area "b" showing the wear debris, worn and unworn ball surface. (c) High magnification SEM-BSE image of selected area "c" from the middle of worn ball surface shows smooth surface.

In contrast, Figure 5-27 demonstrates the wear behaviour of the sintered WC-6Co ball following sliding against the WC-17CoF coated disc under severe wear conditions. The selected area “b” in Figure 5-27a, is characterised in the SEM-SE image in Figure 5-27b which shows worn ball surface significantly covered by a brittle tribofilm oxide-based layer. It is recognised that this layer could have been transferred from the coated disc (although distinguishing between the debris from the disc and the ball is not straightforward). The selected area “c” is illustrated in SEM-SE image in Figure 5-27c showing the brittle oxide-based debris layer and the fracture of this layer from the top worn surface of the ball through the severe wear. Additionally, Figure 5-27d shows the high magnification SEM-BSE image of the selected area “d”, where the angular WC grains provide evidence for the fracture of the top polished layer of the counterface sintered WC-6Co ball.

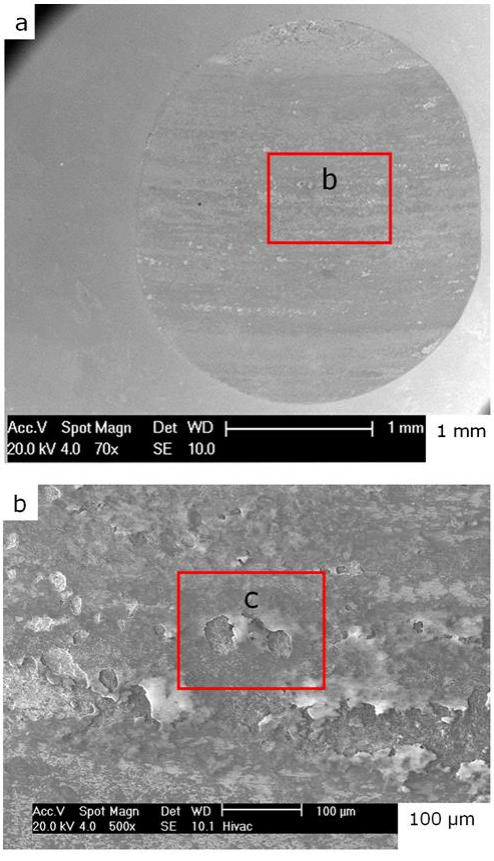

Figure 5-27: Severe wear behaviour of sintered WC-6Co ball sliding against WC-17CoF coated disc. (a) Low magnification SEM-SE image of ball worn surface. (b) SEM-SE image of selected area "b" shows that the brittle oxide layer is covering the majority of the worn ball surface and the fracture of this layer in some places.

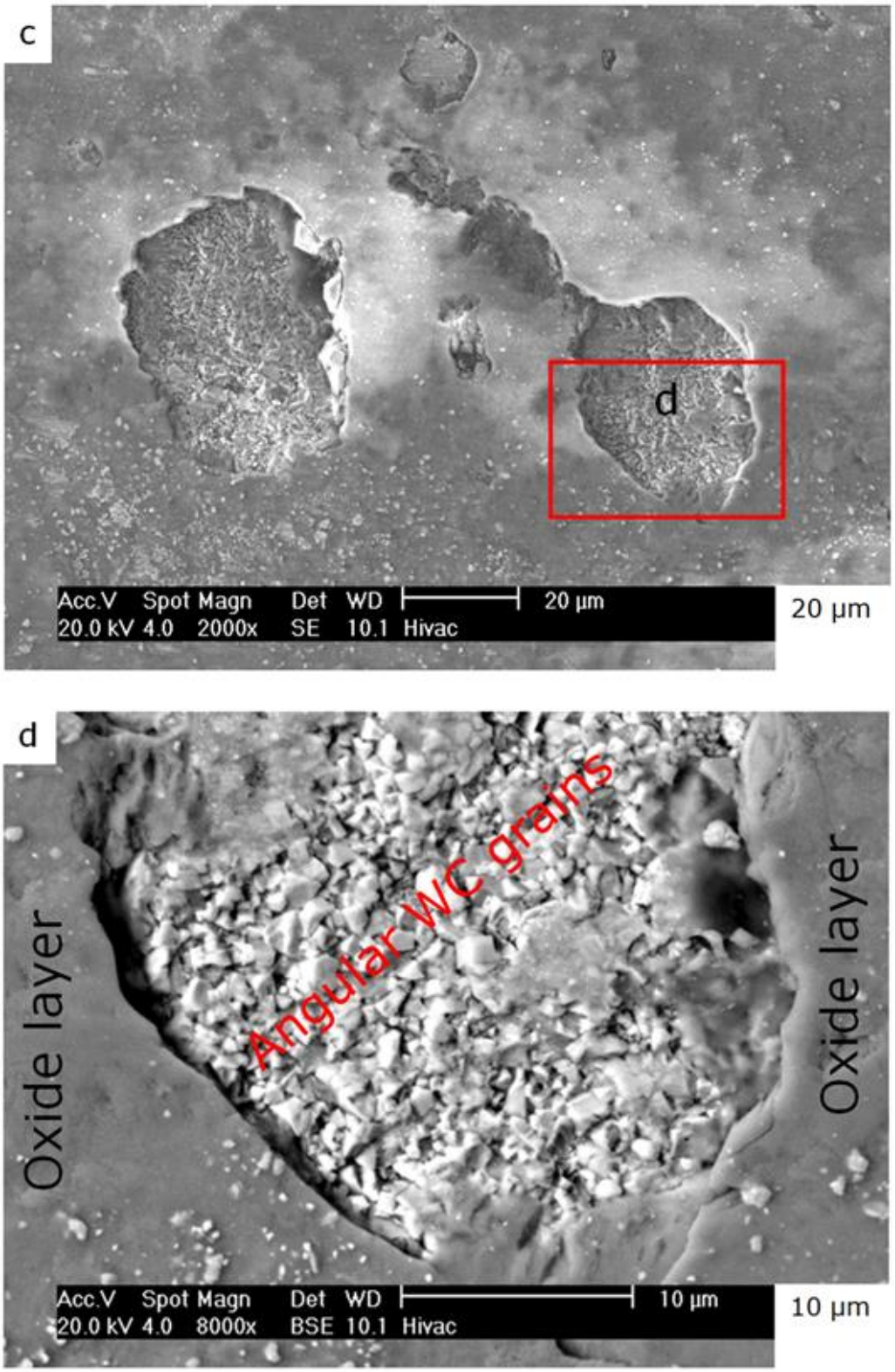

Figure 5-27 (Cont.): Severe wear behaviour of sintered WC-6Co ball following sliding against WC-17CoF coated disc. (c) High magnification SEM-SE image of selected area "c" shows the fracture of the brittle oxide layer. (d) High magnification SEM-BSE image of selected area "d". The angular WC grains provide evidence for the fracture of the worn ball surface.

5.1.4.2 Wear behaviour of WC-17CoC coating

To investigate the wear behaviour of WC-17CoC coating, the surfaces of WC-17CoC coating worn below and above the mild - severe transition load (141 N and 212 N, respectively) have been characterised and are shown in Figure 5-28 and Figure 5-29 respectively.

The plan view of the WC-17CoC coating worn under a load of 141 N (below the transition load) is shown in Figure 5-28. A smooth surface can be seen in the low magnification SEM-SE image in Figure 5-28a. The wear track width is about 0.8 mm after sliding for a distance of 1500 m. Figure 5-28b shows a SEM-BSE image from the middle of the wear track, it can be seen that localised transfer layers (oxide layers) have been generated during the sliding wear test. Narrow intergranular cracks in the coating top surface are observed (red arrows). Selected area "c" in Figure 5-28b is shown in a high magnification SEM-BSE image in Figure 5-28c which shows the narrow intergranular crack propagating through the brittle tribofilm layer. The polished surface of WC grains (flat WC grains) that indicates there was no severe fracture in the coating.

A cross-section has been made through the wear track of WC-17CoC coating to investigate the wear behaviour of this coating. Figure 5-28d shows the wear scar cross-section following mild wear (worn under a load of 141 N). The selected area “e” in Figure 5-28d is illustrated in Figure 5-28e which shows a thick localised tribofilm layer on the coating top surface. There are no significant subsurface cracks observed following this mild wear process.

The energy dispersive X-ray analysis (EDX) of the transferred layer, shown in Figure 5-28f indicates the presence of tungsten, cobalt, and oxygen. The increase of the fraction of oxygen in the tribofilm layer indicates that this layer is an oxide layer.

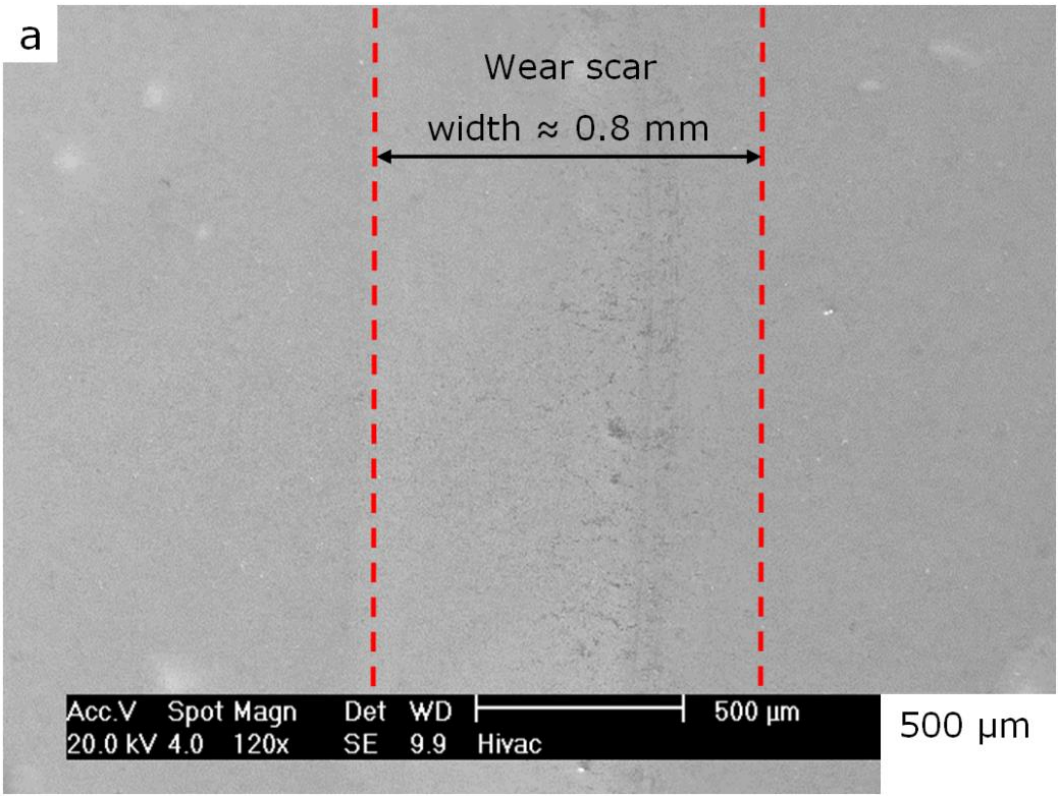

Figure 5-28: Mild wear behaviour of WC-17CoC coating. (a) Top view of wear scar of WC-17CoC coating worn under normal load 141 N. Sliding directions is from top to bottom.

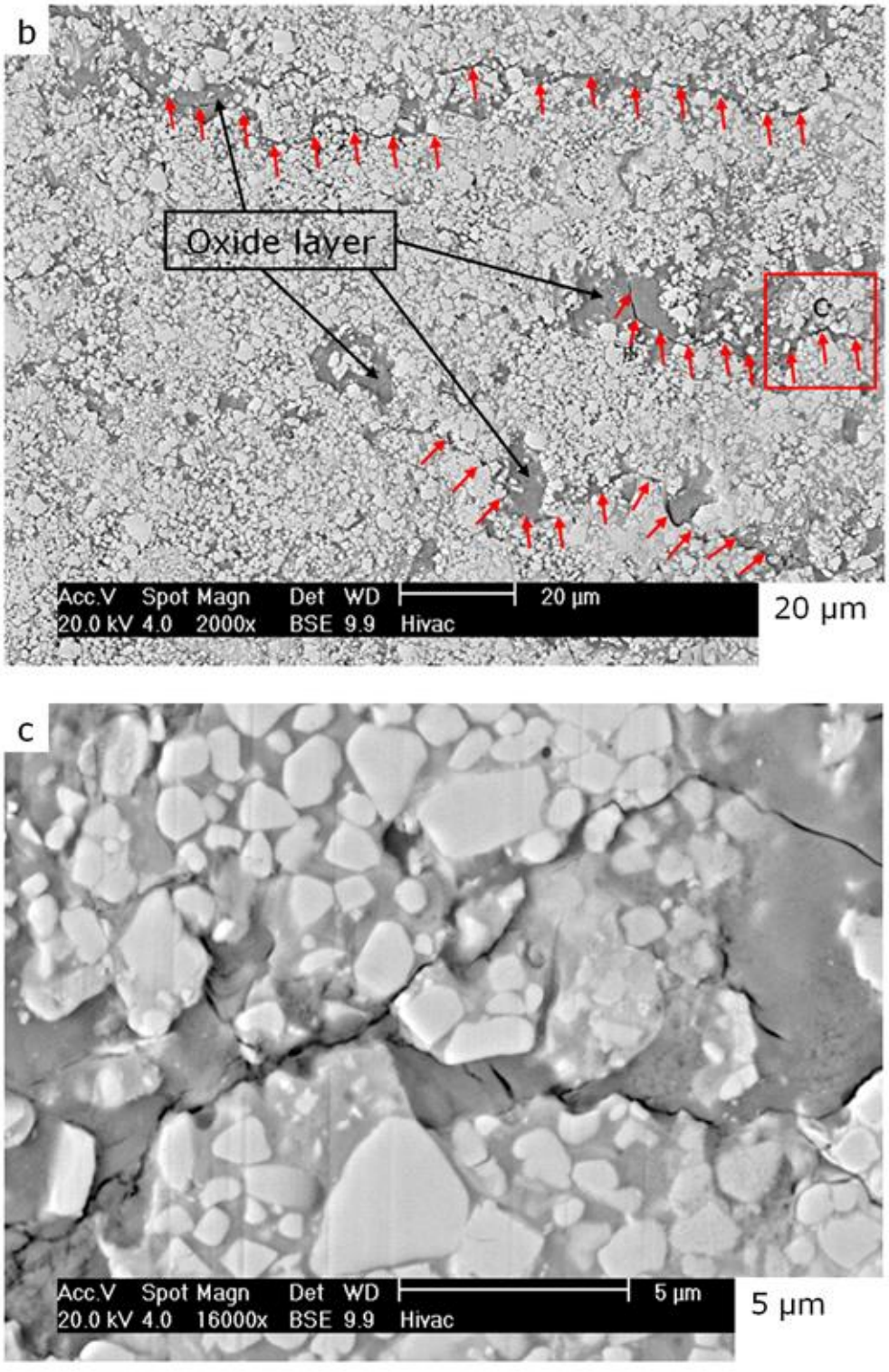

Figure 5-28 (Cont.): Mild wear behaviour of WC-17CoC coating. (b) SEM-BSE image from the middle of the wear track showing the localised oxide layers and the narrow cracks in the coating surface (red arrows). (c) High magnification SEM-BSE image of selected area "c" showing narrow cracks in the brittle oxide layer. Polished WC grain surfaces indicate that there is no fracture in the coating.

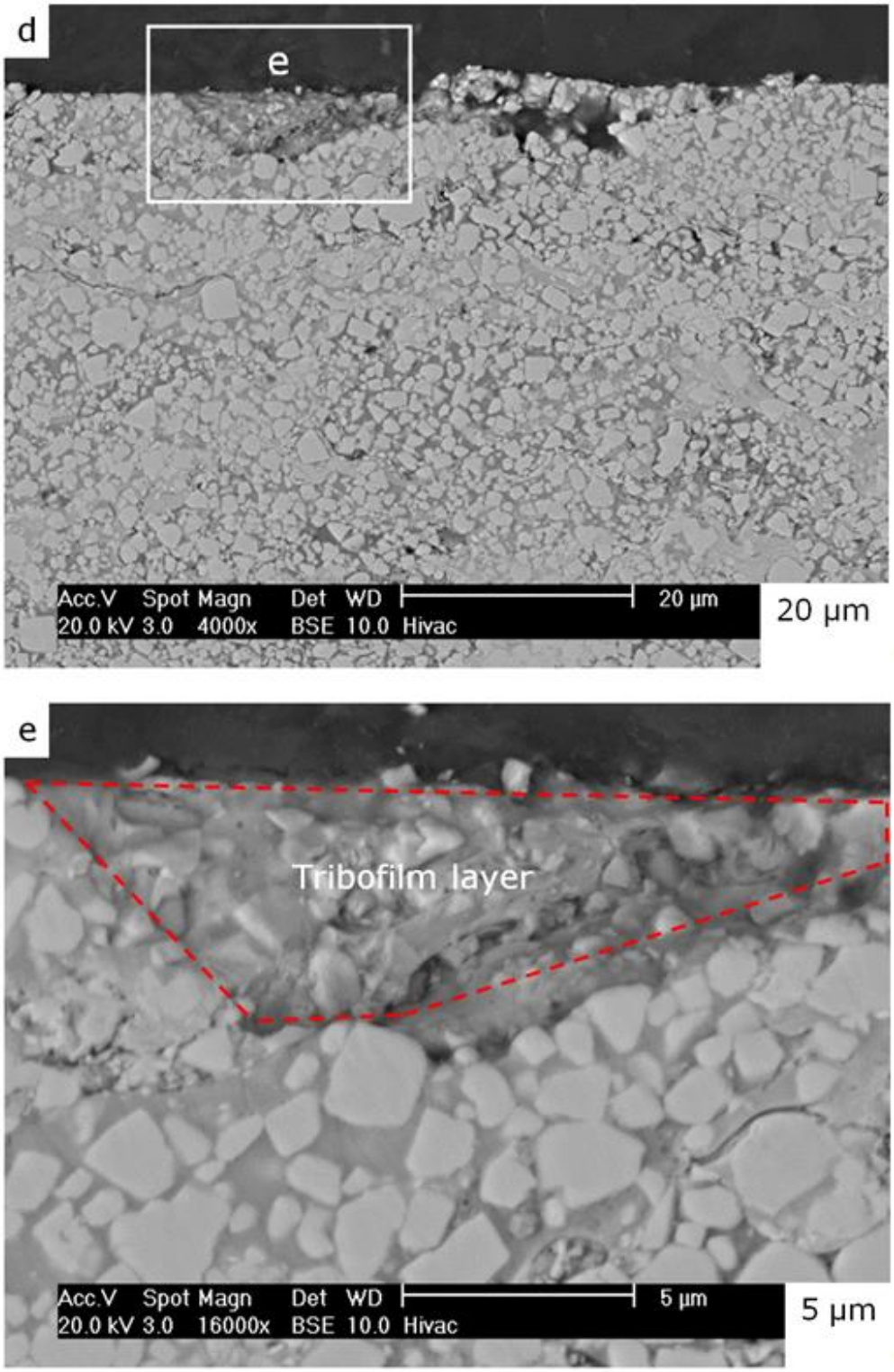

Figure 5-28 (Cont.): Mild wear behaviour of WC-17CoC coating. (d) Cross-section in the mild wear track of WC-17CoC coating (normal load = 141 N) showing localised regions of oxide layer on the top surface. (e) High magnification SEM-BSE image of selected area "e"; there is no evidence of any subsurface cracking and no cracks in WC grains themselves are observed either.

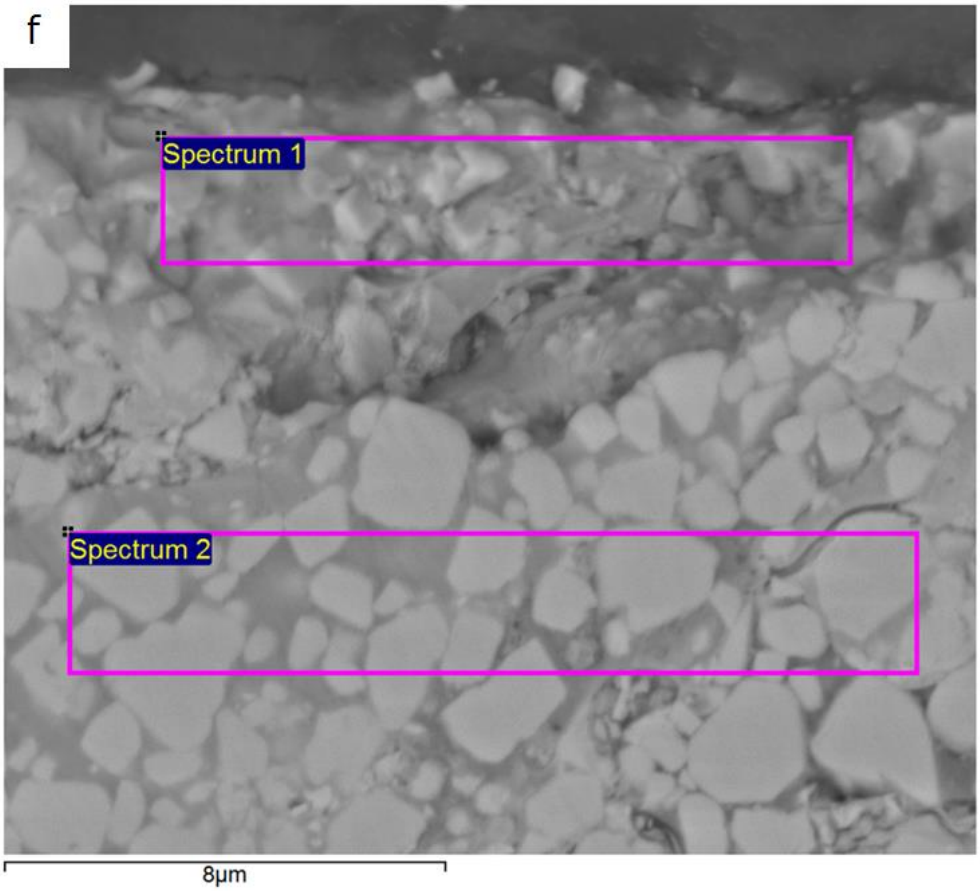

Spectrum	O wt%	Co wt%	W wt%
Spectrum 1	6	22	72
Spectrum 2	1	17	82

Figure 5-28 (Cont.): Mild wear behaviour of WC-17CoC coating. (f) EDX investigation of transfer layer (spectrum 1). The increase in the oxygen fraction indicates that this layer is an oxide layer.

The surface of the WC-17CoC coating worn under the load of 212 N exhibited more severe wear as shown in low magnification SEM-SE image in Figure 5-29a. The wear track has developed a width of about 1.5 mm after a sliding distance of only 300 m. Figure 5-29b is an SEM-SE image from the middle of the wear track; it indicates very severe wear and nearly the entire wear scar is covered by the transfer layer. The selected area "c" in Figure 5-29b is shown in the SEM-BSE image in Figure 5-29c which illustrates the cracks on the brittle oxide layer which lead to the fracture of this layer. The angular WC grains observed in the high magnification SEM-BSE in Figure 5-29d indicate that the top coating surface (which is mainly the brittle oxide layer) has been severely fractured.

To investigate the wear behaviour of WC-17CoC coating following severe wear, a cross-section has been made through the wear track following wear and a load of 212 N. The image in Figure 5-29e shows a thin transfer layer covering complete wear track top surface. Selected area “f” indicated in Figure 5-29e is shown in a higher magnification SEM-BSE image in Figure 5-29f which indicates that the coarse wear debris is bonded to the underlying coating material. No subsurface cracks or cracks in WC grains themselves are observed in this cross-section.

The energy dispersive X-ray analysis (EDX) of the transferred layer during severe wear of WC-17CoC coating is demonstrated in Figure 5-29g which indicates the presence of tungsten, cobalt, and oxygen. The higher oxygen fraction in the transferred layer indicates that this layer is an oxide layer.

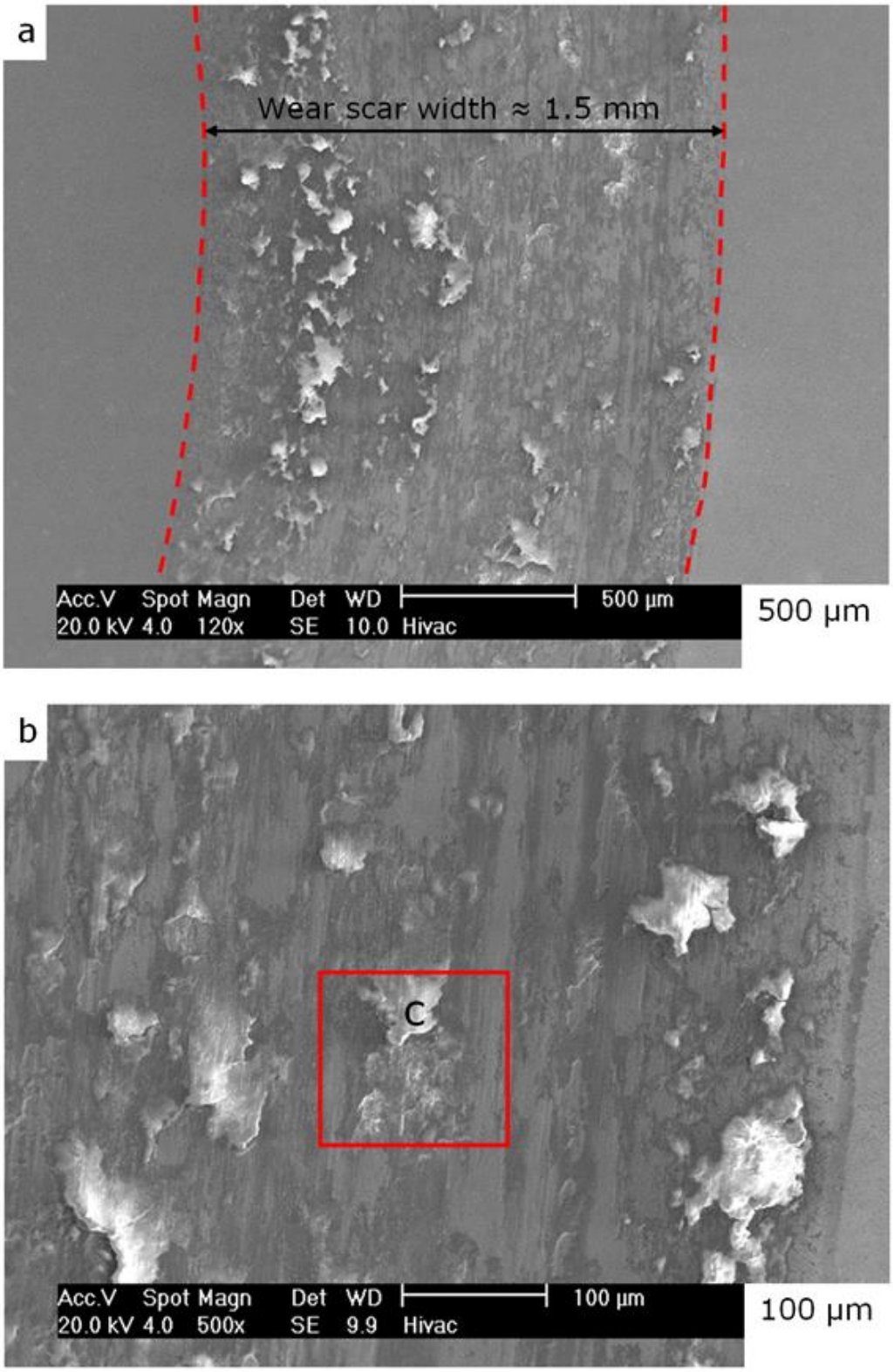

Figure 5-29: Severe wear behaviour of WC-17CoC coating. (a) Top view if wear track of WC-17CoC coating worn with load above transition load (212 N). (b) SEM-SE image taken from the middle of the wear track indicating very severe wear. Sliding direction is from top to bottom.

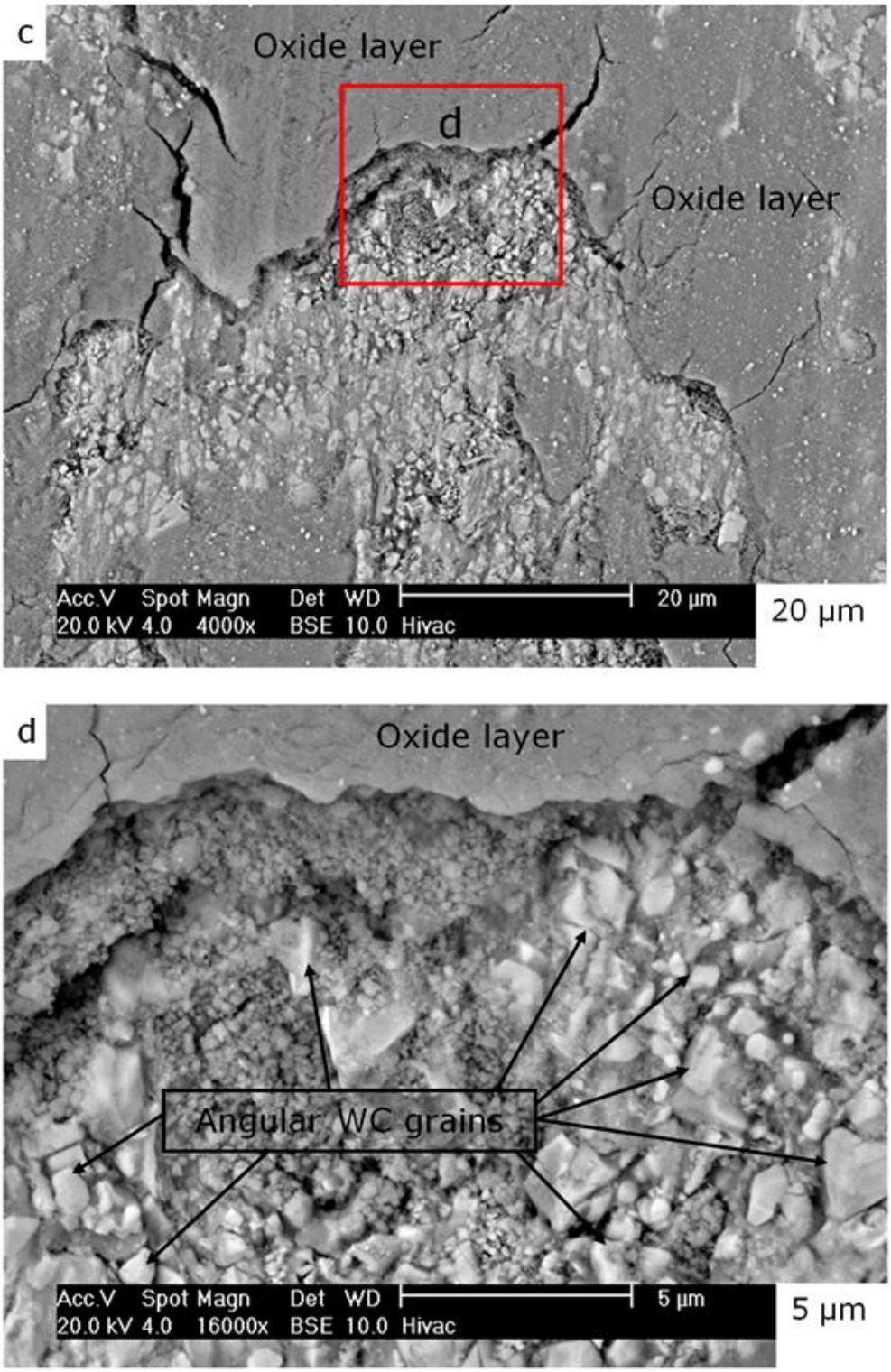

Figure 5-29 (Cont.): Severe wear behaviour of WC-17CoC coating. (c) SEM-BSE image of selected area "c" in previous figure shows the brittle oxide layer which covers a large friction of the coating worn surface. (d) High magnification SEM-SE image of selected area "d" showing angular WC grains which indicate the fracture of the top oxide layer.

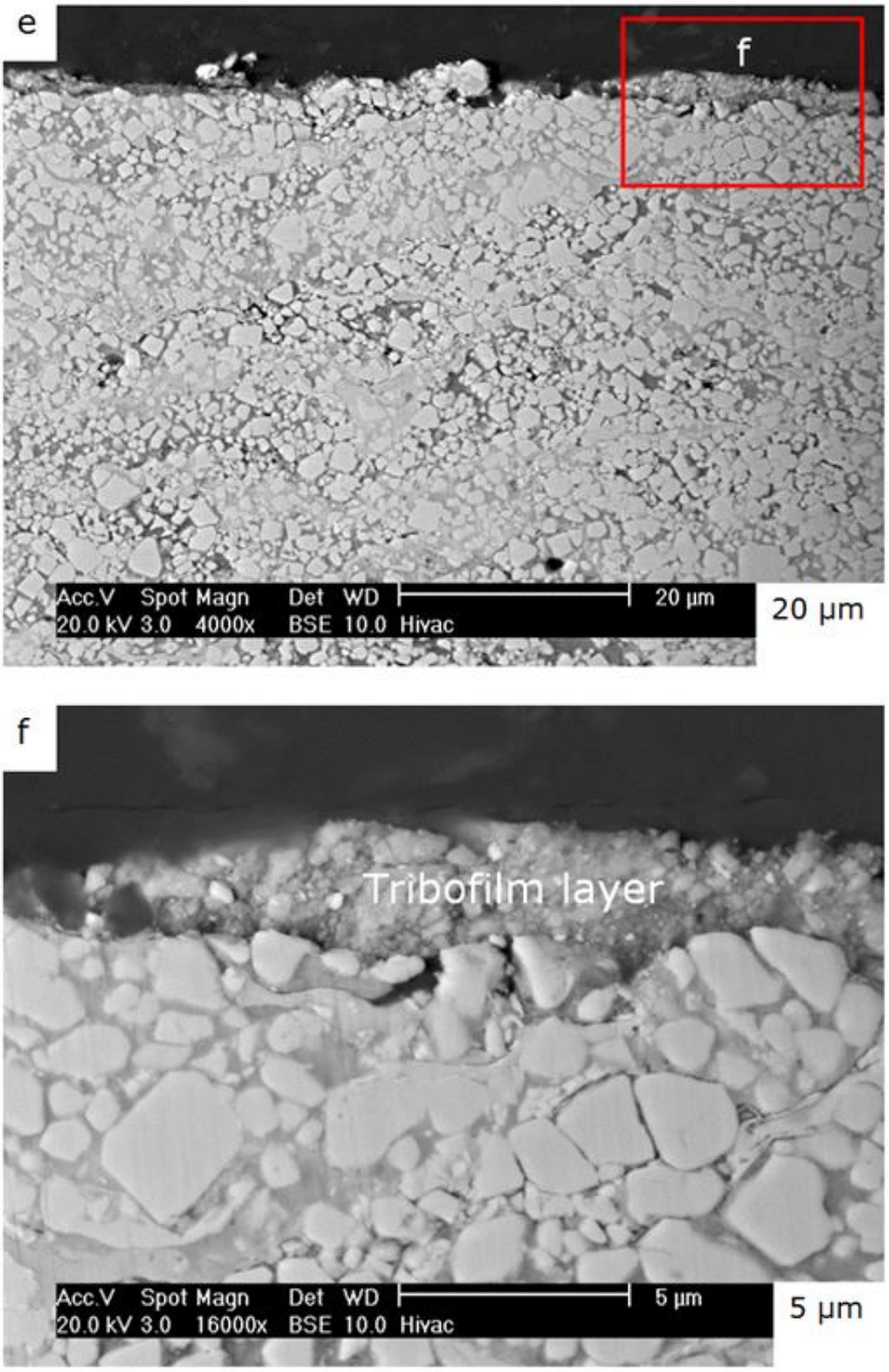

Figure 5-29 (Cont.): Severe wear behaviour of WC-17CoC coating. (e) Cross-section in the severe wear scar of WC-17CoC coating (normal load = 212 N) showing thin oxide-based debris layer on the top surface. (f) High magnification SEM-BSE image of selected area "e" indicating detail of the tribofilm on the top of worn surface. There is no indication of any subsurface cracks or cracks in WC grains.

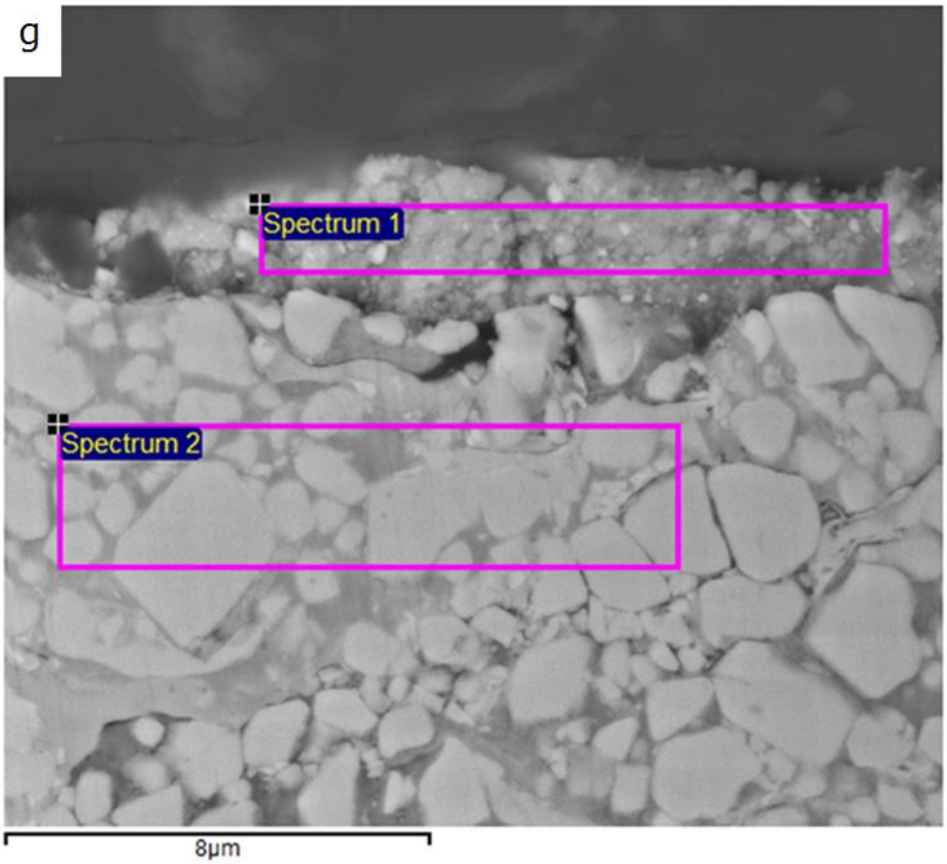

Spectrum	O wt%	Co wt%	W wt%
Spectrum 1	17	14	69
Spectrum 2	1	13	86

Figure 5-29 (Cont.): Severe wear behaviour of WC-17CoC coating. (g) EDX analysis of transfer layer (spectrum 1). The higher oxygen fraction indicates that this debris layer is an oxide layer.

The wear debris of WC-17CoC coating worn under high load (212 N) contains plate-like debris (resulting from delamination of the oxide-based debris layer) and agglomerated fine particles. Figure 5-30 illustrates the morphology of this wear debris.

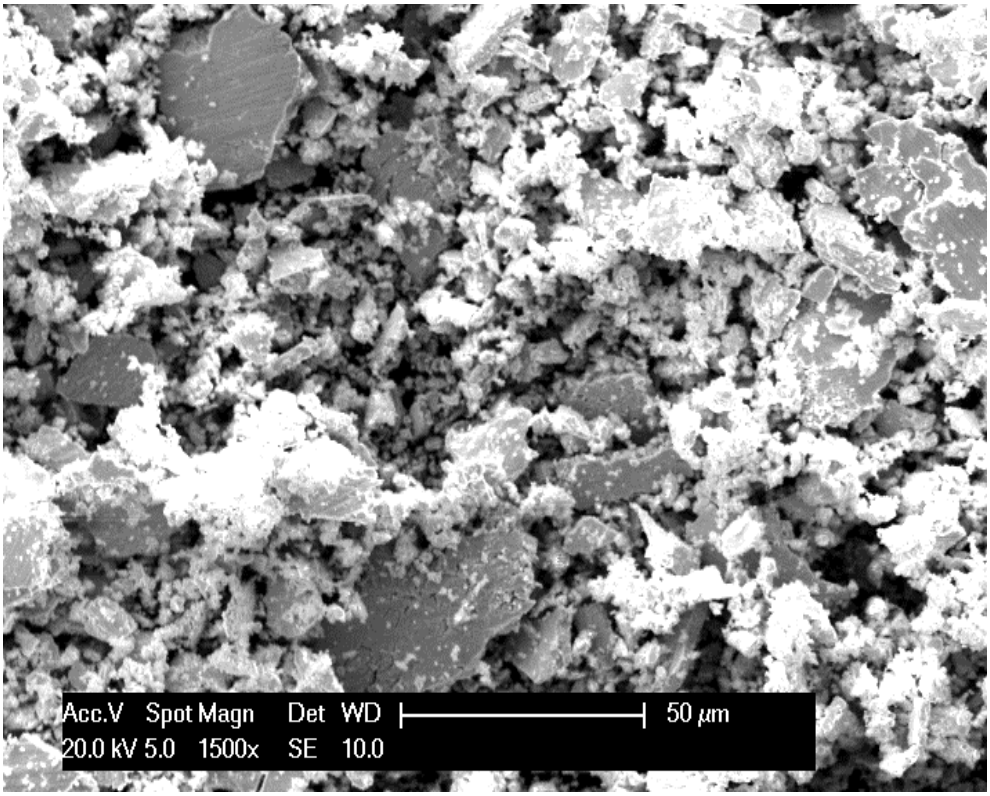

Figure 5-30: The wear debris from the WC-17CoC coated disc worn in severe conditions (normal load = 212 N) showing plate like debris and fine agglomerated particles.

A Bruker ContourGT Optical Profiler has been used to study wear scars in the WC-17CoC coating. Figure 5-31a, shows the 2D Bruker image of the coating following sliding under mild wear conditions below the transition load (141 N) and shows a smooth wear track. In contrast, Figure 5-31b shows the 2D Bruker image of the coating following wear under severe conditions (applied load of 212 N), indicating a rough wear track. The wear scar profile of the WC-17CoC coating following mild wear is shown in Figure 5-31c where the wear scar depth and width are around 0.25 μm and 0.8 mm respectively, after a 1500 m sliding distance. In contrast, Figure 5-31d shows the wear scar profile following severe wear, indicating that the wear scar depth and width are about 13 μm and 1.5 mm, respectively after only 300 m sliding distance.

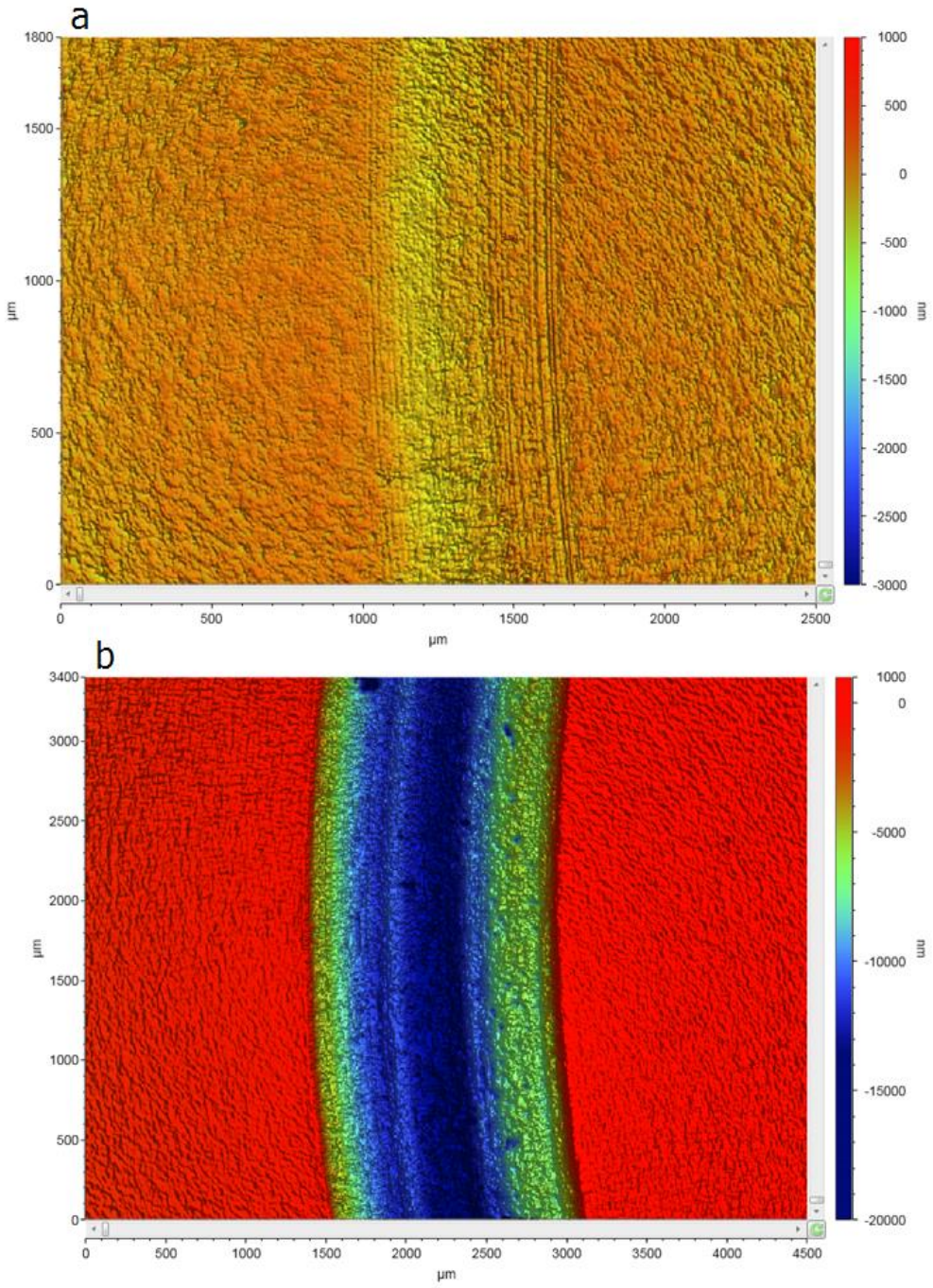

Figure 5-31: Bruker ContourGT Optical profiler investigation of wear track of WC-17CoC coating. (a) 2D Bruker optical image following mild wear (normal load = 141 N); (b) 2D Bruker optical image by severe wear (normal load = 212 N).

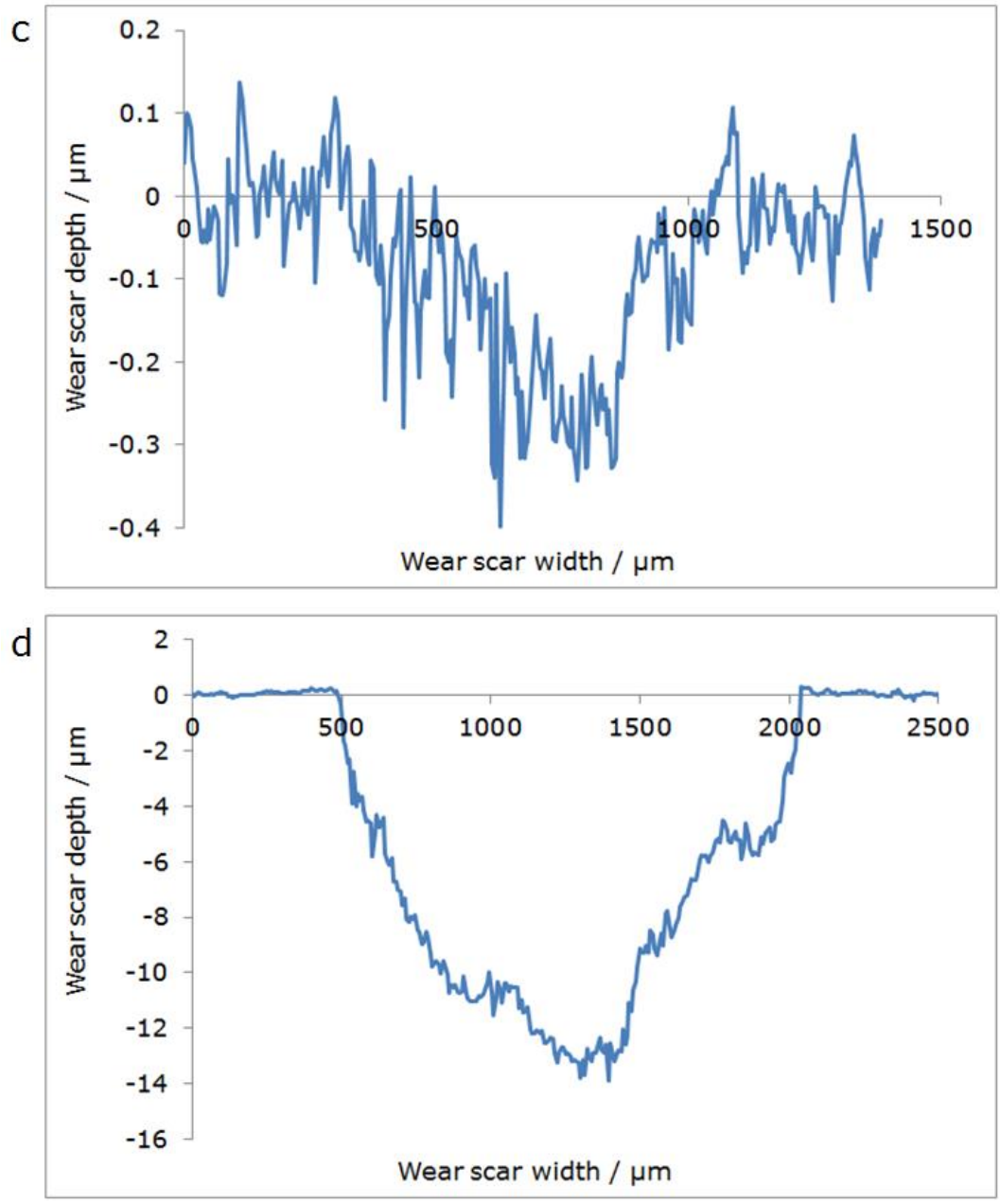

Figure 5-31 (Cont.): Bruker ContourGT Optical profiler investigation of wear track of WC-17CoC coating. (c) The plot of the wear profile following sliding under mild conditions (141 N); (d) the plot of the wear profile following sliding under severe conditions (212 N).

Figure 5-32 represents the variation of the friction coefficient with sliding distance for WC-17CoC coating during mild and severe wear. During sliding under mild wear conditions (normal load = 141 N), the friction coefficient jumped to $\mu = 0.03$ during the running-in period through the first 50 m of the wear test. Then it increased gradually through the wear test, with the test ending with the coefficient of friction at

maximum value of μ = 0.11 with maximum sliding distance 1500 m. Through the severe wear test (normal load = 212 N), the friction coefficient increased sharply during the running-in period (the first 100 m) to reach its maximum value μ = 0.17, whereupon it began to decrease to μ = 0.1 at sliding distance 300 m where the test has been stopped due to the high wear observed.

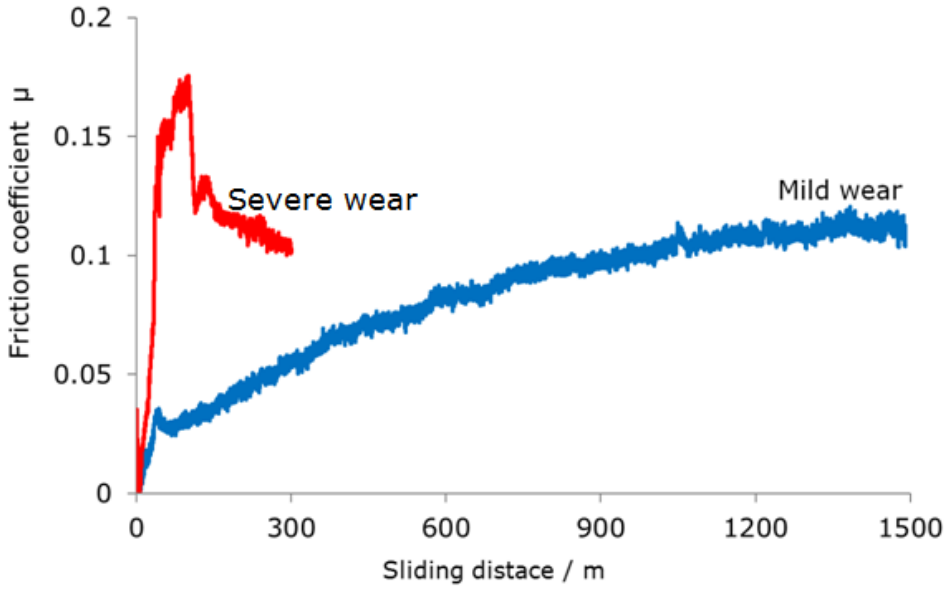

Figure 5-32: Variation of the friction coefficient with sliding distances for WC-17CoC coating through wear test.

SEM imaging has been used to investigate the worn surfaces of the sintered WC-6Co ball following sliding against the WC-17CoC coated disc. Figure 5-33 shows the wear behaviour of the sintered ball through the mild wear of WC-17CoC coating. Figure 5-33a shows the SEM-SE low magnification of ball worn surface. The selected area "b" presented in Figure 5-33b shows a largely unworn surface; the small amount of debris (transformed from the coated disc and bonded to the ball surface), and the worn surface of counterface ball can be observed. The figure shows a very smooth worn surface, indicating that there has been insignificant change in the ball microstructure.

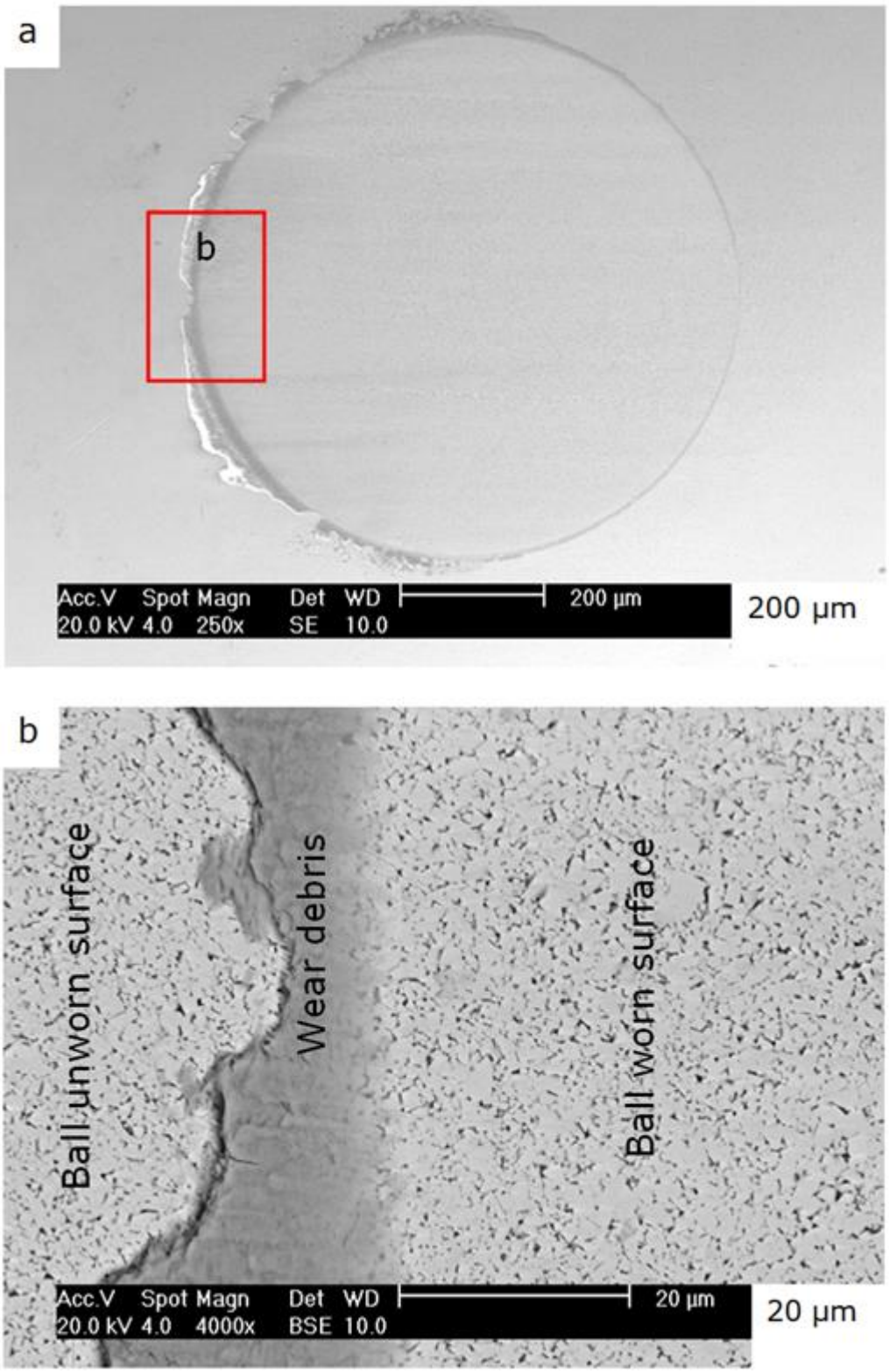

Figure 5-33: Mild wear behaviour of sintered WC-6Co ball following sliding against WC-17CoC coated disc. (a) Low magnification SEM-SE image of the ball worn surface. (b) SEM-BSE image showing a smooth worn surface and also the debris attached to the ball surface. Sliding direction is from right to left.

In contrast, the wear of the sintered WC-6Co ball sliding against the WC-17CoC coated disc following severe wear is illustrated in Figure 5-34. Low magnification SEM-SE image in Figure 5-34a shows the ball worn surface. The selected area "b" in Figure 5-34a is shown in a higher magnification SEM-SE image in Figure 5-34b which indicates the morphology of the wear debris transformed from the WC-17CoC coated disc and adhered to the ball surface. The selected area "c" from the middle of the image of the ball in Figure 5-34a, is shown in a SEM-BSE image in Figure 5-34c which illustrates damage associated with severe wear of the ball. Some WC grains have been pulled out and in the oxide-based debris layer appears to fill the voids left by these WC grains (this illustrated by red arrows in Figure 5-34c).

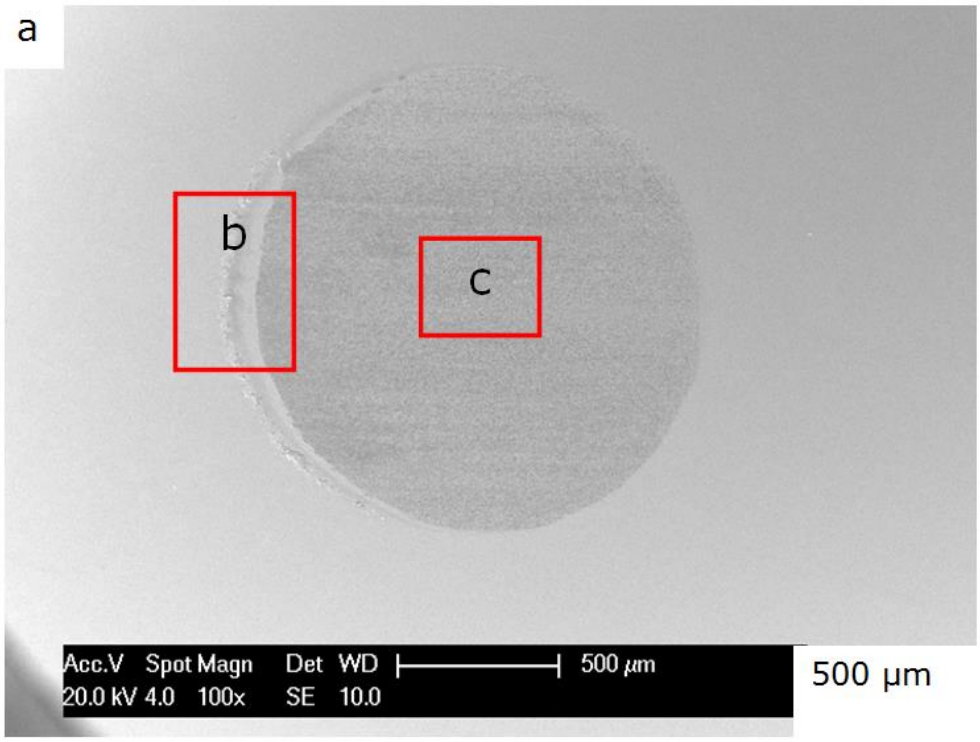

Figure 5-34: Severe wear behaviour of sintered WC-6Co ball for link sliding against WC-17CoC coated disc; (a) Low magnification SEM-SE image of ball worn surface. Sliding direction is from right to left.

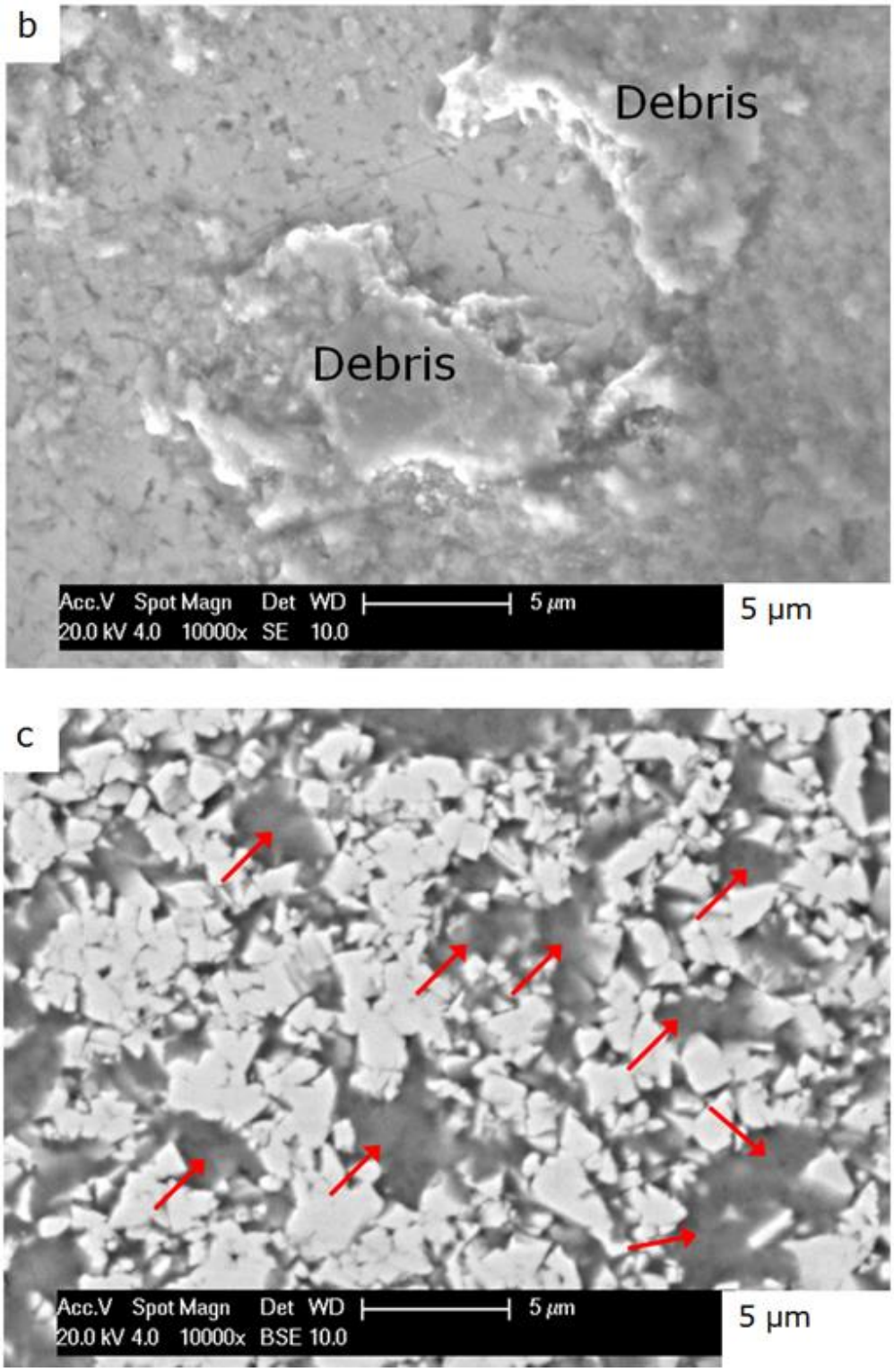

Figure 5-34 (Cont.): Severe wear behaviour of sintered WC-6Co ball for link sliding against WC-17CoC coated disc; (b) High magnification SEM-SE image of selected area "b" showing the morphology of the wear debris. (c) High magnification SEM-SE image of selected area "c" illustrating the severe wear of ball surface. Red arrows indicate pulled-out WC grains.

5.2 Discussion

The results of the experimental tests related to the effect of the WC grain size of both WC-17CoF (with fine WC grains) and WC-17CoC (with coarse WC grains) coatings will be discussed in this section. This will include the effect of WC grain size on coating microstructure, mechanical properties and sliding wear behaviour. Starting with the coatings microstructure, results of XRD and SEM will be discussed in detail. Conclusion reflecting the differences between the coarse and fine WC grain size coating will be given. Microhardness, fracture toughness and scratch test are the mechanical properties of WC-17CoF and WC-17CoC coatings which will be discussed and final summary of these mechanical properties will be given. Dry sliding wear behaviour of the corresponding coatings will be discussed in the influence of coating microstructure and their mechanical properties, followed by related conclusions. The whole chapter conclusion will be given at the end of this section to illustrate the effect of WC grain size.

5.2.1 Coating Microstructure

Coating microstructure is an important factor in order to get favourable mechanical properties and tribology performance. The deposition process, process parameters and starting powder are main factors affecting coating microstructure. It is well known that the carbide grain size is playing an essential role on coatings mechanical properties and their wear resistance. In this study two same size range WC-17Co powders with different WC grain size (fine/coarse) were selected to investigate the WC grain size effect on coating microstructure, mechanical properties and sliding wear behaviour (see section 5.1.1).

Comprehensive description of the microstructural formation mechanism throughout HVOF spraying of WC–Co has been given by Stewart at el. (2000), as summarised in section 4.2.1. However, through this section the effect of WC grains will be analysed. For this, two identical powders, Woka 3202 (WC-17wt%Co) with coarse WC grain size, and Woka 3202 FC (WC-17wt%Co) with fine WC grain size, both

manufactured by an agglomeration and sintering process with a similar nominal size (-45+15 µm), were used.

Figure 5-1 shows the XRD patterns of both WC-17CoF and WC-17CoC powders and coatings. In addition to retained WC and cobalt peaks, both coatings (as coated and after polishing) show peaks related to W_2C and W. The discovery of W_2C and W traces in the coatings indicates that decomposition took place through spraying. Nevertheless, from Figure 5-1 there is no significant different in decomposition between the fine and coarse coatings.

Previous studies (Chivavibul et al. 2007; Lekatou et al. 2015; Stewart et al. 2000; Usmani et al. 1997; Watanabe et al. 2006; Yang et al. 2003b) reported that a decrease in carbide size in the feedstock powder led to a higher degree of decomposition of the WC, and consequently higher amount of W_2C in the coating. This extensive degree of decomposition of the fine carbide grains is attributed to the more rapid dissolution of the fine-scale WC grains into the liquid metal binder (Co) during spraying (Chivavibul et al. 2007; Stewart et al. 1999), Figure 5-35. However, the degree of decomposition of the powders during spraying depends mainly upon the time–temperature history of the particle and the particle characteristics such as size, porosity and WC grain size. Decomposition will be increased by high temperatures and low velocities, leading to a long residence time in the flame, and by small carbide grain sizes within the powder particles, all of which promote carbide dissolution in the molten metal binder and subsequent decomposition (Guilemany and De Paco 1996; Sudaprasert et al. 2003).

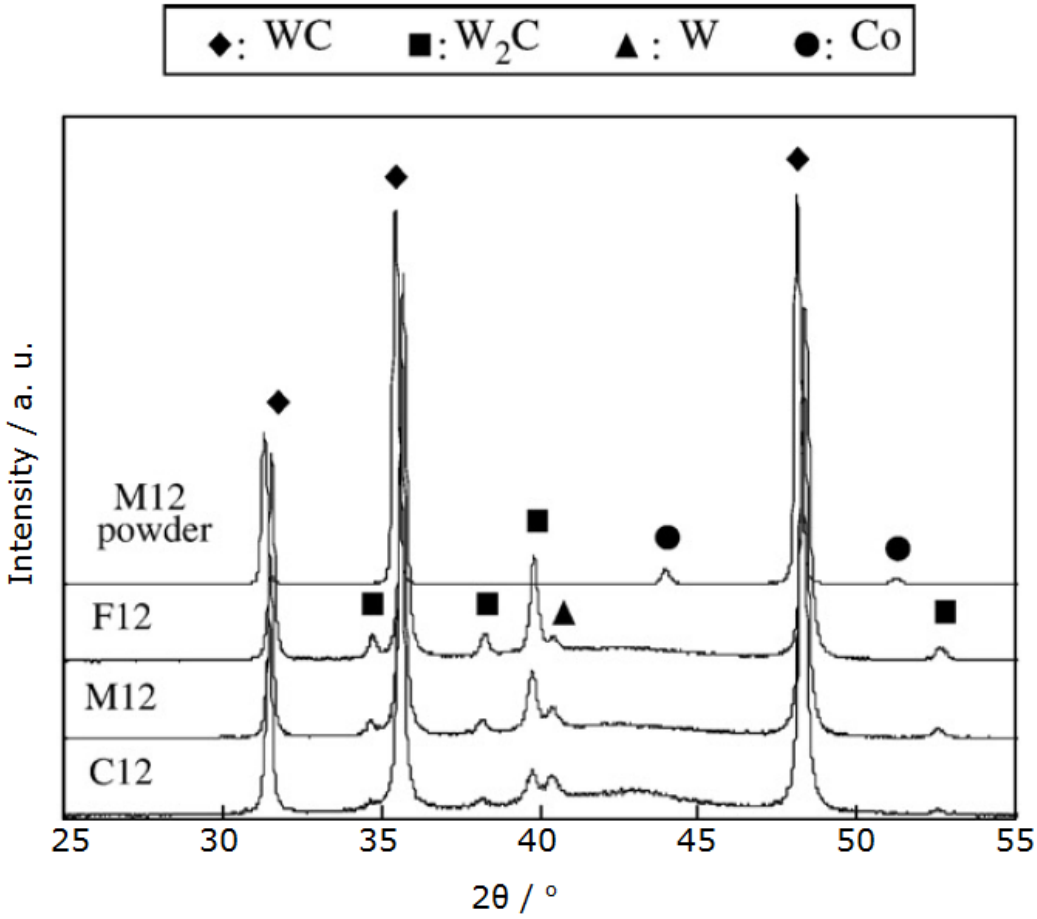

Figure 5-35: XRD results of the WC-Co coatings show the effect of WC grain size on the coating decomposition, where F, M and C related to fine, medium and coarse WC grain size (Chivavibul et al. 2007).

Most of these studies were performed by HVOGF systems, whereas the Met-Jet 4L system used in this study is HVOLF. The gas temperature and velocity in kerosene-fuelled HVOF thermal spray coating process was reported about 2300 K and 1700 m s^{-1} respectively (Kamnis and Gu 2006). The HVOGF processes show higher gas temperature and lower velocity, approximately 2700 K and 1500 m s^{-1} respectively, (Gu 2000). The spraying with HVOLF shows less degree of decomposition compared to spraying with HVOGF as reported by several researchers such as (Schwetzke and Kreye 1999; Sudaprasert et al. 2003).

Even though, the quantitative X-ray diffraction analysis, (Table 5-2), is not so accurate since it does not account for the fraction of the metal binder phase (cobalt).

However, it is expected to provide some useful information related to the weight percentage of carbide phases in the coatings. There is no significant different decomposition between both of fine and coarse coating.

In most previous studies of HVOF sprayed WC-Co, a broad diffraction halo appears, which indicates the presence of amorphous or nanocrystalline phase in these coating, (Karimi et al. 1993; Stewart et al. 2000; Verdon et al. 1998). This amorphous/nanocrystalline phase is due to the solid solution phase formed by dissolution of decomposition products such as W_2C, W and C in metallic binder, (cobalt), during spraying process. However, cobalt phase is retained in both WC-17CoF and WC-17CoC coatings in this study (Figure 5-1). Such retention of cobalt phase has been reported for coatings by HVAF process (Jacobs et al. 1999) and HVOF process (Yang et al. 2003b). The high level of retention of WC and cobalt phases in the coatings could be attributed to the low temperature of HVOLF during the spraying process, therefore, the cobalt matrix cannot be melted completely (Yang et al. 2003b).

The peaks of cobalt were broadened and shifted to lower angles, (Figure 5-1). This is a result of their very small crystals, in other words, it is an increase of lattice parameter in the binder phase, (cobalt), due to the dissolution of decomposition products, (W_2C, W and C) in the metallic binder during spraying process (Cullity and Stock 2001; Yang et al. 2003b).

SEM-BSE images of the cross-section of the coatings in Figure 5-4 and Figure 5-5 indicate distinct differences in the carbide grain size among the WC-17CoF and WC-17CoC coatings. The average value of carbide size in the starting powders and coatings are listed in Table 5-1. There is no significant difference in carbide grain sizes between the powders and the coatings. Both coatings show a similar microstructure. The semi-melted/un-melted matrix zones in both coatings could be attributed to the low temperature of HVOLF spray system (Sudaprasert et al. 2003). The formation of a light contrast shell around the WC grains confirm the presence of W_2C phase in both WC-17CoF and WC-17CoC coatings as illustrated in Figure 5-4b and Figure 5-5b respectively (Lekatou et al. 2015; Stewart et al. 2000). However, there is no clear

evidence in SEM images of both coatings that show the difference in decomposition degree between fine and coarse coatings.

In conclusion, both WC-17CoF and WC-17CoC coatings show similar microstructure features. There is no clear evidence that fine carbide WC-17CoF coating shows higher decomposition degree compared to coarse carbide WC-17CoC coating. This is supported by XRD and the quantitative X-ray diffraction analysis results. The low degree of decomposition could be attributed to the HVOLF spray system used in this study.

5.2.2 Mechanical Properties

When the high hardness and wear resistance are required, cermet coatings are frequently used. WC-Co sprayed by HVOF coating system is the common one due to their high wear resistance. The carbide phases provide the coating with high hardness, while the metal binder phase provides the coating with toughness. These mechanical properties are essential factors to improve the coating wear resistance. Recently, researches show that reducing the WC grain size to submicron or nanometre scale can improve the mechanical and wear performance of WC-Co coatings (Guilemany et al. 2006; Lekatou et al. 2015; Sánchez et al. 2010; Sudaprasert et al. 2003; Yin et al. 2010; Zhao et al. 2004; Zhao et al. 2006).

In this section, the results of microhardness and fracture toughness of both WC-17CoF and WC-17CoC coatings will be discussed, and the effect of WC grains size on these coating mechanical properties will be analysed. The scratch test is introduced as a new method to assess thermal sprayed coatings, (thick coatings). The results of this test on both two coatings will be discussed in the lightness of the effect of WC grains size. At the end, overall conclusion of the effect of WC grains size on the coatings mechanical properties will be given.

Microhardness

The microhardness average value of fine coating WC-17CoF is slightly higher than the microhardness of coarse coating WC-17CoC (see Table 5-3). The small difference in hardness between fine and coarse coatings could be attributed to the reduction of mean free path of the matrix as the carbide grains size is decreased (for given metal binder content) causing more restraint against deformation which leads to higher hardness (Chivavibul et al. 2007).

The earlier studies on HVOF-sprayed coatings stated that the coating hardness increases with decreasing carbide grains size, due to the higher degree of decomposition of WC in the finer carbide coatings (He and Schoenung 2002; Lekatou et al. 2015; Marple and Lima 2005; Upadhyaya 1998; Usmani et al. 1997; Yang et al. 2003b). It is sensible that the hardness increases with increasing content of W_2C in the coatings, since the W_2C phase (Hv=3000) is harder than the WC phase (Hv=1300–2300) (Engqvist et al. 1999).

However, the WC–Co coatings with nano/fine WC grains size usually exhibited higher hardness but lower wear resistance than conventional coatings (Chen et al. 2005; Dent et al. 2002; Qiao et al. 2003; Stewart et al. 1999). This disappointing performance of HVOF-sprayed nano/fine carbide coatings has been attributed to their higher tendency to decomposition.

Fracture toughness

It is well known that the fracture toughness of WC–Co thermally sprayed coatings mostly depends on the intersplat bond strength (Babu et al. 2008; Yang et al. 2003b).

The fracture toughness of the coarse WC-17CoC coating is higher than that of fine WC-17CoF coating, (see Table 5-3). This result agrees with the previous studies, which show that the fracture toughness of the HVOF coatings is increased with increasing of the carbide grains size (Upadhyaya 1998; Usmani et al. 1997; Yang et al. 2003b). Furthermore, the fracture toughness decreased with increased decomposition,

(since coatings with fine carbide grains normally show higher degree of decomposition), suggesting that the degree of decomposition is a more controlling factor for fracture toughness than the carbide grains size (Chivavibul et al. 2007; Usmani et al. 1997).

There is an optimum level of decomposition, which provides convenient inter-splat bond strength and, simultaneously, does not cause excessive deterioration of hardness and toughness of WC–Co coatings (Babu et al. 2008; Verdon et al. 1997).

SEM observations of crack paths generated from indentation test (shown in Figure 5-7) show that cracks favourably propagated through the interface between WC and the metal matrix. The same results reported by other researcher (Chivavibul et al. 2007).

Scratch test

The normal load at which the primary cracks are observed in scratch test is called critical load. Figure 5-36 shows the critical load at different sections of scratch test of both of fine WC-17CoF and coarse WC-17CoC coatings. The fine WC-17CoF coating exhibited higher critical load at all scratch sections, except at splats delamination where the load is same for both coatings. These higher critical loads appearing with fine carbide coating could be attributed to the fine carbide size which, for given cobalt content, reduced the mean free path of the matrix, consequently causing more restraint against deformation and increasing coating hardness (Chivavibul et al. 2007). As can be seen in Figure 5-36, the fine WC-17CoF coating endures a higher critical load (14 N), compared to the coarse WC-17CoC coating (10 N).

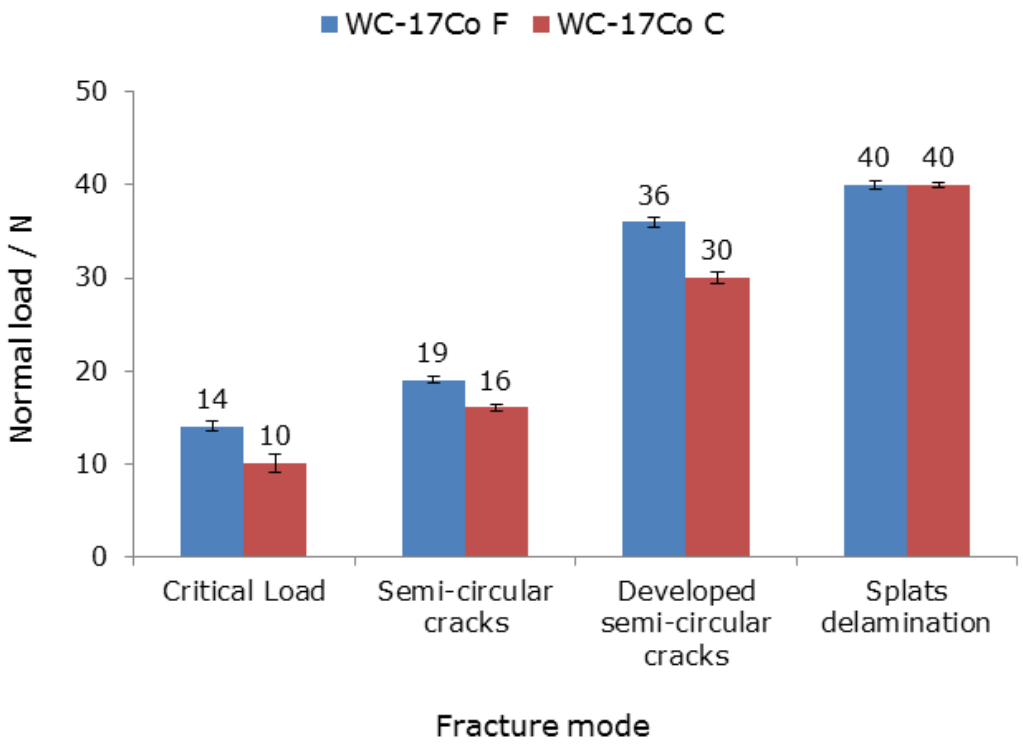

Figure 5-36: Critical loads of scratch test of WC-17CoF and WC-17CoC coatings at different fracture modes.

SEM-BSE images in Figure 5-14 show the mode of these initial narrow intergranular cracks, they are short and have no specific shape in both coatings. There are no cracks observed in the WC grains with fine WC-17CoF coating. While with coarse WC-17CoC coating, few cracks have been observed in the WC grains itself. Higher hardness of the fine WC grain coating could explain the lower level of damage observed on the scratched surface of this coating (Holmberg et al. 2006; Zuñega et al. 2012).

Semi-circular cracks travelling through the matrix are observed in scratch track of both fine WC-17CoF and coarse WC-17CoC coatings (Figure 5-15). Similar cracks were reported with thin coatings scratch test (Bull 1997; Holmberg et al. 2006). The cracks in the WC grains become very obvious with coarse WC-17CoC coating. Semi-circular cracks might follow the maximum tensile stress on the coating surface which developed in the tail of moving style tip (Ghabchi et al. 2014). Figure 5-16 shows the

mode of developed semi-circular cracks; they propagate through the matrix and the carbides grains and cover the complete scratch width in both WC-17CoF and WC-17CoC coatings.

At the high loads, (40 N), the delamination of the coating splats appears at the edges of the scratch track of both fine WC-17CoF and coarse WC-17CoC coatings, Figure 5-17. Delamination critical load might be indicating the cohesion of coating layers.

In conclusion, the coating with fine carbide grains, WC-17CoF, shows slightly higher hardness than coarse WC-17CoC coating. This could be attributed to the reduction of mean free path of the matrix as the carbide grains size is decreased. Due to the fracture toughness, the coating with coarse carbide grains, WC-17CoC, exhibited higher fracture toughness. In scratch test both coatings are following the same mechanism of failure. However, the fine carbide coating, WC-17CoF, shows higher critical loads approximately in all fracture sections through the scratch test. The scratch test might be considered as a tool to characterise thick coatings. Delamination critical load could be used to evaluate coating cohesion.

5.2.3 Sliding Wear Behaviour

The dry sliding wear behaviour of both WC-17CoF and WC-17CoC coatings will be discussed through this section. The sliding wear behaviour of thermally sprayed WC-Co coatings will be discussed in terms of the different in WC grain size.

In this research, both WC-17CoF, (with fine carbide grains), and WC-17CoC, (with coarse carbide grains), coatings show a similar wear mechanism. Nevertheless, the WC-17CoF coating endures a higher applied load before it shows the transition from mild to severe wear. The higher wear resistance of WC-17CoF coating could be attributed to its high hardness and low mean free path.

During the mild wear, both coatings approximately show a similar low wear rate, ($\approx 0.003 \times 10^{-6}$ $mm^3/N.m$), (Table 5-4), after same sliding distance of 1500 m for both

coatings. Although, the normal load with WC-17CoF (fine) coating (212 N) is higher than that with the WC-17CoC (coarse) coating (141 N). The wear rate of counter ball (sintered WC-6wt%Co) was same (0.009 x 10^{-6} mm^3/N.m) with both coatings, (Table 5-4), during mild wear.

Sintered WC-Co cermet with nano/fine carbide grain size has been reported to show higher performance in both sliding and abrasive wear resistance (Akasawa and Ai 1998; Jia and Fischer 1996b; Jia and Fischer 1997; O'quigley et al. 1997; Wayne et al. 1990).

The thermally sprayed WC–Co coatings with nano/fine carbide grain size normally exhibited higher hardness but lower performance in both sliding and abrasive wear resistance than conventional coatings (Chen et al. 2005; Chivavibul et al. 2007; Dent et al. 2002; Qiao et al. 2003; Stewart et al. 1999; Stewart et al. 2000; Usmani et al. 1997; Watanabe et al. 2006; Yang et al. 2003b). This poor wear resistance of thermally sprayed coatings with nano/fine carbide grain size has been attributed to their higher tendency to decomposition.

However, it is well-known that the formation of W_2C is largely dependent on the heating degree of the powders, higher heating degree leads to more W_2C phase (Guilemany and De Paco 1996). Since most of these studies were sprayed with gas-fuelled (HVOGF) system, which means that staring powders experience higher temperature during spraying process (compared to liquid-fuelled (HVOLF) system). This high temperature led to increase the decomposition degree especially with fine/nano carbide grain size coatings (Schwetzke and Kreye 1999; Sudaprasert et al. 2003). Decomposition through thermal spraying is normally understood to be deleterious for a wear performance of WC–Co cermet coating (Akasawa and Ai 1998; Qiao et al. 2001).

Some exceptions of improvement in mechanical and wear performance of WC–Co coatings achieved if the WC grain size is reduced to submicron or nanostructured were reported by (Basak et al. 2012; Fedrizzi et al. 2004; Guilemany et al. 2006;

Sánchez et al. 2010; Yang et al. 2006; Yin et al. 2010; Zhao et al. 2006; Zhu et al. 2001). They suggest that optimisation of spray parameter is necessary to improve the properties. The superior wear performance of the fine/nano coating is mainly attributed to the more uniform and finer distribution of the carbide particles and the existence of stronger intersplat boundaries (Lekatou et al. 2015).

There is an ideal level of decomposition, which provides acceptable intersplat bond strength and, simultaneously, does not lead to excessive deterioration of hardness and toughness of WC–Co coatings (Babu et al. 2008; Verdon et al. 1997). With the new HVOF thermal spray systems, especially liquid fuel systems and powder injection points; it could spray fine/nano carbide size coatings with lower levels of decomposition, resulting in microstructures and wear rates similar to that, or even better than their conventional counterparts (Stewart et al. 1999).

The Metallisation MET-JET 4L (Figure 3-1), which is the latest development of kerosene fuelled HVOF system used during this study, leads to low degree of decomposition in both fine and coarse carbide grain size coatings. This is due to the low temperature and short dwell time the powders experience during the spraying process. This favourable degree of decomposition by using HVOLF system, with the uniform and finer distribution of the carbide particles and the existence of stronger intersplat boundaries of fine carbide coating could be the main reasons leading to higher hardness and sliding wear resistance of WC-17CoF fine carbide coating compared to WC-17CoC coarse carbide coating.

The worn surface of coated discs, through mild wear, of both WC-17CoF and WC-17CoC coatings were shown in Figure 5-21 (a-d) and Figure 5-28 (a-c) respectively. Both coatings follow the same wear mechanism (as explained in detail in chapter 4, section 4.2.3).

During the preparation of coated discs for wear test, some pits will be generated on the coating top surface. These pits are simply the opening of porosity in the top surface of the coating after the grinding and polishing process, Figure 5-37.

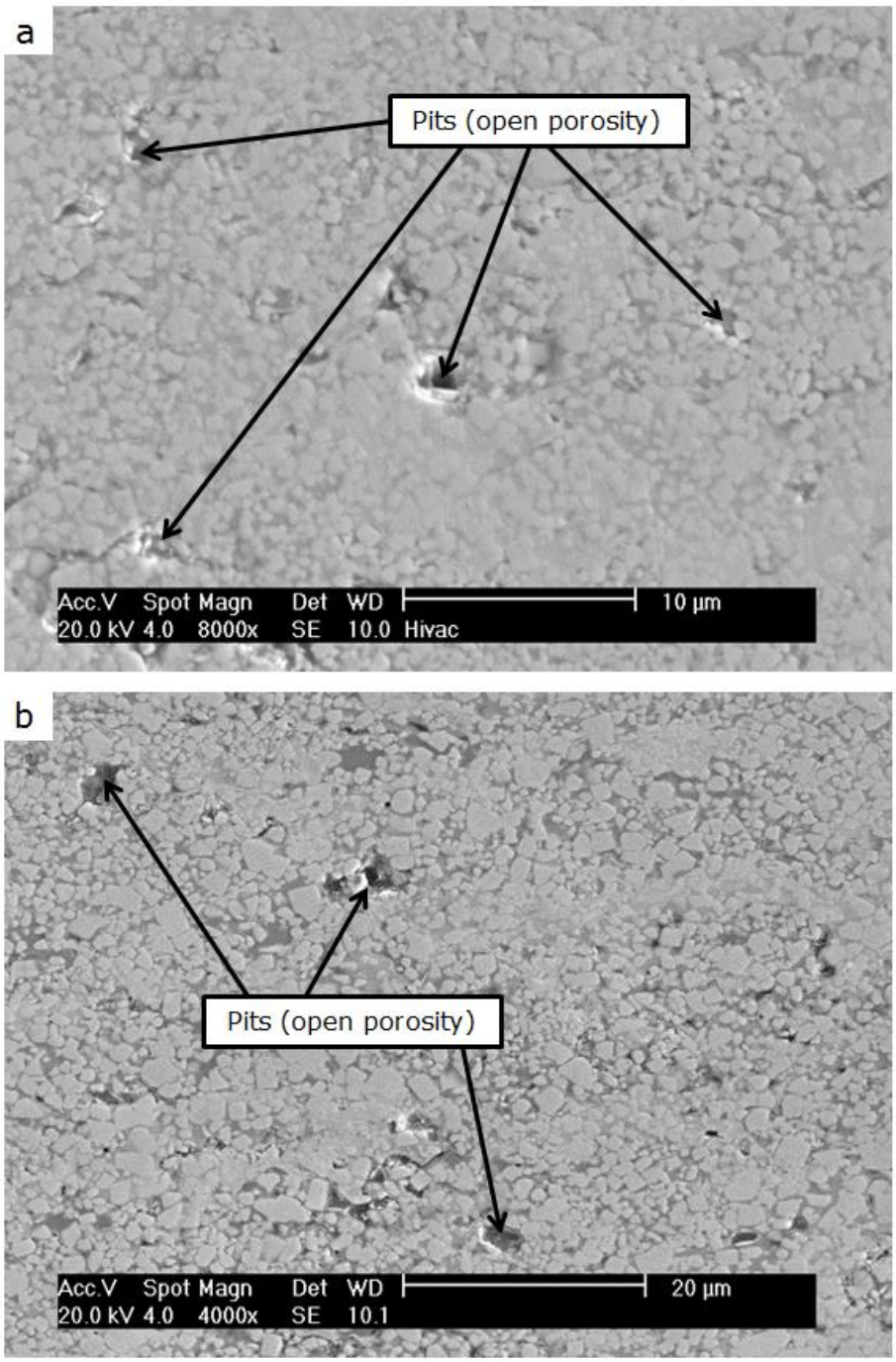

Figure 5-37: The SEM images of unworn coated discs show the pits on the top surface of the coating, (a) WC-17CoF coating and (b) WC-17CoC coating.

The wear debris will be generated after few rotations of the sliding wear test. This debris mostly will contain hard particles which work to increase the abrasive wear between the coated disc and the counterface ball. Consequently, the wear debris well be increased and moved through the test motion and adhere into these pits (Guilemany et

al. 2001), some protrusions were formed when the pits are completely filled with the wear debris.

Furthermore, due to the abrasive wear these protrusions will be ground away from the surface of the coating, (Luo et al. 2015). This transfer of tribofilm material between the coating and the counterpart is continuing through the whole time of wear test. As a result, the pits in the top surface of coating will be enlarged and filled by the brittle oxide film, which could be fracture easily under the repeatable load.

Figure 5-26b and Figure 5-33b are showing the wear debris adherent on the worn surface of the counterface ball sliding against WC-17CoF and WC-17CoC coatings respectively. Nevertheless, it is well known that through the mild wear the wear debris will be very fine, and works as a solid lubricant between the coated disc and the counterpart. This consequently will reduce the wear rate, (Yang et al. 2003b; Zhao et al. 2006).

Additionally, Figure 5-21(c-d) and Figure 5-28(b-c) exhibited narrow intergranular cracks in the worn coating top surface in both WC-17CoF and WC-17CoC coatings respectively during mild wear. These narrow cracks mostly start at the localised pits and propagate through the brittle oxide layer and between the grains boundaries. These cracks might be attributed to the interlaminar micro-cracks existence in the coating and the concentration of the stresses at the opening of these micro-cracks under normal and friction force. The repeatedly applied forces lead to plastic deformation in the coating layer and propagation of these cracks, (Celik et al. 2006; Luo et al. 2015; Shipway et al. 2005).

Due to the hard particles in wear debris, the sliding wear could be converted to the three-body abrasion rather than two-body sliding (Mohanty et al. 1996). This abrasive wear mechanism increases the scratches in the coated surface, and consequently increases the wear rate. However, due to the low load and fine wear debris particles during the mild wear this abrasive wear mode does not change the sliding wear rate. The

scratches on the top coated surfaces of both WC-17CoF and WC-17CoC coatings are very clear in Figure 5-24 and Figure 5-31 respectively.

The cross-section in the worn surface of both WC-17CoF and WC-17CoC coatings during mild wear are illustrated in Figure 5-21(e-f) and Figure 5-28(d-e) respectively. In both coatings, localised thick tribofilm layer is observed on the top of worn surface. Previous studies report that the cermet coatings through mild wear tests resulted in a few μm thick tribofilm (Engqvist et al. 2000; Yang et al. 2003b).

The EDX analysis of this tribofilm layers indicate that it is an oxide layer. This oxide layer was examined by other researchers and they report that it consist of WO_3 and M-$WO_{x,}$ where M is the metal binder (e.g. $CoWO_4$), (Bolelli et al. 2014; Engqvist et al. 2000). There is no evidence of any subsurface cracks, also no cracks were observed in the WC grains themselves in both WC-17CoF and WC-17CoC coatings.

The transition from mild to severe wear suddenly happens as a certain level of load is exceeded. This critical transition load depends on the properties of the material subjected to wear and also on the mechanical and thermal properties of the coating and the counterpart. Severe wear involves massive surface damage and large scale of coating material will transfer to the counterpart (Zhang and Alpas 1997).

The transition load from mild to severe wear for WC-17CoC coating (with coarse carbide grains) is somewhere between 141 N and 212 N. While, the WC-17CoF coating, (with fine carbide grains), endures for higher transition load, it is between 212 N and 282 N (see Table 5-4). The wear rate of counterface ball, (WC-6Co), sliding against WC-17CoF coating during severe wear (5×10^{-6} mm^3/N.m) is about seven times higher than the wear rate of the same ball sliding against WC-17CoC coating (0.7×10^{-6} mm^3/N.m), Table 5-4. The low wear of the ball sliding against WC-17CoC coating could be attributed to the low normal load and the low hardness of this coating.

Both WC-17CoF and WC-17CoC coatings demonstrate highly severe wear when worn with normal load above the transition load, this is very clear from Figure 5-22 (a-

d) and Figure 5-29 (a-d) respectively. The fragmentation of the WC grains under high loads will causes severe wear and the fractured hard particles will work as abrasives and lead to three-body abrasion (Zhu et al. 2001).

The cross-sections of the worn surface of both WC-17CoF and WC-17CoC coatings, show a thin tribofilm layer covering the whole wear track, Figure 5-22 (e-f) and Figure 5-29 (e-f) respectively. Severe wear tests produce thinner tribofilm layers, most likely the higher surface temperatures during the severe wear test, due to the high load, made the tribofilm softer and therefore thinner (Engqvist et al. 2000). Plate-like chips of severe wear debris that formed due to the fracture of the brittle transfer layer of both WC-17CoF and WC-17CoC coatings are shown in Figure 5-23 and Figure 5-30 respectively.

In conclusion, both WC-17CoF and WC-17CoC coatings show similar wear mechanisms. However, WC-17CoF coating, (with fine carbide grains), edures a higher load before it transitions from mild to severe wear. During the mild wear both coatings approximately show a similar wear rate. The high wear resistance of WC-17CoF coating could be attributed to the high hardness of this fine carbide coating which consequently increased with the reduction of mean free path of the matrix as the carbide grains size is decreased (for given metal binder content).

5.3 Conclusion

Through this chapter, the effect of WC grain size on the coating microstructure, mechanical properties and dry sliding wear behaviour was studied. Two identical feedstock powders have been used, Woka 3202 (WC-17wt%Co) with coarse WC grain size, and Woka 3202 FC (WC-17wt%Co) with fine WC grain size, which are denoted in this study as WC-17CoC and WC-17CoF, respectively. Both powders are agglomerated and sintered with a similar nominal size (-45+15 µm) produced by Sulzer Metco.

Both WC-17CoF and WC-17CoC coatings show similar microstructure features. There is no clear evidence that fine WC-17CoF coating shows higher decomposition degree compared to the coarse WC-17CoC coating. This is very clear from coatings

XRD pattern, (Figure 5-1) and from the coatings quantitative X-ray diffraction analysis (Table 5-2). The low degree of decomposition of both coatings could be related to the liquid-fuelled HVOF spray system, which is well-known its produce low temperature during the spraying process compared to the gas-fuelled HVOF system.

The coating with fine carbide grains, WC-17CoF, shows slightly higher hardness than conventional coating. The coating with coarse carbide grains, WC-17CoC, exhibited a higher fracture toughness, which could be attributed to the high mean free path of this coating compared to the coating with fine carbide grains. Through the scratch test, both coatings are following the same mechanism of coating failure. However, the fine carbide coating, WC-17CoF, shows higher critical loads approximately in all sections of the scratch test. The scratch test might be considered as a favourable tool to characterise thick coatings. Yet, more work should be done with this test for thick coatings to confirm that.

According to the sliding wear behaviour, both fine (WC-17CoF) and coarse (WC-17CoC) coating show similar wear mechanisms. However, WC-17CoF coating, with fine carbide grains, withstands a higher load before the transition from mild to severe wear. Through the mild wear both coatings approximately show a similar wear rate. The high wear resistance of WC-17CoF, (with fine carbide grains), coating could be attributed to the high hardness of this fine coating compared to the conventional coating.

CHAPTER 6 Effect of Metal Binder Content on Microstructure and Properties of WC-Co Coatings: Results and Discussion

6.1 Introduction

In the cermet coatings, the carbides ensure the coatings high hardness, while the metal binder is responsible for coatings cohesion and toughness.

In chapter 4, the effect of metal binder type on coating microstructure, mechanical properties and dry sliding wear behaviour was investigated in detail. Two powders, Amperit 518.074 (WC-12wt%Co) and Amperit 547.074 (WC-12wt%Ni), have been used. While, in chapter 5, the effect of WC grain size on coating microstructure, mechanical properties and dry sliding wear behaviour was examined in detail. Two powders, Woka 3202 (WC-17wt%Co) with coarse WC grain size, and Woka 3202 FC (WC-17wt%Co) with fine WC grain size have been used.

The effect of metal binder content on coating microstructure, mechanical properties and dry sliding wear behaviour can be obtained by comparing the results of coatings got from, Amperit 518.074 (WC-12wt%Co) and Woka 3202 (WC-17wt%Co) powders. Both powders have been produced through an agglomeration and sintering process with a similar nominal size (-45+15 µm). Also, the WC grains are coarse in both powders, as illustrated in Table 6-1. These powders will be denoted through this chapter as WC-12Co and WC-17Co respectively.

Table 6-1: WC grain size change between the powders and the coatings of WC-12Co and WC-17Co.

Coating material	WC grain size of powder / µm	WC grain size of coating / µm
WC-12Co	0.8 – 2.3	0.7 – 2.1
WC-17Co	0.8 – 2.5	0.6 – 2.1

6.2 Results and Discussion

6.2.1 Coatings Microstructure

The XRD patterns of both WC-12Co and WC-17Co starting powders and coatings are shown in Figure 6-1. The powders are completely identical, and consist of WC peaks with hexagonal close-packed (hcp) crystal structure and Co peaks with face-centred-cubic crystal structure (fcc).

For both coatings the retained peaks of WC (hcp) are very obvious. The cobalt peaks were retained with WC-17Co coating. Even though, the cobalt peaks in this coating were shifted to low angles compared to its powder and have been broader. The changes in cobalt peaks shape and position are attributed to the increase of lattice parameter of the metal binder phase, due to the formation of Co-base solid solution phase by dissolution of decomposition products such as W and C in metallic cobalt [Co(W, C)] during spraying process. Similar results of retained cobalt phase were reported by other researchers such as (Jacobs et al. 1999; Yang et al. 2003b). The retained cobalt phase of WC-17Co coating in this study could be explained by the low temperature of HVOLF used and the higher cobalt content compared to WC-12Co coating. In contrast, the cobalt peaks with WC-12Co coating are not observed any more in the XRD pattern of the WC-12Co coating. However, the WC-12Co coating has a diffuse diffraction halo centred at about $2\theta=43^{\circ}$, indicating an amorphous/nanocrystalline material. Similar amorphous/nanocrystalline phase were reported by many studies of thermally sprayed WC-Co coatings (Stewart et al. 2000; Sudaprasert et al. 2003). Furthermore, a number of decomposition phases can be seen in both coatings. Peaks corresponding to W_2C (hcp) and W (bcc), can be seen in both traces. However, the intensity of these phases with WC-12Co coating is higher compared with the same phases in WC-17Co coating. This higher intensity and the amorphous/nanocrystalline phase appearing with XRD pattern of WC-12Co coating, could be confirmation that this coating experienced higher decomposition during the coating process compared to WC-17Co coating.

Table 6-2 shows the quantitative X-ray diffraction analysis (Appendix B) of both WC-12Co and WC-17Co coatings; the relative portions of carbide phases weight percentage. Even though the accuracy of this method is not so precise since it does not account for the fraction of the amorphous and the metal binder (Co) phases. However, it still provides some useful information about the weight percentage of carbide phases. It shows that the W_2C and W phases are much higher in WC-12Co coating comparing to WC-17Co coating. This supporting the results of XRD diffraction and could be confirmation of the high decomposition of WC-12Co coating.

Table 6-2: Quantitative X-ray diffraction analysis of the crystalline tungsten-containing phases in WC-12Co and WC-17Co coatings.

Coating	WC (wt %)	W_2C (wt %)	W (wt %)
WC-12Co	87	10	4
WC-17Co	96	3	1

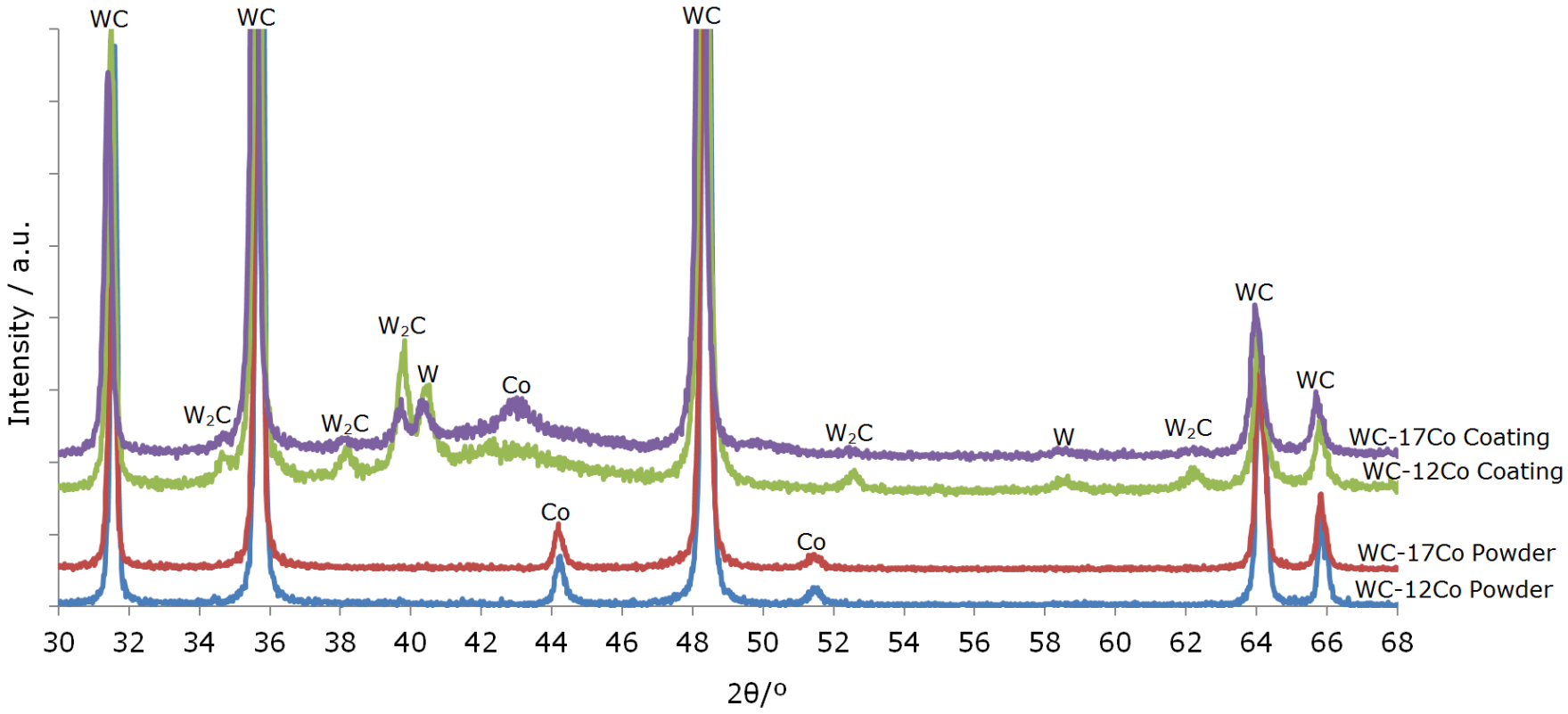

Figure 6-1: XRD pattern of WC-12Co and WC-17Co powders and coatings. Appendix A presents the ICDD-PDF of all phases appearing in this study.

Chivavibul et al. (2007) study the effect of cobalt content on the microstructure and mechanical properties of HVOF-sprayed WC-Co coatings. Figure 6-2 illustrate the XRD of their study, it shows that coating decomposition is increased as the cobalt content is decrease.

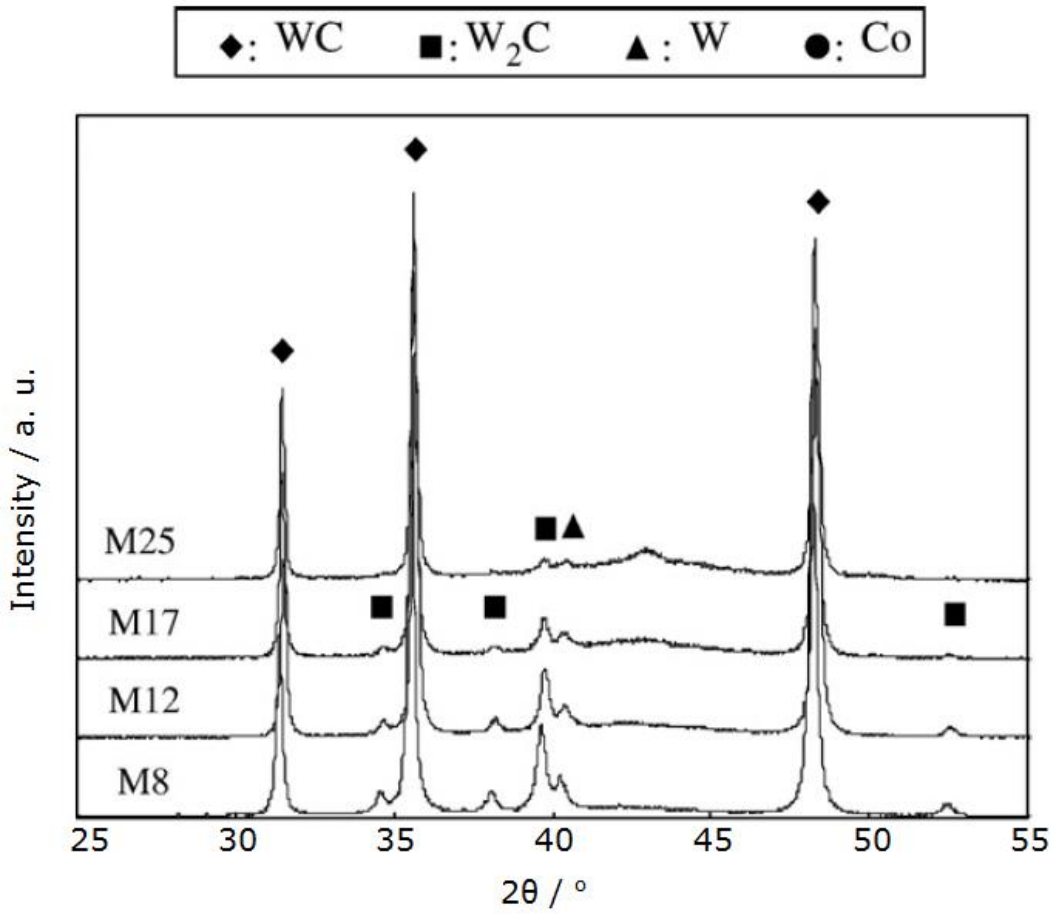

Figure 6-2: XRD results of the WC-Co coatings shows the effect of metal binder content on the coating decomposition (8, 12, 17 and 25 Co wt%) where M related to medium WC grain size (Chivavibul et al. 2007).

Also, they reported that the temperature of particles surface decreased with increasing Co content, Figure 6-3. The lower temperatures of powders with higher Co contents was attributed to the higher specific heat value of Co (0.42 J/g K) compared to that of WC (0.05 J/g K). Moreover, as the powder temperature at impact is higher than the melting point of Co (1495 °C), so the latent heat required for melting the Co is higher when Co content is higher. The in-flight particle temperature decreased as the Co

content of the powder increased and consequently, lowers the heating degree. The W_2C tended to decrease as the Co content increases.

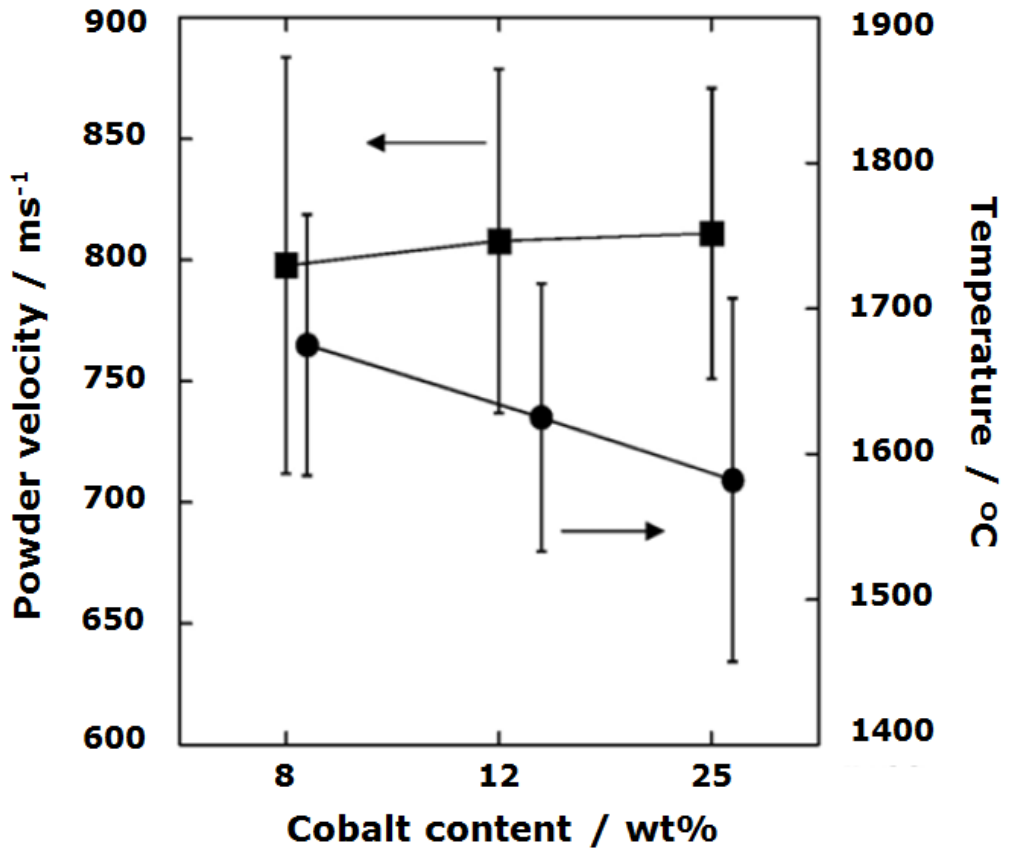

Figure 6-3: Variation of particles velocity and temperature with metal binder content (Chivavibul et al. 2007).

The coating microstructure of both WC-12Co and WC-17Co coatings are illustrated in SEM-BSE images in Figure 4-4 and Figure 5-5 respectively. Both coatings microstructure show the similar features. However, from Figure 4-4a its clear that WC-12Co coating shows more melted matrix areas compared to WC-17Co coating, and this could be related to the amorphous/nanocrystalline solid solution phase generated with WC-12Co coating, and the higher degree of decomposition with this coating.

6.2.2 Mechanical Properties

The results of microhardness and fracture toughness of both of WC-12Co and WC-17Co coatings are presented in Table 6-3. The WC-17Co coating, with higher Co content shows lower hardness and higher fracture toughness compared to WC-12Co coating.

The previous studies on HVOF-sprayed coatings reported that the coatings hardness decreased with increasing Co content, while the fracture toughness is increased. Generally, the toughness of such composites should increase as the binder content increases, because of crack blunting afforded by plastic deformation (Chivavibul et al. 2007; He and Schoenung 2002; Marple and Lima 2005; Milman et al. 1999; Saito et al. 2006; Usmani et al. 1997; Yandouzi et al. 2007; Yang et al. 2003b).

Table 6-3: Microhardness and fracture toughness of coatings of WC-12Co and WC-17Co coatings

Coating material	Microhardness $HV_{0.3/15}$ Kgf mm^{-2}	Fracture toughness K_{IC} (Evans & Wilshaw) MPa $m^{1/2}$	Fracture toughness K_{IC} (Niihara) MPa $m^{1/2}$
WC-12Co	1257 ± 27	5.6 ± 0.2	5.4 ± 0.2
WC-17Co	1056 ± 24	6.6 ± 0.1	7.3 ± 0.2

Fracture toughness equations, (Evans and Wilshaw) and (Niihara), explained in details in section 3.1.4.2 (±values represent the standard error in the mean, i.e. $\sigma/\sqrt{n}$).

Figure 6-4 summarises the scratch test results of both of WC-12Co and WC-17Co coatings. The WC-12Co coating, with low Co content, shows higher critical load at all scratch test sections; this could be related to the higher hardness of this coating. So, we can conclude that the critical load during scratch test is decreased with increasing of the metal binder, (cobalt), content.

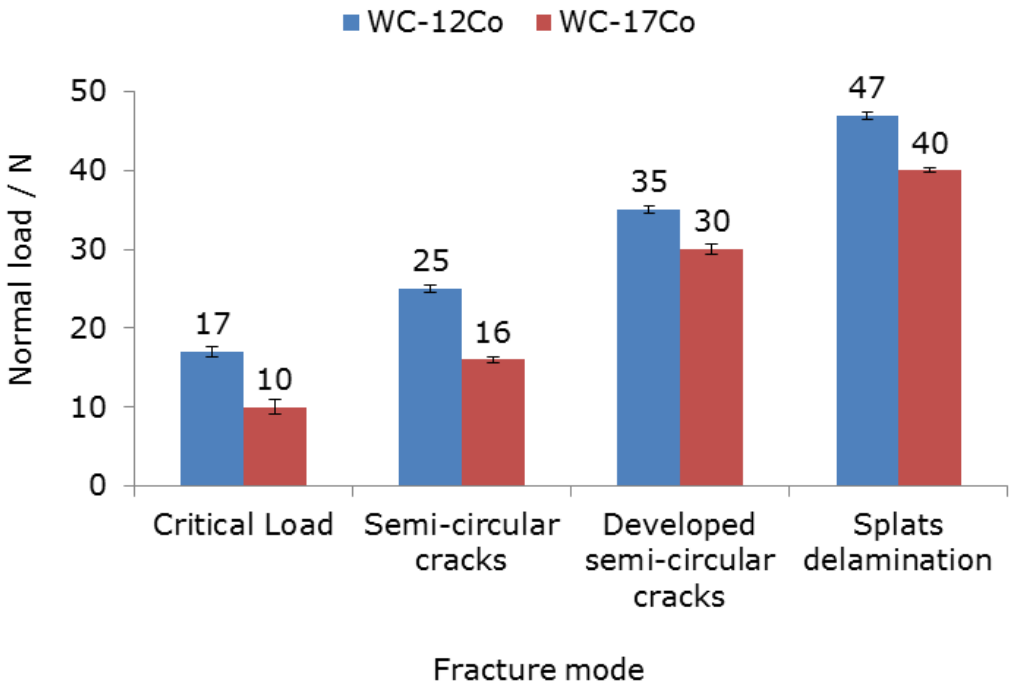

Figure 6-4: Critical loads of scratch test of WC-12Co and WC-17Co coatings at different scratch sections.

6.2.3 Sliding Wear Behaviour

Table 6-4 summarises the results of dry sliding test of WC-12Co and WC-17Co coatings. It shows that WC-12Co coating withstands a higher load before the transition from mild to severe wear. As discussed in chapters 4 and 5, both coatings follow the similar wear mechanism. However, comparing the wear rate during mild wear, (which is the wear mode of interest during industrial applications), when both WC-12Co and WC-17Co coatings are sliding under the same load, 141 N, for the same sliding distance, 1500 m, the wear rate of WC-17Co coating (with higher Co content) is four times higher than the wear rate of WC-12Co coating. In other words, the wear resistance of WC-12Co coating, (with low Co content), is four times higher than the wear resistance of WC-17Co coating. This could be attributed to the higher hardness of WC-12Co coating. This result fully agrees with the previous studies which reported that wear resistance is increased with a decrease in cobalt content (Saito et al. 2006; Sudaprasert 2002; Yandouzi et al. 2007).

In contrast, the wear rate of the counter ball, (WC-6Co sintered ball) sliding against the WC-12Co coating, under normal load of 141 N and sliding distance 1500 m, is more than sixteen times higher than the wear rate of the same ball sliding against the WC-17Co coating with similar conditions. This result could be attributed to the high hardness of WC-12Co coating.

Table 6-4: Results of dry sliding wear test of WC-12Co and WC-17Co coated discs and WC-6Co sintered balls.

Coating	Normal load N	Sliding distance m	Disc wear 10^{-6} mm^3	Disc wear rate 10^{-6} mm^3/N.m	Disc wear scar depth µm	Friction coefficient µ	Ball wear rate 10^{-6} mm^3/N.m
WC-12Co	141	1500	139	0.0007±0.00001	0.13	0.17	0.15±0.03
	212	1500	1187	0.004±0.0007	0.15	0.27	0.2±0.04
	282	1500	327310	0.8±0.1	2.50	0.59	0.9±0.2
	353	100	392736	11±2	4.60	0.08	16±3
WC-17Co	141	1500	583	0.0028±0.0002	0.25	0.08	0.009±0.001
	212	300	7490526	7.7±1.5	13.40	0.11	0.7±0.2
	282	225	5926227	93.3±10.3	54.38	0.13	6.7±0.9
	353	50	1443221	81±8.2	21.94	0.09	3.6±0.4

6.3 Conclusion

In conclusion, thermally sprayed cermet coating with low metal binder content, (WC-12Co coating), shows higher decomposition compared with one with high metal binder content (WC-17Co coating). Microhardness, scratch critical load and sliding wear resistance are increased as the metal binder, (cobalt), content decreased. Whereas, the coating fracture toughness is increased with the increase of the metal binder content.

CHAPTER 7 Summary, conclusions and recommendations

7.1 Summary and conclusions

Tungsten carbide cermet has become extensively used in a great number of applications, such as cutting tools, rock and earth drilling tools, and other engineering applications. This is attributed to its good corrosion and wear resistance. However, finding alternative materials for replacing cobalt is essential due to the shortage, high cost, the limitation of meeting the increasing requirements of work conditions, and its high toxicity and carcinogenic nature.

Based on these reasons, there has been a significant need to replace cobalt with other metals, especially iron and nickel. Nickel has received the most attention as an alternative binder where its structure and physical properties are about similar to cobalt. However, compared with WC–Co system which has been widely investigated due to its commercial importance, there is still limited information and a lack of knowledge on alternative binders based on Nickel. Thus it appeared to be worthwhile to carry out respective and reliable investigations to cover these points which will be the focus of this research.

The aim behind this project has been to provide more investigations on microstructure, mechanical properties and sliding wear behaviour of thermally sprayed cermet coatings. This has been carried out throughout a number of objectives which have been investigated in details during this project. The conclusions of this project can be illustrated in the following points:

1. In the first objective, the effect of metal binder type on the coating microstructure, mechanical properties and dry sliding wear behaviour of WC-M thermally sprayed coatings has been investigated. Two identical feedstock powders, Amperit 518.074 (WC-12wt%Co) and Amperit 547.074 (WC-12wt%Ni), have been used, denoted in this study as WC-12Co and WC-12Ni

respectively. Both powders are agglomerated and sintered with a similar nominal size (-45+15µm).

According to the coating microstructure, the W-Co-C system shows low temperature at which liquid forms compared to the W-Ni-C system. This leads to higher solubility of WC during WC-12Co coating, which means more decomposition of WC through WC-12Co coating compared with WC-12Ni coating. From the XRD diffraction, the cobalt peaks detected in the powder and not in the coating, suggest that most of the cobalt is present as amorphous/nanocrystalline binder phase. This amorphous/nanocrystalline phase is due to the solid solution phase formed by dissolution of decomposition products such as W_2C, W and C in metallic binder, (cobalt), during spraying process, whereas nickel phase is retained in the WC-12Ni coating. In spite of limitations of the quantitative X-ray diffraction analysis, however, it is expected to provide some useful information related to the degree of decomposition. It shows that WC-12Co coating represents a high degree of decomposition compared to the WC-12Ni coating.

Regarding the mechanical properties, WC-12Co coating shows higher hardness compared to the WC-12Ni coating. This could be attributed to the higher decomposition and the generation of hard phase of W_2C as discussed in microstructure section. Also, WC-12Co coating exhibited a higher fracture toughness compared to WC-12Ni coating, which could be related to the higher solubility of WC in the liquid cobalt binder than the nickel binder. Through the scratch test, both WC-12Co and WC-12Ni coatings are following the same mechanism of coating failure. However, WC-12Co coating withstands higher critical loads in all fracture sections through the scratch test. The scratch test could be used to characterise thick coatings and to predict the wear behaviour of these coatings. However, more work should be done with this test for thick coatings to confirm it as an investigation tool.

Due to the sliding wear behaviour, both WC-12Co and WC-12Ni coatings show similar wear mechanism. However, WC-12Co coatings endure higher loads before the transition from mild to severe wear. During mild wear both coatings

show a similar wear rate. The high wear resistance of WC-12Co coating could be attributed to its favourable hardness and fracture toughness compared with WC-12Ni coating. These good mechanical properties of WC-12Co coating can be related to the coating microstructure. WC-12Co coating shows higher decomposition and also higher solubility of WC in liquid cobalt compared to WC-12Ni coating.

2. Through the second objective, the effect of WC grain size on the coating microstructure, mechanical properties and dry sliding wear behaviour was studied. Two identical feedstock powders have been used, Woka 3202 (WC-17wt%Co) with coarse WC grain size, and Woka 3202 FC (WC-17wt%Co) with fine WC grain size, denoted in this study as WC-17CoC and WC-17CoF, respectively. Both powders are agglomerated and sintered with a similar nominal size (-45+15µm).

   Both coatings WC-17CoF (with fine carbide grains) and WC-17CoC (with coarse carbide grains) show similar microstructure features. There is no clear evidence that WC-17CoF coating with fine WC grain size shows higher decomposition degree compared to conventional WC-17CoC coating with coarse WC grain size, (as mentioned in the most previous studies in the subject). The low degree of decomposition of fine coating could be related to the liquid-fuelled HVOF spray system, which is well-known to produce low temperature during the spraying process compared to the gas-fuelled HVOF system, since the decomposition degree mainly depends on the spray process temperature. It increases as the spray process temperature increased.

   The coating with fine carbide grains, WC-17CoF, shows slightly higher hardness than conventional coating. The coating with coarse carbide grains, WC-17CoC, exhibited a higher fracture toughness, which could be attributed to the high mean free path of this coating compared to the fine coating. Through the scratch test, both coatings are following the same mechanism of coating failure. However, the fine carbide coating, WC-17CoF, shows higher critical loads approximately in all sections of the scratch test. The scratch test might be considered as a

favourable tool to characterise thick coatings. Yet, more work should be done with this test for thick coatings to confirm that.

According to the sliding wear behaviour, both fine carbide grains (WC-17CoF) coating and coarse carbide grains (WC-17CoC) coating show similar wear mechanism. However, WC-17CoF coating withstands a higher load before the transition from mild to severe wear. Through the mild wear both coatings approximately show a similar wear rate.

3. Objective three investigates the effect of metal binder content on the coatings microstructure, mechanical properties, and dry sliding wear behaviour using WC-12wt%Co and WC-17wt%Co feedstock powders. Both powders are agglomerated and sintered with similar particle size (-45+15 µm). Thermally sprayed cermet coating with low metal binder content, (WC-12Co coating), shows higher decomposition compared with one with high metal binder content (WC-17Co coating). Microhardness, scratch critical load and sliding wear resistance are increased as the metal binder, (cobalt), content decreased. Whereas, the coating fracture toughness is increased with the increase of the metal binder content.

4. The fourth objective of this study is to see if the sliding wear behaviour could be predicted from scratch test data. In previous chapters, when only one variable is investigated, in all cases coatings with higher scratch critical load shows at the same time higher wear resistance.

   In chapter four, where the effect of metal binder type is analysed, WC-12Co coating shows higher critical load through all scratch test sections compared to WC-12Ni coating (Figure 4-40). Also, WC-12Co coating exhibits higher wear resistance compared to WC-12Ni coating (Table 4-4).

   When the effect of WC grain size assessed in chapter five, the WC-17CoF coating with fine carbide grains shows higher scratch critical load at all scratch sections (Figure 5-36) and higher wear resistance as well compared with WC-17CoC coating with coarse carbide grains (Table 5-4).

Due to the metal binder content effect, as discussed in chapter six, WC-12Co coating with low cobalt content shows higher scratch critical load in all scratch sections (Figure 6-4) and also exhibited higher wear resistance (Table 6-4) compared to WC-17Co coating.

Figure 7-1 show the relationship between the average wear transition load, (where the wear behaviour changes from mild to severe wear), and the scratch test critical load at different scratch sections. Figure 7-1(a, b and d) illustrate the relation between wear transition load and scratch load at critical cracks (first cracks observed), semi-circular cracks load and splats delamination load respectively, these figures do not show any unique relation between these scratch loads and wear transition load. However, Figure 7-1c which draws the relation between the wear transition load and scratch critical load at developed semi-circular cracks section shows a linear relationship between scratch load at this section and wear transition load. So, scratch critical load at developed semi-circular cracks section might be used to predict sliding wear behaviour and which coating material will withstand higher loads before the transition from mild to severe wear takes place.

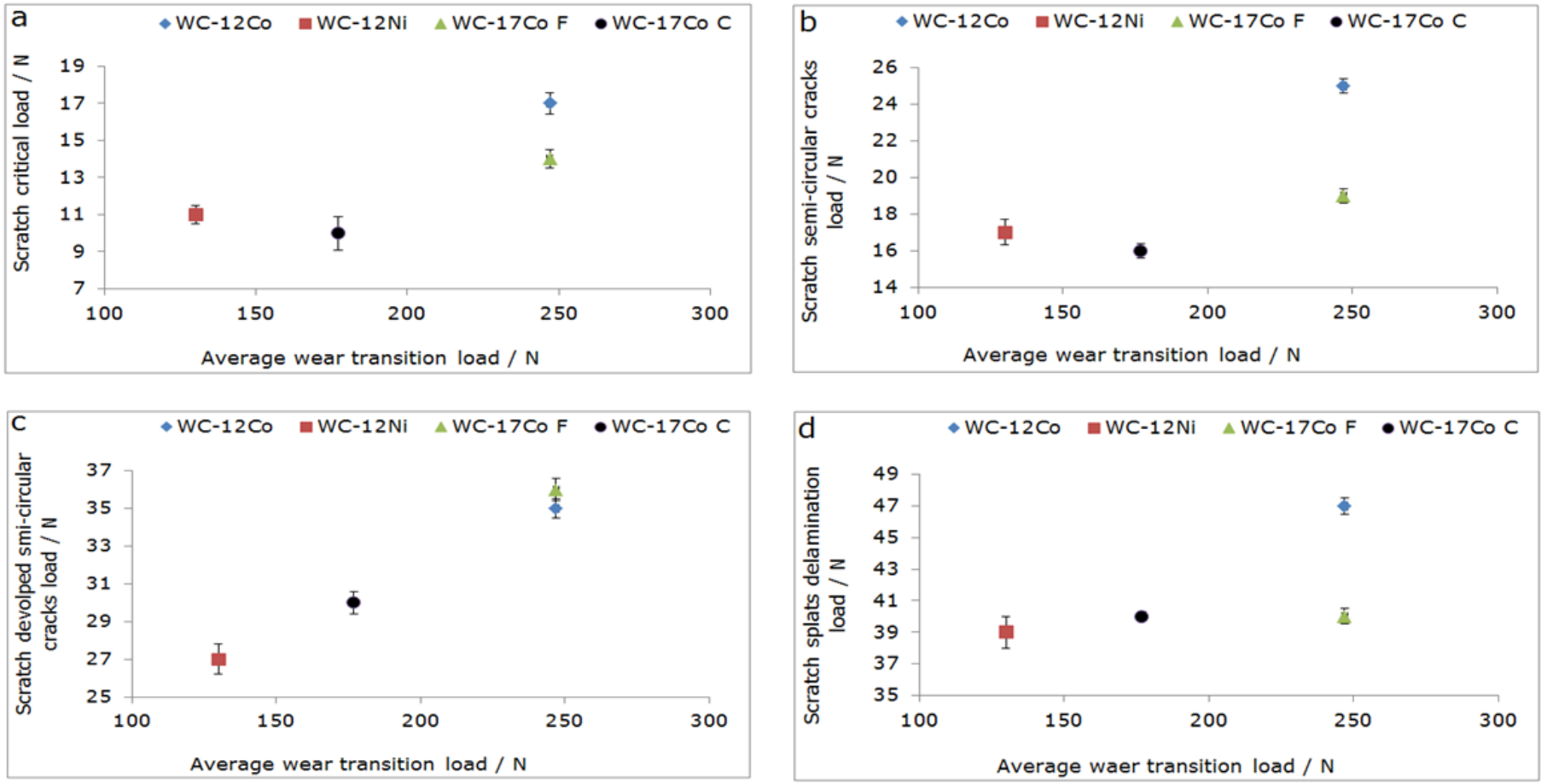

Figure 7-1: The relation between the scratch critical load (at different scratch sections) and the average wear transition load to show if the scratch critical load can be used to predict the wear behaviour.

7.2 Recommendations and future works

The attempt of replacing cobalt by nickel as a metal binder in the cermet thermal spray coating in this study gives very promising results with coating mechanical properties and sliding wear resistance, especially during mild wear conditions. However, further work should be done in this subject of knowledge, which can include the following points:

- Due to the limited polished studies to assess the nickel as a metal binder in WC-M cermet coatings and partially or completely replacing cobalt as a metal binder, extra work can be done in this area.

- Examining the WC-Ni thermal spray coatings with different spray systems, various metal binders content and with different carbide grain size.

- Using other metals, such as chromium, with nickel metal binder for WC-M cermet coatings to study their mechanical and wear performance.

- Phase diagrams study of W-C-Co and W-C-Ni systems with different metal binder content and when additional metals like Cr is added could lead to essential improvements in mechanical properties and wear resistance of WC-Ni coatings.

Scratch test could be an appropriate new method to evaluate the cohesion of thermal spray coatings, and predict the wear behaviour of these thick coatings. However, to confirm this, extra work of scratch test with thermally sprayed coatings should be done.

Appendixes

Appendix A: Powder Diffraction Standards

The powder diffraction standards are taken from the 2005 ICDD-International Centre for Diffraction Data. The PDF-Powder Diffraction File consisting of WC, Co, Ni, W_2C and W are shown.

Tungsten Carbide (WC)		$2\theta^{\circ}$	d (A°)	Intensity	h	k	l
Lattice	Hexagonal	31.511	2.83690	4.44	0	0	1
S.G.	P-6m2 (187)	35.641	2.51702	99.9	1	0	0
a	2.90620	48.300	1.88278	84.1	1	0	1
c	2.83780	64.021	1.45320	15.6	1	1	0
Radiation	Cuka1	65.784	1.41845	4.7	0	0	2
Pattern	00-073-1047	73.107	1.29338	15.6	1	1	1
I/I_{cor}	14.70	75.479	1.25851	7.3	2	0	0
		77.123	1.23573	13.5	1	0	2
		84.072	1.15039	10.8	2	0	1

Cobalt (Co)		$2\theta^{\circ}$	d (A°)	Intensity	h	k	l
Lattice	FCC	44.217	2.04670	100	1	1	1
S.G.	Fm3m (225)	51.524	1.77230	40	2	0	0
a	3.5447	75.855	1.25320	25	2	2	0
Radiation	Coka1	92.227	1.06880	30	3	1	1
Pattern	00-015-0806	97.660	1.02330	12	2	2	2

Nickel (Ni)		2θ°	d (A°)	Intensity	h	k	l
Lattice	FCC	44.508	2.034	100	1	1	1
S.G.	Fm3m (225)	51.847	1.762	42	2	0	0
a	3.52380	76.372	1.246	21	2	2	0
Radiation	Cuka1	92.947	1.0624	20	3	1	1
Pattern	00-004-0850	98.449	1.0172	7	2	2	2
		121.936	0.881	4	4	0	0
		144.679	0.8084	14	3	3	1
		155.666	0.788	15	4	2	0

Tungsten (W)		2θ°	d (A°)	Intensity	h	k	l
Lattice	BCC	40.265	2.238	100	1	1	0
S.G.	Im3m (229)	58.276	1.582	15	2	0	0
a	3.16480	73.198	1.292	23	2	1	1
Radiation	Cuka1	87.024	1.1188	8	2	2	0
Pattern	00-004-0806	100.651	1.0008	11	3	1	0
I/I_{cor}	18.00	114.928	0.9137	4	2	2	2
		131.184	0.8459	18	3	2	1
		153.603	0.7912	2	4	0	0

Tungsten carbide ($W_2C_{0.85}$)		$2\theta^{\circ}$	d (A°)	Intensity	h	k	l
Lattice	Hexagonal	18.773	4.72300	0.1	0	0	1
S.G.	P-3m1 (162)	19.755	4.49034	0.1	1	0	0
a	5.18500	27.384	3.25429	0.1	1	0	1
c	4.72300	34.570	2.59250	22.3	1	1	0
Radiation	Cuka1	38.075	2.36150	23.8	0	0	2
Pattern	01-075-0768	39.625	2.27264	99.9	-1	-1	1
I/I_{cor}	11.19	43.252	2.09009	0.1	1	0	2
		44.653	2.02772	0.1	2	0	1
		52365	1.74580	15.0	-1	-1	2
		53.984	1.69719	0.1	2	1	0
		56.511	1.62715	0.1	2	0	2
		57.669	1.59720	0.1	2	1	1
		58.588	1.57433	0.1	0	0	3
		61.947	1.49678	16.4	3	0	0
		65.349	1.42684	0.1	3	0	1
		69.841	1.34565	15.7	-1	-1	3
		72.919	1.29625	2.1	2	2	0
		75.078	1.26423	15.9	3	0	2
		76.082	1.25003	11.9	-2	-2	1
		79.533	1.20423	0.1	-3	-1	1
		81.443	1.18075	2.2	0	0	4
		83.731	1.15421	0.1	-2	-1	3
		85.358	1.13632	3.0	-2	-2	2
		86.657	1.12259	0.1	4	0	0
		88.736	1.10159	0.1	-3	-1	2
		89.708	1.09216	0.1	4	0	1

Appendix B: Quantitative X-ray diffraction analysis (QXRD)

The intensities of diffraction peaks from a given phase are related to the phase's abundance in a mixture, this is the base of Quantitative X-ray diffraction analysis (QXRD). A popular method for general quantitative phase analysis is the Reference Intensity Ratio (RIR). This method consist of comparing the intensity of one or more peaks of a phase with the intensity of a peak of a standard (usually the corundum 113 reflection) in a 50:50 mixture by weight. The weight abundance can be determined for every phase in the sample, if these intensity ratios are known for all phases in a sample. The advantage of RIR method is that it is straight forward and easy to implement. Corundum has been chosen as internal standard due to it is stability, readily available, and has relatively few diffraction peaks, reducing the probability of overlaps on the phases of interest in the unknown samples. Corundum as a reference material also facilitates analysis and preparation of standards, a databases such as the ICDD powder diffraction file often list I/Icor value (intensity of the phase 100% peak divided by the 100% peak of corundum), (Chipera and Bish 2013). Equation 12-2, (Cullity and Stock 2001), represent the intensity of the most intense peak for phase α in a mixture of two phases α and β:

Cullity equation 12-2:

$$I_\alpha = \frac{K_\alpha C_\alpha}{\mu_m}$$

Where: C_α = The volume friction of α in the mixture.

μ_m= The linear absorption coefficient of the mixture.

K_α= Constant.

In terms of the weight fraction: $C_\alpha = \frac{w_\alpha \rho_m}{\rho_\alpha}$

Where: ρ_m= Density of the mixture.

ρ_α= Density of phase α.

w_α= Weight fraction of phase α.

Therefore: $I_\alpha = \frac{K_\alpha w_\alpha \rho_m}{\rho_\alpha \mu_m}$

Dividing by the equivalent expression for β:

$$\frac{I_\alpha}{I_\beta} = \frac{K_\alpha \rho_\beta}{K_\beta \rho_\alpha} . \frac{w_\alpha}{w_\beta} \qquad 1$$

For an equal mixture of α and corundum:

$$\left(\frac{I}{I_c}\right)_\alpha = \frac{K_\alpha \rho_c}{K_c \rho_\alpha}$$

Divide by the equivalent expression for β:

$$\frac{\left(\frac{I}{I_c}\right)_\alpha}{\left(\frac{I}{I_c}\right)_\beta} = \frac{K_\alpha \rho_\beta}{K_\beta \rho_\alpha}$$

Substitute into 1:

$$\frac{w_\alpha}{w_\beta} = \frac{I_\alpha}{I_\beta} \frac{\left(\frac{I}{I_c}\right)_\beta}{\left(\frac{I}{I_c}\right)_\alpha}$$

Summary:

The intensity of a diffraction peak depends not only on the concentration of the phase, but also on many other factors, some of which depend on the setup of the diffractometer and others that depends on the material, its crystal structure, and which plane is diffracting –e.g. structure factor, multiplicity, temperature factor and others that depend on the diffraction angle –e.g. Lorentz-polarisation factor. These are represented in the above equations by the constant K. Hence, to calculate concentrations from peak intensities, these other factors must be taken into account. A simple way to doing this is with the Reference Intensity Ratios (RIR) for each phase, I/Icor, the ratio of the most intense peak for the phase to the most intense peak for corundum in equal masses. This method will only be accurate if the measurement is from powder diffraction – a statistically large enough number of randomly oriented crystals.

Appendix C: The volume of spherical cap

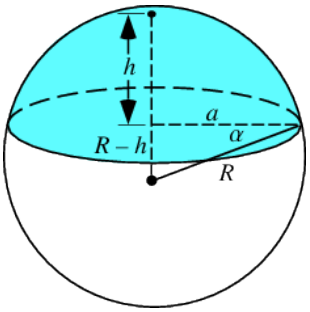

A portion of a ball which cut by a plane is called a spherical cap or a spherical segment, as illustrated in the figure above. The volume of the spherical segment, (Polyanin and Manzhirov 2006), giving by the following equation:

$$V = \frac{1}{6}\pi h(3\,a^2 + h^2) \quad (1)$$

Where: R = The radius of the ball (mm).

h = The height of a spherical cap (mm).

a = The radius of the spherical segment (mm).

Appling the Pythagorean theorem gives:

$$R^2 = a^2 + (R - h)^2 \quad (2)$$

$$a^2 = 2Rh - h^2 \quad (3)$$

By substituting 3 in 1, the equation of the volume of spherical cap can be written as follow:

$$V = \pi h^2\left(R - \frac{h}{3}\right) \quad (4)$$

Where the height of spherical cap (h) is:

$$h = R - (R - h) \quad (5)$$

From equation 2:

$$(R - h) = \sqrt{(R^2 - a^2)} \quad (6)$$

So, the height of spherical cap can be given by the following equation:

$$h = R - \sqrt{(R^2 - a^2)} \quad (7)$$

References

Akasawa T. and K. Ai, 1998. Wear properties of WC–Co coatings with plasma and high velocity oxyfuel spraying, in: C. Coddet (Ed.), Thermal Spray: Meeting the Challenges of the 21st century, ASM Int., Materials Park, OH, USA, pp. 281–286.

Alcala J., A. C. Barone and M. Anglada. 2000. The influence of plastic hardening on surface deformation modes around Vickers and spherical indents. Acta Materialia 48(13):3451-3464.

Aristizabal M., N. Rodriguez, F. Ibarreta, R. Martinez and J. M. Sanchez. 2010. Liquid phase sintering and oxidation resistance of WC–Ni–Co–Cr cemented carbides. International Journal of Refractory Metals and Hard Materials 28(4):516-522.

ASM Handbook Volume 5: Surface Engineering. ASM International, Metals Park, OH, USA; (1994)

Babu P. S., Basu B. and G. Sundararajan. 2008. Processing–structure–property correlation and decarburization phenomenon in detonation sprayed WC–12Co coatings. Acta Materialia 56(18):5012-5026.

Ban Z.G. and Shaw L.L. 2003. Characterization of thermal sprayed nanostructured WC-Co coatings derived from nanocrystalline WC-18wt.% Co powders. Journal of Thermal Spray Technology 12(1):112-119.

Bartuli C., T. Valente, F. Casadei and M. Tului. 2007. Advanced thermal spray coatings for tribological applications. Proceedings of the Institution of Mechanical Engineers, Part L: Journal of Materials: Design and Applications 221(3):175-185.

Bartuli C., Valente T., Cipri F., Bemporad E. and Tului M. 2005. Parametric study of an HVOF process for the deposition of nanostructured WC-Co coatings. Journal of Thermal Spray Technology 14(2):187-195.

Basak A. K., J. P. Celis, M. Vardavoulias and P. Matteazzi. 2012. Effect of nanostructuring and Al alloying on friction and wear behaviour of thermal sprayed WC–Co coatings. Surface and Coatings Technology 206(16):3508-3516.

Bell T. 1992. Surface engineering: its current and future impact on tribology. Journal of Physics D: Applied Physics 25(1A):A297.

Bell T., H. Dong and Y. Sun. 1998. Realising the potential of duplex surface engineering. Tribology International 31(1):127-137.

Berger L. M. 2007. Hardmetals as thermal spray coatings. Powder Metallurgy 50(3):205-214.

Berger L. M. 2015. Application of hardmetals as thermal spray coatings. International Journal of Refractory Metals and Hard Materials 49:350-364.

Berger L. M., S. Saaro, T. Naumann, M. Wiener, V. Weihnacht, S. Thiele and J. Suchánek. 2008. Microstructure and properties of HVOF-sprayed chromium alloyed WC-Co and WC-Ni coatings. Surface and Coatings Technology 202(18):4417-4421.

Birks N, G. H. Meier and F. S. Pettit. 2006. Introduction to the high temperature oxidation of metals: 2nd Edition, Cambridge University Press, UK.

Bolelli G., L. M. Berger, M. Bonetti and L. Lusvarghi. 2014. Comparative study of the dry sliding wear behaviour of HVOF-sprayed WC–(W, Cr) 2 C–Ni and WC–CoCr hardmetal coatings. Wear 309(1):96-111.

Borrero-López O., M. Hoffman, A. Bendavid and P. J. Martin. 2010. The use of the scratch test to measure the fracture strength of brittle thin films. Thin Solid Films 518(17):4911-4917.

Bull S. J. 1991. Failure modes in scratch adhesion testing. Surface and Coatings Technology 50(1):25-32.

Bull S. J. 1997. Failure mode maps in the thin film scratch adhesion test. Tribology International 7(30):491-498.

Bull S. J. 1999. Can scratch testing be used as a model for the abrasive wear of hard coatings? Wear 233:412-423.

Bunshah R. F. 2001. Handbook of hard coatings: deposition technologies, properties and applications. Noyes Publication. William Andrew Publishing, LLC. Norwich, New York, U.S.A.

Cantera E. L. and B. G. Mellor. 1998. Fracture toughness and crack morphologies in eroded WC–Co–Cr thermally sprayed coatings. Materials Letters 37(4):201-210.

Çelik O. N. 2013. Microstructure and wear properties of WC particle reinforced composite coating on Ti6Al4V alloy produced by the plasma transferred arc method. Applied Surface Science 274:334-340.

Celika E., O. Culha, B. Uyulgan, N. F. Ak Azem, I. Ozdemir and A. Turk. 2006. Assessment of microstructural and mechanical properties of HVOF sprayed WC-based cermet coatings for a roller cylinder. Surface and Coatings Technology 200(14):4320-4328.

Chang -Jiu Li, A. Ohmori and Y. Harada. 1996. Effect of powder structure on the structure of thermally sprayed WC-Co coatings. Journal of materials science 31(3):785-794.

Chena H., C. Xu, Q. Zhou, I. M. Hutchings, P. H. Shipway and J. Liu. 2005. Micro-scale abrasive wear behaviour of HVOF sprayed and laser-remelted conventional and nanostructured WC-Co coatings. Wear 258(1-4):333-338.

Cheng D., Q. Xu, G. Tapaga and E. J. Lavernia. 2001. A numerical study of high-velocity oxygen fuel thermal spraying process. Part I: Gas phase dynamics. Metallurgical and Materials Transactions A 32(7):1609-1620.

Cheng-Chang Jia, Hua Tang, Xue-Zhen Mei, Fa-Zhang Yin, and Xuan-Hui Qu. 2005. Spark plasma sintering on nanometer scale WC–Co powder. Materials Letters 59(19–20):2566-2569.

Chipera S. J. and Bish D. L. 2013. Fitting full X-ray diffraction patterns for quantitative analysis: a method for readily quantifying crystalline and disordered phases. Advances in Materials Physics and Chemistry, Vol. 3 No. 1A, pp. 47-53.

Chivavibul P., M. Watanabe, S. Kuroda and K. Shinoda. 2007. Effects of carbide size and Co content on the microstructure and mechanical properties of HVOF-sprayed WC-Co coatings. Surface and Coatings Technology 202(3):509-521.

Choi W. B., L. Prchlik, S. Sampath and A. Gouldstone. 2009. Indentation of metallic and cermet thermal spray coatings. Journal of Thermal Spray Technology 18(1):58-64.

Culha O., M. Toparli, E. Celik, T. Aksoy and H. S. Soykan. 2009. Indentation size effect on mechanical properties of HVOF sprayed WC based cermet coatings for a roller cylinder. Surface & Coatings Technology 203(14):2052-2057.

Cullity B. D. and S. R. Stock. 2001. Elements of X-ray Diffraction. 3rd ed. Prentice-Hall, Upper Saddle River, NJ. USA.

Davis J. R. 2004. Handbook of thermal spray technology. ASM International, Materials Park, OH, USA.

Dent A. H., S. DePalo and S. Sampath. 2002. Examination of the wear properties of HVOF sprayed nanostructured and conventional WC-Co cermets with different binder phase contents. Journal of Thermal Spray Technology 11(4):551-558.

DePalo S., M. Mohanty, H. Marc-Charles and M. Dorfman. 2000. Fracture toughness of HVOF sprayed WC-Co coatings. ASM International, Thermal Spray: Surface Engineering via Applied Research(USA):245-250.

Dvornik M. I. and A. V. Zaytsev. 2013. Research of surfaces and interfaces increasing during planetary ball milling of nanostructured tungsten carbide/cobalt powder. International Journal of Refractory Metals and Hard Materials 36:271-277.

Engqvist H., H. Hogberg, G. A. Botton, S. Ederyd and N. Axén. 2000. Tribofilm formation on cemented carbides in dry sliding conformal contact. Wear 239(2):219-228.

Engqvist H., S. Ederyd, N. Axen and S. Hogmark. 1999. Grooving wear of single-crystal tungsten carbide. Wear 230(2):165-174.

Ettmayer P. 1989. Hardmetals and cermets. Annual Review of Materials Science 19(1):145-164.

Evans A. G. and T. R. Wilshaw. 1976. Quasi-static solid particle damage in brittle solids—I. Observations analysis and implications. Acta Metallurgica 24(10): 939-956.

Exner H. E. 1979. Physical and chemical nature of cemented carbides. International metals reviews 24(1):149-173.

Fedrizzi L., S. Rossi, R. Cristel and P.L. Bonora. 2004. Corrosion and wear behaviour of HVOF cermet coatings used to replace hard chromium. electrochimica acta 49(17):2803-2814.

Fernandes C. M. and A. M. R. Senos. 2011. Cemented carbide phase diagrams: a review. International Journal of Refractory Metals and Hard Materials 29(4):405-418.

Gabriel A., H. Pastor, D. M. Deo, S. Basu and C. H. Allibert. 1986. New experimental data in the C--Fe--W, C--Co--W, C--Ni--W, C--Fe--Ni--W and C--Co--Ni--W cemented carbides systems and their application to sintering conditions. Int J Refract Hard Met 5(4):215-221.

Ghabchi A. 2011. Wear resistant carbide-based thermal sprayed coatings: process, properties, mechanical degradation and wear. PhD thesis. State University of New York at Stony Brook.

Ghabchi A., S. Sampath, K. Holmberg and T. Varis. 2014. Damage mechanisms and cracking behavior of thermal sprayed WC–CoCr coating under scratch testing. Wear 313(1):97-105.

Gouldstone A., N. Chollacoop, M. Dao, J. Li, A. M. Minor and Y. L. Shen. 2007. Indentation across size scales and disciplines: Recent developments in experimentation and modeling. Acta Materialia 55(12):4015-4039.

Gu S. 2000. Numerical simulations of a high velocity oxy-fuel thermal spraying system. PhD thesis. The University of Nottingham, UK.

Gu W. H., Y. S. Jeong, Kim, K. Kim, J. C. Kim, S. H. Son and S. Kim. 2012. Thermal oxidation behavior of WC–Co hard metal machining tool tip scraps. Journal of Materials Processing Technology 212(6):1250-1256.

Guilemany J. M. and J. M. DePaco. 1996. Structure/properties relationship of WC-Co coatings obtained by HVOF spraying using starting powders with different content in metallic matrix. Thermal Spraying Conference, (Thermische Spritzkonferenz). Düsseldorf (Germany). pp. 390-393.

Guilemany J. M., J. M. Miguel, S. Vizcaino and F. Climent. 2001. Role of three-body abrasion wear in the sliding wear behaviour of WC-Co coatings obtained by thermal spraying. Surface and Coatings Technology 140(2):141-146.

Guilemany J. M., J. Nutting, J. R. Miguel and Z. Dong. 1995. Microstructure characterization of WC-Ni coatings obtained by HVOF thermal spraying. Scripta metallurgica et materialia 33(1):55-61.

Guilemany J. M., J. Nutting, J. R. Miguela and Z. Dong. 1997. Microstructure formation of HVOF sprayed WC-Ni coatings deposited on low alloy steel. Materials and Manufacturing Processes 12(5):901-909.

Guilemany J. M., S. Dosta, J. Nin and J. R. Miguel. 2005. Study of the properties of WC-Co nanostructured coatings sprayed by high-velocity oxyfuel. Journal of Thermal Spray Technology 14(3):405-413.

Guilemany J.M., S. Dosta and J. R. Miguel. 2006. The enhancement of the properties of WC-Co HVOF coatings through the use of nanostructured and microstructured feedstock powders. Surface and Coatings Technology 201(3):1180-1190.

Guillermet A. F. 1989. Thermodynamic properties of the Co-WC system. Metallurgical transactions A 20(5):935-956.

Hashmi S. 2014. Comprehensive materials processing. Vol 4, Chapter 10. Elsevier, Newnes.

He J. and J. M. Schoenung. 2002. A review on nanostructured WC–Co coatings. Surface and Coatings Technology 157(1):72-79.

Holmberg K. and A. Mathews. 1994. Coatings tribology: a concept, critical aspects and future directions. Thin Solid Films 253(1):173-178.

Holmberg K. and Matthews A. 2009. Coatings tribology: properties, mechanisms, techniques and applications in surface engineering. 2nd edition. Elsevier Science.

Holmberg K., A. Laukkanen, H. Ronkainen, K. Wallin and S. Varjus. 2003. A model for stresses, crack generation and fracture toughness calculation in scratched TiN-coated steel surfaces. Wear 254(3):278-291.

Holmberg K., A. Laukkanen, H. Ronkainen, K. Wallin, S. Varjus and J. Koskinen. 2006. Tribological contact analysis of a rigid ball sliding on a hard coated surface: Part I: Modelling stresses and strains. Surface and Coatings Technology 200(12):3793-3809.

Ingelstrom N. and H. Nordberg. 1974. The fracture toughness of cemented tungsten carbides. Engineering Fracture Mechanics 6(3):597-607.

Ishikawa Y., J. Kawakita, S. Osawa, T. Itsukaichi, Y. Sakamoto, M. Takaya and S. Kuroda. 2005. Evaluation of corrosion and wear resistance of hard cermet coatings sprayed by using an improved HVOF process. Journal of Thermal Spray Technology 14(3):384-390.

Jacobs L., M. M. Hyland and M. De Bonte. 1999. Study of the influence of microstructural properties on the sliding-wear behavior of HVOF and HVAF sprayed WC-cermet coatings. Journal of Thermal Spray Technology 8(1):125-132.

Jacobs R., J. Meneve, G. Dyson, D. G. Teer, N. M. Jennett, P. Harris, J. von Stebut, C. Comte, P. Feuchter, A. Cavaleiro, H. Ronkainen, K. Holmberg, U. Beck, G. Reiners and C.D. Ingelbrecht. 2003. A certified reference material for the scratch test. Surface and Coatings Technology 174:1008-1013.

Jaworski R., L. Pawlowski, F. Roudet, S. Kozerski and F. Petit. 2008. Characterization of mechanical properties of suspension plasma sprayed TiO_2 coatings using scratch test. Surface and Coatings Technology 202(12):2644-2653.

Jia K. and T. E. Fischer. 1996. Abrasion resistance of nanostructured and conventional cemented carbides. Wear 200(1):206-214.

Jia K. and T. E. Fischer. 1997. Sliding wear of conventional and nanostructured cemented carbides. Wear 203:310-318.

K. H. Zum Gahr. 1998. Wear by hard particles. Tribology International 31(10):587-596.

Kamnis S. and S. Gu. 2006. 3-D modelling of kerosene-fuelled HVOF thermal spray gun. Chemical Engineering Science 61(16):5427-5439.

Karimi A., Ch. Verdon and G. Barbezat. 1993. Microstructure and hydroabrasive wear behaviour of high velocity oxy-fuel thermally sprayed WC-Co (Cr) coatings. Surface and Coatings Technology 57(1):81-89.

Kear B. H. and L. E. McCandlish. 1993. Chemical processing and properties of nanostructured WC-Co materials. Nanostructured Materials 3(1):19-30.

Kenny P. 1971. The application of fracture mechanics to cemented tungsten carbides. Powder Metallurgy 14(27):22-38.

Kübarsepp J., H. Klaasen and J. Pirso. 2001. Behaviour of TiC-base cermets in different wear conditions. Wear 249(3):229-234.

Kuiry S. 2012. Advanced Scratch Testing for Evaluation of Coatings. https://www.bruker.com/service/education-training/webinars/tribology.html (23/05/2016)

Lancaster J. K. 1967. The influence of substrate hardness on the formation and endurance of molybdenum disulphide films. Wear 10(2):103-117.

Laukkanen A., K. Holmberg, J. Koskinen, H. Ronkainen, K. Wallin and S. Varjus. 2006. Tribological contact analysis of a rigid ball sliding on a hard coated surface, Part III: Fracture toughness calculation and influence of residual stresses. Surface and Coatings Technology 200(12):3824-3844.

Lee C.W., J. H. Han, J. Yoon, M. C. Shin and S. I. Kwun. 2010. A study on powder mixing for high fracture toughness and wear resistance of WC-Co-Cr coatings sprayed by HVOF. Surface and Coatings Technology 204(14):2223-2229.

Lekatou A., D. Sioulas, A. E. Karantzalis and D. Grimanelis. 2015. A comparative study on the microstructure and surface property evaluation of coatings produced from nanostructured and conventional WC–Co powders HVOF-sprayed on Al7075. Surface and Coatings Technology 276:539-556.

Liu Y., Y. Qiao, J. He, E. J. Lavernia and T. E. Fischer. 2002. Near-nanostructured WC-18 Pct Co coatings with low amounts of non-WC carbide phase: Part I. Synthesis and characterization. Metallurgical and Materials Transactions A 33(1):145-157.

Luo W., W. Tillmann and U. Selvadurai. 2015. In situ wear test on thermal spray coatings in a large chamber scanning electron microscope. Journal of Thermal Spray Technology 24(1-2):263-270.

Maizza G., S. Grasso, Y. Sakka, T. Noda and O. Ohashi. 2007. Relation between microstructure, properties and spark plasma sintering (SPS) parameters of pure ultrafine WC powder. Science and Technology of Advanced Materials 8(7–8):644-654.

Marple B. R. and R. S. Lima. 2005. Process temperature/velocity-hardness-wear relationships for high-velocity oxyfuel sprayed nanostructured and conventional cermet coatings. Journal of thermal spray technology 14(1):67-76.

Mateen A., G. C. Saha, T. I. Khan and F. A. Khalid. 2011. Tribological behaviour of HVOF sprayed near-nanostructured and microstructured WC-17wt.% Co coatings. Surface and Coatings Technology 206(6):1077-1084.

Michalski A. and D. Siemiaszko. 2007. Nanocrystalline cemented carbides sintered by the pulse plasma method. International Journal of Refractory Metals and Hard Materials 25(2):153-158.

Milman Yu. V., S. Luyckx and I. T. Northrop. 1999. Influence of temperature, grain size and cobalt content on the hardness of WC–Co alloys. International Journal of Refractory Metals and Hard Materials 17(1):39-44.

Mohanty M., R. W. Smith, M. De Bonte, J. P. Celis and E. Lugscheider. 1996. Sliding wear behavior of thermally sprayed 75/25 Cr 3 C 2/NiCr wear resistant coatings. Wear 198(1):251-266.

Mura G., E. Musu and F. Delogu. 2013. Early stages of the mechanical alloying of TiC–TiN powder mixtures. Materials Chemistry and Physics 137(3):1039-1045.

Nahvi S. M. and M. Jafari. 2016. Microstructural and mechanical properties of advanced HVOF-sprayed WC-based cermet coatings. Surface and Coatings Technology 286:95-102.

Nerz J., B. Kushner and A. Rotolico. 1992. Microstructural evaluation of tungsten carbide-cobalt coatings. Journal of Thermal Spray Technology 1(2):147-152.

Niihara K. 1983. A fracture mechanics analysis of indentation-induced Palmqvist crack in ceramics. Journal of materials science letters 2(5):221-223.

Nohava J., B. Bonferroni, G. Bolelli and L. Lusvarghi. 2010. Interesting aspects of indentation and scratch methods for characterization of thermally-sprayed coatings. Surface and Coatings Technology 205(4):1127-1131.

O'Quigley D. G. F., S. Luyckx and M. N. James. 1997. An empirical ranking of a wide range of WC-Co grades in terms of their abrasion resistance measured by the ASTM standard B 611-85 test. International Journal of Refractory Metals and Hard Materials 15(1):73-79.

Oliver W. C. and G. M. Pharr. 1992. An improved technique for determining hardness and elastic modulus using load and displacement sensing indentation experiments. Journal of materials research 7(06):1564-1583.

Ortner H. M., P. Ettmayer, H. Kolaska amd I. Smid. 2014. The history of the technological progress of hardmetals. International Journal of Refractory Metals and Hard Materials 44:148-159.

Pawlowski L. 2008. The science and engineering of thermal spray coatings. 2nd edition. New York: John Wiley & Sons.

Perry A. J. 1981. The adhesion of chemically vapour-deposited hard coatings to steel—the scratch test. Thin Solid Films 78(1):77-94.

Perry A. J. 1983. Scratch adhesion testing of hard coatings. Thin Solid Films 107(2):167-180.

Pirso J., M. Viljus and S. Letunovits. 2006. Friction and dry sliding wear behaviour of cermets. Wear 260(7):815-824.

Polyanin A. D. and A. V. Manzhirov. 2006. Handbook of mathematics for engineers and scientists. Chapman and Hall/CRC, Boca Raton.

Pugsley V. A. and C. Allen. 1999. Microstructure/property relationships in the cavitation erosion of tungsten carbide–cobalt. Wear 233:93-103.

Qiao Y., T. E. Fischer and A. Dent. 2003. The effects of fuel chemistry and feedstock powder structure on the mechanical and tribological properties of HVOF thermal-sprayed WC–Co coatings with very fine structures. Surface and Coatings Technology 172(1):24-41.

Qiao Y., Y. Liu and T. E. Fischer. 2001. Sliding and abrasive wear resistance of thermal-sprayed WC-Co coatings. Journal of Thermal Spray Technology 10(1):118-125.

Rajinikanth V. and K. Venkateswarlu. 2011. An investigation of sliding wear behaviour of WC-Co coating. Tribology International 44(12):1711-1719.

Saha G. C. and T. I. Khan 2010. The corrosion and wear performance of microcrystalline WC-10Co-4Cr and near-nanocrystalline WC-17Co high velocity oxy-fuel sprayed coatings on steel substrate. Metallurgical and Materials Transactions a-Physical Metallurgy and Materials Science 41A(11):3000-3009.

Saito H., A. Iwabuchi and T. Shimizu. 2006. Effects of Co content and WC grain size on wear of WC cemented carbide. Wear 261(2):126-132.

Sanchez E., E. Bannier, M. D. Salvador, V. Bonache, J. C. Garcıa, J. Morgiel, and J. Grzonka. 2010. Microstructure and wear behavior of conventional and nanostructured plasma-sprayed WC-Co coatings. Journal of thermal spray technology 19(5):964-974.

Schubert W. D., M. Fugger, B. Wittmann and R. Useldinger. 2015. Aspects of sintering of cemented carbides with Fe-based binders. International Journal of Refractory Metals and Hard Materials 49:110-123.

Schwetzke R. and H. Kreye. 1999. Microstructure and properties of tungsten carbide coatings sprayed with various high-velocity oxygen fuel spray systems. Journal of Thermal Spray Technology 8(3):433-439.

Shao Gang-qin, Xing-long Duan, Ji-ren Xie, Xiao-hua Yu, Wei-feng Zhang and Run-zhang Yuan. 2003. Sintering of nanocrystalline WC-Co composite powder. Reviews on Advanced Materials Science 5(4):281-286.

Shetty D. K., I. G. Wright, P. N. Mincer and A. H. Clauer. 1985. Indentation fracture of WC-Co cermets. Journal of Materials Science 20(5):1873-1882.

Shipway P. H. and J. J. Hogg. 2005. Dependence of microscale abrasion mechanisms of WC-Co hardmetals on abrasive type. Wear 259(1):44-51.

Shipway P. H., D. G. McCartney and T. Sudaprasert. 2005. Sliding wear behaviour of conventional and nanostructured HVOF sprayed WC-Co coatings. Wear 259(7-12):820-827.

Sivaprahasam D, Chandrasekar SB, and Sundaresan R. 2007. Microstructure and mechanical properties of nanocrystalline WC–12Co consolidated by spark plasma sintering. International Journal of Refractory Metals and Hard Materials 25(2):144-152.

Sivaprahasam D., S. B. Chandrasekar and R. Sundaresan. 1985. Adhesion of TiC and Ti (C, N) coatings on steel. Journal of Vacuum Science & Technology A 3(6):2394-2400.

Stachowiak G. W. 2006. Wear: materials, mechanisms and practice. John Wiley & Sons, Inc.

Stewart D. A., P. H. Shipway and D. G. McCartney. 1999. Abrasive wear behaviour of conventional and nanocomposite HVOF-sprayed WC-Co coatings. Wear 225:789-798.

Stewart D. A., P. H. Shipway and D. G. McCartney. 2000. Microstructural evolution in thermally sprayed WC-Co coatings: comparison between nanocomposite and conventional starting powders. Acta Materialia 48(7):1593-1604.

Sudaprasert T. 2002. An investigation of microstructure and sliding wear in thermally sprayed WC-Co coatings. PhD thesis. The University of Nottingham, UK.

Sudaprasert T., P. H. Shipway and D. G. McCartney. 2003. Sliding wear behaviour of HVOF sprayed WC-Co coatings deposited with both gas-fuelled and liquid-fuelled systems. Wear 255(7-12):943-949.

Tekmen Ç., H. Çetinel, A. Türk and E. Çelik. 2004. Wear behaviour of plasma sprayed WC-Ni coatings. In: Mandal H, and Ovecoglu L, editors. Euro Ceramics Viii, Pts 1-3. p 589-592.

Tracey V. A. 1992. Nickel in hardmetals. International Journal of Refractory Metals and Hard Materials 11(3):137-149.

Uhrenius B., K. Forsen, B. O. Haglund and I. Andersson. 1995. Phase equilibria and phase diagrams in carbide systems. Journal of phase equilibria 16(5):430-440.

Upadhyaya G S. 1998. Cemented tungsten carbides: production, properties and testing. Noyes, New Jersey, USA.

Usmani S., S. Sampath, D. L. Houck and D. Lee. 1997. Effect of carbide grain size on the sliding and abrasive wear behavior of thermally sprayed WC-Co coatings. Tribology Transactions 40(3):470-478.

Vencl A., S. Arostegui, G. Favaro, F. Zivic, M. Mrdak, S. Mitrovic and V. Popovic. 2011. Evaluation of adhesion/cohesion bond strength of the thick plasma spray coatings by scratch testing on coatings cross-sections. Tribology International 44(11):1281-1288.

Verdon C., A. Karimi and J. L. Martin. 1997. Microstructural and analytical study of thermally sprayed WC-Co coatings in connection with their wear resistance. Materials Science and Engineering: A 234:731-734.

Verdon C., A. Karimi and J. L. Martin. 1998. A study of high velocity oxy-fuel thermally sprayed tungsten carbide based coatings. Part 1: Microstructures. Materials Science and Engineering A 246(1-2):11-24.

Vinayo M. E., F. Kassabji, J. Guyonnet and P. Fauchais. 1985. Plasma sprayed WC–Co coatings: influence of spray conditions (atmospheric and low pressure plasma spraying) on the crystal structure, porosity, and hardness. Journal of Vacuum Science & Technology A 3(6):2483-2489.

Voitovich V. B., V. V. Sverdel, R. F. Voitovich and E. I. Golovko. 1996. Oxidation of WC-Co, WC-Ni and WC-Co-Ni hard metals in the temperature range 500-800 C. International Journal of Refractory Metals and Hard Materials 14(4):289-295.

Voyer J. and B. R. Marple. 1999. Sliding wear behavior of high velocity oxy-fuel and high power plasma spray-processed tungsten carbide-based cermet coatings. Wear 225:135-145.

Wang Y., C. Chen, Z. Zhang, J. Long, T. Xu, X. Liu, L. Zhang, Y. Peng, P. Zhou and Y. Du. 2014. Phase equilibria in the Al–C–Ni–W quaternary system. International Journal of Refractory Metals and Hard Materials 46:43-51.

Watanabe M., A. Owada, S. Kuroda and Y. Gotoh. 2006. Effect of WC size on interface fracture toughness of WC–Co HVOF sprayed coatings. Surface and Coatings Technology 201(3):619-627.

Wayne S. F. and S. Sampath. 1992. Structure/property relationships in sintered and thermally sprayed WC-Co. Journal of Thermal Spray Technology 1(4):307-315.

Wayne S. F., J. G. Baldoni and S. T. Buljan. 1990. Abrasion and erosion of WC-Co with controlled microstructures. Tribology Transactions 33(4):611-617.

Wood R. J. K. 2010. Tribology of thermal sprayed WC-Co coatings. International Journal of Refractory Metals and Hard Materials 28(1):82-94.

Wu Y., J. Xiong, Z. Guo, M. Yang, J. Chen, S. Xiong, H. Fan and J. Luo. 2011. Microstructure and fracture toughness of Ti (C 0.7 N 0.3)-WC-Ni cermets. International Journal of Refractory Metals and Hard Materials 29(1):85-89.

Xie M., S. Zhang and M. Li. 2013. Comparative investigation on HVOF sprayed carbide-based coatings. Applied Surface Science 273:799-805.

Xie Y. and H. M. Hawthorne. 1999. The damage mechanisms of several plasma-sprayed ceramic coatings in controlled scratching. Wear 233:293-305.

Yandouzi M., E. Sansoucy, P. Richer, B. Jodoin and L. Ajdelsztajn. 2007. Deposition and characterization of WC–Co coatings prepared by continuous-and pulsed-cold spray processes. Proceedings of the The international thermal spray conference Beijing, China: ASM International (OH).

Yang Q., T. Senda and A. Hirose. 2006. Sliding wear behavior of WC-12% Co coatings at elevated temperatures. Surface & Coatings Technology 200(14-15):4208-4212.

Yang Q., T. Senda and A. Ohmorib. 2003. Effect of carbide grain size on microstructure and sliding wear behavior of HVOF-sprayed WC-12% Co coatings. Wear 254(1-2):23-34.

Yin B., H. D. Zhou, D. L. Yi, J. M. Chen, and F. Y. Yan. 2010. Microsliding wear behaviour of HVOF sprayed conventional and nanostructured WC–12Co coatings at elevated temperatures. surface Engineering 26(6):469-477.

Ying Chun Zhu, Chuan Xian Ding, Ken Yukimura, T. Danny Xiao and Perter R. Strutt. 2001. Deposition and characterization of nanostructured WC–Co coating. Ceramics International 27(6):669-674.

Ying-chun Zhu, Ken Yukimura, Chuan-xian Ding and Ping-yu Zhang 2001. Tribological properties of nanostructured and conventional WC–Co coatings deposited by plasma spraying. Thin solid films 388(1):277-282.

Yingfang X., W. Xingqing, C. Lidong, L. Xiaodong and G. Hailiang. 2006. Preparation of superfine-cemented carbide by spark plasma sintering. Journal of Wuhan University of Technology-Mater Sci Ed 21(1):42-45.

Zhang D., S. J. Harris and D. G. McCartney. 2003. Microstructure formation and corrosion behaviour in HVOF-sprayed Inconel 625 coatings. Materials Science and Engineering: A 344(1):45-56.

Zhang J. and A. T. Alpas. 1997. Transition between mild and severe wear in aluminium alloys. Acta Materialia 45(2):513-528.

Zhao L., M. Maurer, F. Fischer, R. Dicks and E. Lugscheider. 2004. Influence of spray parameters on the particle in-flight properties and the properties of HVOF coating of WC-CoCr. Wear 257(1):41-46.

Zhao X. Q., H. D. Zhou and J. M. Chen. 2006. Comparative study of the friction and wear behavior of plasma sprayed conventional and nanostructured WC-12%Co coatings on stainless steel. Materials Science and Engineering a-Structural Materials Properties Microstructure and Processing 431(1-2):290-297.

Żórawski, Wojciech 2013. The microstructure and tribological properties of liquid-fuel HVOF sprayed nanostructured WC–12Co coatings. Surface and Coatings Technology 220:276-281.

Zunega J. C. P., M. G. Gee, R. J. K. Wood and J. Walker. 2012. Scratch testing of WC/Co hardmetals. Tribology International 54:77-86.